STRESS FIELDS NEAR HOLES OR CUT-OUTS IN A UNIDIRECTIONAL FIBER REINFORCED COMPOSITE LAMINA

A Dissertation

Presented to the Faculty of the Graduate School

of Cornell University

In Partial Fulfillment of the Requirements for the Degree of

Doctor of Philosophy

by

Jing Shi

January 2008

STRESS FIELDS NEAR ELIPTICAL AND DIAMOND –SHAPED HOLES IN A UNIDIRECTIONAL FIBER REINFORCED COMPOSITE LAMINA

Jing Shi, Ph.D.

Cornell University 2008

Using shear-lag theory we analyze fiber tensile and matrix shear stresses near elliptical holes and diamond shaped cut-outs in a unidirectional composite lamina under a remote tensile stress applied in the fiber direction. Such holes and cut-outs are traditionally treated by modeling the material as a homogeneous orthotropic continuum, where the details of the fiber and matrix length-scale are lost. In this thesis, we extend the shear-lag framework (Hedgepeth, 1961) to build a computational model that can treat not only the removed material, viewed as a group of removed fiber segments, but also groups of fiber breaks adjacent to the hole as would occur as the remote load is increased.

In the shear-lag setting, the response to the hole ideally can be viewed as equivalent in effect to the superposition of the stress field responses of a sufficiently large number of isolated fiber breaks, which have a distribution of weights chosen to satisfy the stress free boundary condition around the hole. By appropriate modeling of the weight distribution of the isolated fiber break solutions, we apply the break influence superposition technique (BIS), developed in the context of the shear-lag model by Sastry, Beyerlein and Phoenix (1996), to calculate the stress field in the composite. Stress fields for three different hole shapes have been studied and compared to elastic continuum-based solutions.

This technique is more efficient than other numerical techniques as the computation time is tied only to the damaged area and the weight distributions can be approximated well using linear, and occasionally quadratic, polynomial functions. Once all the influence functions are computed, a priori, and stored as reusable quantities,

subsequent simulations take only a few minutes. The biggest advantage of this technique is that we can let the holes propagate in any fashion and calculate the stress field in a few minutes simply by adding the influence functions from the new fiber break to the initial ones and re-computing the weights. The same task would take a much longer time for finite element or finite difference methods since every single change demands a new mesh and remodeling the whole lamina.

BIOGRAPHICAL SKETCH

Jing Shi was born in Yan'an, China. She went to Nanjing No. 1 middle school in Nanjing and earned her undergraduate degree in Engineering Mechanics from Tsinghua University in Beijing, focusing on fluid mechanics.

She joined the department of Theoretical and Applied Mechanics in September 2003 and started working with professor Phoenix on the composite failure process in her second year.

She was not only the co-founder of the Cornell Chinese Folk Dance Troupe but also the first official president of the troupe.

To,

My parents

and

in loving memory of my grandfather

ACKNOWLEDGMENTS

Although a few words do not do justice to their contribution I would like to thank the following people for making this work possible. Arun Subbian for the discussion on the research. The staff at the department of Theoretical and Applied Mechanics, especially Cindy Twardokus for her support in solving all my trouble in the past four years. To Carlos Torre for his endless support, love and encouragement. All the girls in the Cornell Chinese Folk Dance Troupe (Amber) for keeping me happy and fit.

Special thanks to Leigh Phoenix for his guidance through all weathers. Without his tireless moral and academic support it would not have happened.

TABLE OF CONTENTS

LIST OF FIGURES

1. Introduction

Due to their high strength and stiffness and the availability of matrix materials in a wide range of properties, fiber-reinforced material are widely used as building blocks in advanced composites. However, their anisotropy and lack of ductility make it necessary to fully understand the effect of stress concentrations on fracture behavior. Traditional approaches have been focused on cracks where no material is actually removed, and efficient methods to simulate the propagation of the holes in the composite plane have been hard to develop. The aim of this work is to study the stress concentrations near elliptical holes, notches or cuts in a unidirectional, fiber-reinforced lamina under tension where the material is removed by drilling, sawing, or by a hypervelocity projectile or inactivated by severe debonding. Using the influence superposition technique we investigate the micro-structural factors which govern the transverse propagation of a hole by breaking fibers. Though actual structures may consist of several layers of unidirectional or multidirectional laminate, a fundamental issue is to understand the fracture behavior of a single lamina.

Predicting the fracture behavior of unidirectional fibrous composites consisting of elliptical holes or cuts has been tackled in several ways including (1) computational methods, (2) elasticity methods treating the material as a homogeneous orthotropic continuum where all shapes have finite curvatures and crack singularities are observed through limiting arguments (Sarah M. Bishop,1972; R. T. Potter, 1977, Williams, 1953) and (3) the mathematical stress field solutions for idealized models that are built on classical shear-lag analysis (Hedgepeth and Van Dyke, 1969; Beyerlein and Phoenix 1996; Beyerlein, Phoenix and Sastry 1996).

Computational approaches, such as finite element methods and finite difference techniques typically require the full discretization of the composite so only very small composites can be treated. Furthermore, it is extremely difficult to simulate the propagation of the hole because each new fiber break requires a new discretization and much more calculation. On the other hand, the shear-lag model uses orders of magnitude less degrees of freedom than similar 3-D finite element analyses and the computation effort is mainly determined by the size of the crack or hole, not the composite volume. Most importantly, the extra load related to the new fiber break is only dependent on the number of the broken fibers and all the original influence functions can be stored and reused leading to a much faster and more efficient simulation. Therefore, compared to finite element analysis, the shear-lag model can handle much larger composites with holes and notches of any shape.

There has been a tremendous amount of theoretical work done using elastic analysis assuming that the lamina is infinite, homogeneous, and linearly elastic and in a state of plane stress. Williams (1953) studied stress singularities due to a wedge in a plate subjected to extension in plane for different kinds of boundary conditions. He found that unbounded stresses occur for all boundary conditions for vertex angle between 180 and 360 degrees. The log scale of the tensile stress and the shear stress decays along the crack plane linearly with the distance to the crack tip. Several researchers (Savin, 1961; Green, 1945; Smith, 1944) derived theoretical solutions for the stresses near an elliptical hole in an orthotropic sheet under tension. Bishop (1972) worked out the general solution for stress field in an orthotropic material with an elliptical hole and applied it to a unidirectional carbon fiber composite with tension applied parallel to the fiber direction. The results show that the maximum tensile stress occurs at the tip of the elliptical hole and its magnitude is inversely proportional of the eccentricity of the ellipse $\varepsilon = b/a$. Furthermore, the maximum

tensile stress is solely dependent on the shape of the hole and the orthotropic material stiffness properties. The magnitude of the tension maxima multiplied by the eccentricity of the ellipse $\varepsilon(\sigma_x/\sigma_\infty)_{\max}$ is of very similar magnitude throughout the eccentricity range $0 \le \varepsilon \le 1$.

At the same time, experimental studies of the effect of a hole on the tensile fracture of multidirectional fiber-reinforced plastic laminates have enjoyed considerable success. It was shown that the fracture stress is a function of hole size (Waddoups, Eisenmann and Kaminski, 1971; Whitney and Nuismer, 1974) and the propagation or restraint of a hole depends on the micro-structural conditions at the crack tip (Mandell et al, 1965). Potter (1977) showed that cavities in the laminate may be divided into 'large' or 'small' categories as defined by their tendency to cause catastrophic fracture behavior and the hole size effect is a direct result of the material heterogeneity, governed by the properties of the fiber, matrix and fiber/matrix interface. A lamina with a 'large' cavity may be treated as a homogeneous brittle material and its fracture property can be predicted by elastic analysis such as Bishop (1972). On the other hand, for small holes, the stable tensile stress at the hole tip indicated by elastic analysis may become considerably greater than the apparent composite tensile strength before fracture occurs. "Small" holes have to be characterized by the fact that the fiber failures do not initiate the sequential fiber failure process but form stable damage zones which consist of matrix and fiber-matrix interface failures propagating parallel to the fiber direction. Mandell, Wang and McGarry (1975) observed that localized failure at the hole tip increases the damage zone from which failure ultimately propagates.

In the case of elastic analysis, questions of validity arise. First, the fibrous composite sheet with an elliptical hole in it may be considered homogeneous if the radius of the hole tip in the sheet is large compared to the fiber diameter and the

sheet is large compared to the size of the hole. Meanwhile, the matrix interfaces have several crucial properties that can't be homogeneous. The matrix and fiber-matrix interface can be much weaker in shear compared to comparable shear strength in a homogeneous metal material. Yielding, debonding or fiber pull-out over several fiber diameters may occur to some extent. Also, it is very unclear how to interpret the stress fields with the inherent local length scales such as the fiber diameter, fiber spacing and the effective fiber load transfer length near a break, assuming the lamina is actually anisotropic and heterogeneous. Nevertheless, in many engineering situations, circular holes and notches in the composite lamina satisfy the homogeneous assumption and elastic analysis is a good enough approach.

Second, the failure in a composite lamina involves a complex statistical progression of random fiber failures once one or more weak fibers break under increasing load. The matrix transfers the local stress from the broken fibers to the surviving fibers through shear. Experiments show that matrix plasticity and sliding frictional resistance of fiber pull-out largely determine the composite fracture properties. In the crack tip, fibers do not break precisely along one perpendicular plane even though that may be the location of the highest stress concentration. Previous studies show that fiber strength is typically highly random and strongly dependent on the length scale of the loaded fiber segment. In continuous fiber composites, for instance, fiber elements may show coefficients of variation up to 40%, leading to significant fluctuation in the local fiber strength. As a result, fiber elements, which are both overstressed and weak, are the most likely to break. Therefore, the length scales of load transfer along overstressed fibers are just as important as the actual stress concentrations in the area of the hole.

Finally, elastic analysis formulations become intractable once fiber breaks are not nicely aligned but are close enough that the stress fields can interact with

each other. In this case it very unlikely one can get analytical solutions for the progression of fiber failure ahead of the edge of the hole. Thus the use of elastic analysis from a homogeneous material perspective is very limited.

All these factors lead to a complex failure process at the edge of a hole in a unidirectional composite material, thus leading to inapplicability of continuum models where the hole shape rather than the diameter is the crucial characteristic. In order to model failure activity around a hole, we need an efficient computational model that can not only treat the hole where the material is removed or inactivated, but also can accommodate new fiber breaks near the hole edge and the local stress transfer activity among surviving and failed fiber and matrix elements at the high local tensile and shear stresses.

The shear-lag model for fibers originated, in its simplest form, with Cox (1952). The model so far has been explored in many versions and applications for planar and regular geometric arrays of fiber breaks (Goree and Gross, 1979; Hedgepeth and Van Dyke, 1967; Van Dyke and Hedgepeth, 1969; Hikami and Chou, 1990; Fukuda and Chou, 1981; Fichter, 1969; Beyerlein and Phoenix, 1996). Chou (1992) summarizes and highlights results of many studies on shear-lag analysis. As mentioned earlier, Hedgepeth's (1961) shear-lag model takes on the Cox (1952) assumptions that the fiber carries the entire tensile load, and deforms only in simple tension as modified by shear tractions imposed by the matrix. On the other hand, the matrix, under relative axial displacements between the fibers, deforms only in shear between the fibers, but sustains no axial load. With these simplifications of the full elasticity equations, the differential equilibrium equations reduce to a form in which the stresses found in any given fiber or matrix bay depend only on fiber axial coordinates, ξ, and fiber location, n. Essential features of the failure propagation can be tackled including matrix plasticity in shear, fiber matrix

debonding, matrix closing tractions at a fiber break or tip of a larger break cluster and fiber pull-out effects. This model is appropriate for a unidirectional fiber-matrix lamina in tension, in which the fiber extensional stiffness greatly exceeds the matrix shear modulus.

Several authors have extended this original model of Hedgepeth (1961) by modifying the geometric arrangement of fiber breaks, by accounting for matrix yielding and friction after debonding at the fiber-matrix interface, by allowing the matrix to carry appreciable tensile load and by considering tensile stress transverse to the fiber direction (Goree et al., 1989; Rossettos and Olia, 1993; Sastry and Phoenix, 1993; Wolla and Goree, 1987; Ochiai et al., 1991). Hedgepeth and Van Dyke (1967, 1969) developed the two-dimensional elastic-perfectly plastic matrix model and a complete debonding model where they obtained an implicit analytical solution for the stress concentration in fiber elements immediately adjacent to a single, isolated fiber break. Goree and Gross (1979, 1980) extended Hedgepeth's two dimensional model to include the effects of various arrangements of fiber breaks as well as matrix yielding and splitting. Dharani et al. (1983) developed another extension of Hedgepeth's model to account for both longitudinal yielding and longitudinal fiber "damage" ahead of the crack. The main drawback in work other than Sastry and Phoenix (1983) was that symmetry was assumed where all breaks existed in a transverse plane. The work in Sastry and Phoenix (1983) and later work by Bayerlein and Phoenix (1977, 1993) allowed breaks to be placed anywhere in the plane, as is the case in this thesis.

The major criticism of the shear-lag model is that it doesn't model the full field equations of linear elasticity. Though adequate when the fiber volume fraction V_f is high enough for the fibers to support almost all the tensile load, the shear-lag model is not adequate when the fiber and matrix stiffness are comparable and matrix

yield strength is high, or when the fiber volume fraction, V_f is very low. Tripathi et al. (1996) and Nairn (1988) show various shortcomings of the axisymmetric shear-lag model in such circumstances. Nedele and Wisnom (1994) and Case and Reifsnider (1995) suggest that the shear-lag model is locally inaccurate compared to their exact analysis and accurate numerical calculations for one fiber break in a three dimensional composite. However these models ignore the inability of the matrix to support singular shear stress, or even shear stresses that are at their largest an order of magnitude less than the fiber tensile strength. These effects dramatically attenuate tensile stress gradients in the fiber compared to the assumption that the matrix shear strength and interface strength are unbounded.

Shear-lag models for higher effective V_f values often catch the main features of experimental data to the level of resolution experimentally possible (Netravali et al. 1989; Gulino et al. 1991; Sastry et al. 1993; Schadler and Galiotis 1995; Amer and Schadler, 1998; van den Heuvel et al. 1998; and He et al. 1999). Reedy (1984) shows that the stresses determined by shear-lag model are a good reflection of the true stresses, at least locally averagely down to a length scale of about one fiber diameter, by comparing the results with detailed 3-D finite element calculations on a composite lamina of several fibers and with a few breaks. Beyerlein, Phoenix and Sastry (1996) show that the stress calculations from the LEFM and shear-lag model actually do achieve good agreement in the crack tip region where LEFM is valid. Their study also shows that the agreement actually improves as the transverse stiffness becomes much greater than the matrix shear stiffness, as may occur in plane strain situations. Since a unidirectional composite is inhomogeneous, agreement for a crack containing only a few fiber breaks is not truly expected but nonetheless turns out to be quite good. These results for a transverse central crack lamina not only boost confidence in the shear-lag model and

increase its validity, but they also emphasize some fundamental advantages of the shear-lag model.

A key development in handling shear-lag problems has been the break influence superposition (BIS) technique (Sastry and Phoenix, 1993) where hundreds of non-aligned fiber breaks and random sequences of such breaks can be handled easily (Beyerlein and Phoenix,1996a and b), but the matrix was treated as elastic. To treat matrix yielding and debonding, Beyerlein, Phoenix and Sastry (1995) developed an initial, simplified version, where uniformly shaped, corrective shear loads are applied to each matrix element in order to compensate for its 'virtual' elastic behavior beyond the point where it physically undergoes plastic yielding. However, the shear stress profiles across matrix elements near fiber breaks have high slope and curvature so that the method becomes inaccurate for longer yield zones. The quadratic influence superposition technique (QIS) technique, introduced by (Beyerlein and Phoenix, 1996), was designed to overcome this shortcoming by making use of uniform, linear and parabolic corrections in the influence function technique.

Compared to other approaches, the influence superposition technique has the advantages of evaluating the stress distributions everywhere in an inhomogeneous unidirectional fiber composite given any number and any configuration of fiber breaks. This was a major shortcoming of the Hedgepeth (1961) version where breaks were aligned only along the vertical axis of symmetry.

In this thesis, we extended BIS and QIS technique to study the effect of holes of various shapes on the tensile fracture of a unidirectional fiber reinforced lamina. The basic idea is similar to the continuously distributed dislocation technique.

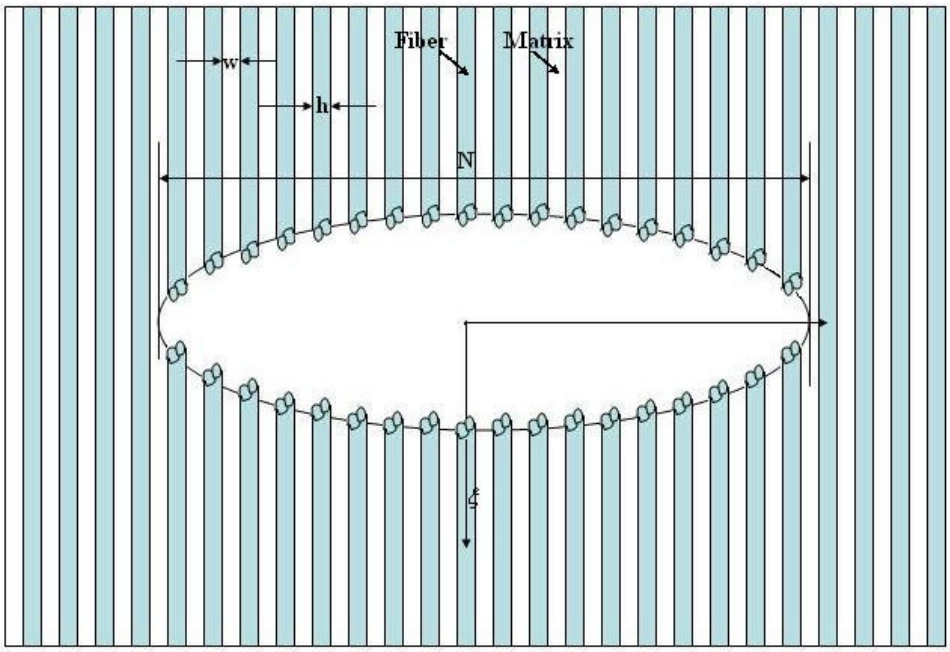

Figure 1. 1. Two-dimensional infinite lamina with a central hole consisiting of N broken fibers where the material is removed.

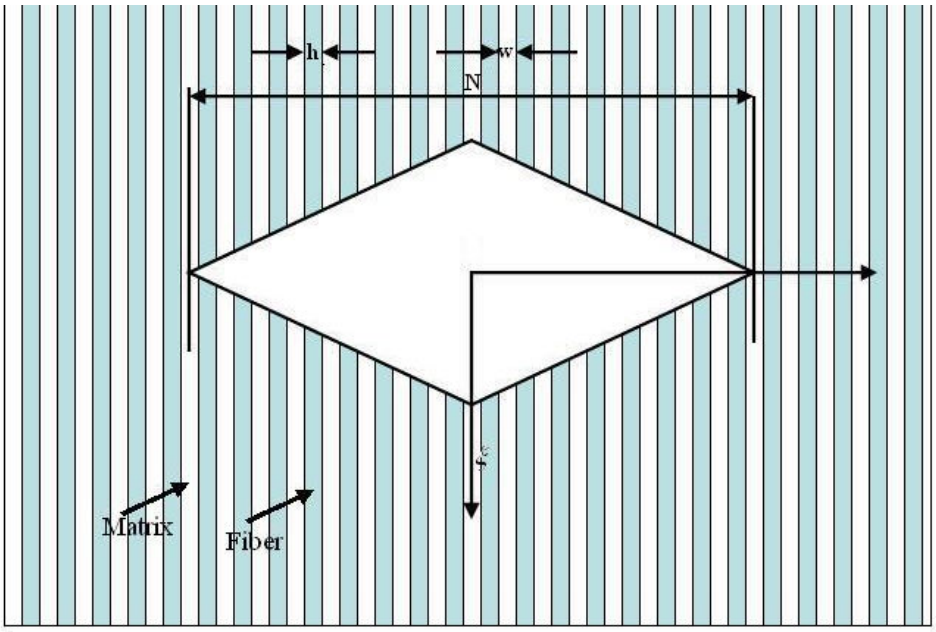

Figure 1. 2. Two-dimensional infinite lamina with a central diamond-shaped wedge consisiting of N broken fibers where the material is removed.

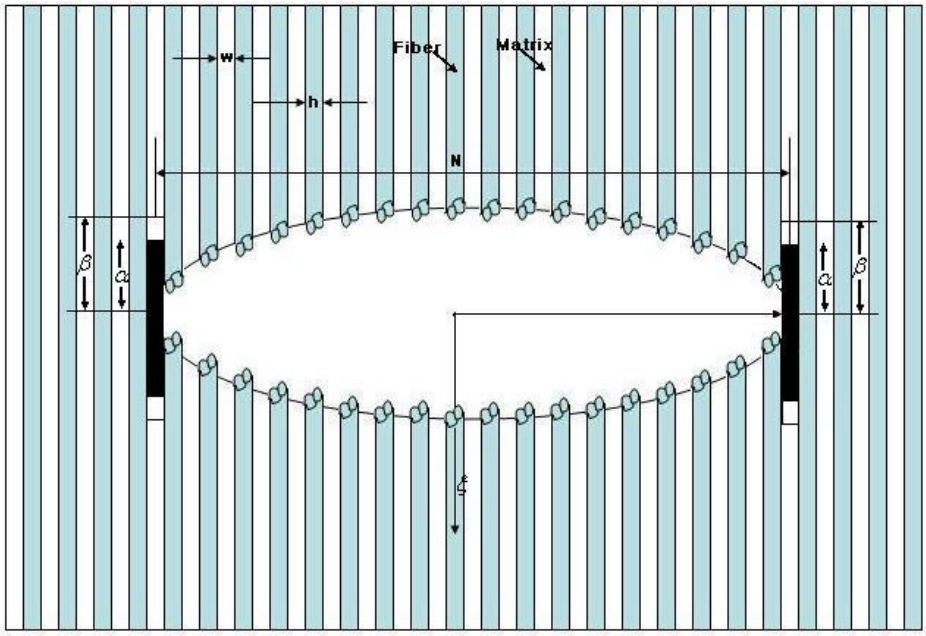

Figure 1. 3. Two-dimensional infinite lamina with a central hole where material is removed from *N* fibers and, debond $0 \le \xi \le \alpha$ and yield zones $\alpha \le \xi \le \beta$ at the tip.

In the actual problem the fiber is physically absent from the hole, but in our model the same effect is accomplished by modeling the fiber, originally within the hole boundary, as a sufficiently large number of linked fiber breaks with appropriate influence weights to unload them in such a way as to satisfy the traction free boundary condition at the hole edge. In our model, instead of placing many fiber breaks along each fiber in the hole, in order to deactivate them, we introduce a weight distribution of fiber breaks but also use segments with distributed fiber breaks to model the physical gap between fiber ends along the hole edge. The goal is to evaluate the stress field more efficiently, and to eliminate the need for small elements in the hole.

Our computationally efficient model will not only treat the removed material around the hole but we will also introduce new fiber breaks at the hole edge as would occur if the far field applied stress were high enough to break fibers at flaws.

The idea is to see whether these breaks will cause even more breaks as though the hole were simply a crack.

The simple geometry we use in the following chapters is described in Figures 1.1, 1.2 and 1.3. Figure 1.1 and 1.2 illustrate the two dimensional lamina with a transverse central hole or wedge where the material is removed containing N broken fibers aligned perpendicular to the fiber axis respectively, and Figure 1.3 shows a hole in a two-dimensional laminate with local matrix yielding, and where α and β are the normalized extent of the yield and debond zones, respectively.

We will first briefly present the fundamentals of the shear-lag method and investigate the weight distribution of distributed fiber breaks for different cases. Then we study the tensile and shear stress fields near different kinds of holes in an infinite fibrous composite plane under tension when the fiber and matrix deform elastically. Connection will be drawn and comparison will be made between the elastic solutions of Bishop (1972) and Williams (1953) and the shear lag solution. We will also extend the hole size in the plane by introducing new fiber breaks at the edge of the hole forming short crack tips and assuming all the fiber elements have uniform strength. Some key factors that would allow further propagation at the tips are identified based on the numerical results. Finally, we will investigate the stress field involving the cases of an elastic matrix, an elastic-plastic matrix in shear, and fiber matrix debonding, and obtain some insight into the effect of the damage zone on the local stress distribution and conditions for eventual propagation of the hole.

In principle, this computational technique can handle an arbitrarily shaped hole of any size. This gives us the advantage of being able to compare the stress field before and after propagation of a small crack way from the hole edge, and we can study the effect of the new fiber breaks on the stress distribution in the plane. For cases involving matrix yielding or debonding, the stress and strain distribution

everywhere as well as the extent and shape of the yield and debond zones near the hole are calculated for a given the applied stress and hole shape. To make the method more effective and to improve the computation speed, all the influence functions are computed a priori and stored in memory. In this way, the subsequent computation takes only a few minutes for any given hole.

In the infinite, planar, composite lamina containing N broken fibers, the stresses and strains develop monotonically under an increasing remote tensile load and we extend the hole by introducing new fiber breaks at the most overloaded loaded points on the assumption that all the fibers have uniform strength. As mentioned, in reality this is far from true since the fiber elements may exhibit coefficients of variation that can exceed 40%, suggesting significant fluctuations in the local material strength and possible patterns of breaks. Clearly in the case of such high variability in fiber strength the criterion for hole propagation may not be reflective of the actual failure of weak fibers occurring at random in the composite plane. However, although the progression of fiber breaks from the side of the hole and through the entire plane is subjected to the variations in individual fiber strengths, the mean position of the growing crack front will largely behave as though the fibers are of uniform strength. Furthermore, it is fundamental to the failure progression that the fiber stress concentration is limited by the matrix shear strength. Together with the fiber strength distribution, the limitation on the fiber stress concentration determines the effective or apparent fiber strength and controls the fiber load carrying efficiency of the composite.

2. Fundamentals of the Shear-Lag Analysis

Consider a large two-dimensional fiber reinforced composite lamina loaded in tension and containing a central group of N contiguous fiber breaks transverse to the fiber direction. Hedgepeth (1961) formulated and solved this problem for an aligned transverse array using a shear-lag model, and the most quoted results are the stress concentration factors on the fiber immediately adjacent to the last broken fiber.

As mentioned earlier this shear-lag theory (Hedgepeth, 1961) assumes that the fibers carry all the tension and the matrix transmits the load between fibers as it deforms only in shear. This assumption greatly simplifies the analysis and considerably decouples the differential equilibrium equations, leading to the result that the tensile stress and shear stress are only dependent on the fiber axial coordinate ξ and fiber number n. Hedgepeth (1961) suggested that this model is only appropriate for unidirectional fiber-matrix lamina in tension where the fiber stiffness is much larger than the matrix shear modulus. In recent years much work has been done on the shear-lag model as mentioned in the Introduction (Goree et al., 1989; Rossettos and Olia, 1993; Sastry and Phoenix, 1993; Wolla and Goree, 1987; Ocjoao et al., 1991; Hikami and Chou, 1990; Gross, 1979 and 1980; Dharani et al., 1983; Beyerlein and Phoenix 1996; Beyerlein and Phoenix 1996a,b; Beyerlein, Phoenix and Sastry 1996).

Thus far most studies have been devoted to obtaining the tensile and shear stress distribution along the crack plane and near a crack, with some modifications to the original analysis and its connection to elastic analyses assuming the material is an orthotropic continuum. In this thesis, we will focus on the stress field near a hole in a infinite, planar two-dimensional fiber reinforced composite with and without matrix yielding or debonding between fibers, and connection will be made

to the stress and strain fields calculated from an elastic analysis of a homogeneous orthotropic continuum.

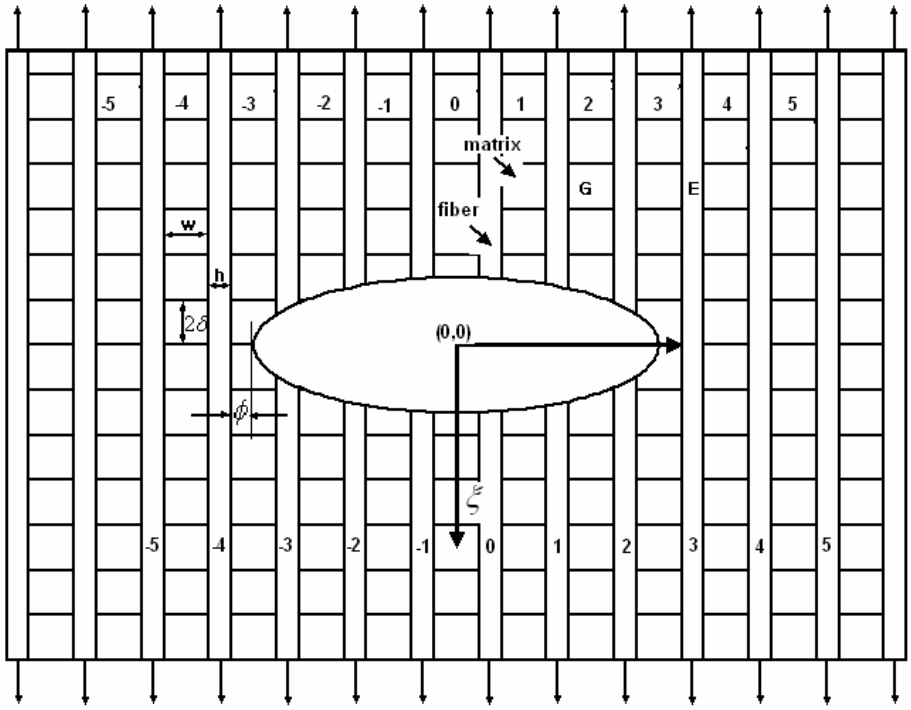

Figure 2.1. Discretized two-dimensional fiber-reinforced composite with equal length fiber and matrix elements with dimensions as labeled.

To determine fiber and matrix stress and displacement distributions near an arbitrarily shaped hole, it is convenient to discretize the composite in the hole and the damaged matrix (yielded or debonded) regions outside the hole. Elsewhere, the discretization is used merely to establish spatial fiber and matrix points at which to calculate the stresses of interest for plotting purpose. Unlike the finite element or other computational scheme, which requires full discretization of the whole composite, the shear-lag analysis is more exact and efficient.

2.1 Shear-lag analysis

Figure 2.1 illustrates the two-dimensional lamina with an elliptical hole in the form of a long row of N broken and removed fiber segments of varying lengths and with the transverse hole axis aligned perpendicular to the fiber axis. Here N is decided by the fiber spacing and volume fraction and the transverse dimension of the hole. Evenly spaced fiber and matrix elements are arranged in a brick-like fashion mainly for location addressing and plotting purposes. All the fiber and matrix elements are elastic and of length 2δ, where δ is much smaller than the characteristic load transfer length, which is the required length for an isolated broken fiber to recover its elastic load as determined for instance by Hedgepeth (1961). In the infinite lamina, the center fiber is numbered $n = 0$, the fibers to the right are numbered $n = 1,2,...,\infty$ and those to the left, $n = -1,-2,...,-\infty$. The matrix bay to the right of fiber n is matrix bay n. Likewise, along the loading axis, the respective fiber and matrix elements are numbered in the positive direction from $(n, m = 0)$ to $(n, m = \infty)$ and in the negative direction from $(n, m = -1)$ to $(n, m = -\infty)$. Thus (n, m) refers to a specific fiber element or matrix element. Also indicated in Figure 2.1 is E, the Young's modulus of the fibers; G, the effective shear modulus of the matrix; w, the effective fiber spacing; h, the fiber width and laminate thickness; and A the cross-sectional area of a fiber. (For the idealization of square fibers $A = h^2$.)

The shear-lag assumptions are incorporated when deriving the force equilibrium equations for fiber and matrix elements along the fiber axis. Let $p_n(x)$ and $u_n(x)$ be the force and displacement in fiber n at location x, under the remote load p per fiber applied at $x = \pm\infty$. Since the matrix transmits only shear forces, the shear force per unit fiber length is related to the differential displacements of the

two adjacent fibers. The effective shear stress τ_n and the shear strain γ_n in matrix bay n are

$$\tau_n(x) = \frac{G\left[u_{n+1}(x) - u_n(x)\right]}{w} \tag{2. 1}$$

and

$$\gamma_n(x) = \frac{\left[u_{n+1}(x) - u_n(x)\right]}{w} \tag{2. 2}$$

Therefore, the shear force per unit length applied on the fiber by the matrix is $\tau_n(x)h$. For fiber regions not in contact with yielded or debonded matrix elements, balance of forces in the fiber direction results in the following equilibrium conditions:

$$p_n(x) = EA\frac{du_n(x)}{dx} \tag{2. 3}$$

and

$$\frac{EAd^2u_n(x)}{dx^2} = \frac{-Gh\left[u_{n+1}(x) - u_n(x)\right] + Gh\left[u_n(x) - u_{n-1}(x)\right]}{w} \tag{2. 4}$$

For convenience, the above variables are normalized into non-dimensional variables. The normalized fiber loads P_n, fiber displacements U_n, matrix shear strain Γ_n and axial coordinate ξ are

$$P_n = \frac{p_n}{p^*} \tag{2. 5}$$

$$U_n = \frac{u_n}{p^*\sqrt{\frac{w}{EAGh}}} \tag{2. 6}$$

$$T_n = \frac{\tau_n}{p^*}\sqrt{\frac{wEAh}{G}} \tag{2. 7}$$

$$\Gamma_n = U_{n+1} - U_n = \frac{\gamma_n}{p^*}\sqrt{wEAGh} \tag{2. 8}$$

and

$$\xi = \frac{x}{\sqrt{\frac{EAw}{Gh}}} \tag{2. 9}$$

When the matrix deforms elastically, $\tau_n = G\gamma_n$ and thus T_n and Γ_n are equivalent. The previously mentioned Hedgepeth characteristic load transfer length is the denominator of equation (2.9) $\sqrt{EAw/Gh}$. In previous work (Beyerlein and Phoenix, 1996; Beyerlein, Phoenix and Sastry, 1996), the matrix size is nominally set as $2\delta = 1/5$. One interest in this work is whether we can choose δ to be much larger than in previous approaches.

Note that if the matrix is deforming elastically and there is no debonding, then notationally, p^* is the remote load. If the elastic matrix has local yielding or debonding, we use p_y^*, which is the remote tensile force per fiber at the threshold of matrix yielding around a single fiber break at shear stress τ_y, or the interfacial threshold stress for debonding. The remote load per fiber P is then

$$P = \frac{p}{p^*} \quad \text{or} \quad P = \frac{p}{p_y^*} \tag{2. 10}$$

where

$$p_y^* = \tau_y \sqrt{\frac{wEAh}{G}} \tag{2. 11}$$

By introducing these non-dimensional parameters, the equilibrium equations for fibers flanking the damaged matrix bays are

$$\frac{d^2U_n(\xi)}{d\xi^2} + U_{n+1}(\xi) - 2U_n(\xi) + U_{n-1}(\xi) = 0 \tag{2. 12}$$

$$P_n(\xi) = \frac{dU_n(\xi)}{d\xi} \tag{2. 13}$$

and

$$P_n(\pm\infty) = P \tag{2. 14}$$

In the case of a central crack, the additional boundary conditions are zero tensile loads on all N broken fibers, i.e.

$$P_n(0) = 0 \quad \text{for } -(N-1)/2 \le n \le (N-1)/2 \tag{2. 15}$$

In general, the fiber loads at all the broken fiber ends are zero no matter what the hole shape is. Consequently, the form of the solution is independent of the elastic constants and volume fraction of fiber $V_f = h/(h+w)$.

Elastic-perfectly plastic behavior is captured by an interface constitutive model. The matrix shear stress T_n at a given position increases elastically up to the normalized yield stress T_y and in the case of pure yielding remains constant at T_y under increasing applied composite load, P. Alternatively when the shear strain Γ_n reaches the normalized debond strain Γ_d, the matrix debonds from the fiber. As a result, the fiber slides exerting a constant interfacial frictional shear stress T_d on the matrix. The nonlinear deformation under increasing shear strains basically includes the features that shear stress rises to a maximum, the matrix separates from the fiber and then undergoes relative sliding under a frictional shear resistance.

In our first example of pure yielding, we assume $\Gamma_d = \infty$ so that pure yielding occurs under shear stress $T_n = T_y$ as the shear strain exceeds the yield strain Γ_y. For our pure debonding example, we assume that once the interfacial shear strength T_y is reached, as the shear strain $\Gamma_n \ge \Gamma_y = \Gamma_d$. In the mixed case one may have yielding beginning at shear strain Γ_y but up the point Γ_d at which point a sliding frictional shear stress T_d takes over.

The equilibrium equations for the last broken fiber $n = N^* = (N-1)/2$ and the first surviving fiber flanking the matrix yielded region $n = N^* + 1$ in $\xi > 0$ are, respectively,

$$\frac{d^2 U_{N^*}(\xi)}{d\xi^2} + U_{N^*-1}(\xi) - U_{N^*}(\xi) - T^* = 0 \qquad (2.16)$$

and

$$\frac{d^2 U_{N^*+1}(\xi)}{d\xi^2} + U_{N^*+2}(\xi) - U_{N^*+1}(\xi) + T^* = 0 \qquad (2.17)$$

where $T^* = T_d$ for the debonded region and $T^* = T_y = 1$ for yielded region.

For many broken fibers (i.e. a very large circular hole) and for high remote load $(P >> P_y)$, the neighboring matrix bays will also begin to yield at some distance away from the crack plane or at the boundary of the hole. However, our study shows that the matrix bay between the last broken fiber and the first surviving fiber has by far the largest stress concentration and the load decays fairly fast in either direction. Therefore it is reasonable to assume that yielding and debonding develops only in the neighboring matrix regions at both crack tips in our investigation, i.e, as the remote load increases beyond P_y, the yielded region will only extend parallel to the fibers.

2.2 Three basic problems

The influence superposition analysis (Sastry and Phoenix, 1993) in the shear-lag model is able to solve for fiber and matrix stress profiles due to arbitrary holes where the material is removed or inactivated in the lamina. In this paper, the location of the N initial broken fibers is positioned at the centers of the N fiber elements along the central transverse plane. There are three "building block", elastic solutions required to approximate the complete solution for a composite

containing arbitrarily shaped holes where the material is removed, and for a perfectly-plastic matrix, as well relatively weak fiber-matrix interfacial shear strength followed by frictional sliding. The first problem is called "isolated break problem" which is the stress concentration due to a single break located at fiber element $(0,0)$ and first solved by Hedgepeth (1961). The second one is the "load couple problem", which is the stress distribution due to a counter-clockwise point shear force couple, solved by Sastry (1994) and adapted by Beyerlein and Phoenix (1996). The third basic element in this computational model is called "isolated segment with distributed breaklets" (ISDB). To model the gap between broken fiber ends at the hole edge and where the material has been removed, we extend the first basic problem using the philosophy of distributed dislocation theory by putting a distribution of infinitesimal fiber breaks with distributed weight along the gap to satisfy the boundary condition that the tensile stress is zero in the gap. We name this segment filled with infinitesimal distributed fiber breaks as an "isolated segment with distributed breaklets" (ISDB). In a later section we will provide more details on how to distribute the weights and apply the concept in the influence function technique.

2.2.1 Basic solution 1: Isolated break problem

In this problem, a unit compressive force is applied to each end of the break (with no material removed) and zero tensile force is applied at infinity. For the positive half plane, $\xi > 0$, the boundary conditions are

$$L_{b,0}\left(0^{+}\right) = -1 \tag{2. 18}$$

$$V_{b,n}(0) = 0 \text{ for } n \geq 1 \text{ and } n \leq 1 \tag{2. 19}$$

and

$$\frac{dV_{b,n}(\infty)}{d\xi} = 0 \text{ for } -\infty < n < \infty \tag{2. 20}$$

where L and V are the fiber loads and displacements respectively. For the full plane solution, L and V are constructed to be symmetric and anti-symmetric, respectively, about $\xi = 0$. We apply the subscript "b" to distinguish the single break problem from the general problem. The solutions to equation (2.12) with the above boundary conditions are called virtual quantities, $L_{b,n}$ and $V_{b,n}$.

This problem was originally solved by Hedgepeth (1961) but Beyerlein, Phoenix and Sastry (1996) gave a more useful method by considering an equivalent problem with displacement boundary conditions, that is, to replace equation (2.18) with $V_{b,0}\left(0^+\right) = -\pi/4$, which in the end gives exactly the desired solution since the loads on the broken fiber ends become exactly -1. We can obtain the solution by using the following discrete Fourier transform approach:

$$V\left(\xi,\theta\right) = \sum_{n=-\infty}^{\infty} V_n\left(\xi\right)\exp\left(-in\theta\right) \tag{2. 21}$$

$$V_n\left(\xi\right) = \frac{1}{2\pi}\int_{-\pi}^{\pi} V\left(\xi,\theta\right)\exp\left(in\theta\right)d\theta \tag{2. 22}$$

For $\theta > 0$, the equilibrium equation thus become

$$\frac{\partial^2 V\left(\xi,\theta\right)}{\partial\xi^2} - 4\sin^2\left(\theta/2\right)V\left(\xi,\theta\right) = 0 \tag{2. 23}$$

The transformed boundary conditions of the isolated break problem for $\xi > 0$ then become:

$$V_b\left(0^+,\theta\right) = \pi/4 \tag{2. 24}$$

$$\frac{\partial V_b\left(\infty,\theta\right)}{\partial\xi} = 0 \tag{2. 25}$$

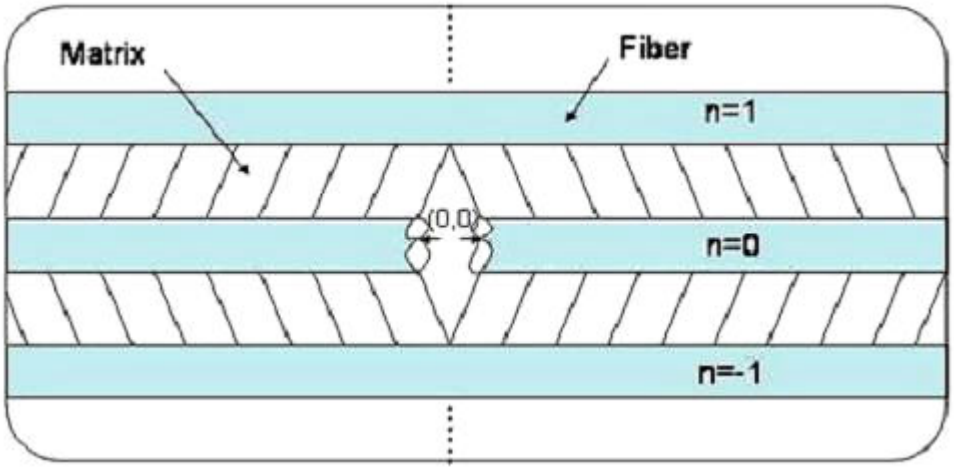

(a) Isolated break problem

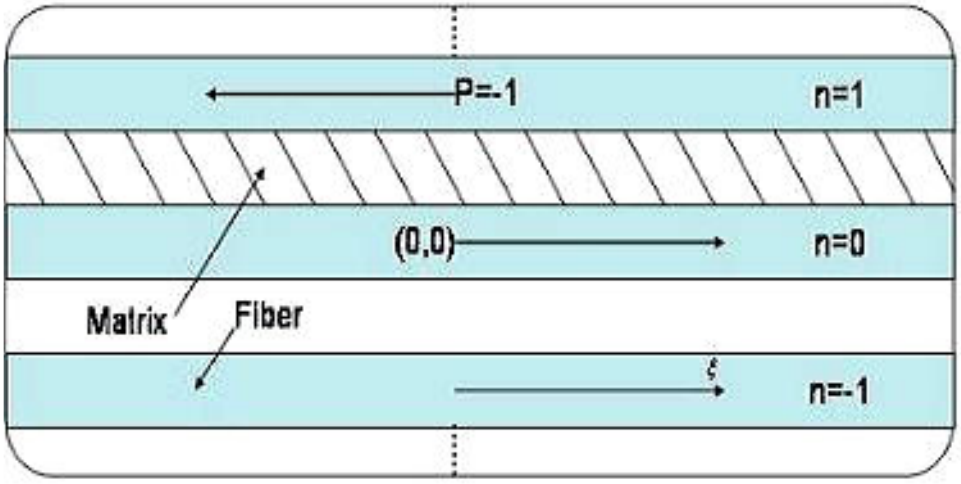

(b) Load couple problem

Figure 2. 2. Two basic elastic problems: (a) isolated break and (b) isolated point shear couple, with unit force applied as indicated with zero remote tensile force.

The transformed solution for $-\pi \le \xi \le \infty$ is then

$$V_{b,n}(\xi) = \operatorname{sgn} \frac{1}{4} \int_0^{\pi} \cos(n\theta) \exp\left(-2|\xi| \sin(\theta/2)\right) d\theta \tag{2. 26}$$

So the solution for the full plane, $-\infty \le \xi \le \infty$, we obtain

$$V_{b,n}(\xi,\theta) = \operatorname{sgn}(\xi) \frac{1}{4} \int_0^{\pi} \cos(n\theta) \exp\left(-2|\xi| \sin\left(\frac{\theta}{2}\right)\right) d\theta \tag{2. 27}$$

$$L_{b,n}(\xi,\theta) = -\frac{1}{2} \int_0^{\pi} \cos(n\theta) \sin(\theta/2) \exp\left(-2|\xi| \sin\left(\frac{\theta}{2}\right)\right) d\theta \tag{2. 28}$$

$$\Gamma_{b,n}(\xi,\theta) = \operatorname{sgn}(\xi) \frac{1}{4} \int_0^{\pi} \left\{\cos\left[(n+1)\theta\right] - \cos(n\theta)\right\} \exp\left(-2|\xi| \sin\left(\frac{\theta}{2}\right)\right) d\theta \tag{2. 29}$$

where $\operatorname{sgn}(\xi) = 1$ when $\xi \ge 0$ and $\operatorname{sgn}(\xi) = -1$ when $\xi < 0$, which is used to account for the asymmetry in the fiber loads.

2.2.2 Basic solution 2: Load couple problem

In this problem, a counterclockwise unit force couple is applied at $\xi = 0$ between fibers $n = 0$ and $n = 1$, and zero edge force is applied at infinity. The point force induces negative and positive unit load jumps at $\xi = 0$ in fibers $n = 0$ and negative shear displacements in the matrix element $(0,0)$. Thus for the positive half plane $\xi > 0$, the boundary conditions are

$$L_{c,0}(0^+) = \frac{dV_{c,0}(0^+)}{d\xi} = -\frac{1}{2} \tag{2. 30}$$

$$L_{c,1}(0^+) = \frac{dV_{c,1}(0^+)}{d\xi} = \frac{1}{2} \tag{2. 31}$$

$$L_{c,n}(0^+) = \frac{dV_{c,n}(0^+)}{d\xi} = 0 \text{ for } n \ge 2 \text{ and } n \le -1 \tag{2. 32}$$

and

$$L_{c,n}(\infty)=\frac{dV_{c,n}(\infty)}{d\xi}=0 \text{ for } -\infty<n<\infty \tag{2. 33}$$

Similarly, we apply subscript "*c*" to distinguish the load couple problem from the general problem and the solutions are called the virtual quantities $L_{c,n}$ and $L_{c,n}$. Using the discrete Fourier transform approach, we obtain the solution in the full plane,

$$V_{c,n}(\xi)=\frac{1}{4\pi}\int_0^{\pi}\left\{\cos(n\theta)-\cos\left[(n-1)\theta\right]\right\}\left\{\sin(\theta/2)\right\}^{-1}\exp\left(-2|\xi|\sin(\theta/2)\right)d\theta \tag{2. 34}$$

$$L_{c,n}(\xi)=-\operatorname{sgn}(\xi)\frac{1}{2\pi}\int_0^{\pi}\left\{\cos(n\theta)-\cos\left[(n-1)\theta\right]\right\}\exp\left(-2|\xi|\sin(\theta/2)\right)d\theta \tag{2. 35}$$

$$\begin{aligned}T_{c,n}(\xi)&=\Gamma_{c,n}(\xi)=V_{c,n+1}(\xi)-V_{c,n}(\xi)\\&=-\frac{1}{\pi}\int_0^{\pi}\cos(n\theta)\sin\theta\exp\left(-2|\xi|\sin(\theta/2)\right)d\theta\end{aligned} \tag{2. 36}$$

2.2.3 Basic problem 3: Isolated broken segment with distributed fiber breaks

Following the method of the isolated break problem, we introduce the third necessary element for this influence superposition technique: an isolated segment with distributed breaklets (ISDB), which will be referred as an isolated segment for convenience in later chapters. Similar to the philosophy of distributed dislocation theory, we integrate the isolated break solution along the gap between the broken fiber ends, applying a weight function in terms of polynomials yielding the integration coefficients. The result is thus the influence at a point of the full segment.

From the first basic solution, we know the solution for a fiber break is:

$$V_{b,n}(\xi,\theta)=\operatorname{sgn}(\xi)\frac{1}{4}\int_0^{\pi}\cos(n\theta)\exp\left(-2|\xi|\sin\left(\frac{\theta}{2}\right)\right)d\theta$$

$$L_{b,n}(\xi,\theta)=-\frac{1}{2}\int_0^{\pi}\cos(n\theta)\sin(\theta/2)\exp\left(-2|\xi|\sin\left(\frac{\theta}{2}\right)\right)d\theta$$

$$V_{b,n}(\xi,\theta)=\operatorname{sgn}(\xi)\frac{1}{4}\int_0^{\pi}\left\{\cos\left[(n+1)\theta\right]-\cos(n\theta)\right\}\exp\left(-2|\xi|\sin\left(\frac{\theta}{2}\right)\right)d\theta$$

Next we compute the impact of a segment of length 2δ with distributed breaklets assuming the coefficient distribution is $T_\kappa(\zeta)$, $\kappa=0,1,2$. We apply subscript "*I*" to distinguish the broken segment problem from the general problem and the solutions are called the virtual quantities $L_{I,n}$ and $L_{I,n}$.

$$V_{I,n}(\xi)=\int_{-\delta}^{\delta}T_\kappa(\zeta)V_{b,n}(\xi-\zeta)d\zeta \tag{2. 37}$$

$$L_{I,n}(\xi)=\int_{-\delta}^{\delta}T_\kappa(\zeta)L_{b,n}(\xi-\zeta)d\zeta \tag{2. 38}$$

$$T_{I,n}(\xi)=\int_{-\delta}^{\delta}T_\kappa(\zeta)T_{b,n}(\xi-\zeta)d\zeta \tag{2. 39}$$

where

$$T_0(\zeta)=1$$
$$T_1(\zeta)=\zeta$$
$$T_2(\zeta)=\zeta^2-\frac{\delta^2}{3}$$

$L_{I,n}(\zeta)$, $T_{I,n}(\xi)$ and $V_{I,n}(\xi)$ can be integrated semi-analytically. The solutions are given in Appendix A and are used in subsequent computations. Not all the numerical examples need the second order coefficients for the distributed breaklets; in fact, our numerical experiments show that the uniform approximation is good enough for most cases, especially when the gap length between two

neighboring broken fibers is small. In the examples, we will indicate what order coefficients are used for the particular cases.

The solutions for these three basic problems are translation invariant, which means the solution for an arbitrarily located break or couple or segment at (n_i, ξ_i) is obtained by simply shifting n and ξ in the standard solutions by $-n_i$ and $-\xi_i$. In later chapters, the shifted solution will be used to determine load transmission factors, which are used to calculate the effects of fiber breaks and yielded matrix elements on the displacements and loads of all the other elements in the composite.

2.3 Load transmission factors

The next step is to consider an auxiliary problem where the broken fibers are loaded on the ends by a compressive force of magnitude $-P$ and no load is applied at $\xi = \pm\infty$, as shown in Figure 2.3. Assume there are N' fiber breaks, s isolated segments and t damaged or yielded matrix elements. In order to solve this problem, we need load transmission factors among all possible pairs of breaks and shear couple distributions from the three "building block" solutions.

We define Λ_{ji} as the load transmitted onto the position of fiber break j due to a unit compressive load -1 on the break opening in fiber i, indicating that the proportion of the load on fiber break j transmitted from a load $-P_i$ at fiber break i is $\Lambda_{ji}P_i$. Define Φ_{ik} as the load on fiber break i due to an isolated segment with weight distribution $T_\kappa(\zeta), \kappa = 0,1,2$ across fiber element k at position $(n_k, \xi_k + \zeta)$, where δ is the local axial coordinate about the center of the fiber element and $-\delta \le \zeta \le \delta$. Define Ω_{ki} as the load imposed on an isolated segment centered at ξ_k due to a single fiber break i at (n_i, ξ_i). Next, we define $\Psi_{lk}^{(\kappa)}$ as the effective tension load distribution across isolated segment l at $(n_l, \xi_l + \zeta)$ due to isolated segment centered at (n_k, ξ_k) with distributed weight $T_\kappa(\zeta)$, $\kappa = 0,1,2$. For the

tension transmitted from the shear couple on the matrix, we define $\Pi^{(\nu)}_{ki}$ as the tension on isolated segment k due to the shear load $S_\nu(\zeta), \nu = 0,1$ across matrix element i with length 2η, where $-\eta \le \zeta \le \eta$, $i = 1,2,...,t$ and t is the number of damaged matrix elements.

For the shear stress in the matrix, define Θ_{ij} as the shear load on matrix element i due to a fiber break at (n_j, ξ_j). Let $\mathrm{H}^{(\kappa)}{}_{ji}, \kappa = 0,1,2$ be the shear stress transmitted to onto matrix element (n_i, ξ_i) due to an isolated broken segment with distributed fiber breaks centered at (n_j, ξ_j) with length 2δ. Define X_{ki} as the effective force distribution transmitted onto fiber break k at (n_k, ξ_k) due to a shear load couple $S_\nu(\zeta), \nu = 0,1$ imposed across matrix element i at position $(n_i, \xi_i + \zeta)$ with length 2η. Lastly, we define $\mathrm{N}^{(\nu)}_{lk}$ as the effective shear load distribution across matrix element l at (n_l, ξ_l) due to shear distribution couple, $S_\nu(\zeta), \nu = 0,1$ imposed across matrix element k centered at (n_k, ξ_k) with length 2η.

All the load transmission factors depend only on the relative distance between respective breaks. We will give the full mathematical expressions for all the load transmission factors in later chapter. Assuming we have already calculated all the transmission factors, the next step is to calculate the weighting factors for the isolated breaks, isolated segments, and the matrix elements.

2.4 Weighting factors, K_b, K_I, and K_c

In the influence superposition technique, the net tensile load on each fiber break or isolated segment is the weighted sum of the "self-applied" tensile load plus the tensile load transmitted from all other fiber breaks, isolated segments and yielded or debonded matrix elements in the lamina. Similarly, the shear load distribution on each damaged matrix equals the weighted sum of the "self-applied" shear loads and the shear load distributions transmitted from all other fiber breaks,

isolated broken segments and damaged matrix elements in the composite lamina. Thus, the next step is to determine weighting factors for all the elements such that the overall compressive load on the broken fiber boundary is $-P_b = -P$, the load on the isolated segment is $-P_I{}^* = -P$ and the shear load on the damaged matrix is $\pm T_y$ (for a perfectly plastic yielding matrix element) and $\pm T_d$ (for a debonded, sliding matrix element, $T_d < T_y$.

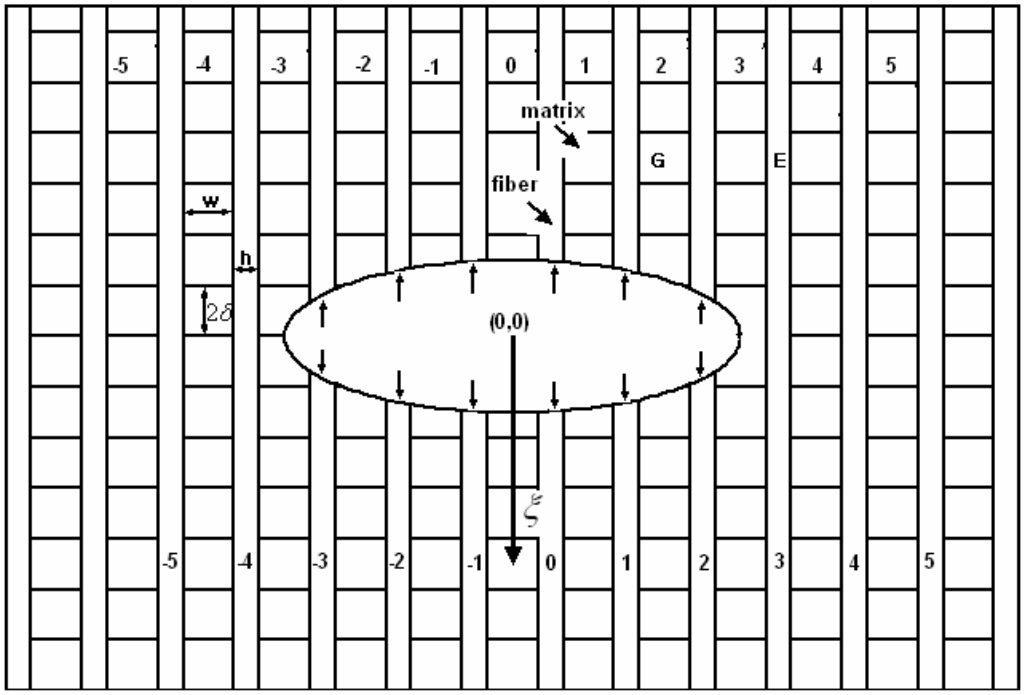

Figure 2. 3. Auxiliary problem: Two dimensional fiber-reinforced composite with a central hole where material is removed and subject to a remote uniform tensile load.

Define $K_{b,i}$ as the weighting factors corresponding to each fiber break i, $K_{I,k}^{(\kappa)}$ as the weights corresponding to each of the three weight distribution profiles for isolated segment $T_\kappa(\zeta), \kappa = 0,1,2$ and $K_c^{(\nu)}$ as the weights corresponding to each of the two shear load profiles $S_\nu(\zeta), \nu = 0,1$ on each yielded or debonded matrix element . Here, $T_\kappa(\zeta)$ and $S_\nu(\zeta)$ are both polynomials:

$$T_0(\zeta) = 1$$
$$T_1(\zeta) = \zeta$$
$$T_2(\zeta) = \zeta^2 - \frac{\delta^2}{3}$$

and

$$S_0(\zeta) = 1$$
$$S_1(\zeta) = \zeta$$

Obtaining all the weighting factors requires solution of a linear system of $N' + 3s + 2t$ equations for weighting factors.

$$\begin{bmatrix} \Lambda & \Phi^{(0)} & \Phi^{(1)} & \Phi^{(2)} & X^{(0)} & X^{(0)} \\ \Omega^{(0)} & \Psi^{(0,0)} & \Psi^{(0,1)} & \Psi^{(0,2)} & \Pi^{(0,0)} & \Pi^{(0,1)} \\ \Omega^{(1)} & \Psi^{(1,0)} & \Psi^{(1,1)} & \Psi^{(1,2)} & \Pi^{(1,0)} & \mathrm{T}^{(1,1)} \\ \Omega^{(2)} & \Psi^{(2,0)} & \Psi^{(2,1)} & \Psi^{(2,2)} & X^{(2,0)} & X^{(2,1)} \\ \Theta^{(0)} & \mathrm{H}^{(0,0)} & \mathrm{H}^{(0,1)} & \mathrm{H}^{(0,2)} & \mathrm{N}^{(0,0)} & \mathrm{N}^{(0,1)} \\ \Theta^{(1)} & \mathrm{H}^{(1,0)} & \mathrm{H}^{(1,1)} & \mathrm{H}^{(1,2)} & \mathrm{N}^{(1,0)} & \mathrm{N}^{(1,1)} \end{bmatrix} \begin{bmatrix} K_b \\ K_I^{(0)} \\ K_I^{(1)} \\ K_I^{(2)} \\ K_c^{(0)} \\ K_c^{(1)} \end{bmatrix} = \begin{bmatrix} -P_b \\ -P_I * \\ P_1 * \\ P_2 * \\ T_0 * \\ T_1 * \end{bmatrix} \qquad (2.40)$$

In this matrix equation, $-P_b$ and K_b are both N'-dimensional vectors, $-P_I *, P_1 *, P_2 *$ and $K_I^{(\kappa)}, \kappa = 0,1,2$, are all s-dimensional vectors, and $T_0 *$, $T_1 *$ and $K_c^{(\nu)}, \nu = 0,1$ are all t-dimensional vectors. Λ, $\Phi^{(\kappa)}$, $\mathrm{X}^{(\kappa,\nu)}$, $\Omega^{(\kappa)}$, $\Psi^{(\kappa,\kappa)}$, $\Theta^{(\nu)}$, $\mathrm{H}^{(\nu,\kappa)}$ and $N^{(\nu,\nu)}$ are matrices whose elements have been defined above and, respectively, have dimensions $N' \times N'$, $N' \times s$, $N' \times t$, $s \times N'$, $s \times s$, $t \times N'$, $t \times s$ and $t \times t$. The N'-dimensional vector $-P_b$ has components $-P_{b,i} = -P$ for $i = 1,...,N'$, the s-dimensional vector $-P_I *$ has components $-P_{I,k} * = -P$ for

$k = 1,...,s$ and the t-dimensional vector T_0^* has components $T_{0,j}^* = \pm T_y$ or $\pm T_d$ for $j = 1,...,t$ depending on whether the particular element is yielded or debonded, as described above. On the other hand, the s-dimensional vectors P_1^* and P_2^* have components $P_{1,k}^* = P_{2,k}^* = 0$ for $k = 1,...,s$ and the t-dimensional vector T_1^* has components $T_{1,j}^* = 0$ for $j = 1,...,t$.

Note that the load couple weight factors $K_{c,j}^{(\nu)}$, $\nu = 0,1$ represent the differential shear forces exerted by a damaged matrix element j on its adjacent flanking fibers. In another words, these $K_{c,j}^{(\nu)}$ decide the difference in shear force between what a damaged matrix elements actually exerts and what it would exert if it were deforming elastically under the same shear displacement. If the matrix, in fact, deforms elastically then its $K_{c,j}^{(\nu)}$ vanishes.

Thus for the auxiliary problem, the fiber and matrix loads and displacements at arbitrary position (n, ξ) are the weighted sums of the influences of fiber breaks, continuously distributed breaks and damaged matrix elements in the lamina.

$$\begin{aligned} L_n(\xi) = &\sum_{i=1}^{N'} K_{b,i} L_{b,n-n_i}(\xi - \xi_i) + \sum_{\nu=0}^{2} \sum_{k=N'+1}^{N'+s} K_{c,k}^{(\nu)} \int_{-\delta}^{\delta} T_\nu(\zeta) L_{b,n-n_k}(\xi - \xi_k - \zeta)\, d\zeta \\ &+ \sum_{\nu=0}^{1} \sum_{k=N'+3s+1}^{N'+3s+t} K_{m,k}^{(\nu)} \int_{-\eta}^{\eta} S_\nu(\zeta) L_{c,n-n_k}(\xi - \xi_k - \zeta)\, d\zeta \end{aligned} \tag{2. 41}$$

$$\begin{aligned} V_n(\xi) = &\sum_{i=1}^{N'} K_{b,i} V_{b,n-n_i}(\xi - \xi_i) + \sum_{\nu=0}^{2} \sum_{k=N'+1}^{N'+s} K_{c,k}^{(\nu)} \int_{-\delta}^{\delta} T_\nu(\zeta) V_{b,n-n_k}(\xi - \xi_k - \zeta)\, d\zeta \\ &+ \sum_{\nu=0}^{1} \sum_{k=N'+3s+1}^{N'+3s+t} K_{m,k}^{(\nu)} \int_{-\eta}^{\eta} S_\nu(\zeta) V_{c,n-n_k}(\xi - \xi_k - \zeta)\, d\zeta \end{aligned} \tag{2. 42}$$

$$\begin{aligned} \Gamma_n(\xi) = &\sum_{i=1}^{N'} K_{b,i} L_{b,n-n_i}(\xi - \xi_i) + \sum_{\nu=0}^{2} \sum_{k=N'+1}^{N'+s} K_{c,k}^{(\nu)} \int_{-\delta}^{\delta} T_\nu(\zeta) \Gamma_{b,n-n_k}(\xi - \xi_k - \zeta)\, d\zeta \\ &+ \sum_{\nu=0}^{1} \sum_{k=N'+3s+1}^{N'+3s+t} K_{m,k}^{(\nu)} \int_{-\eta}^{\eta} S_\nu(\zeta) \Gamma_{c,n-n_k}(\xi - \xi_k - \zeta)\, d\zeta \end{aligned} \tag{2. 43}$$

The matrix shear stress T_n is then

$$T_n(\xi) = \Gamma_n(\xi) + \sum_{k=N'+3s}^{N'+3s+t} K_{c,k}^{(0)} I_{n-n_k}(\xi - \xi_k) + \sum_{k=N'+3s}^{N'+3s+t} K_{c,k}^{(0)} I_{n-n_k}(\xi - \xi_k)\zeta \qquad (2.44)$$

where

$$I_n(\xi) = \begin{matrix} 1, & |\xi| \le \eta \quad \text{and} \quad n = 0 \\ 0, & \text{otherwise} \end{matrix} \qquad (2.45)$$

Finally, to calculate the desired exact solution for the lamina loaded by P at $\xi = \pm\infty$, a tensile load of unity is superimposed onto the solutions, thus canceling out the load applied to the hole boundary. The dimensionless matrix shear strain Γ_n and stress T_n remain the same, but the fiber loads $P_n(\xi)$ and displacements $U_n(\xi)$ become

$$P_n(\xi) = L(\xi) + P \qquad (2.46)$$

and

$$U_n(\xi) = V_n(\xi) + P\xi \qquad (2.47)$$

3. Weighting Factor and Distributions at Fiber Breaks

In this chapter, we will investigate the weighting factors for the distributed fiber breaks in the isolated segment. As we mentioned earlier, to simulate a broken fiber where the material is removed or inactivated, similar to the philosophy of the distributed dislocation theory, we integrate the isolated break solution along the gap between the broken fiber ends, applying weight functions in terms of simple polynomials, and integrating to determine the multiplying coefficients. Thus the integral provides the influence of the distributed fiber breaklets on the other locations in the lamina. We will study three cases: a longitudinal crack consisting of a single broken fiber, a hole containing multiple broken fibers, and a rectangular hole.

3.1 Single broken fiber

We begin with the simplest case and study the weighting factor distribution of the isolated breaks, i.e., a longitudinal crack made of a fiber broken in two places with the resulting segment removed. To simulate the broken fiber with removed segment $2a$, we ideally put a sufficient number of isolated breaks with different weights in the cavity. However, this is not very realistic for the numerical simulation, especially for a large removed segment. Instead, we investigate the distribution of weights imposed at each isolated break in the cavity and try to develop suitable functions to yield integration coefficients to simulate the corresponding weight distribution. In this way, we can greatly reduce the computational load.

Figure 3.1 (a) illustrates the cavity profile and notation for our computation scheme. Fiber 0 is broken at two places to yield segment of length $2a$. In the figure, we use big dots to denote the two fiber breaks and thick straight lines to

represent the resulting isolated segment which have distributed fiber breaklets. We use q to show the position of the surviving fiber and matrix bays: $q = 1$ represents the first surviving fiber or matrix bay.

Figure 3.2 shows the weight distribution for 100 fiber breaks embedded in the cavity of length $2a = 1$, which is the Hedgepeth characteristic load transfer length. Clearly, all the isolated breaks have almost uniform weight except the two breaks at the ends of the cavity. The magnified picture in the figure shows the weight changes more steeply toward the end of the broken fibers. Mathematically, we can approximate the weight distribution by a zero order or possibly higher order polynomial for the middle piece and two delta functions at the boundary of the cavity. In another words, to capture the physical behavior, we will use an isolated segment, with a continuous distribution, and two isolated fiber breaks at each end to model this gap.

Figure 3.3 shows the weight distribution for 200 fiber breaks which are embedded over a segment in the cavity of much larger length $2a = 20$ between two fiber ends. We can see that unlike the previous case where the weights for the isolated broken segment between two breaks are almost uniform and the zero order approximation is good enough, for the larger gap length the weight distribution is more complicated and higher order polynomials will be required to reflect the slope and curvature effects in the weight distribution.

On the other hand we can instead divide the broken segments into shorter pieces between the broken fiber ends at $\xi = \pm a$. Figure 3.1 (b) shows the structure where the broken segment is divided into three sub-segments with equal length. In general, our numerical experiments show that it is more efficient to split the segments based on the slope and curvature, instead of dividing them evenly. For example, in our case, the broken segments can be divided more densely near the broken fiber tip

because the slope is quite large and the curvature there is changing rapidly. We will discuss the efficiency of both methods in the later chapter.

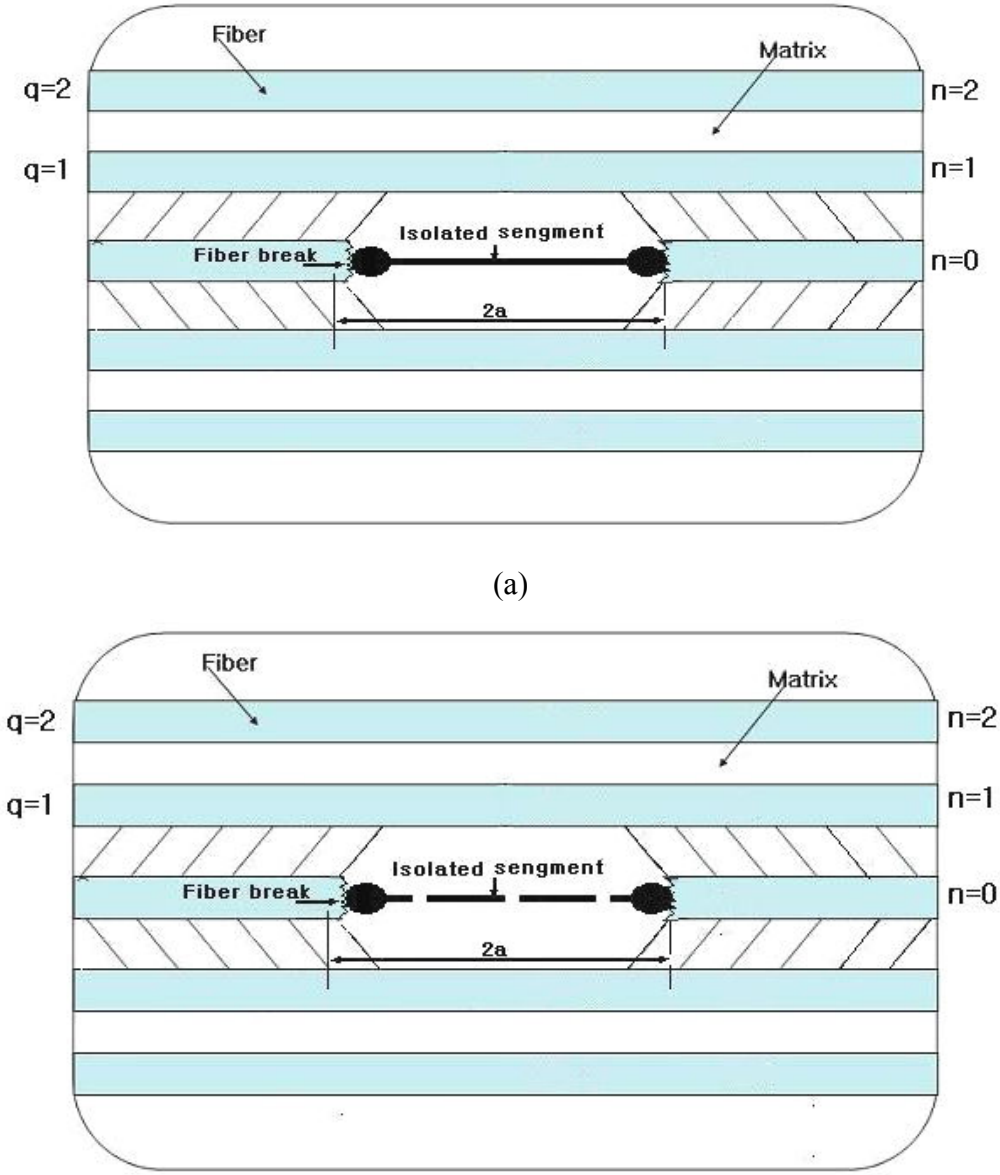

Figure 3. 1. A hole with one broken fiber with gap of length 2a in a laminate: (a) One isolated broken segment in the gap, (b) Three isolated broken segments in the gap.

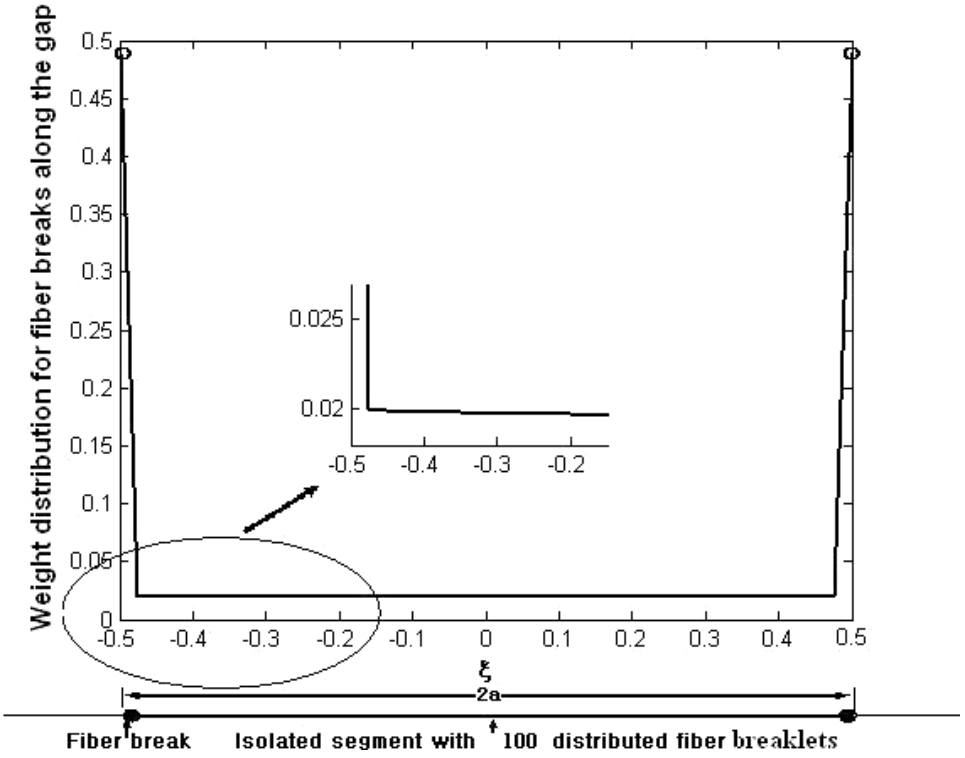

Figure 3. 2. Weight distributions for single broken fiber with gap distance, $2a = 1$.

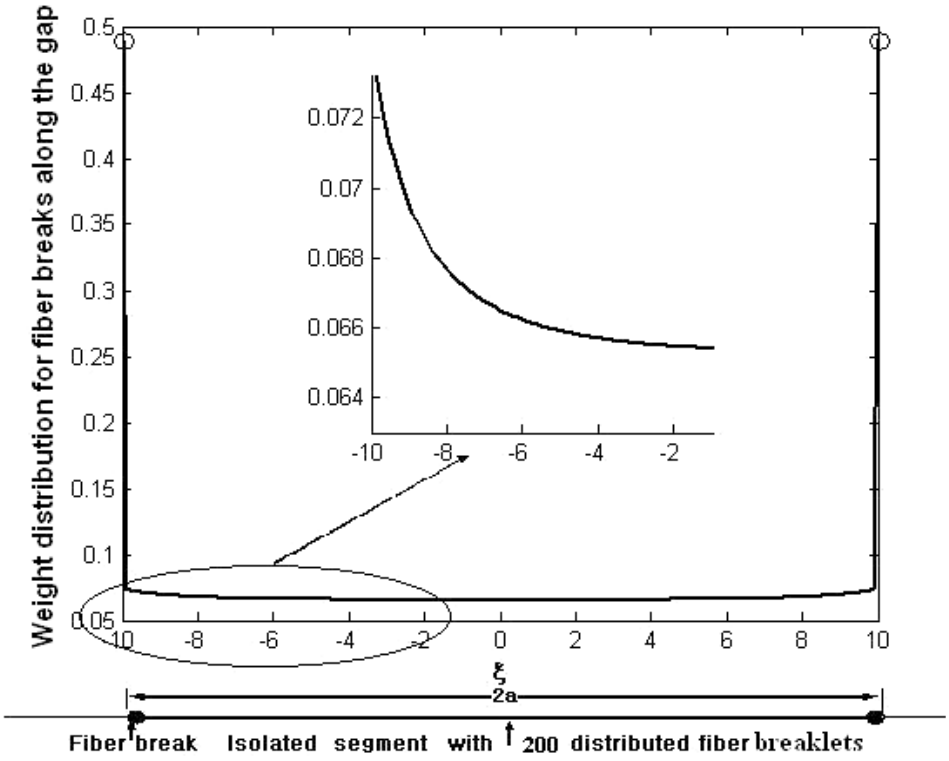

Figure 3. 3. Weight distributions for single broken fiber with gap distance, $2a = 20$.

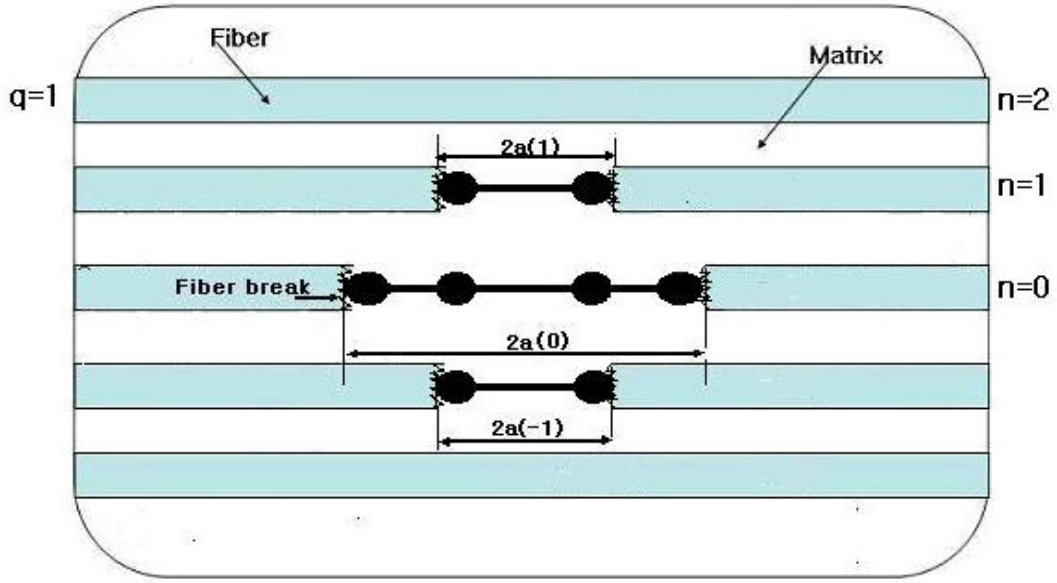

Figure 3. 4. A hole containing three broken fiber segments.

3.2 Holes containing multiple broken fibers

Next, we study the weight distribution of isolated breaks for cavities containing multiple adjacent broken fibers. This particular example contains three broken fibers and the gap profile for the broken fibers is shown in Figure 3.4.

Figure 3.5 and 3.6 plot the weight distribution for fiber $n = 0$ and $n = \pm 1$. For broken fiber $n = \pm 1$, the weights for all the isolated breaks are approximately uniform except in the region close to the broken fiber ends, which has similar trends to the single broken fiber case. At the boundary of the cavity, $|\xi| = a(\pm 1)$, the fiber break at each tip has a much higher weight in contrast to the uniform weight in the middle, which suggests two fiber breaks at the edge are needed to catch the spikes in the displacements and weights.

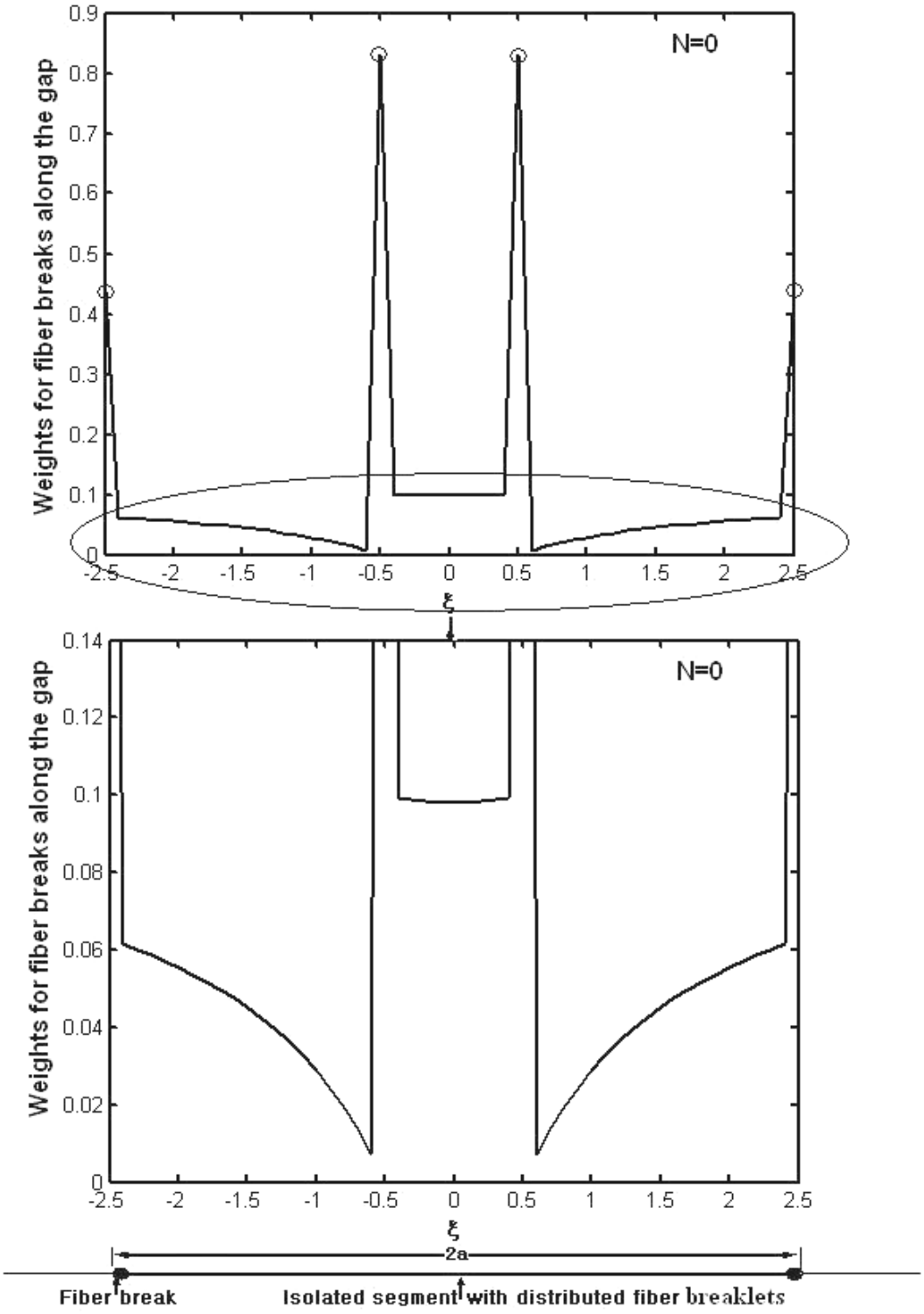

Figure 3. 5. Weight distribution for fiber $n = 0$ for the hole profile, $\left(2a(-1)\ 2a(0)\ 2a(1)\right) = (1\ \ 5\ \ 1)$.

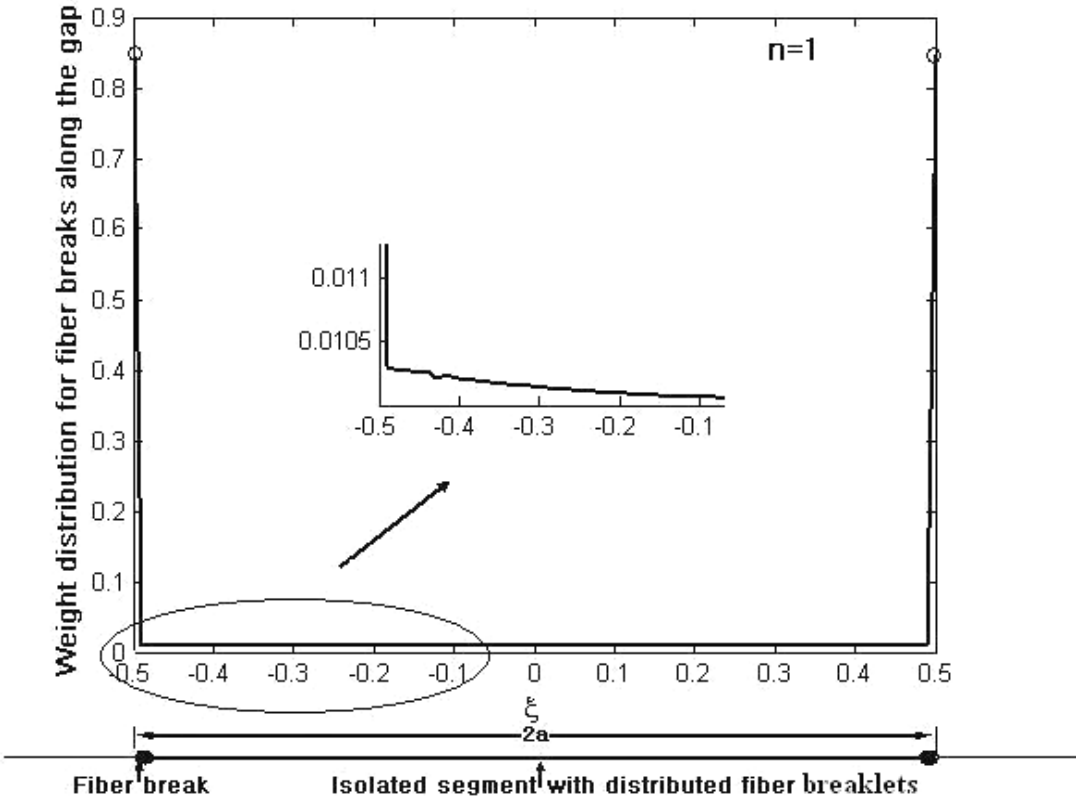

Figure 3. 6. Weight distribution for fiber $n=1$ for the hole profile, $\left(2a(-1)\ 2a(0)\ 2a(1)\right)=\left(1\ \ 5\ \ 1\right)$.

For the broken fiber in the middle of the cavity, $n=0$, the weight distribution consists of three parts and is symmetric about the center, $\xi=0$. Four isolated fiber breaks and at least three isolated segments will be needed to approximate the spikes and the three continuous regions between the spikes. For the region $|\xi|\le a(1)$, overlapped by the gap of the neighboring broken fiber, the weights are distributed uniformly approximately. On the other hand, for $|\xi|\ge a(1)$, the weight distribution for the fiber breaks increases fairly rapidly and its curvature decreases approaching the hole boundary, $\xi=a(0)$, which suggests using at least a linear polynomial to approximate the weight distribution for the fiber breaks.

From the figure, we can see that the fracture effect of the tips of each broken fiber is spread out in the entire cavity. The total number of fiber breaks and the isolated segments needed to model the hole for each fiber is determined by the number of broken fibers and the gap length of each fiber. The fiber breaks and isolated segments for the broken fiber with shorter gap lengths are always inherited by the ones with a longer gap length. In our example as shown in Figure 3.4, the fiber in the middle has four fiber breaks, two inherited from the neighboring fiber tips at $|\xi| = a(1)$ and two from its own tips.

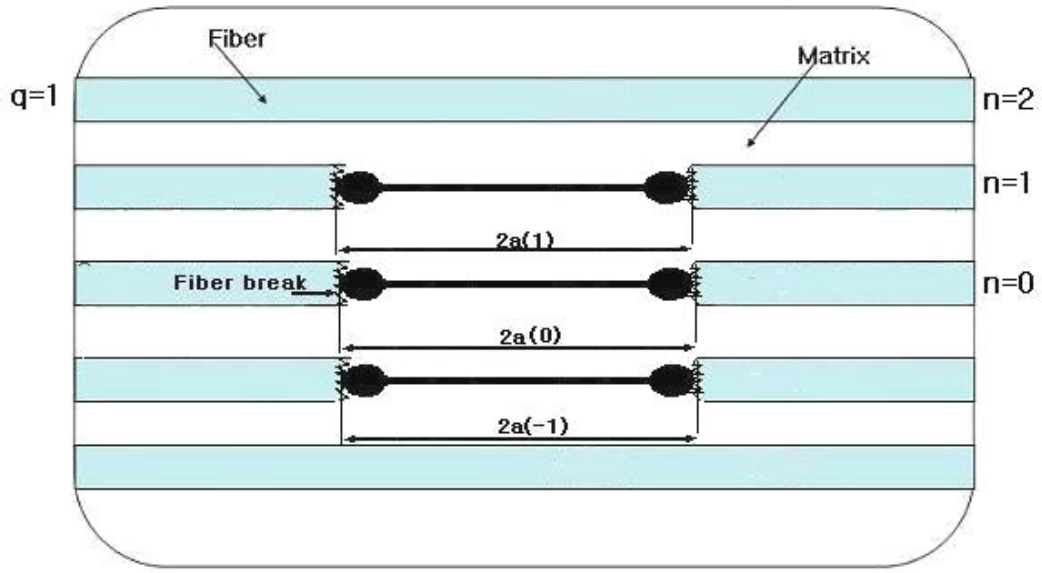

Figure 3. 7. A rectangular cavity containing three broken fibers, $(2a(-1)\ 2a(0)\ 2a(1)) = (5\ \ 5\ \ 5)$.

Overall, the total number of fiber breaks and broken segments needed for a hole is proportional to N^2.

3.3 Rectangular cavity

Lastly, we will try a rectangular cavity (i.e. all the gaps of the broken fibers have equal length) and study the weight distribution for the fiber breaks in

the gap. Figure 3.7 shows the cavity profile and the basic notation for our computational scheme.

Figure 3.8 shows the weight distribution for fiber breaks embedded in the gap. All the isolated segments between the broken fiber tips have almost the same distribution except that fiber $n = 0$ has higher spikes at $\xi = \pm a(0)$ than fiber $n = \pm 1$. Furthermore, the distribution profile is actually very similar to the profile of the single broken fiber case. Therefore, introducing new broken fibers with the same gap distance doesn't change the structure of weight distribution much. Three isolated segment with distributed fiber breaks and six isolated fiber breaks are good enough for a rectangular cavity in our case. If there are N broken fibers, the total number of fiber breaks and broken segments with distributed fiber breaks needed for a rectangular cavity are $2N$ and N, respectively. If the cavity gets larger, as suggested in Section 3.2, we can divide the segments into shorter pieces in the gap near the cavity boundary for every broken fiber or use higher order polynomials to approximate the distribution.

3.3 Conclusion

In this chapter we have put a sufficient number of fiber breaks in the cavity containing one single broken fiber or multiple broken fibers to simulate the stress field near a hole where the material has been removed from fibers in a fibrous composite plane with tension applied at infinity. We have studied the weight distribution for the fiber breaks in the hole and have proposed a basic computational scheme to simulate all the fiber breaks using the concept of distributed dislocation theory. Basically, using different order of polynomials to approximate the weight distribution of the fiber breaks for different parts of the broken fiber will be the key

technique. Isolated fiber breaks and isolated segments with distributed fiber breaks are the key elements to realize this technique.

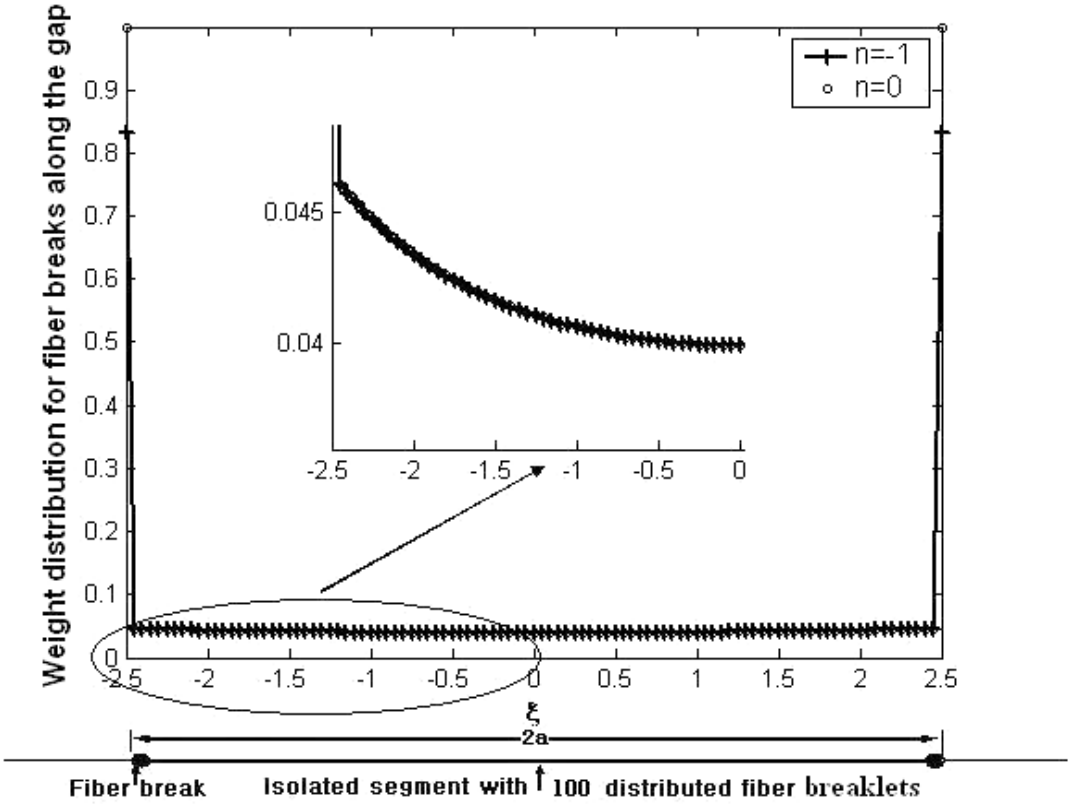

Figure 3. 8. Weight distribution for fiber $n=1$ and $n=0$ for the rectangular cavity . $\left(2a(-1)\ 2a(0)\ 2a(1)\right)=\left(5\ \ 5\ \ 5\right)$.

The number of fiber breaks is decided by the number of the broken fibers and the shape of the cavity. If all the broken fiber has the same gap length, we only need to put fiber breaks at the boundary of the cavity and isolated segments with distributed fiber breaks in the middle. Otherwise, the broken fiber with longer gap requires the fiber breaks and broken segments paced above and below the break ends in the fiber with shorter gap in the cavity.

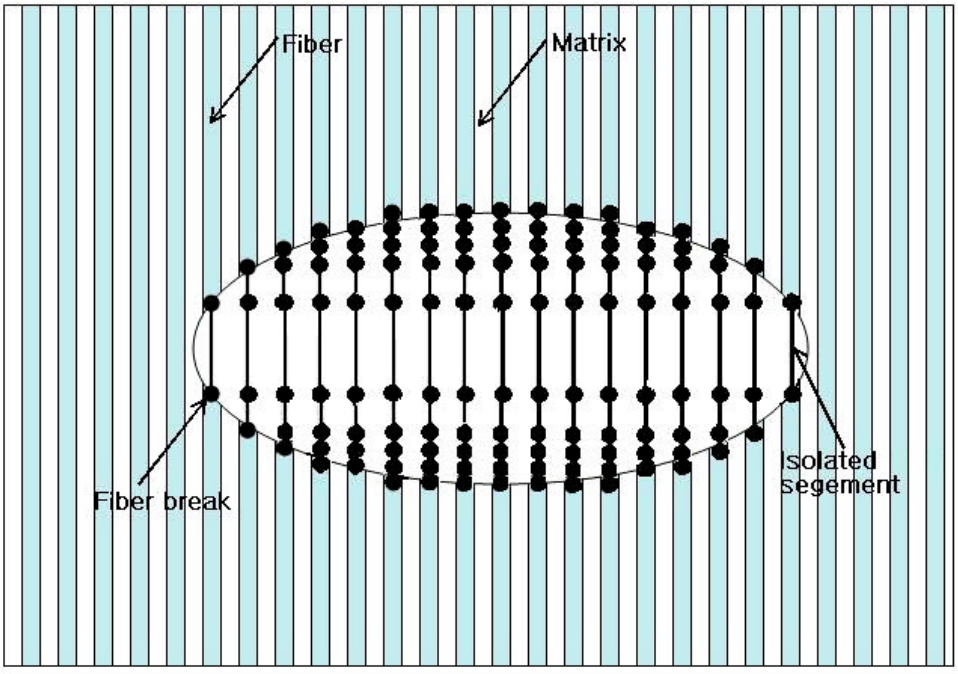

Figure 3. 9. An elliptical hole in a two dimensional composite plane

Figure 3.9 shows the structure made for an elliptical cavity as an example. The big dots denote the fiber breaks and the solid line between the dots denotes the isolated segment. The shortest gap is at the cavity tip and the gap gets larger as one moves towards the central broken fiber in the cavity. Therefore, two fiber breaks are put at the broken fiber ends for the last broken fiber and an isolated segment exists between its two end fiber breaks. The second last broken fiber inherits the fiber breaks and isolated segments of the last broken fiber and this adds two more fiber breaks near its own fiber ends. There are two more isolated segments accordingly if its gap length is larger than the previous fiber gap. Similarly, the next fiber inherits everything from the previous one and adds its own fiber breaks and segments if it has a larger gap than the previous one until we reach the middle fiber, $n = 0$, which has all the fiber breaks and segments introduced by the other broken fibers. In general, the broken fiber ends always have isolated fiber breaks there to

catch the spike brought about by the edge of the hole and the segments can be divided into shorter pieces for more accurate approximation. Therefore, we can see that the total number of fiber breaks and broken segments are of the order of N^2 if all the broken fibers have different gap lengths.

There is always at least one broken segment between two fiber breaks, which can always be divided into short segments if the gap distance is large. It is recommended that shorter segments be used near the broken fiber ends because this is where the curvature of the distribution changes rapidly. We will perform many examples for different cavity shapes to demonstrate the use of the technique in later chapters and then we will introduce matrix yielding and debonding using the QIS technique to get more insight into the fibrous composite fracture.

4. Framework of the Influence Superposition Technique

In the last chapter, we studied the weighting distribution of fictitious fiber breaks, which were placed within a hole of any shape to model the effect of the hole on stress field. In this chapter, we discuss in detail how to calculate the load transmission factors and compute the weighting factors for fiber breaks and segments. Without loss of generality, we will set up the framework for an elliptical hole with elastic fiber and matrix bays. In the last chapter, we will discuss how to include matrix yielding and debonding in the computational model.

We assume there are N broken fiber lengths removed from the hole, which involve N' single fiber breaks and s isolated broken segments with distributed fiber breaks to simulate the hole behavior. Figure 3.9 gives a schematic of the basic computational framework for an elliptical hole with material removed or inactivated. A dot denotes a fiber break and a solid line denotes an isolated segment. As suggested by the weight distribution study in the previous chapter, the broken fiber with longer gap inherits the need for fiber breaks and isolated segments of the adjacent one with shorter gap. Thus the total number of fiber breaks and isolated segments are of order N^2 for an ellipse where all the broken fibers have different gap lengths.

Thomas (1966) studied the effects on the shear stress distribution in an elastic matrix of aligned fibers having various lap lengths both with and without matrix material in the gap. The results show that it made little difference whether the gap ends contained matrix or not. Peak stresses are about the same in the open models as in the filled gap models. Therefore, our model applies to a cavity with or without matrix material inside.

Break influence technique (BIS) was first developed by Sastry and Phoenix (1993) to handle large numbers of breaks in complicated arrays. Results of Beyerlein, Phoenix and Sastry (1996) show that for a sizable crack, the BIS technique and the Mode I LEFM solution for an orthotropic material achieve good agreement down to the scale of one fiber diameter and even better agreement with the complete elasticity solution both in the near crack tip field and far field, regardless of the composite stiffness. The main advantage of this technique is that unlike the other computational methods, it calculates the exact solution of the fiber and matrix loads and displacement and the discretization is only required in the damaged region (inside the hole, or at yielded or debonded matrix bays). Therefore, the shear-lag analysis can handle much larger composites with many more fiber breaks since the computational demands are only decided by the size the damage not the overall composite volume.

On the other hand, thus far, the technique has been applied to cracks (Sastry and Phoenix, 1993; Beylerlein, Phoenix and Sastry,1996) or cracks with damaged matrix (Beyerlein and Phoenix,1996), i.e. the technique has been focused on the composite plane where no fiber material has been removed. No study exist which explores the effect of a hole on the tensile fracture of fiber reinforced laminates and nor studies how well the elastic solution and the shear-lag analysis agree with each other. The goal of this chapter is to build up a computationally efficient method using shear-lag analysis to calculate the stress field near a hole. We will later calculate several examples for holes of different shapes using the scheme built up here, and compare our results with the elastic analysis (Bishop, 1972; Williams, 1953; Potter, 1977). We will draw some connections between the discrete model and the continuum model.

4.1 Load transmission factors

After allocating the fiber breaks and isolated segments, we now consider calculation of the load transmission factors among all possible pairs of breaks and isolated segments in detail using the shifted solutions to the fiber break and the isolated segment. As we discussed before, both solutions are translation invariant, and therefore the load transmission factors depend only on the relative distance between different pairs of fiber breaks and broken segments $(n_i - n_j, \xi_i - \xi_j,)$. For the present analysis, the matrix deforms elastically and no yielding or debonding is considered.

For the isolated fiber break problem, let Λ_{ji} be the load transmitted onto fiber j due to a unit compressive load, -1, on fiber break i. Thus the proportion of the load on fiber break j transmitted from a load $-P_i$ at fiber break i is $\Lambda_{ji}P_i$. The expression for Λ_{ji} is as follows:

$$\begin{aligned}\Lambda_{ji} &= L_{b,n_j-n_i}\left(\xi_j - \xi_i\right) \\ &= -\frac{1}{2}\int_0^{\pi} \cos\left[\left(n_j - n_i\right)\theta\right]\sin\left(\frac{\theta}{2}\right)\exp\left(-2\left|\xi_j - \xi_i\right|\sin\left(\frac{\theta}{2}\right)\right)d\theta\end{aligned} \tag{4. 1}$$

Note that Λ_{ji} is symmetric, $\Lambda_{ji} = \Lambda_{ij}$ and $\Lambda_{ii} = -1$.

Let Φ_{ik} be the effective force distribution transmitted onto fiber break i due to an isolated segment with weight distribution $T_\kappa(\zeta)$, $\kappa = 0,1,2$ across broken segment k at position $(n_k, \xi_k + \zeta)$ where ζ is the local axial coordinate about the center of the fiber element and $-\delta \le \zeta \le \delta$. That is

$$\begin{aligned}\Phi_{ik}^{(\kappa)} &= \int_{\xi_k-\delta}^{\xi_k+\delta} T_\kappa\left(\xi - \xi_k\right) L_{b,n_i-n_k}\left(\xi_i - \xi\right)d\xi \\ &= \int_{-\delta}^{\delta} T_\kappa\left(\zeta\right) L_{b,n_i-n_k}\left(\xi_i - \xi_k - \zeta\right)d\zeta\end{aligned} \tag{4. 2}$$

where

$$T_0(\zeta) = 1$$
$$T_1(\zeta) = \zeta$$
$$T_2(\zeta) = \zeta^2 - \frac{\delta^2}{3}$$

Define Ω_{ki} as the load imposed on isolated segment centered at ξ_k due to a single fiber break i at (n_i, ξ_i). Particularly, Ω_{ki} is a second order polynomial approximation for the induced tension load per unit length across the isolated broken segment at $(n_k, \xi_k + \zeta)$ where $-\delta \le \zeta \le \delta$.

$$\Omega_{ki}(\zeta) = \Omega_{ki}^{(0)} + \Omega_{ki}^{(1)}\zeta + \Omega_{ki}^{(2)}\left(\zeta^2 - \frac{\delta^2}{3}\right) \tag{4. 3}$$

Specifically, we approximate Ω_{ki} with Taylor series,

$$\Omega_{ki}^{(0)} = L_{b,n_k - n_i}(\xi_k - \xi_i) + \Omega_{ki}^{(2)}\delta^2 / 3 \tag{4. 4}$$

for $i = 1,...,N'$ and $k = N'+1,\ldots,N'+s$.

$$\begin{aligned}\Omega_{ki}^{(1)} &= \left.\frac{dL_{b,n_k-n_i}(\xi - \xi_i)}{d\xi}\right|_{\xi=\xi_k} \\ &= \int_0^{\pi} \mathrm{sgn}(\xi_k - \xi_i)\cos\left[(n_k - n_i)\theta\right]\sin^2\left(\frac{\theta}{2}\right)\exp\left(-2|\xi_k - \xi_i|\sin\left(\frac{\theta}{2}\right)\right)d\theta\end{aligned} \tag{4. 5}$$

and

$$\begin{aligned}\Omega_{ki}^{(2)} &= \frac{1}{2}\left.\frac{d^2 L_{b,n_k-n_i}(\xi - \xi_i)}{d\xi^2}\right|_{\xi=\xi_k} \\ &= -2\int_0^{\pi} \mathrm{sgn}(\xi_k - \xi_i)\cos\left[(n_k - n_i)\theta\right]\sin^3\left(\frac{\theta}{2}\right)\exp\left(-2|\xi_k - \xi_i|\sin\left(\frac{\theta}{2}\right)\right)d\theta\end{aligned} \tag{4. 6}$$

Next, we define $\Psi_{lk}^{(\kappa)}$ as the effective tension load distribution across isolated broken segment l at $(n_l, \xi_l + \zeta)$ due to isolated broken segment centered at (n_k, ξ_k) with weight distribution $T_\kappa(\zeta)$, $\kappa = 0,1,2$. We assume

$$\Psi_{lk}{}^{\kappa}(\zeta) = \Psi_{lk}^{(0,\kappa)} + \Psi_{lk}^{(1,\kappa)}\zeta + \Psi_{lk}^{(2,\kappa)}\left(\zeta^2 - \delta^2/3\right) \tag{4. 7}$$

for $-\delta \le \zeta \le \delta$, $l,k = N'+1,...,N'+s$ and $\kappa = 0,1,2$. Using a Taylor series approach about the isolated broken segment centers

$$\begin{aligned}\Psi_{lk}^{(0,\kappa)}(\xi) &= \int_{\xi_k-\delta}^{\xi_k+\delta} T_\kappa(\xi-\xi_k) L_{b,n_l-n_k}(\xi_l-\xi)\,d\xi \\ &= \int_{-\delta}^{\delta} T_\kappa(\zeta) L_{b,n_i-n_k}(\xi_l-\xi_k-\zeta)\,d\zeta + \Psi_{lk}^{(2,\kappa)}\frac{\delta^2}{3}\end{aligned} \tag{4. 8}$$

$$\Psi_{lk}^{(1,\kappa)}(\xi) = \int_{-\delta}^{\delta} T_\kappa(\zeta) \left.\frac{dL_{b,n_l-n_k}(\xi-\xi_k-\zeta)}{d\xi}\right|_{\xi=\xi_l} d\zeta \tag{4. 9}$$

and

$$\Psi_{lk}^{(2,\kappa)}(\xi) = \frac{1}{2}\int_{-\delta}^{\delta} T_\kappa(\zeta) \left.\frac{d^2L_{b,n_l-n_k}(\xi-\xi_k-\zeta)}{d\xi^2}\right|_{\xi=\xi_l} d\zeta \tag{4. 10}$$

$\Psi_{lk}^{(0,\kappa)}$, $\Psi_{lk}^{(1,\kappa)}$ and $\Psi_{lk}^{(2,\kappa)}$ also can be integrated semi-analytically. See Appendix B for all the related results. As mentioned earlier, once all the influenced functions are computed a priori and stored, the following computations will only take a few minutes.

4.2 Weighting factors

After determining all the load transmission factors, for the N' fiber breaks and s broken segments, a system of $N'+3s$ equation is solved for the weighting factors of all the fiber breaks and broken segments with distributed fiber breaks by applying the boundary condition that the tensile stress in the cavity and at the boundary is zero. Keep in mind that both the fiber and the matrix deform elastically in this chapter, so we don't apply the load couple to the matrix bays here to cancel out the difference in shear force between what a damaged matrix element actually exerts and what it would exert if it were deforming elastically under the same shear displacement. In another word, we don't need T_0^*, T_1^*, Θ and H terms to solve for

the coefficients. The necessary linear system is made of $N'+3s$ equations in this case. The matrix equation is

$$\begin{bmatrix} \Lambda & \Phi^{(0)} & \Phi^{(1)} & \Phi^{(2)} \\ \Omega^{(0)} & \Psi^{(0,0)} & \Psi^{(0,1)} & \Psi^{(0,2)} \\ \Omega^{(1)} & \Psi^{(1,0)} & \Psi^{(1,1)} & \Psi^{(1,2)} \\ \Omega^{(2)} & \Psi^{(2,0)} & \Psi^{(2,1)} & \Psi^{(2,2)} \end{bmatrix} \begin{bmatrix} K_b \\ K_I^{(0)} \\ K_I^{(1)} \\ K_I^{(2)} \end{bmatrix} = \begin{bmatrix} -P_b \\ -P_I * \\ P_1 * \\ P_2 * \end{bmatrix} \tag{4. 11}$$

In this matrix equation, $-P_b$ and K_b are both N'-dimensional vectors, $-P_I *$, $P_1 *$, $P_2 *$ and $K_I^{(\kappa)}, \kappa = 0,1,2$, are all s-dimensional vectors. Λ, $\Phi^{(\kappa)}$, $\Omega^{(\kappa)}$ and $\Psi^{(\kappa,\kappa)}$ are matrices whose elements have been defined above and respectively have dimensions $N' \times N'$, $N' \times s$, $s \times N'$ and $s \times s$. The N'-dimensional vector $-P_b$ has components $-P_{b,i} = -P$ for $i = 1,...,N$, the s-dimensional vector $-P_I *$ has components $-P_{I,k} * = -P$ for $k = 1,...,s$ and on the other hand, the s-dimensional vectors $P_1 *$ and $P_2 *$ have components $P_{1,k} * = P_{2,k} * = 0$ for $k = 1,...,s$.

The fiber and matrix loads and displacements for any n and at any axial distance ξ are the weighted sums of the influences of all the fiber breaks and isolated segments.

$$L_n(\xi) = \sum_{i=1}^{N'} K_{b,i} L_{b,n-n_i}(\xi - \xi_i) + \sum_{\nu=0}^{2} \sum_{k=N'+1}^{N'+s} K_{c,k}^{(\nu)} \int_{-\delta}^{\delta} T_\nu(\zeta) L_{b,n-n_k}(\xi - \xi_k - \zeta) d\zeta \tag{4. 12}$$

$$V_n(\xi) = \sum_{i=1}^{N'} K_{b,i} V_{b,n-n_i}(\xi - \xi_i) + \sum_{\nu=0}^{2} \sum_{k=N'+1}^{N'+s} K_{c,k}^{(\nu)} \int_{-\delta}^{\delta} T_\nu(\zeta) V_{b,n-n_k}(\xi - \xi_k - \zeta) d\zeta \tag{4. 13}$$

$$\Gamma_n(\xi) = \sum_{i=1}^{N'} K_{b,i} L_{b,n-n_i}(\xi - \xi_i) + \sum_{\nu=0}^{2} \sum_{k=N'+1}^{N'+s} K_{c,k}^{(\nu)} \int_{-\delta}^{\delta} T_\nu(\zeta) \Gamma_{b,n-n_k}(\xi - \xi_k - \zeta) d\zeta \tag{4. 14}$$

The matrix shear stress is equal to the shear strain here since the matrix is deforming elastically.

Finally, to calculate the desired exact solution for the lamina loaded at $\xi = \pm\infty$, a tensile load of unity is superimposed onto the solutions, thus canceling out the load applied to the hole boundary. The dimensionless matrix shear strain Γ_n

and stress T_n remain the same, but the fiber loads $P_n(\xi)$ and displacements $U_n(\xi)$ become

$$P_n(\xi) = L(\xi) + P \tag{4. 15}$$

and

$$U_n(\xi) = V_n(\xi) + P\xi \tag{4. 16}$$

As mentioned earlier, if the numerical results are not satisfactory, we can always subdivide the isolated segments into smaller segments to improve accuracy or increase the order of the polynomials to simulate the weight distribution of fiber breaks. However, smaller segments always lead to more computation load and slower speed. Most of the time, it's not necessary to add degrees of freedom. Instead, we can also force the shear stress in the broken matrix bays to be zero simply by adding a few rows in the load transmission factor matrix. In this way, the number of unknowns is larger than the number of equations and the system is solved by the least square method.

For the shear stress in the matrix, we define Θ_{ij} as the shear load in matrix element centered at (n_i, ξ_i) due to a fiber break at (n_j, ξ_j), and this is

$$\begin{aligned}\Theta_{j,i} &= \operatorname{sgn}(\xi_j - \xi_i)\frac{1}{4} \\ &\times \int_0^{\pi} \left\{\cos\left[(n_j - n_i + 1)\theta\right] - \cos\left[(n_j - n_i)\theta\right]\right\} \exp\left\{-2\left|\xi_j - \xi_i\right|\sin(\theta/2)\right\} d\theta\end{aligned} \tag{4. 17}$$

We define $\mathrm{H}_{ji}^{(\nu)}$, $\nu = 0,1$ as the shear stress transmitted onto matrix element (n_i, ξ_i) due to an isolated segment centered at (n_j, ξ_j) andwith length 2δ, and we have

$$\begin{aligned}\mathrm{H}_{ji}^{(\nu)} &= \int_{\delta}^{\delta} T_{\nu}(\zeta)\Gamma_{b,n_j-n_i}(\xi_j - \xi_i - \zeta)\, d\zeta \\ &= \frac{1}{4}\int_{-\delta}^{\delta}\int_0^{\pi} T_{\nu}(\zeta)\operatorname{sgn}(\xi_j - \xi_i - \zeta)\left\{\cos\left[(n_j - n_i + 1)\theta\right] - \cos\left((n_j - n_i)\theta\right)\right\} \\ &\quad \times \exp\left(-2\left|\xi_j - \xi_i - \zeta\right|\sin(\theta/2)\right) d\theta\end{aligned} \tag{4. 18}$$

$\mathrm{H}_{ji}^{(\nu)}$ can also be integrated semi-analytically. See Appendix B for the details and results.

Assuming we have m allocation points for the shear, the linear system becomes

$$\begin{bmatrix} \Lambda & \Phi^{(0)} & \Phi^{(1)} & \Phi^{(2)} \\ \Omega^{(0)} & \Psi^{(0,0)} & \Psi^{(0,1)} & \Psi^{(0,2)} \\ \Omega^{(1)} & \Psi^{(1,0)} & \Psi^{(1,1)} & \Psi^{(1,2)} \\ \Omega^{(2)} & \Psi^{(2,0)} & \Psi^{(2,1)} & \Psi^{(2,2)} \\ \Theta^{(0)} & \mathrm{H}^{(0,0)} & \mathrm{H}^{(0,1)} & \mathrm{H}^{(0,2)} \end{bmatrix} \begin{bmatrix} K_b \\ K_I^{(0)} \\ K_I^{(1)} \\ K_I^{(2)} \\ K_c^{(0)} \end{bmatrix} = \begin{bmatrix} -P_b \\ -P_I * \\ P_1 * \\ P_2 * \\ T_0 * \end{bmatrix} \tag{4. 19}$$

Here $K_c^{(0)}$ and $T_0 *$ are m-dimensional vectors and $\Theta^{(\nu)}$ and $\mathrm{H}^{(\nu,\kappa)}$ are matrices which have dimensions $m \times N$ and $m \times s$. Also $T_0 *$ has components $T_{0,j} * = 0$ for $j = 1,...,m$. The calculation of the tensile stress, shear stress and displacement is the same as in equations (4.12), (4.13) and (4.14).

5. Simulation Results

We now use the break influence technique presented in the last chapter to investigate the stress concentration near a hole in a fiber reinforced composite laminate subjected to tension at infinity as described in Figure 1.1. The far-field stress applied to the composite is assumed to be the stress applied directly to the fiber, and each fiber segment is a linearly elastic body with uniform tensile strength. The central transverse configurations we will study include a transverse array of one broken fiber with removed segment of length $2a$, a diamond-shaped wedge and an elliptical hole. In the algorithm, we take advantage of the configuration's double symmetry in determining the load transmission factors and the stress field near the hole.

We study the following behavior of stresses ahead of the hole tip: (1) the normal stress, σ_x, decaying along the crack plane ahead of the hole tip, (2) the shear stress, τ_{xy}, decaying along the crack plane ahead of the hole tip, (3) the fiber stress, σ_x, vs the fiber axial distance ξ, (4) the shear stress, τ_{xy}, vs the fiber axial distance ξ, and (5) the normal stress gradient along the crack plane. Results will be compared to results from elastic analysis (Bishop, 1972; Williams, 1953; Potter, 1977) and connection will be drawn between the two resulting forms of solution. We begin with a simple example of longitudinal crack consisting of one broken fiber and then move on to the wedge and the hole.

5.1 Example 1: Single Broken Fiber

5.1.1 Short gap distance

Since the previous study shows that the weight distribution is approximately uniform for the short gap of a single broken fiber, we test the zero order approximation here first.

As shown in Figure 5.1, there is only one broken fiber centered at $(0,0)$ and the gap length is $2a = 2$. We use q to indicate the position of the intact or surviving fiber in the figures. For example, fiber $q = 1$ means the first intact fiber. We model this with only one isolated segment and one fiber break at each end of the full gap.

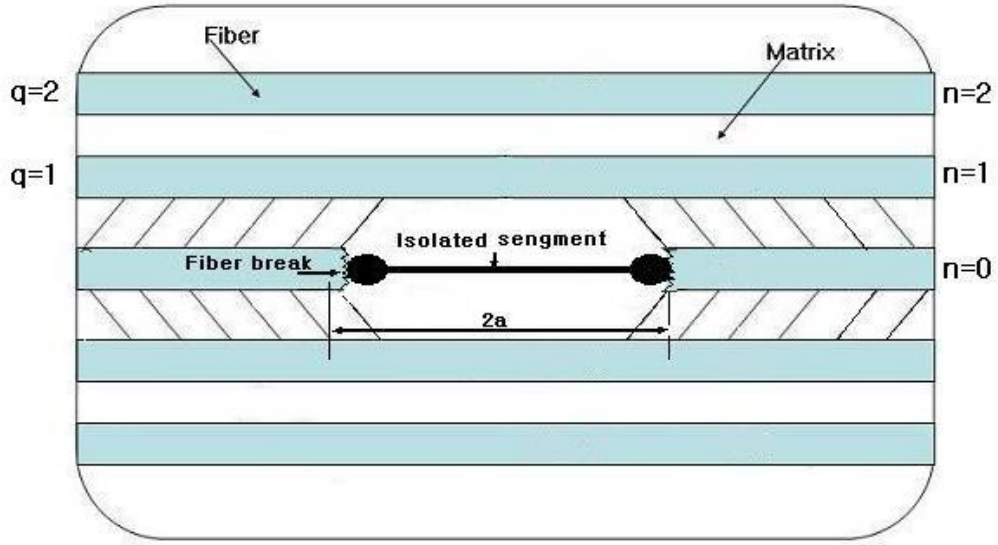

Figure 5. 1. One broken fiber with gap of length 2a in a composite lamina.

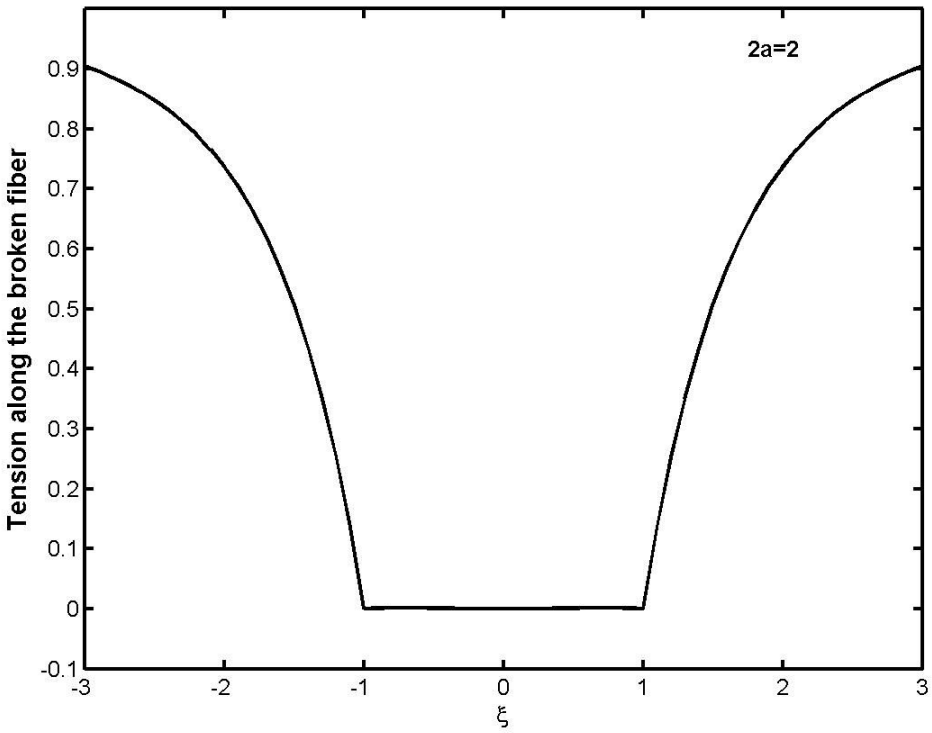

Figure 5. 2. Tension distribution along the broken fiber, $2a = 2$.

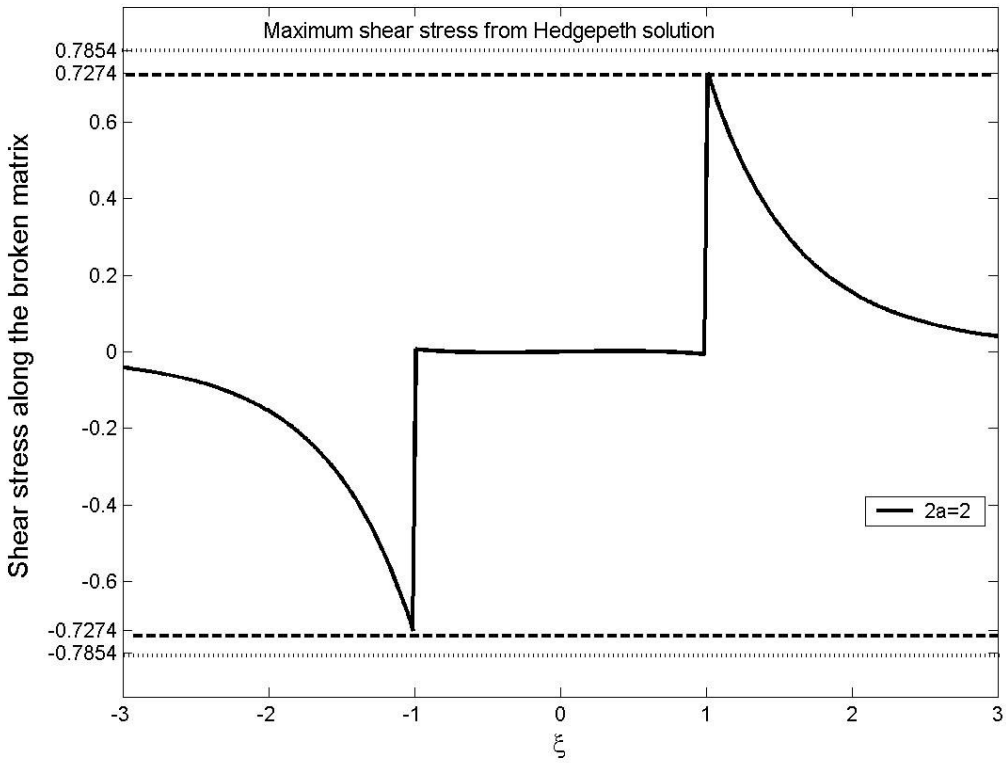

Figure 5. 3. Shear stress distribution along the broken matrix bay, $2a = 2$.

Figures 5.2 and 5.3 show the tension and shear stress distributions along the broken fiber and matrix bay between the first intact fiber and the broken fiber. As expected, the tensile stress and shear stress are zero for $-a \le \xi \le a$. The matrix bay, however, has shear stress concentration since it must transfer the load from the broken fiber to the flanking surviving fibers over a short distance. The maximum shear stress concentration in this case is lower than the stress concentration for an isolated fiber break (Hedgepeth 1961) since the flanking fiber provides less constraint to the broken fiber in the present case. As the gap length increases, the shear stress concentration decreases and eventually converges to about 0.7 .

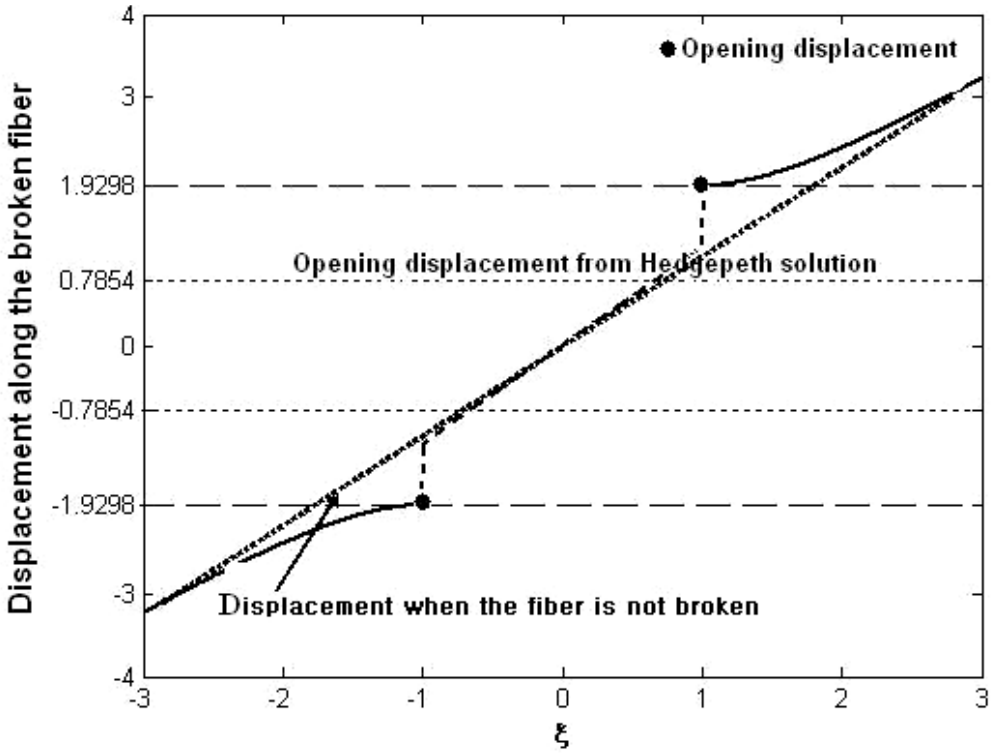

Figure 5. 4. Displacement profile along the broken fiber, $2a = 2$.

The displacement profile along the broken fiber is shown in Figure 4 and the displacements in the isolated segment in the central region $-a \le \xi \le a$ are, of course artificial, because the influence superposition technique actually places virtual fiber elements in the cavity. However, it does indicate the nature of the displacement distribution from body forces that would be needed to have the same effect as a physically removed segment. Since the tension at the broken fiber ends is zero, the displacement profile there is correspondingly flat, and as the tension builds up in the fiber, the slope of the displacement increases and finally the displacement converges to the profile as if the fiber wasn't broken.

In this example of $a = 1$ it takes about two characteristic lengths for the broken fiber to recover its load. In general, as the gap gets larger, it will take a longer distance to recover the load since the lamina outside the gap provides less resistance in constraining the broken fiber, which also leads to larger deformation around the gap. Compared to Hedgepeth (1961), the longitudinal crack has a larger opening displacement than an isolated fiber break as the flanking fiber at $-a \le \xi \le a$ provides more flexibility and the lamina behaves less stiff.

Figure 5.5 and figure 5.6 plot the stress distribution along the first five surviving fibers and matrix bays. We can see that the maximum tensile stress concentration is at the broken fiber end $|\xi| = a$ in the first surviving fiber. The other neighboring fibers have their maximum points at the center $|\xi| = 0$. The shear stress concentration in matrix bays between surviving fibers is much smaller than that in the matrix bay between the broken and the first surviving fiber. This observation leads to our yielding or debonding model in later chapters where yielding or debonding only propagates along the matrix bay between the last broken fiber and the first surviving fiber.

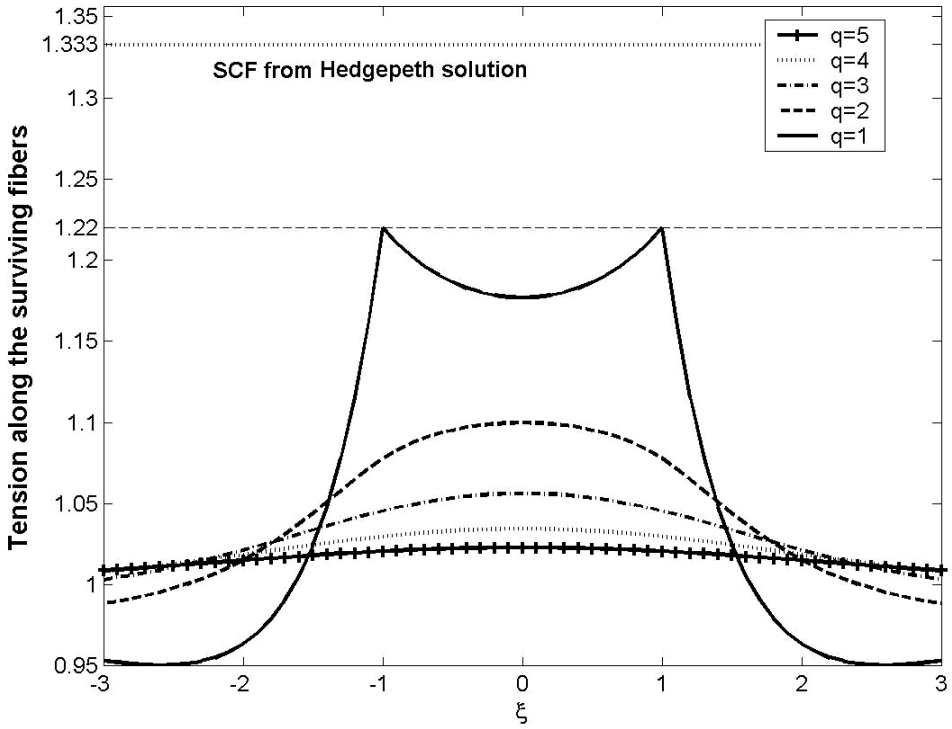

Figure 5. 5. Fiber tensile stress concentration along the first five surviving fibers, $2a = 2$.

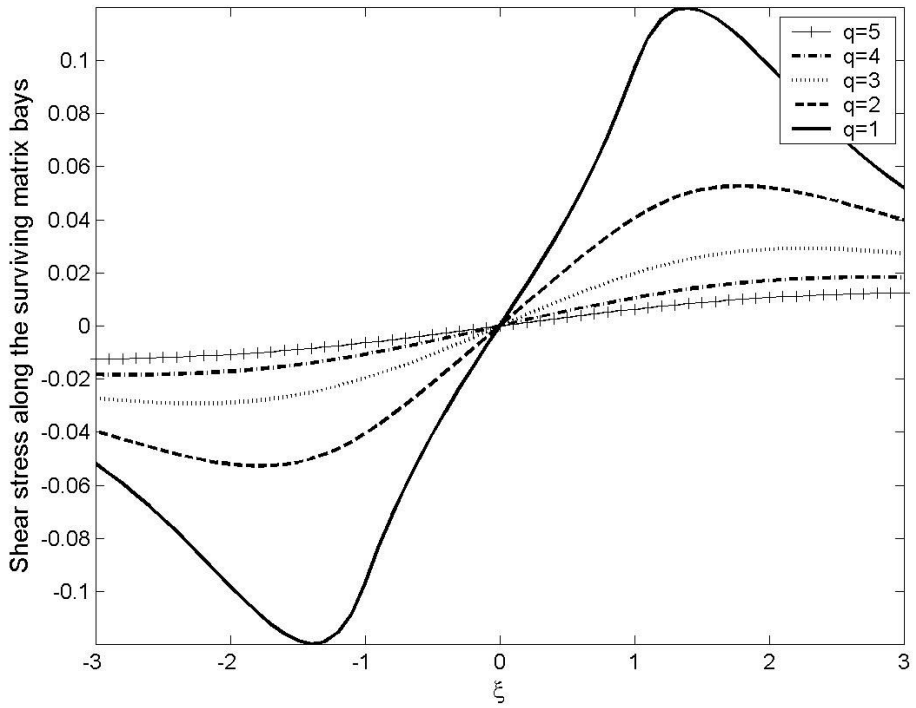

Figure 5. 6. Shear stress concentration along the first five surviving matrix bays, $2a = 2$.

Compared to the stress concentration in Hedgepeth (1961) where there is only one fiber break, the maximum tensile stress concentration factor (SCF) of the first surviving fiber for $2a = 2$ is much smaller. The tensile load concentration is down to about $1/2$ by the second fiber and $3/11$ by the third and $1/7$ by the fourth surviving fiber. On the other hand, the load for the isolated break decays much more rapidly, which compensates the higher stress concentration at the nearest intact fiber. So increasing the gap length of the broken fiber decreases the overload but increases the overstressed length. Note that in reality, fiber elements have significant fluctuations in the local material strength due to flaws. So while a longer gap doesn't induce higher stress concentration, neighboring fibers may actually be more likely to break because of the longer region over which flaws could be found.

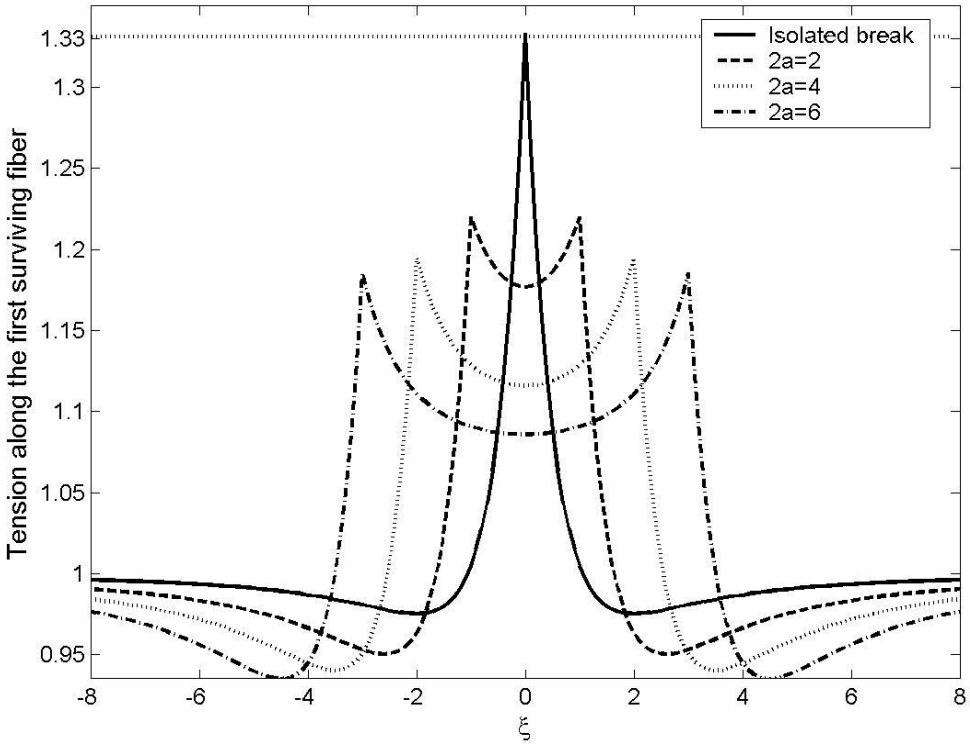

Figure 5. 7. Tension along the first surviving fiber.

Figure 5.7 shows the tensile stress distribution along the first surviving fiber for different gap lengths, $2a$. The maximum stress concentration decreases and the load recovery distance increases as the gap gets larger. It also takes a much shorter length for fibers neighboring a longer gap to drop into slight compression (relative to the far field load) outside the overloaded area. The level of compression changes with the gap length too; the longer the gap, the more severe the compression.

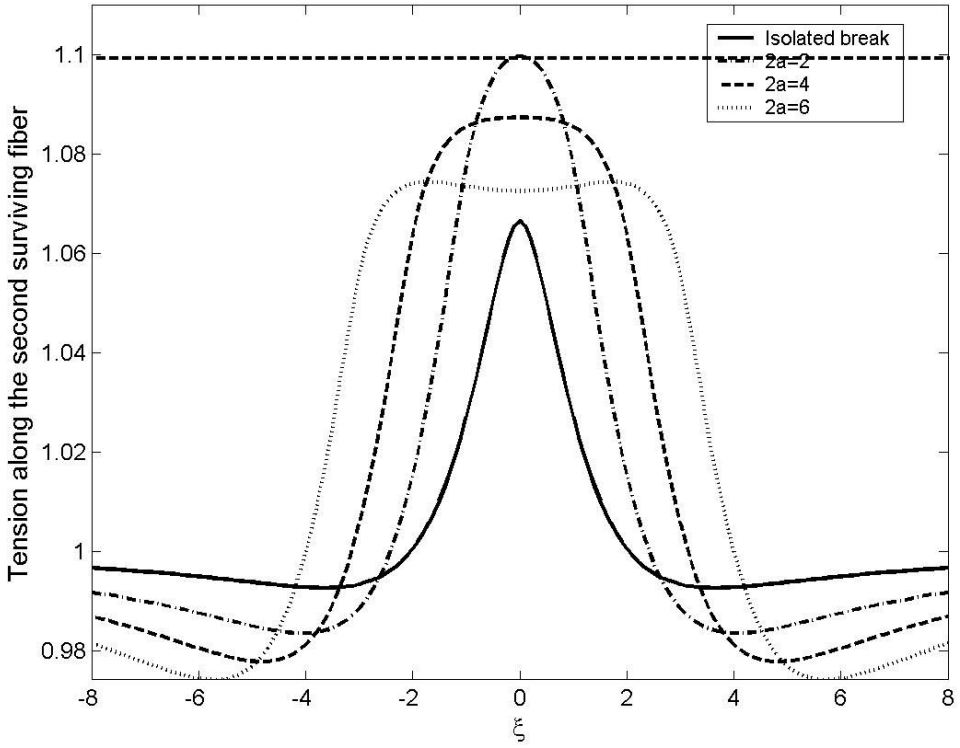

Figure 5. 8. Tension along the second surviving fiber.

Figure 5.8 plots the tension distribution along the second surviving fiber for different gap lengths. The fiber near a gap has higher stress concentration factor than the one neighboring a fiber break because the gap causes a larger overloaded area on the first surviving fiber, whose accumulation of tension determines the stress concentration factor on the second surviving fiber. The stress maximum is at the crack plane, $\xi = 0$, for all the cases due to the symmetry in the geometry. The

longer the gap is, the more severe the compression is and the larger the unloading length is. As the gap distance increases, the maximum stress concentration factor drops, but the overloaded area increases. As the gap length increases, a hump is expected, with shape similar to the first surviving fiber.

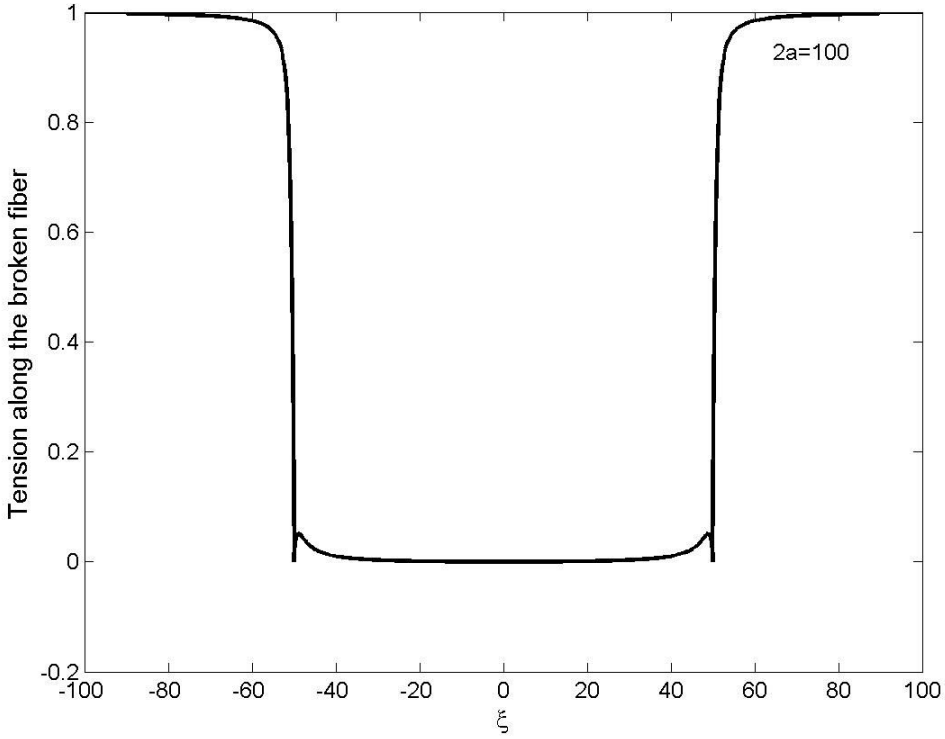

Figure 5. 9. Tensile stress distribution along the broken fiber, $2a = 100$.

5.1.2 Long gap distance

Figures 5.9 and 5.10 plot the tensile stress and shear stress distribution along the broken fiber and the broken matrix bay, respectively, for a large gap $2a = 100$. Both figures show small non-physical spikes towards the end of the broken fiber. There are a few ways to improve the results. As seen in Figure 3.3, the weight distributions of fiber segments towards the end of the broken fiber tend to be more complex than captured by the uniform distribution.

Increasing the number of segments especially near the end of the broken fibers is expected to capture the change of curvature. The second method to be investigated is to use higher order polynomials to approximate the weight distribution. Both methods will be used in later chapters.

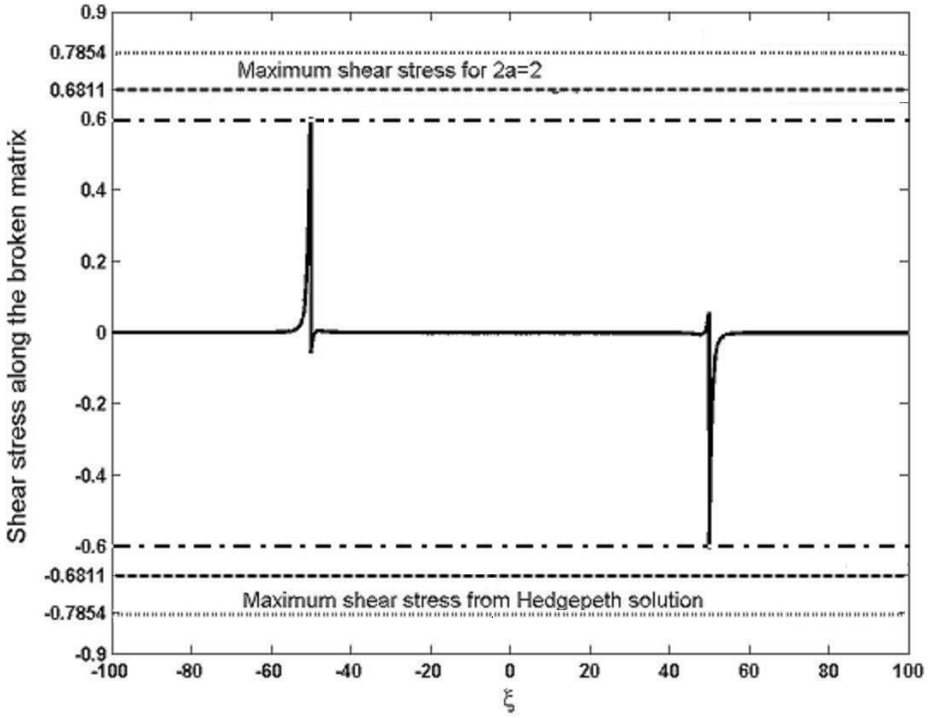

Figure 5. 10. Shear stress distribution along the broken matrix bays, $2a = 100$.

The shear stress distribution along the matrix bay between the first flanking fiber and the broken fiber is presented in Figure 5.11. As mentioned before, as the gap gets larger, the maximum shear stress concentration decreases because the surviving fiber deforms over the region $-a \le \xi \le a$ and overloads become milder. Note that maximum tensile stress concentration drops very rapidly further away from the broken fiber.

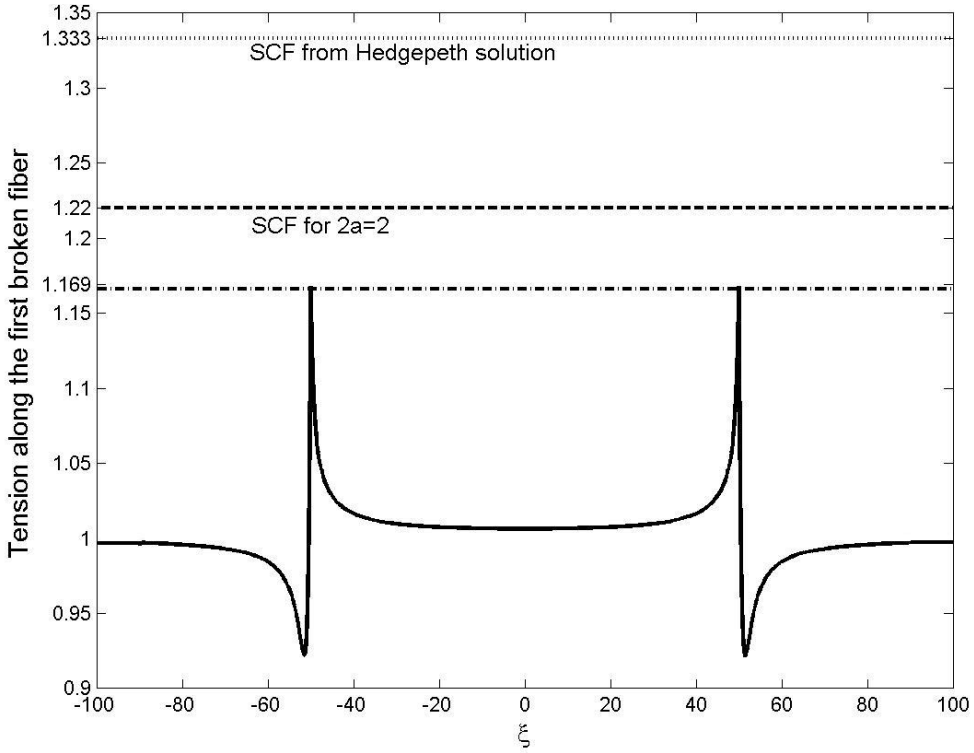

Figure 5. 11. Stress concentration along the broken matrix bays, $2a = 100$.

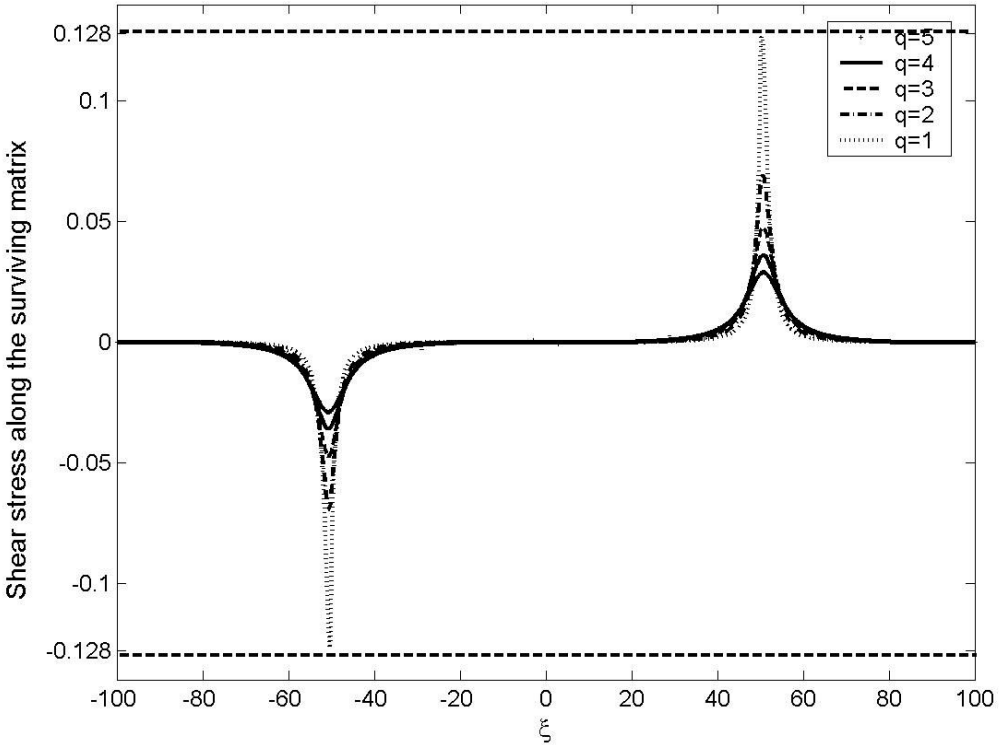

Figure 5. 12. Shear stress along the flanking matrix, $2a = 100$.

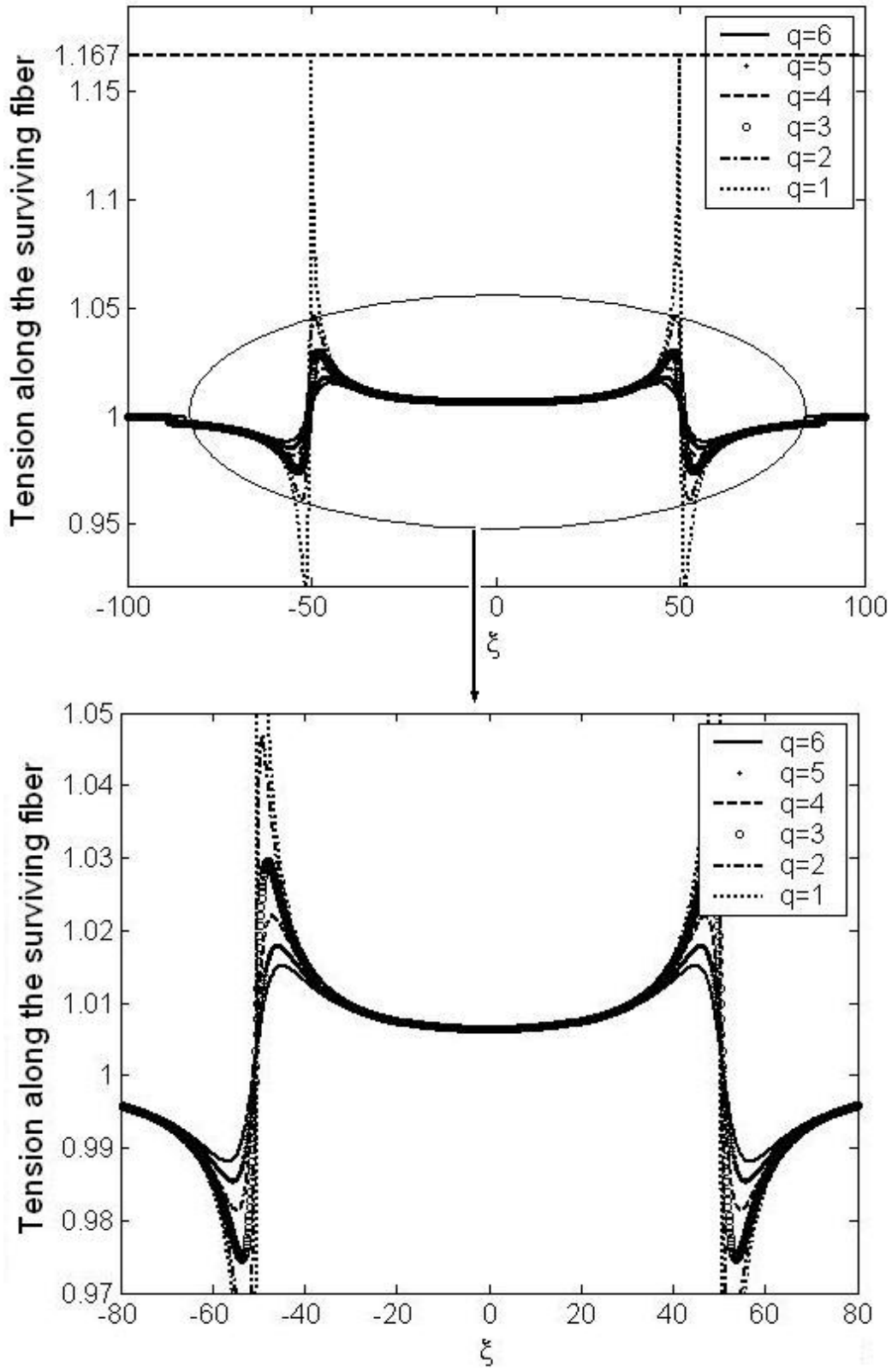

Figure 5. 13. Tension along the surviving fiber, $2a = 100$.

Figure 5.13 shows the tensile stress concentration for the first five surviving fiber. Interestingly, all the fibers have almost the same load profile except at the point $\xi = \pm a$. We have studied up to twenty flanking fibers and the tensile load distribution keeps the same shape in the region overlapped by the gap. The maximum stress concentration is very low at about 1.03, but the overloaded area spreads out by a very significant distance. This observation is also very important evidence for one of the idealized load redistribution models, the equal load sharing (ELS) rule.

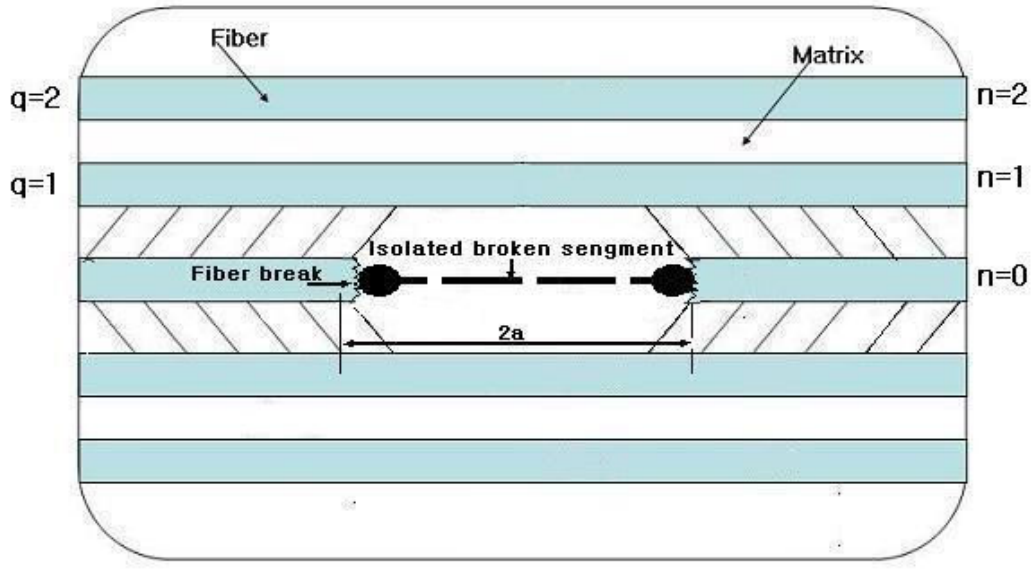

Figure 5. 14. One broken fiber of length $2a$ modeled by three isolated broken segments and two fiber breaks.

5.1.3 Correction with denser segments

As seen in last section, as the gap gets larger, one isolated segment is not accurate enough to catch the weight distribution of fiber breaks, especially near the broken fiber ends. The simplest way to improve this is to use more segments between fiber breaks to catch the rapid change of weighting factors required near the hole edge. The segment can be uniformly divided, but our numerical experiment shows that it's more efficient to place shorter segments near the boundary of the hole where the weighting factors changes sharply. The new allocation of the fiber break and the segment is described in Figure 5.14, which has four segments between the fiber break at each end of the broken fiber.

Figures 5.15, 5.16 and 5.17 show a comparison of results for $2a = 100$. As shown in the figure, the tension and shear stress field simulated by more segments in the cavity is much closer to the "correct" stress field, i.e., the tensile stress and the shear stress in the cavity are approximately zero. Especially the spikes near the edge of the broken fiber in Figure 5.9 are reduced and the unwanted shear stress reversal near the edge of the broken fiber is almost gone. The improved tensile stress concentration is slightly higher because the virtual fiber element no longer supports tension.

Note that more segments lead to more computational demand and longer simulation time. For a hole containing many broken fibers, this increment of load will become more obvious since the longer gap has to inherit the fiber breaks and segments from the shorter gap. One must be aware of the trade-off between the computation load and the improvement of the stress concentration accuracy before dividing the broken segments into smaller pieces.

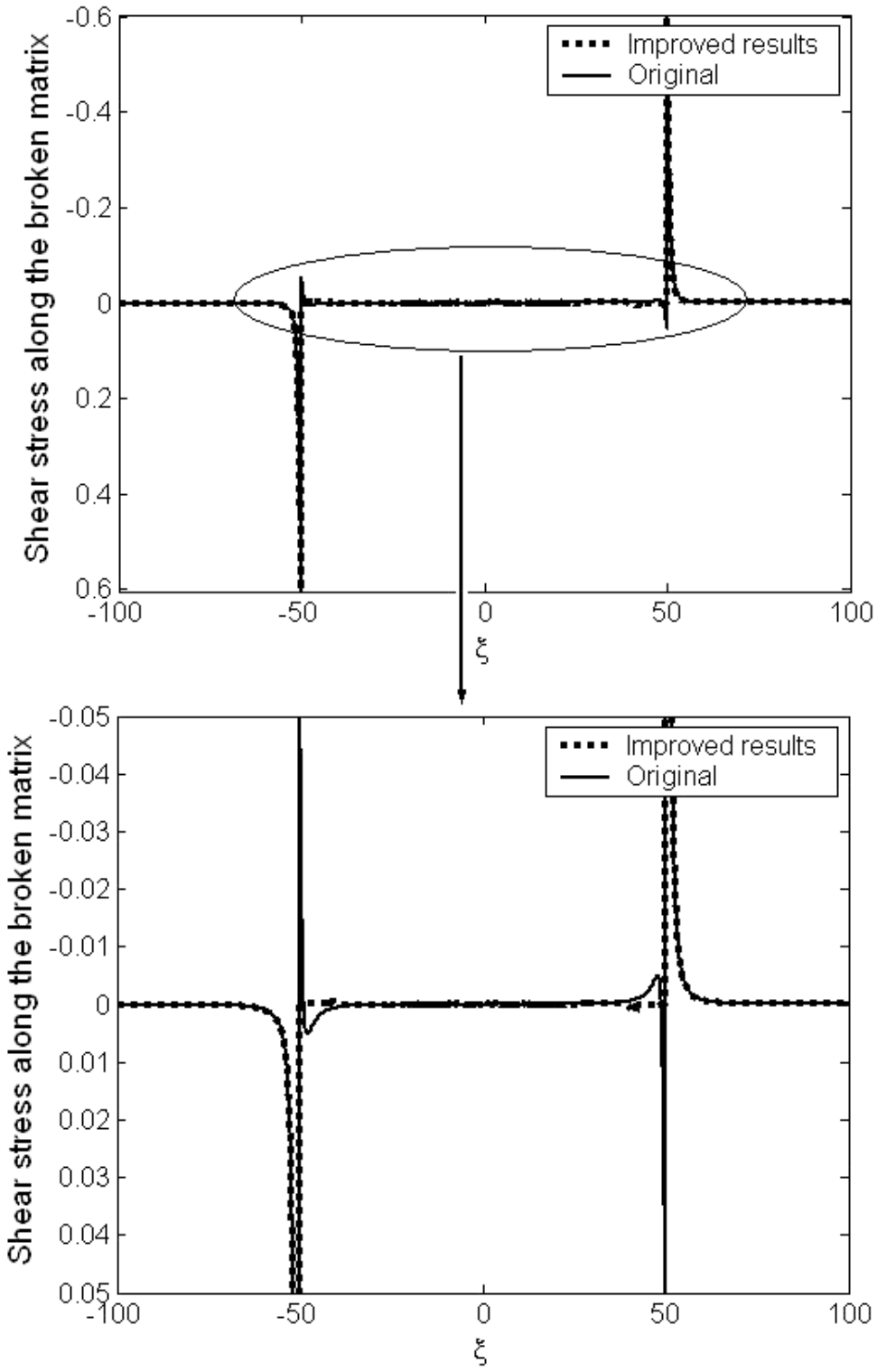

Figure 5. 15. Shear stress distribution along the matrix between the broken fiber and the first surviving fiber, $2a = 100$.

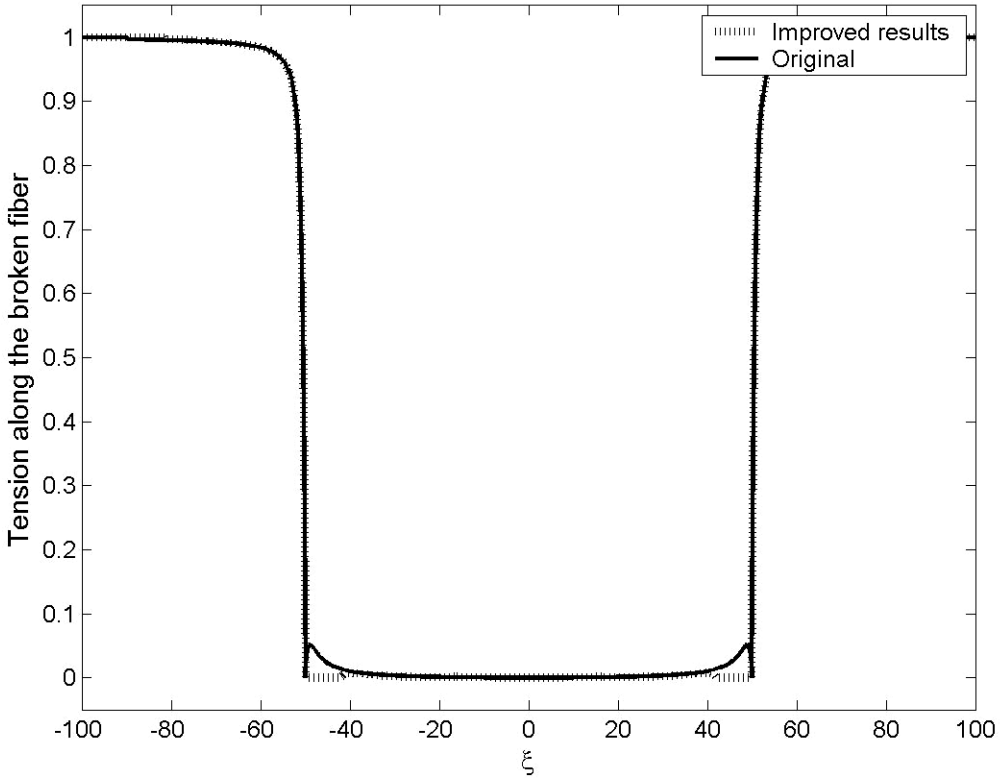

Figure 5. 16. Tension along the broken fiber, $2a = 100$.

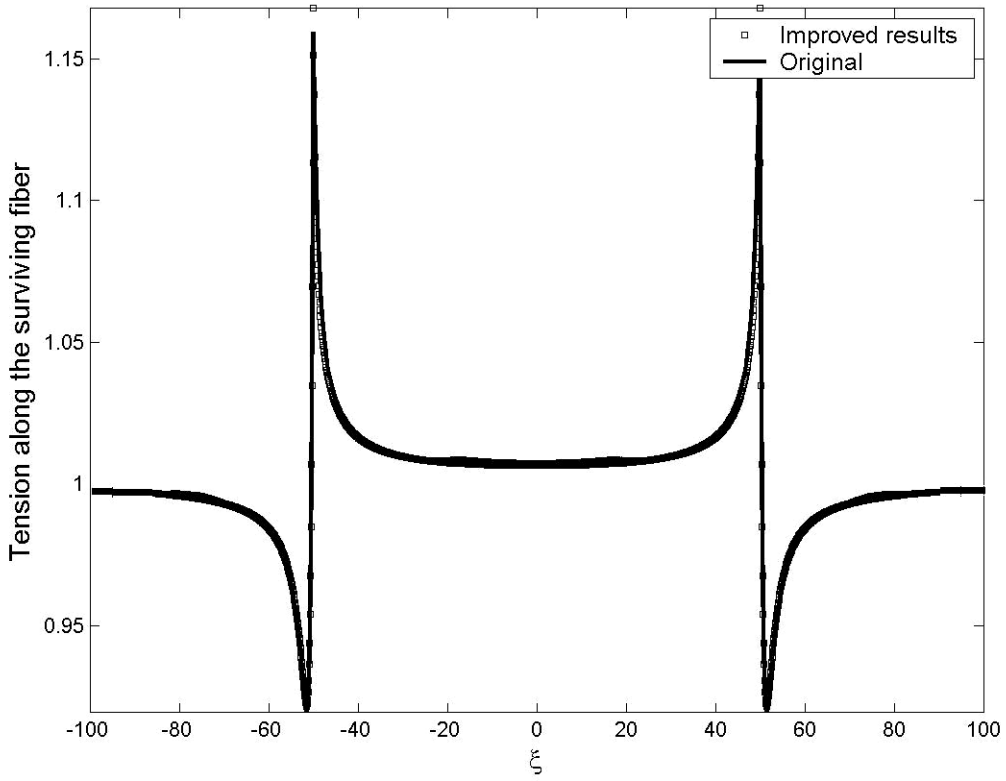

Figure 5. 17. Tension along the first surviving fiber, $2a = 100$.

5.1.4 Correction with linear distributed fiber breaks

In last section, we used smaller segments between fiber breaks to improve results. Here, we study the second: applying higher order weighting distributions. The hole profile is described in Figure 5.18, which has a minimum number of fiber breaks and isolated segments: eight fiber breaks and five isolated segments. Since the tension and the shear stress are closely related to each other, we are only going to show tension comparison before and after improvement by the linear approximation for demonstration purpose.

Figure 5.19 shows the tensile stress distribution along the broken fibers calculated from uniform weight distribution approximation. Obviously, the tension for fiber $n = 0$ in the hole has wavy fluctuations in the gap and deviates from zero by a considerable amount. However, the tensile stress is zero for the middle region overlapped by all the gaps, suggesting we should use linear or higher order approximations for regions that are not overlapped and keep uniform approximations for the overlapped region.

Figure 5.20 plots the tension along the broken fibers using linear approximation for the weight distribution. Clearly, the waves in Figure 5.19 have been greatly reduced and the small bump near the edge of fiber $n = \pm 1$ suggests that we need to use short segments in that area.

Overall, our numerical experiments show that both methods (denser broken segment or higher order approximation) can improve the results greatly by adding more degrees of freedom to the whole system.

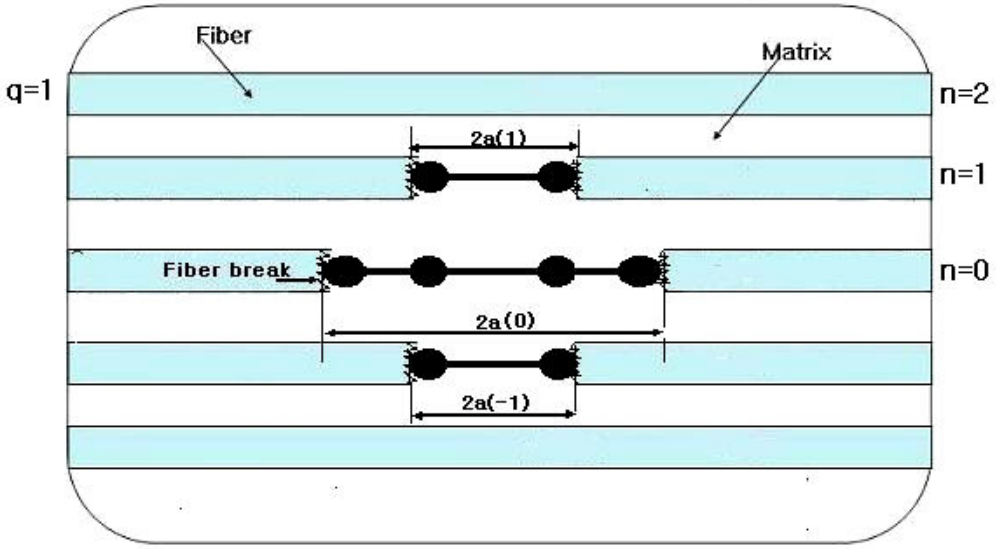

Figure 5. 18. A hole containing three broken fibers in a composite plane.

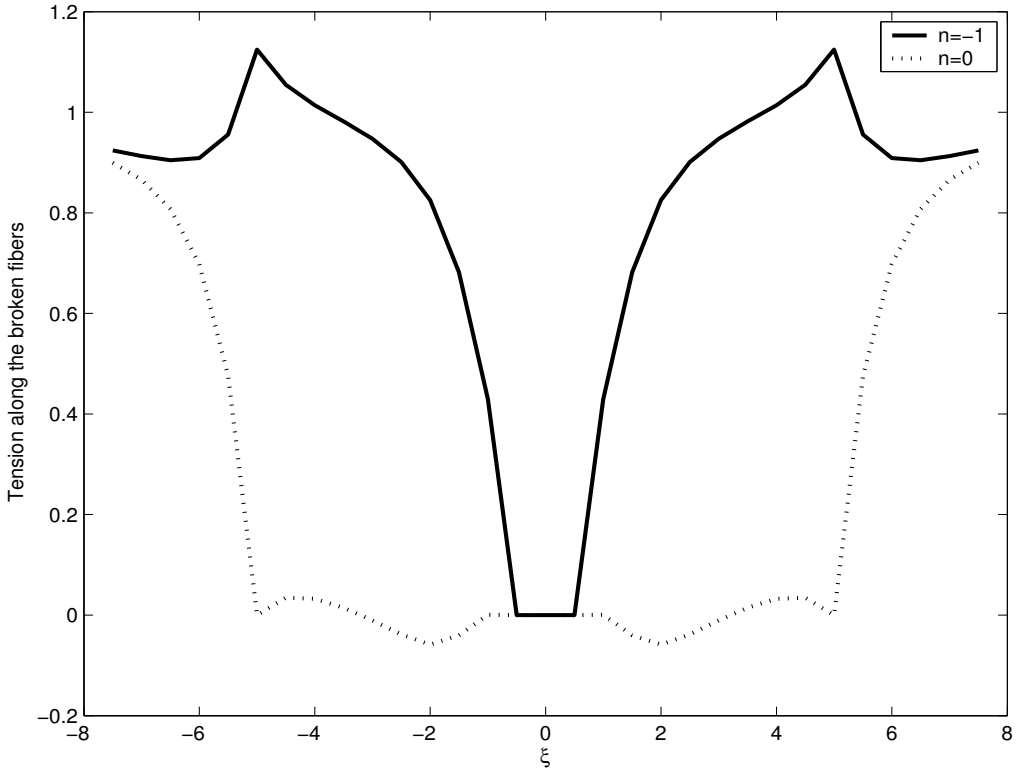

Figure 5. 19. Tension along the broken fibers calculated from the uniform approximation.

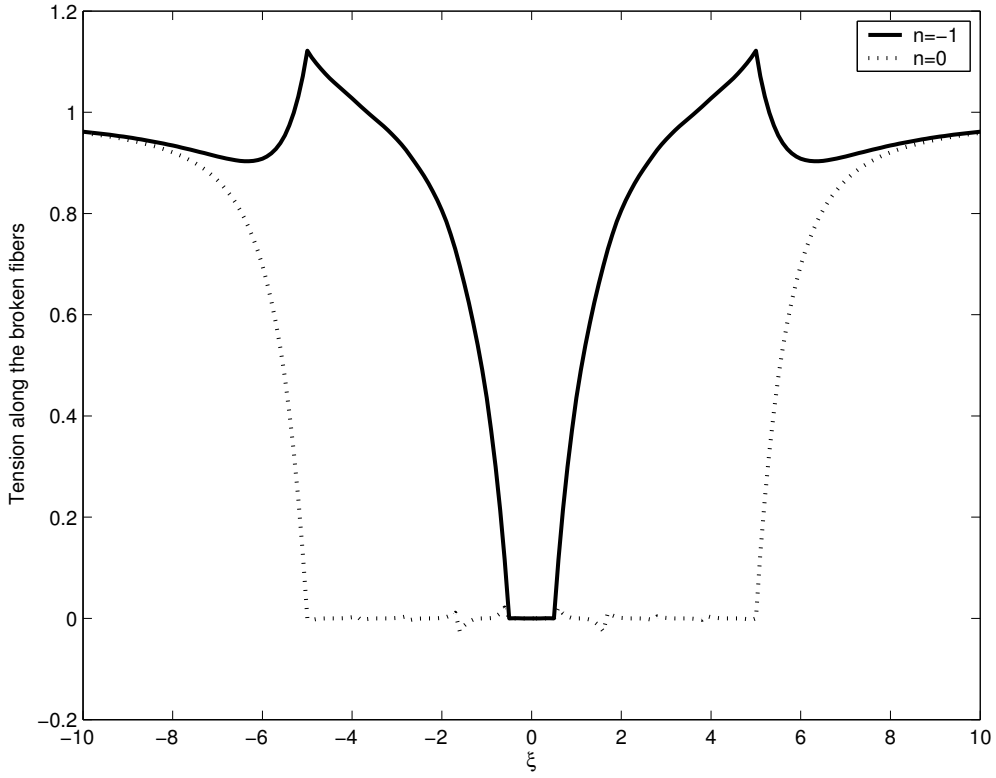

Figure 5. 20. Tension along the broken fibers calculated from the linear approximation.

Lastly, note that in most cases, the uniform approximation is good enough to simulate the stress field near a wedge or an elliptical hole since the difference of gap distance between two adjacent fibers is quite small for these geometries and the improvement from the linear weight function is not so significant. When the hole gets larger, our numerical experiment shows that the importance of the segment that is not overlapped by all gaps in the hole is reduced greatly. We can actually take away all the broken segments that are a few fibers away from the hole edge or tip, and the results are about the same. This is important because we used this observation in the examples to reduce the calculation load and achieved good results. Figure 5.21 shows the simplified computational framework for holes with large numbers of broken fibers. All the segments are taken away except the ones at the

hole tip. Furthermore, we can even reduce the number of fiber breaks for the broken fiber far away from the hole tip and still obtain good results.

The reason why we can reduce the structure for the broken fiber away from the hole tip is because these fibers are far away from the intact fibers and their neighbors are forced to have zero load such that the fiber is not loaded naturally except at the edge of the hole. So the reduction of the computational structure is consistent with physical insight.

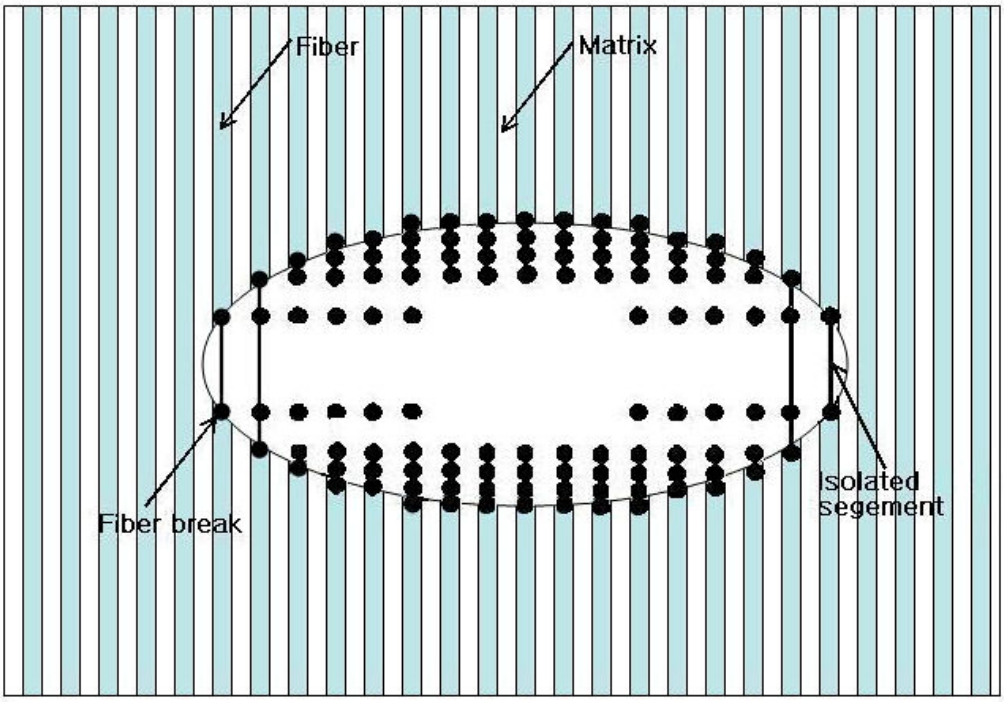

Figure 5. 21. Simplified computational structure for an elliptical hole in the composite lamina.

5.1.5 Stress concentration factor

As an extension of the isolated fiber break problem (Hedgepeth, 1961), we investigate the maximum stress concentration near a single broken fiber with gap

length, $2a$. Hedgepeth (1961) derived the peak tensile stress concentration factor K_N for an isolated fiber break in the following form:

$$K_N = \frac{4 \cdot 6 \cdots (2N+2)}{3 \cdot 5 \cdots (2N+1)}, \quad N = 1,2,3... \tag{5. 1}$$

where $K_0 = 1$. Fichter (1969) found that the normalized shear stress concentration in the matrix bay between the first intact fiber and the last broken fiber is right at the break and is

$$\hat{T}_N = \left(\frac{\pi}{4}\right) \frac{N(2N)!}{2^{2N-1}(N!)^2}, \quad N = 1,2,3... \tag{5. 2}$$

Using Stirling's approximation $r! \approx \sqrt{2\pi} r^{r+1/2} e^{-r}$, Beyerlein, Phoenix and Sastry, (1996) derived an approximation to the above given by

$$K_N \approx \sqrt{1 + \pi N / 4} \tag{5. 3}$$

$$\hat{T}_N \approx \frac{\sqrt{\pi N}}{2} \tag{5. 4}$$

Figures 5.22 and 5.23 plot the maximum tensile stress and the shear stress concentrations, respectively, versus the gap distance $2a$. As just mentioned, the maximum stress concentration factor applies right at the end of the broken fiber. We can see that both the tensile stress concentration and the shear stress concentration decrease as the gap length increases.

The tensile overload imposed by the gap asymptotically converges to about half of the overload from an isolated fiber break. The maximum shear stress drops slightly overall.

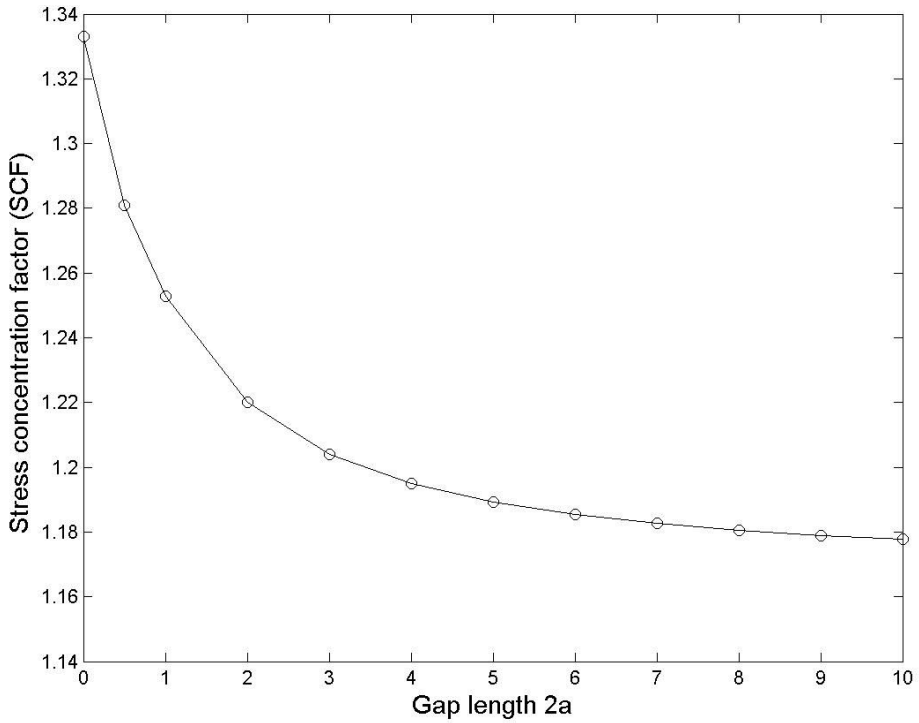

Figure 5. 22. Stress concentration factor (SCF) for different broken length.

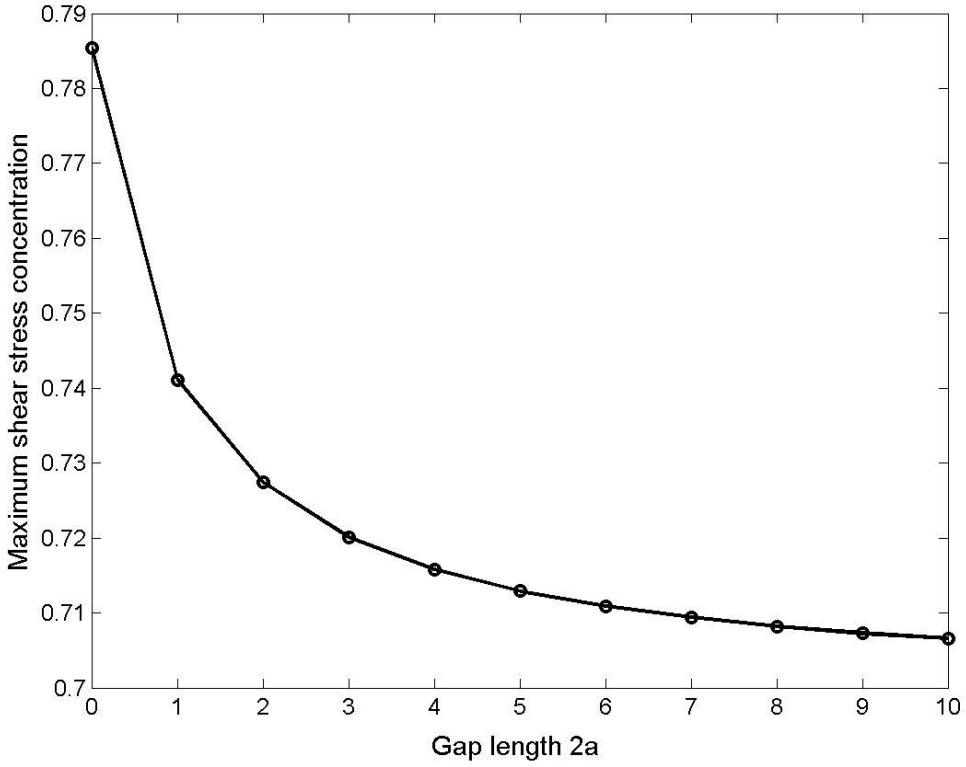

Figure 5. 23. Maximum shear stress concentration for the matrix between the broken fiber and the first intact fiber.

5.1.5 Conclusion

In this one single broken fiber example, we have studied the stress field near a single broken fiber with different gap length. Overall, the stress concentration decreases as the gap distance increases and the distance has more effect on the tensile stress field than on the shear stress field. Compared to the isolated fiber break problem, the broken fiber which has the material removed in the gap needs longer distance to recover its applied load and the overload along the crack plane decays slightly slower, which means more fibers, are in distress.

Particularly, when the gap distance is very large, a very generous amount of fiber will be overloaded and have almost the same load distribution except at the tips of the broken fiber. This provides strong evidence for a more equal load sharing theory near the edge, which states that the overload caused by the broken fiber is equally shared by its nearby neighbors.

In terms of the computational technique, we find that finer segments and higher order approximation for the weighting factors improve the results greatly. However, both methods increase the computation load significantly, especially for holes containing multiple broken fibers. So these should be used selectively, such as only at the hole tip.

We also proposed a much simpler computational structure for holes containing many broken fibers as shown in Figure 5.21. All the segments are taken away except the ones near the hole tip and the number of fiber breaks is also reduced for region away from the hole edge. The simplification lowers the computation load significantly and will be used in later examples.

5.2 Example 2: A wedge

In this section, we consider a central transverse wedge consisting of N broken fibers in a two dimensional fibrous composite laminate which was selected

to allow comparison with corresponding elastic analysis (Williams, 1953) for a wedge of length $2c$ in an infinite orthotropic homogeneous plate(see Figure 5.24). There are a total of nine broken fibers in this example, and the wedge angle is θ as shown in the figure. Figure 5.24 exhibits three ways to view the material system: (a) a lamina containing equally spaced fibers and matrix regions, (b) a material with tension lines and shear stress regions of width $w^* = w + h$, and, (c) an orthotropic continuum. This model is used to draw connection between the shear-lag solution and the elastic solution, first introduced by Beyerlein, Phoenix and Sastry (1996).

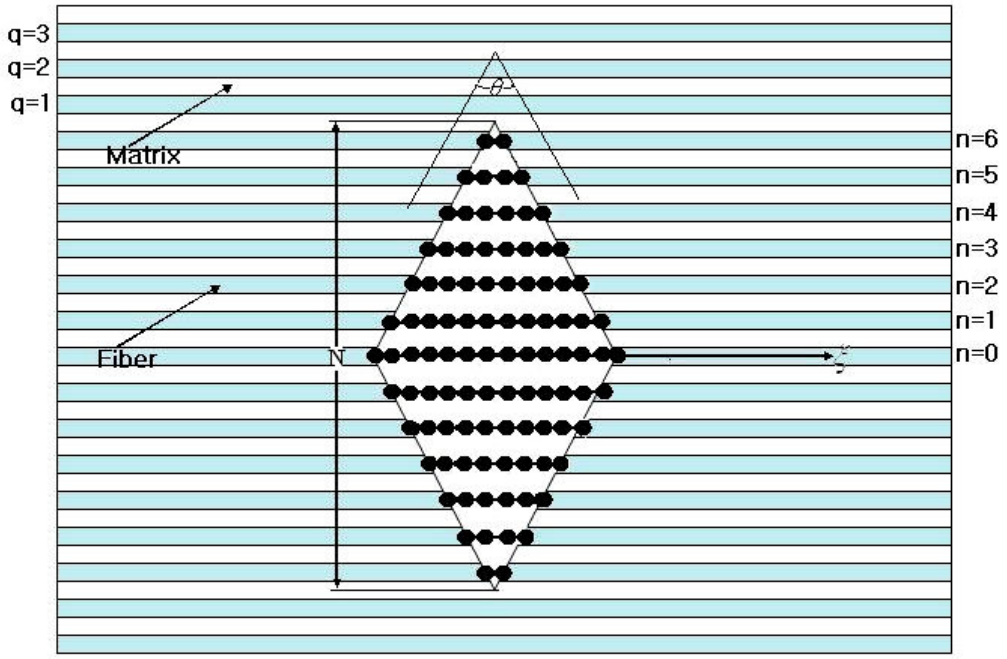

(a)

Figure 5. 24 A transverse central wedge in three material systems: (a) fiber reinforced composite lamina, (b) material with tension lines (along fiber centerlines) and effective matrix regions of width $w*$, and (c) an orthotropic continuum.

Figure 5.24 (Continued)

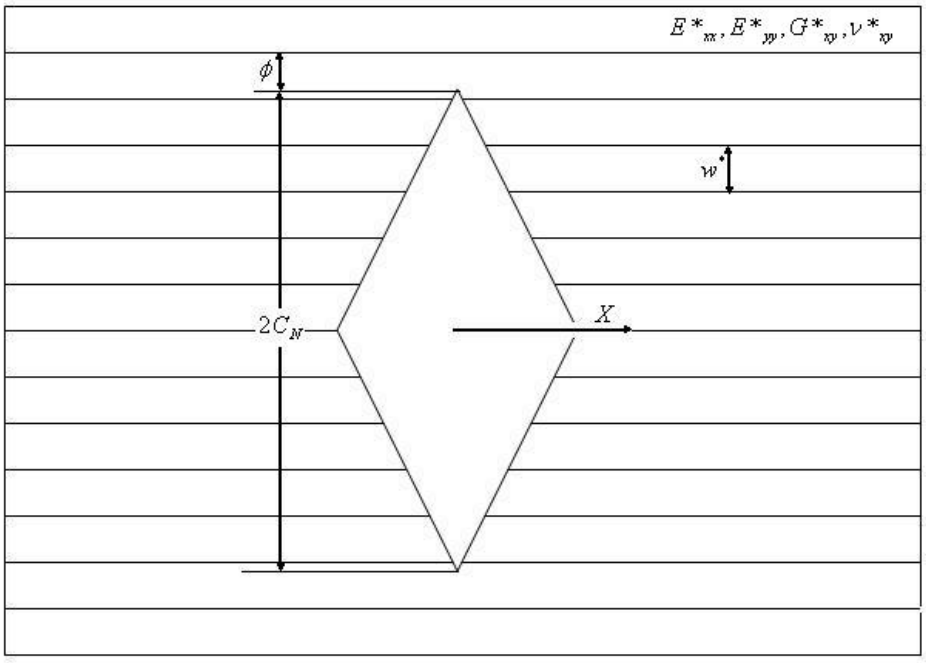

(b)

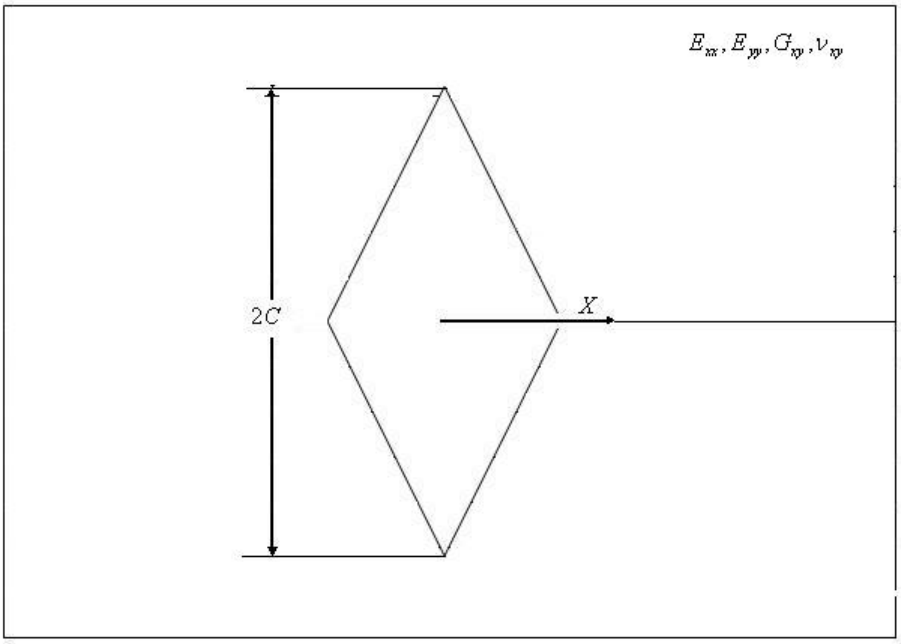

(c)

Associating the results from the shear-lag model to continuum elastic analysis requires defining an equivalent crack length and relating the elastic constants between a composite lamina with discrete fibers of diameter h and matrix regions of width w (see Figure 5.24 (a)) and those of an orthotropic homogeneous continuum (see Figure 5.24 (c)). Following the model in Beyerlein, Phoenix and Sastry (1996), where a fiber has been mathematically collapsed to a tension line with an effective stiffness EA and the matrix has been widened with spacing $w^* = (w+h)$ in place of w compensated by a higher stiffness $G(h+w)/w$, as shown in Figure 5.24 (b), we apply identical shear-lag analysis as seen in Figure 5.24 (b) and study the stress field near the wedge tip.

First, we convert the fiber and matrix parameters $E, G, A, w,$ and h to the elastic constant, namely G^*_{xy}, ν^*_{xy}, $E^*_{yy,}$ and E^*_{xx}. We assume the composite is made of isotropic fibers and matrix with respective elastic constants E_f, $G_f = E_f \big/ \left[2(1+\nu_f)\right]$ and ν_f, and E_m, $G_m = E_m \big/ \left[2(1+\nu_m)\right]$ and ν_m. By rule-of-mixtures formulas in terms of fiber volume fraction V_f, we have the following:

$$E^*_{xx} = E_f V_f + E_m (1 - V_f) \tag{5. 5}$$

$$\frac{1}{G^*_{xy}} = \frac{V_f}{G_f} + \frac{(1 - V_f)}{G_m} \tag{5. 6}$$

$$\frac{1}{E^*_{xy}} = \frac{V_f}{E_f} + \frac{(1 - V_f)}{E_m} \tag{5. 7}$$

and

$$\nu^*_{yx} = \frac{E^*_{yy}}{E^*_{xx}} \left(\nu_f V_f + \nu_m (1 - V_f) \right) \tag{5. 8}$$

The shear-lag model can be extended by replacing the fiber and matrix material constants with the above constants, assuming the entire tensile load carried in the matrix is lumped in with the fiber and any shear deformation in the fiber is lumped in with the matrix as shown in figure 5.24 (b). In another words, we have

$V_f = h/(h+w)$, and the effective shear modulus G^*_{xy}, Young's modulus, E^*_{xx}, cross-sectional area $A^* = h(h+w))$ and effective matrix spacing $w^* = h + w$ replacing G, E, A and w respectively. Also p/A^* and p^*/A^* will be replaced by σ and σ^*. The replacement serves to homogenize the geometric and elastic material properties of the matrix and the fiber, and extend them into proper slots in the shear lag model. The following are the material properties we have used in the example.

$$E_x = 2.39 \times 10^{11}\, Nm^{-2}$$

$$G_{xy} = 5.76 \times 10^{9}\, Nm^{-2}$$

$$V_f = 0.5$$

$$w = h = 2r_f = 1 \times 10^{-5}\, m$$

where r_f is the radius of the fiber. E_x and ν_{xy} are not used in the shear-lag model. They are determined empirically to match the results from both solutions in our computation. In general, the agreement between the elastic analysis and shear-lag model improves when E^*_{yy} is very large because large transverse stiffness constrains both the unbroken and broken fibers to displace only in the fiber direction, as is assumed in shear-lag analysis.

Next we must convert geometric properties of the wedge into our normalized space. Recall that the length is scaled by the characteristic length.

$$\xi = \frac{x}{\sqrt{\frac{EAw}{Gh}}} \tag{5. 9}$$

Using the above relations we find

$$x = \xi w^* \sqrt{\frac{E^*_{xx}}{G^*_{xy}}} \tag{5. 10}$$

For the discrete lamina, the crack length is modeled as an effective width of broken fibers and matrix bays. For a given number of broken fibers, the equivalent wedge length $2c$ consists of $(N-1)$ effective spacings of width $(h+w)$, plus two end portions, each the fraction $(1-\phi)$ of $(h+w)$, which extend into the matrix bay between the last broken fiber and first intact fiber on both sides of the wedge. In another words,

$$\begin{aligned} 2c_N &= \left[(N-1)+2(1-\phi)\right](h+w) \\ &= \left[(N-1)+2(1-\phi)\right]w^*/2 \cong Nw^*/2 \end{aligned} \tag{5. 11}$$

where ϕ is determined empirically in the computation to achieve the best agreement between the two solutions. For the wedge opening angle, θ, the gap length for each broken fiber is decided by

$$a(|n|) = \frac{\left\{4-|n|+(1-\phi)\right\}w^* \tan\left(\frac{\theta}{2}\right)}{\sqrt{\frac{E^*}{G^*}}w^*}, \quad \text{for } n = -4,...,4 \tag{5. 12}$$

The distance away from the wedge tip is defined as

$$r_s = \left[\phi+(q-1)\right]w^* \tag{5. 13}$$

The scaling in shear-lag analysis along the axial x direction to plot the results p_n/σ^* and τ_n/σ^* is defined as

$$\begin{aligned} \xi_{c_N} &= \frac{x}{c_N\sqrt{\frac{E^*_{xx}}{G^*_{xy}}}} \\ &\approx \frac{2\xi}{N} \end{aligned} \tag{5. 14}$$

We are now ready to investigate the extent to which the normalized stress profiles match the elastic analysis. We will consider a single crack first, then extend the results to the wedge with opening angle, θ. Last we will compare the results from both solutions.

5.2.1 Transverse crack

A central transverse crack is the simplest wedge where $\theta = 0$. Due to the symmetric geometry, we will just study the fibers and matrix bays on the right side of fiber $n = 0$. Figures 5.25 and 5.26 show the tensile stress distribution and shear stress distribution along the broken fiber and the broken matrix bay respectively. The fiber in the middle recovers its load with the slowest pace and the matrix bay between the last broken fiber and the first intact fiber has the highest shear stress concentration. The broken fiber away from the crack tip has a very similar tension distribution. Figure 5.27 gives the tensile stress distribution along the surviving fibers ahead of the crack. The tensile stress concentration decays to about $1/3$ by the second fiber, $1/5$ by the third fiber and $1/8$ by the fourth fiber.

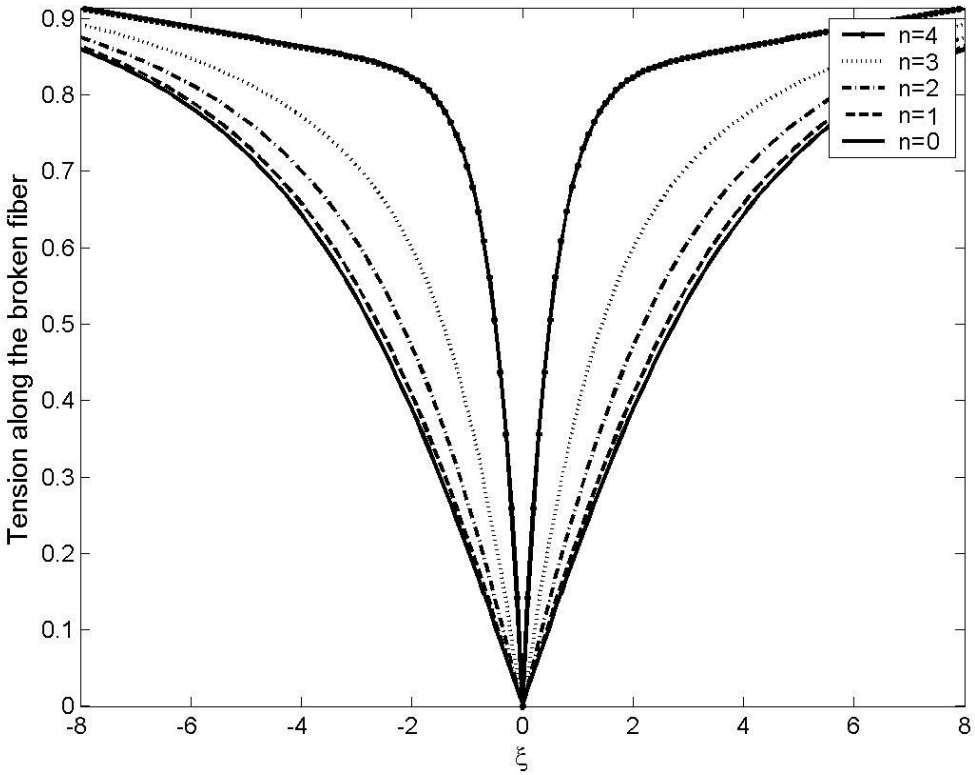

Figure 5. 25. Tension along the broken fiber for a transverse crack, $N = 9$.

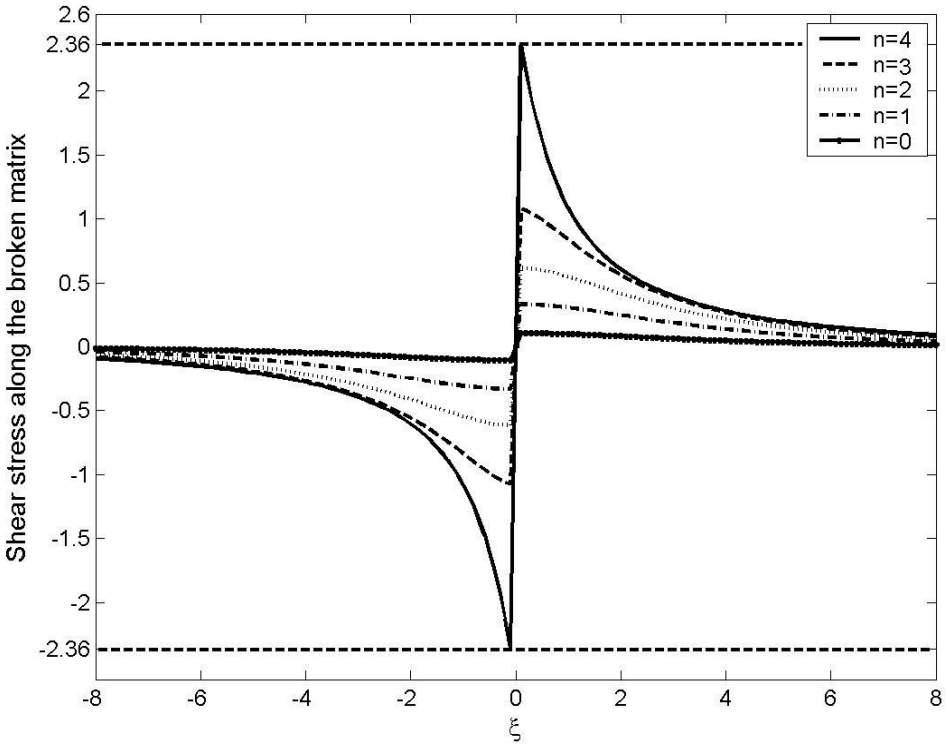

Figure 5. 26. Shear stress distribution along the broken matrix, $N = 9$.

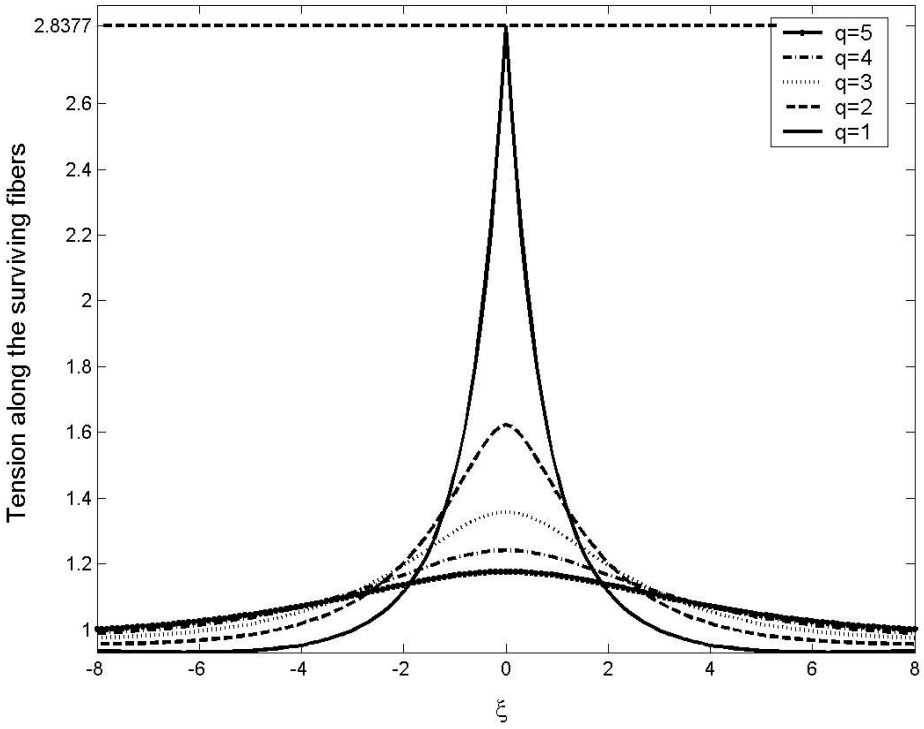

Figure 5. 27. Tension along the first five surviving fibers for a transverse crack, $N = 9$.

For large $r >> s$, asymptotic analysis shows that the over load will decay to $1/2$ by the second fiber, $3/8$ by the third fiber and $5/16$ by the fourth. Thus as the crack length increases, the load decays slower along the crack plane and the overloaded area expands. Compared to the stress field near one fiber break, the surviving fiber takes a much longer distance to unload into compression from the peak stress point..

5.2.2 Transverse wedge with opening angle θ

Next, we study the stress distribution when the wedge opens up by angle θ. The following figures are the results for $\theta = \pi/4$. Figure 5.28 plots the tension along the broken fiber. The fiber closest to the crack tip recovers its applied load fastest among all the broken fibers. Accordingly, the matrix bays at the tip between the last broken fiber and the first intact fiber have highest shear stress concentration. From the tension figure, we see that fiber n has a kink at $\xi = \pm a(n-1)$ for $n = 1,...,4$ due to the end of the adjacent broken fiber with a short gap. Once we pass the kink point, the broken fiber gains more constraint and as a result recovers its load faster.

The shear stress distribution along the matrix bay neighboring the broken fiber is shown in Figure 5.29. Again, the matrix bay between the last broken fiber and the first surviving fiber has the highest shear stress concentration. Compared to the crack with the same number of broken fibers, the maximum stress concentration is reduced due to the smaller deformation of the matrix bay.

From Figure 5.30, we can see that the gap between the ends of the last broken fiber is so small that the first surviving fiber has flat maximum tensile stress concentration at the wedge tip. The maximum tensile stress is lower than the one from the crack with the same number of broken fibers. The fiber load concentration decays to about $1/3$ by the second fiber, $1/5$ to the third fiber and 1/8 to the fourth

fiber. It seems that the decay in distance is very similar to the decay around a crack. The pace that the load decays will be studied thoroughly in the next section together with continuum elastic analysis results.

There is no severe shear stress concentration in the matrix bay between intact neighboring fibers. As a result, we wouldn't worry about yielding or debonding for these matrix bays as the remote load increases. The highest risk is at the matrix bay between the last broken fiber and the first intact fiber.

Figure 5.31 plots the displacement of the broken fiber with the longest gap. As stated in developing the modeling framework, the displacement in the gap between the ends of the broken fiber is artificial. However, we can see how each segment is loaded from the displacement distribution. The flat displacement on each segment suggests that the segment itself is not in tension or compression, which supports our physical instinct that the broken fiber far away from the hole tip is not loaded in the hole except near the edge.

This leads to a much simpler computational scheme as shown in Figure 5.21 where the segment and the fiber break in the cavity are removed for the fiber away from the hole tip. With this simplification, the number of fiber breaks and broken segments needed to model the hole for larger number of broken fibers can be reduced to the magnitude of N instead of N^2. It is already an advantage for the shear-lag model compared to the other computational methods that we only need to discretize the hole area instead of the entire composite plane. This simplification makes the method even more efficient.

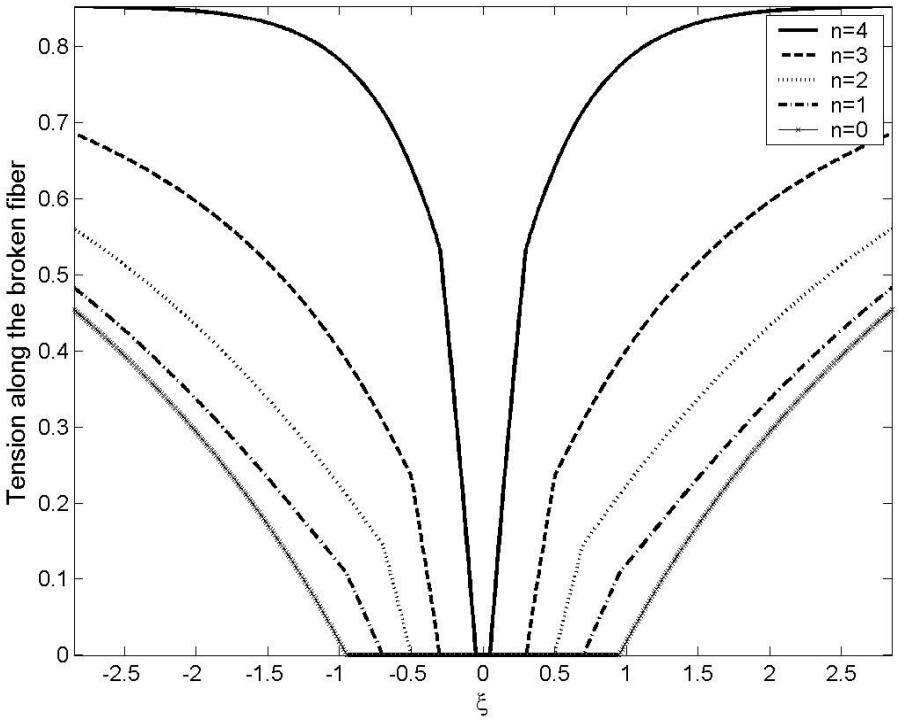

Figure 5. 28. Tension along the broken fiber, $\theta = \pi/4$, $N = 9$.

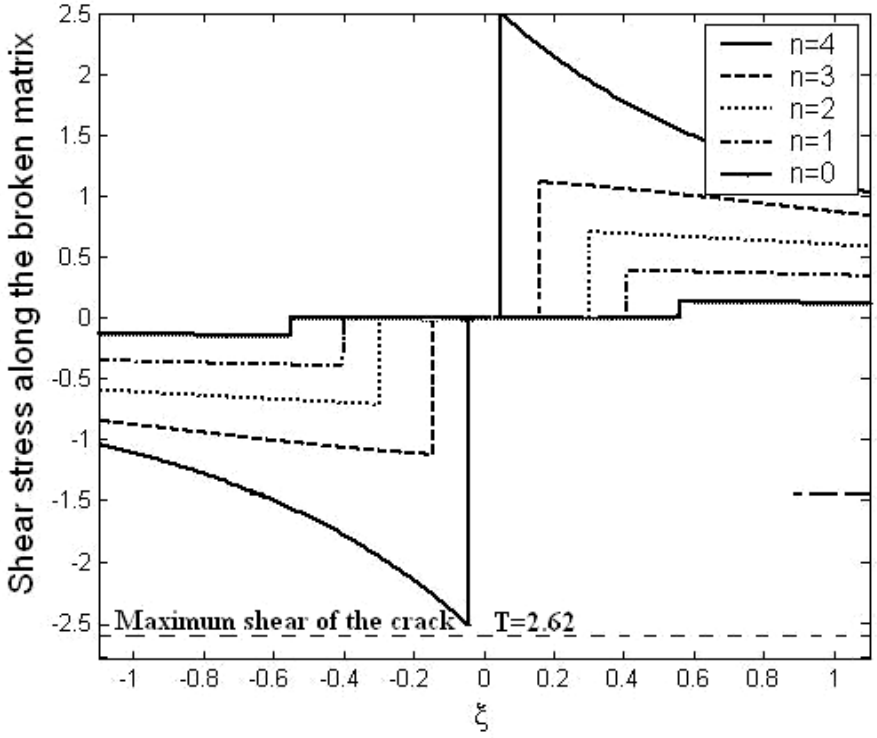

Figure 5. 29. Shear stress distribution along the broken matrix bay, $\theta = \pi/4$, $N = 9$.

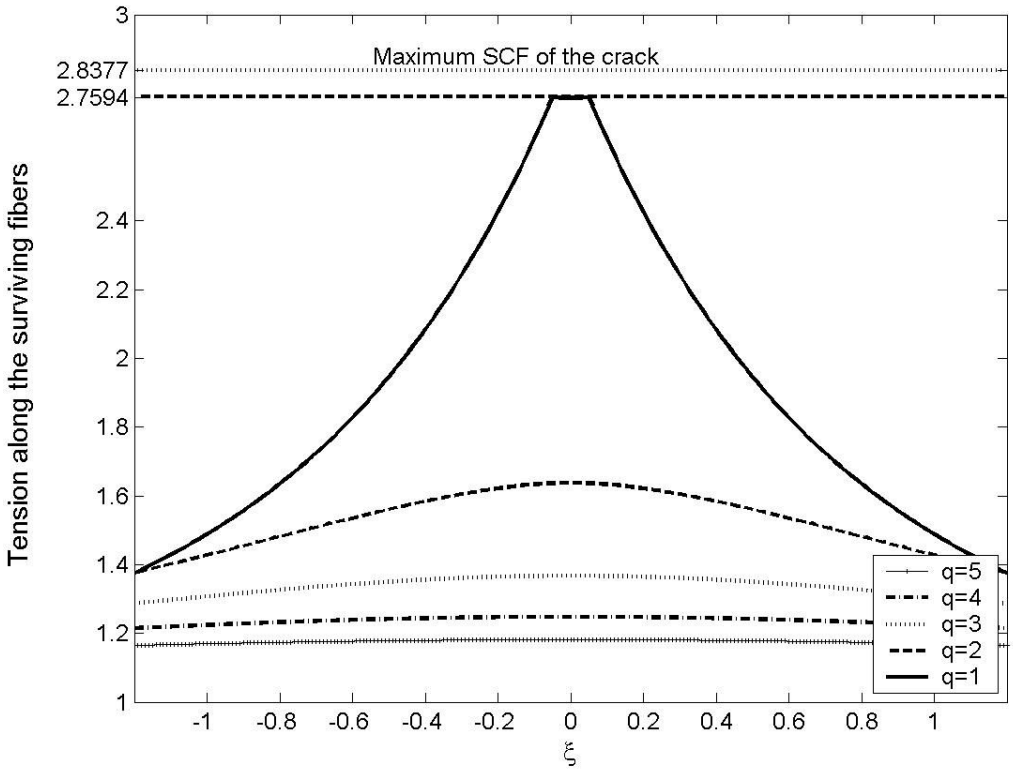

Figure 5. 30. Tension along the flanking fiber, $\theta = \pi/4$, $N = 9$.

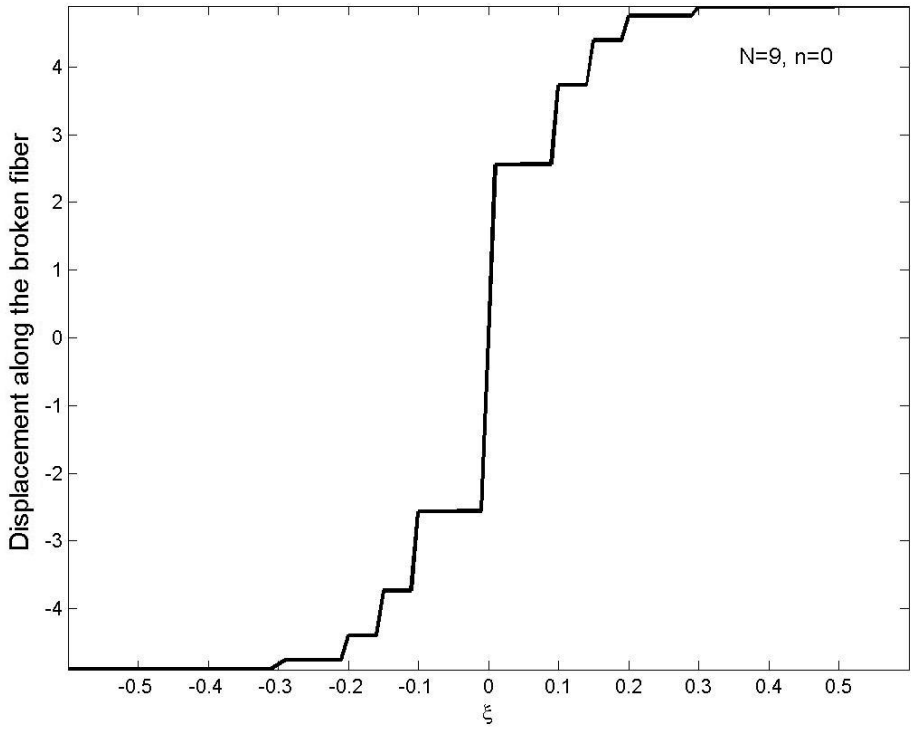

Figure 5. 31. Displacement along the broken fiber, $\theta = \pi/4$, $N = 9$.

5.2.2 Comparison with Elastic Analysis

Williams (1952) studied the stress singularities in plates subjected to extension in the plane. For generalized plane stress in thin plates, he found that for vertex angles $\left(360^\circ - \theta^\circ\right)$ between 180 and 360 degrees, many types of boundary conditions result in a stress singularity. The local tensile stress can be expressed as

$$\sigma = r^{\lambda-1}\left[\lambda(\lambda+1)F(\theta)\right] \tag{5. 15}$$

where

$$F(\theta,\lambda) = b_1\sin(\lambda+1)\theta + b_2\cos(\lambda+1)\theta + b_3\sin(\lambda-1)\theta + b_4\cos(\lambda-1)\theta \tag{5. 16}$$

and where b_1, b_2, b_3 and b_4 are constants decided by the boundary conditions, and r is the radial distance away from the wedge tip. For boundary conditions such that both radial edges are traction free, the following eigenvalue equation:

$$\sin z = C_1 z \tag{5. 17}$$

where

$$z = \lambda(2\pi - \theta) \tag{5. 18}$$

$$C_1 = \pm\left(\sin(2\pi-\theta)\right)/(2\pi-\theta) \tag{5. 19}$$

Inasmuch as the continuity of displacements requires $\lambda > 0$, any value of equation (5.19) satisfying this restriction will give an admissible solution. From equation (5.15), we know a value of λ satisfying $0 < \lambda < 1$ will result in singularities near the wedge tip. Figure 5.32 is the minimum root of equation (5.19), under the restriction that $\lambda > 0$, versus vertex angle $\left(360^\circ - \theta^\circ\right)$, as was given in Williams (1951). From equation (5.15), we know that

$$\ln\sigma_x = (\lambda-1)\ln r + \ln\lambda(\lambda+1)F(\theta) \tag{5. 20}$$

Thus $\ln\sigma$ is a linear function of $\ln r$ with the slope $(\mathrm{Re}\,\lambda - 1)$. For a fixed far field stress, the shape of the singular stress field in elastic continuum theory is not influenced by the size of the wedge, but is decided instead by the vertex angle.

We first test the simplest wedge: a crack in the transverse direction whereby $\theta^{\circ} = 0$. Figure 5.33 shows the effect of crack size, i.e., number of broken fibers *N*, on an effective exponent, $\mathrm{Re}\,\lambda$, which suggests that $(\mathrm{Re}\,\lambda - 1)$ decreases as the number of the broken fibers N increases.

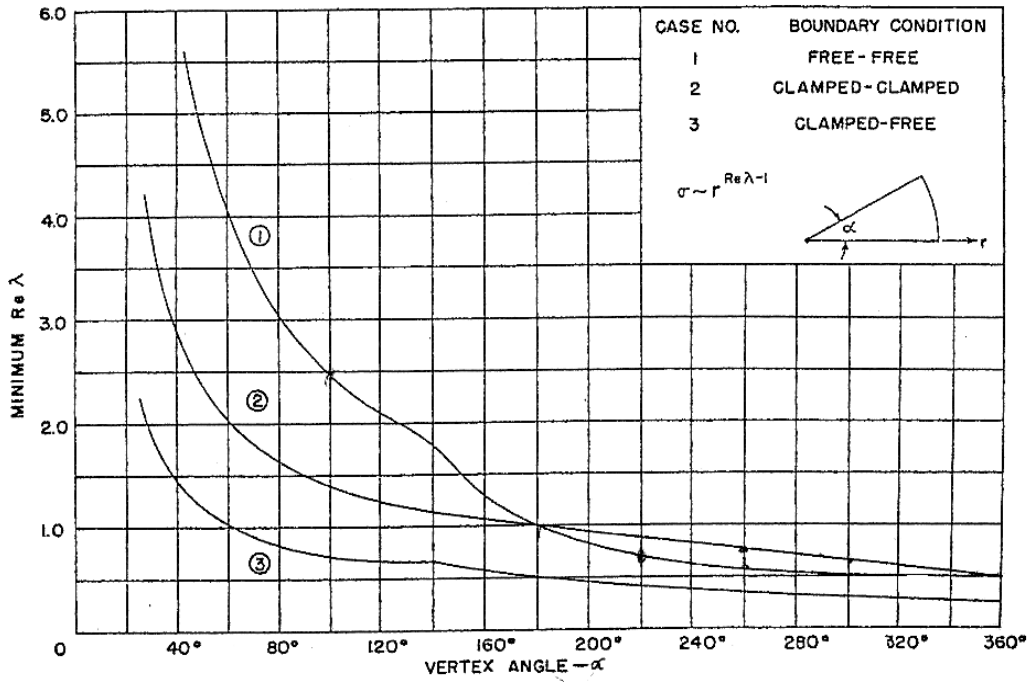

Figure 5. 32. Variation of minimum real part of eigen value with vertex angle.

Note that as the number of broken fibers approaches about 100, the slope converges to -0.5, which is the value for a crack in Williams' figure, Figure 5.32. Figure 5.34 shows the variation of the equivalent of $\mathrm{Re}(\lambda)$ with the vertex angle and for $N = 19$ computed with the shear-lag model. Similar to William's results, the effective exponent $\mathrm{Re}(\lambda)$ decreases as the vertex angle increases and as the

wedge gets closer to the shape of the crack, i.e., the vertex angle approaches 360° or $\theta^\circ = 0$, and the value stays constant at about $\mathrm{Re}(\lambda) = 0.6$. The small difference in the value between William's result and our computed results is mostly likely due to the small size, $N = 19$, of the wedge, which is consistent with the effect in Figure 5.33.

The effective value of $\mathrm{Re}(\lambda)$ near the vertex angle $(360^\circ - \theta) = 360^\circ$ is decided by the value for the corresponding continuum crack. As we discussed before, the slope of the stress distribution actually decreases to -0.5 for larger N in the crack, which means $\mathrm{Re}(\lambda) \to 0.5$, and this is in agreement with Williams' results.

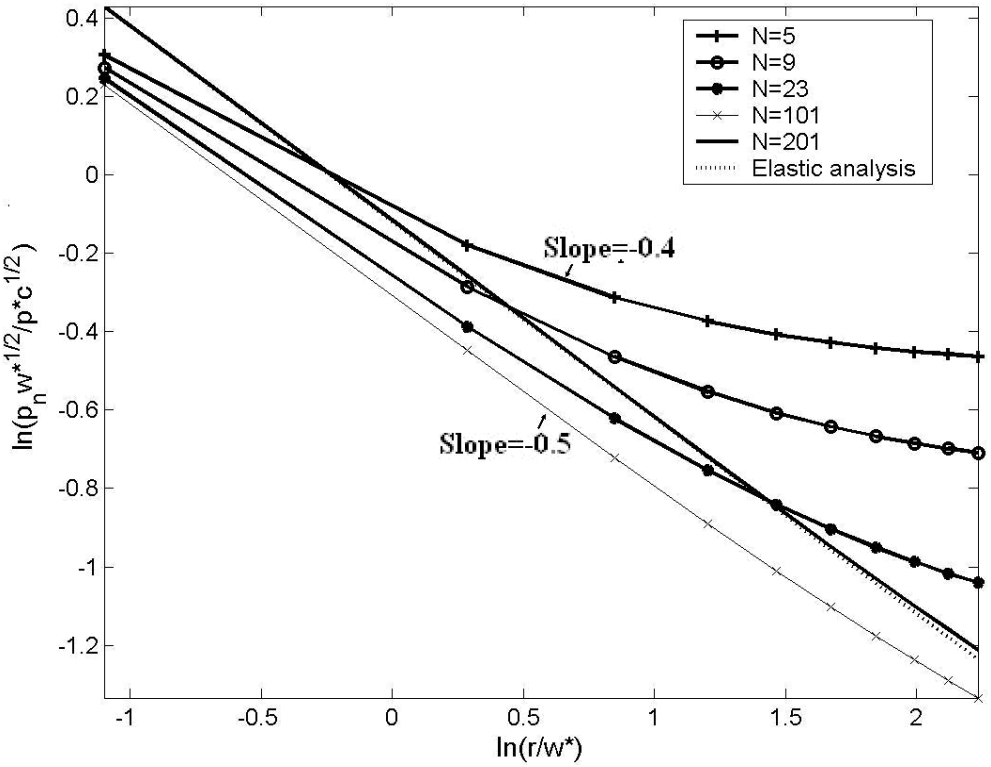

Figure 5. 33. Normal tensile stresses along the crack plane for different number of broken fibers.

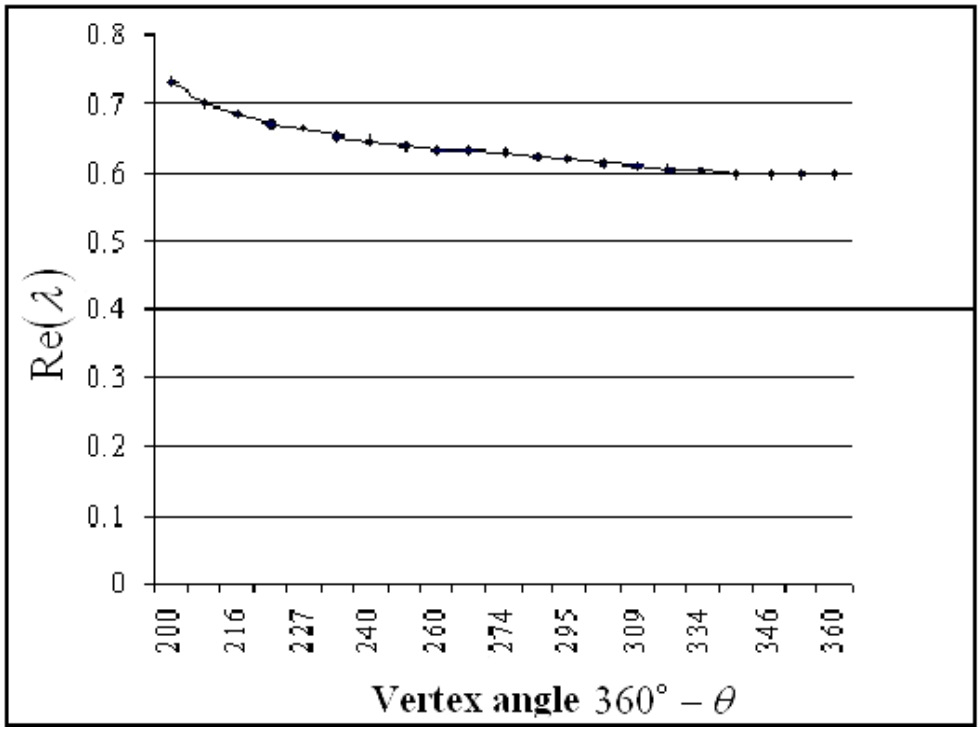

Figure 5. 34. Variation of $\mathrm{Re}(\lambda)$ with vertex angle $360^\circ - \theta$ and for $N = 19$.

Figure 5.35 shows the tensile stress concentration along the crack plane for different opening angles. The crack has steepest slope and as the angle increases, the absolute value of the slope decreases, as Williams (1952). Further away from the wedge tip, the angle effect fades and all the angles have about the same stress concentration.

We have also tested the effect of wedge length on the stress concentration. Figure 5.36 shows that a larger wedge has greater tensile stress concentration along the crack plane and the length of the wedge has mild effect on the slope of the stress right ahead of the tip. Similar to the angle effect, the length effect fades further away from the wedge tip.

Beyerlein, Phoenix and Sastry (1996) tested the appropriate value for ϕ, which is the fraction of the width w^* between the centerline of the first surviving fiber and the wedge tip, for different crack sizes. They found that $\phi = 1/3$ yields the

best agreement of both solutions for crack length $c = c_N$ down to about $N = 21$. For smaller cracks, ϕ needs to be adjusted specifically for each N. Figure 5.37 plots the tensile stress concentration near a wedge along the crack plane for different ϕ. For the angles and sizes used in the figure, $\phi = 1/3$ yields the closest results to the elastic continuum analysis. Note, however, that ϕ could be slightly different for wedge of large size based on the results of Beylerlein, Phoenix and Sastry (1996). Over all, ϕ is a small adjustment in our computational method to achieve the best agreement between shear-lag and elastic analysis, and is determined empirically.

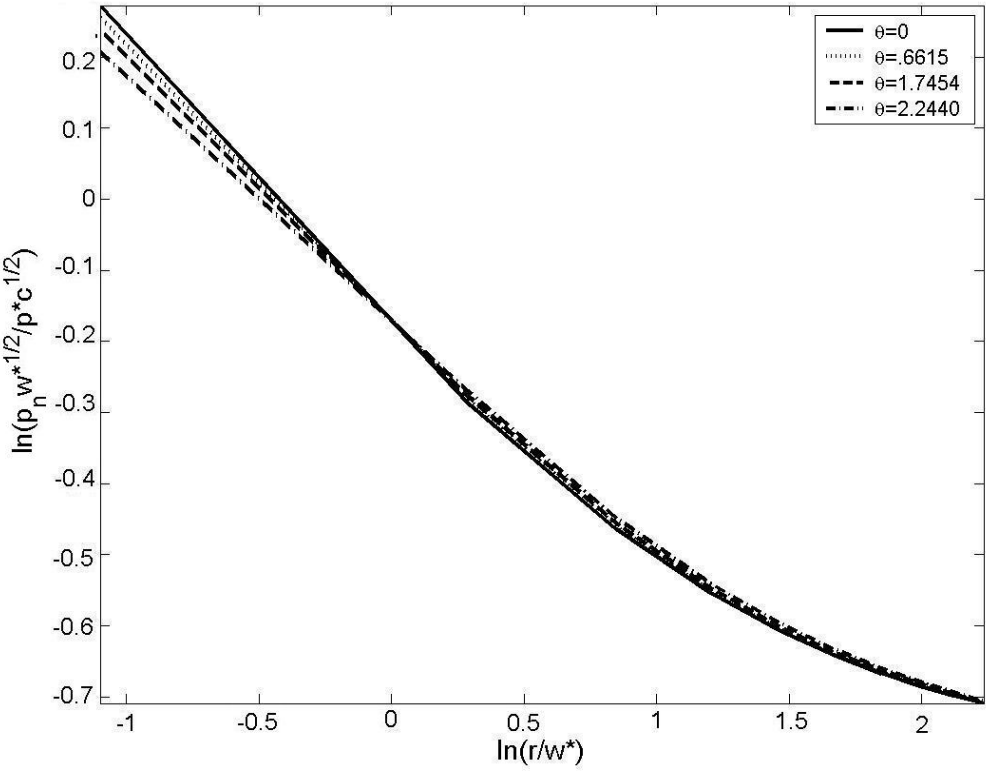

Figure 5. 35. Normal tensile stress along the crack plane when $N = 19$.

Next we study the shear stress distribution ahead of a transverse wedge on the crack plane. In Williams (1952), the shear stress is expressed as

$$\tau_{xy} = r^{\lambda-1}\left[-\lambda F'(\theta)\right] \tag{5. 21}$$

Thus, similar to the tensile stress ahead of the crack, $\ln \tau_{xy}$ is a linear function of $\ln r$ with slope $(\lambda - 1)$. This is also in agreement with the simulation results calculated from our model.

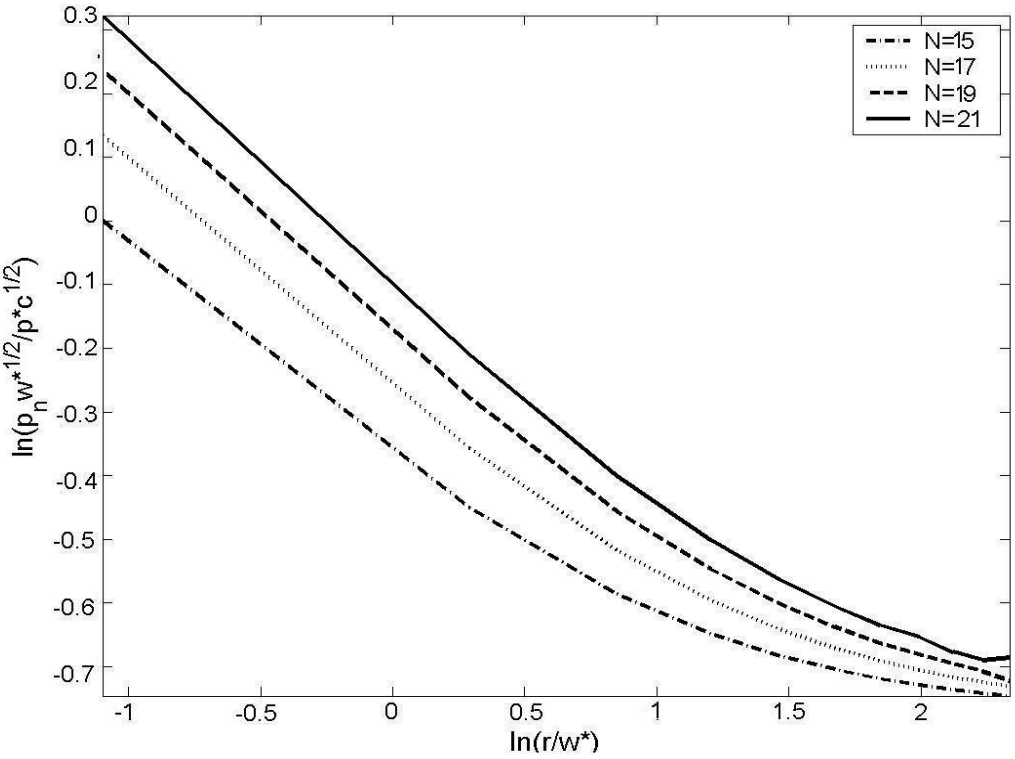

Figure 5. 36. Normal tensile stress along the crack plane when $\theta = 2.24$ degrees.

The shear stress distribution near a transverse wedge along the crack plane for different opening angle θ, is shown in Figure 5.38 when $N = 19$. Smaller opening angles have smaller slope, thus leading to smaller $\mathrm{Re}(\lambda)$ values. Overall, the maximum shear stress along the crack plane drops fairly fast, so the matrix bay between the last broken fiber and first surviving fiber is of most concern for yielding or debonding effects.

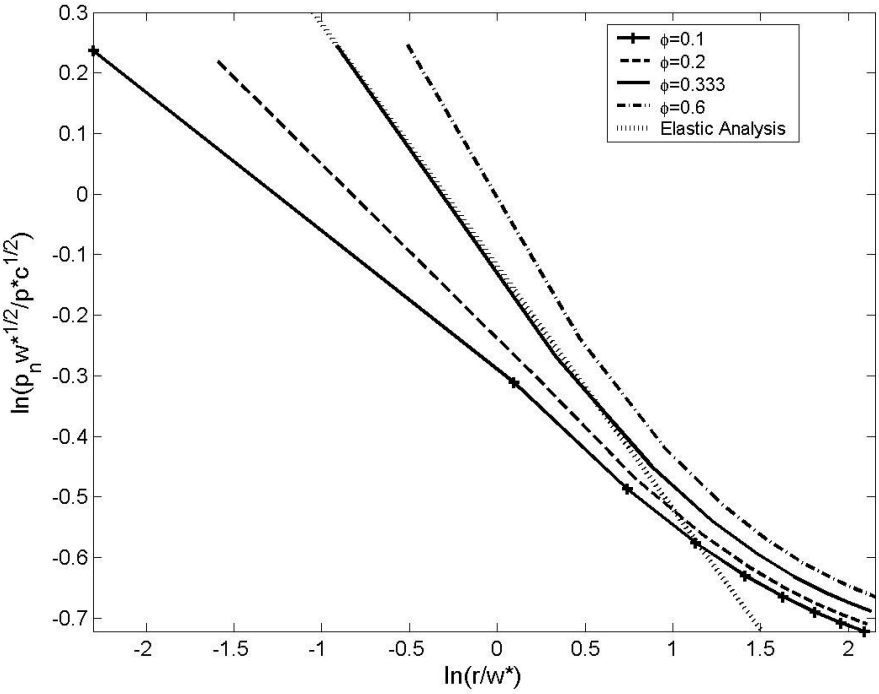

Figure 5. 37. Tensile stresses ahead of the wedge tip for different ϕ, and $N = 19$.

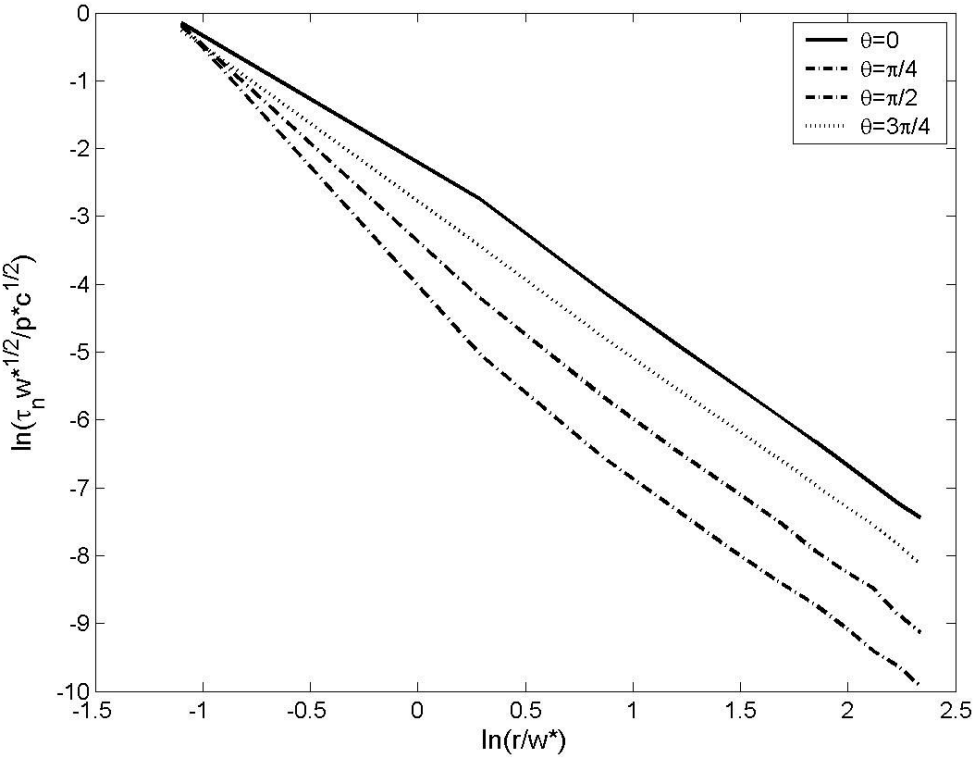

Figure 5. 38. Shear stress along the crack plane for $N = 19$.

Beyerlein, Phoenix and Sastry (1996) used Stirling's approximation $N! \approx \sqrt{2\pi N} N^N e^{-N}$ for large N to get the asymptotic expressions for the stress concentrations on the first surviving fiber, for large N. An improvement over what they found is

$$K_N = \left(1 + \frac{\pi}{4} N\right)^{\frac{1}{2}} \tag{5. 22}$$

and for the shear concentration factor, S_N

$$S_N \approx \left(\sqrt{\pi}/2\right)\sqrt{N} \tag{5. 23}$$

Thus for a crack, the maximum tensile stress and shear stress both increase in N with the power $1/2$. Our numerical calculations shows that the wedge has very similar properties in composite form.

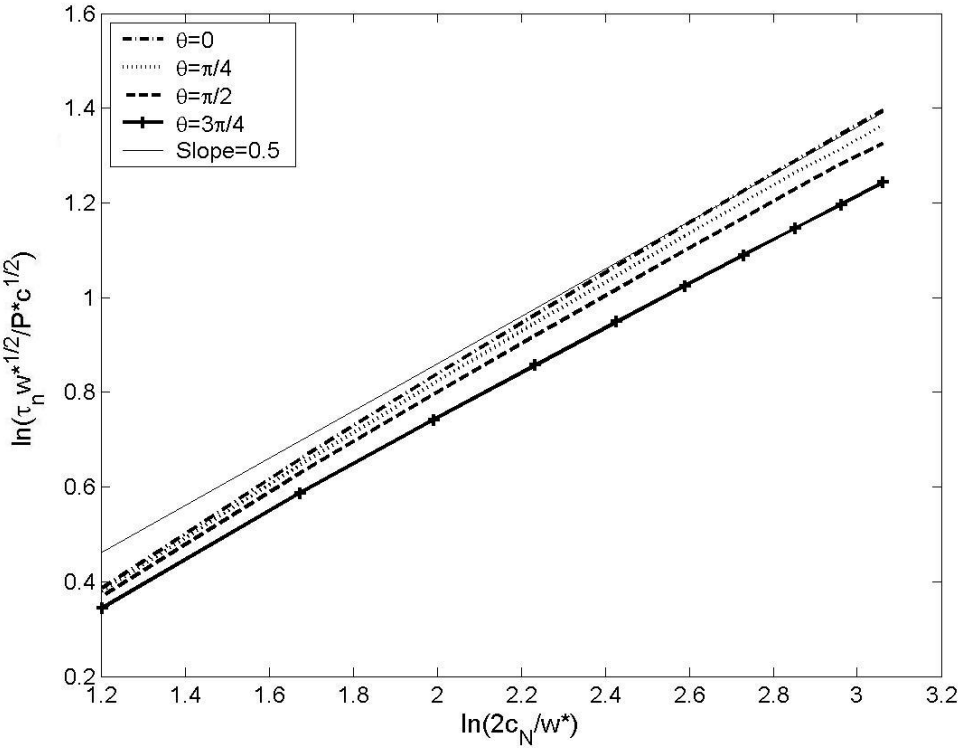

Figure 5. 39. Maximum shear stress for wedges of different transverse dimension.

Figure 5.39 plots the maximum shear stress versus the transverse dimension of the wedge for different opening angles using log-log coordinates. The figure shows that the maximum shear concentration increases linearly with the transverse dimension of the wedge for all angles, and on a log-log scale the slope decreases as the opening angle θ increases. The slope becomes almost constant at $1/2$ for small opening angles, $\theta \le \pi/2$, but starts dipping down sharply after it passes the ninety degree angle, $\theta = \pi/2$. The asymptotic value of the slope for $\theta = \pi$ would be a horizontal line since the composite plane is essentially divided into two separate pieces along the crack with no tractions across the boundary (which is true with or without such a degenerate wedge).

Since the tension and the shear stress increases with the same power, we hypothesize that, for small opening angle θ, the tension increases with the size of the wedge in the following form:

$$K_N = \left(1 + \frac{\pi}{\gamma} N\right)^{\frac{1}{2}} \tag{5. 24}$$

where γ is 4 for a crack.

Figure 5.40 plots the variation of γ against the vertex angle $\left(360^\circ - \theta\right)$ for different wedge sizes. As the opening angle decreases to $\theta = 0$, i.e. the wedge becomes a crack, γ converges to 4 slowly, which is exactly the value for a crack. In fact, the value of γ for different N roughly stays about 4 for opening angles $\theta \le \pi/4$.

Based on the value of γ calculated for different opening angles, as shown in figure 5.41, we plotted the maximum tensile stress concentration factor on the first flanking fiber against the size of a wedge, for different opening angles and using a log-log scale. Figure 5.41 shows that our model is a good approximation to predict the stress intensity factor for opening angles $\theta \le \pi/2$.

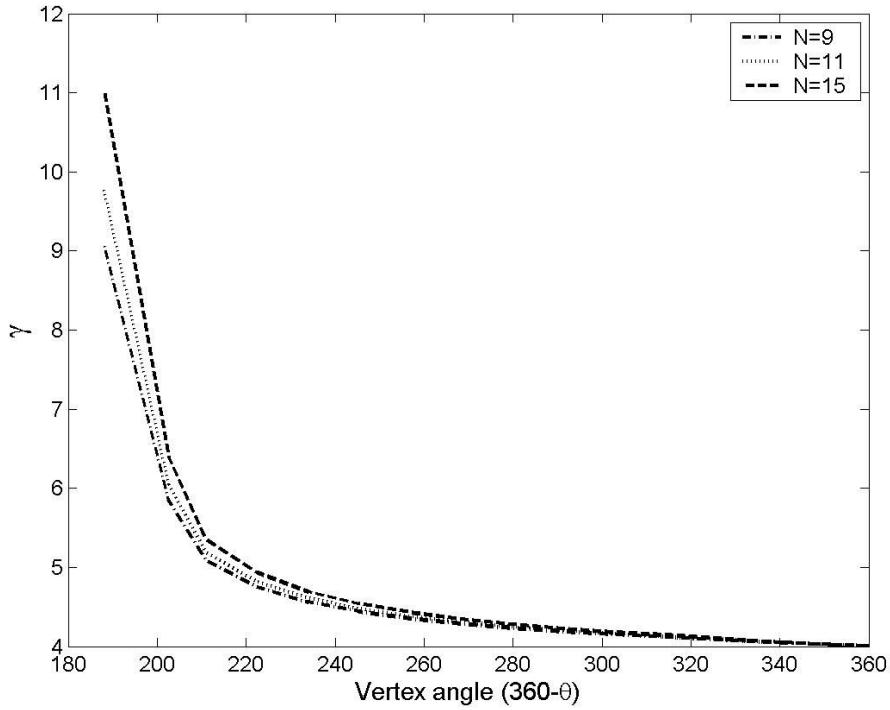

Figure 5. 40. Factor γ versus vertex angle $(360-\theta)$ for different transverse dimensions, where θ is the opening angle at the tip.

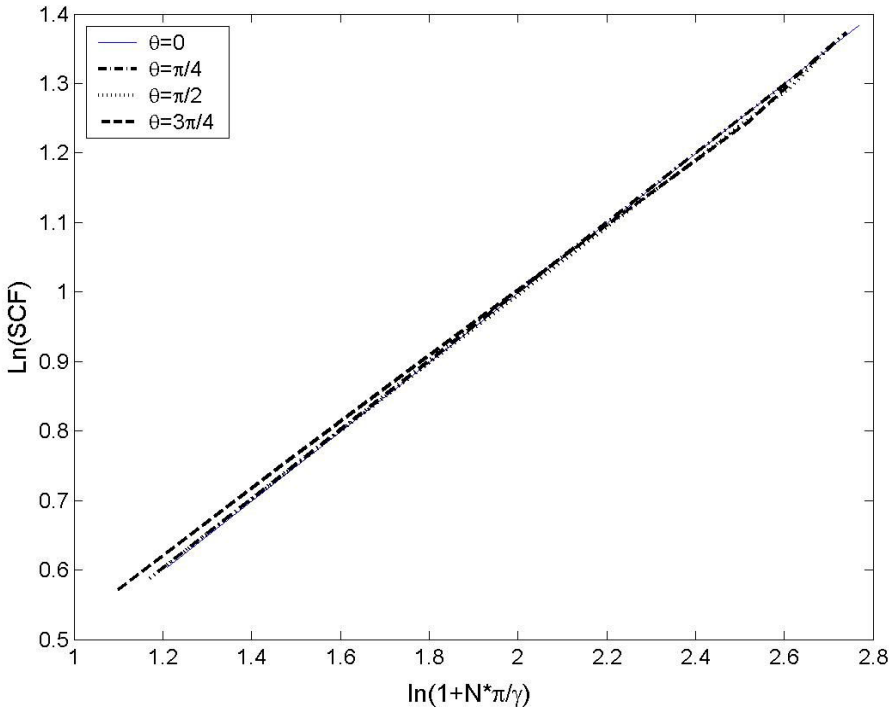

Figure 5. 41. Maximum tensile stress concentration factor versus $(1+N\pi/\gamma)$.

Note that as the transverse size, N, becomes larger, the linear relationship actually improves. For opening angles bigger than $\pi/2$, we can see the line's slope is slightly lower than 0.5, which is expected because we have used small angle approximations for the calculation.

5.2.3 Conclusion

In this section, we have studied the stress field of a two dimensional infinite lamina with a central wedge containing N broken fibers subjected to a remote uniform tensile load. We have made connection between the elastic solution and the shear-lag model and have obtained an empirical formula similar to the crack to compute the maximum tensile stress concentration for different wedge sizes N. Both the tensile stress and shear stress along the crack plane drop down approximately inversely with the distance to the wedge tip, with the power of $\mathrm{Re}(\lambda)-1$. The maximum tensile stress and shear stress concentration factor for a wedge increases with the number of broken fibers N with power $1/2$ for small opening angles θ. The two solutions achieve good agreement on the prediction of the stress field over all. Due to the limitation of computational power, we haven't tested the results for large wedges, for example, a wedge with 100 broken fibers. However, we expect a better agreement with the proper adjustment of ϕ because the validity of the homogeneity assumption will make the elastic analysis more accurate.

5.3: Elliptical hole analysis

The stress concentration and the fracture phenomena near an elliptical hole for composite material have been studied both theoretically and experimentally. (Smith, 1944; Green ,1945; Savin, 1961; Waddoups et al 1971; Whitney &Nuismer, 1974; Bishop, 1972; Potter, 1977). In this section we investigate the stress field using the discrete shear-lag model and compare the results with the previous results

in the literature, especially those from analysis of homogeneous orthotropic materials.

Among all the workers noted above, Bishop (1972) derived the expressions for stress components near an elliptical hole where the material has been removed using elastic analysis assuming the material is homogeneous, orthotropic continuum. Two limiting cases of an elliptical hole were considered, a circular hole and a sharp crack transverse to the applied tension, but with expanded scaling to treat it locally as a parabola. It was shown that an estimation of the stress maxima for elliptical holes between these two extremes can be made using the values of the two limiting cases.

Potter (1977) developed a tensile fracture criterion in which the notch sensitivity is related to the properties of the fiber, matrix and fiber-matrix interface, based on the stress gradient ahead of the notch tip. He also applied Potter's results (1972) to his fracture criteria and compared the predictions of the effect of notch size on the fracture behavior of the composite material with experimental results. A typical failure locus was given and the concept of "small" holes and "big" holes was introduced insofar as they affect how fracture propagation occurs.

Our goal here is to model the stress field near an elliptical hole where the material is removed using shear-lag analysis and study the fracture behavior of the fibrous composite material for different hole sizes and hole shapes. We compare results from the elastic solution and the shear-lag solution and draw connection of stress fields predicted by the different approaches. Furthermore, we introduce broken fibers at the tip of the hole and study the change of the stress concentration that the new fiber breaks cause.

First we consider an infinite, planar, composite lamina whose fibers and matrix bays are linearly elastic. For simplicity, we also assume all the fibers in the

composite plane have uniform strength; hereby the overloaded fiber breaks at the maximum stress concentration point.

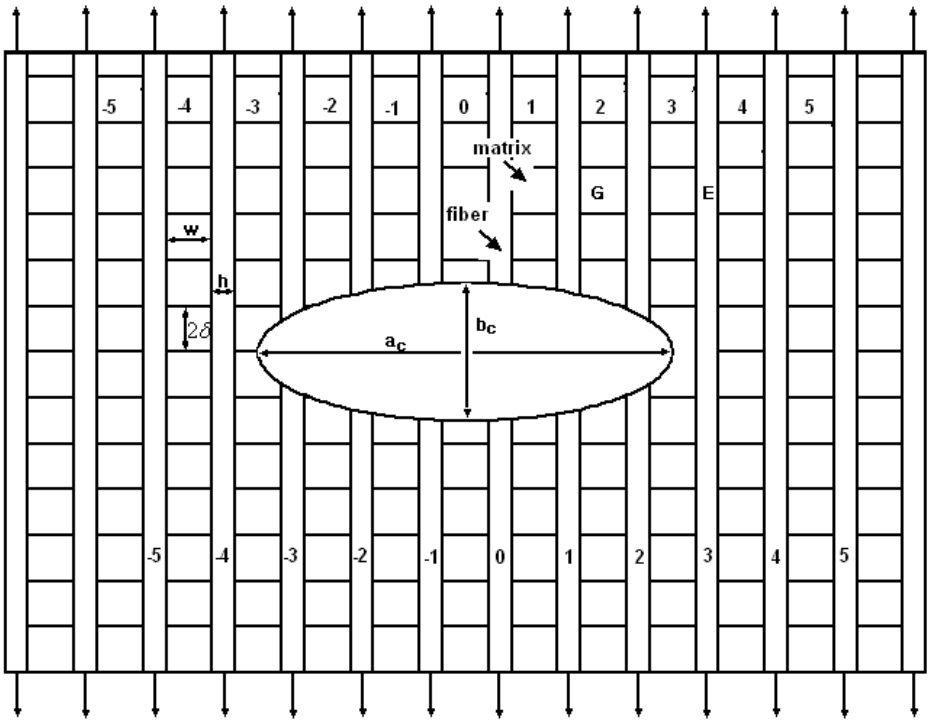

Figure 5. 42. Transverse elliptical hole in a two-dimensional discretized composite lamina.

5.3.1 Elastic analysis

We consider the elastic solution for an infinite, two-dimensional orthotropic composite material with an elliptical hole inside transverse to the fiber direction. Figure 5.42 shows the elliptical hole in an infinite orthotropic sheet with the directions of symmetry of the material coincident with the x and y directions. A uniform tension σ_∞ is applied at infinity in the y direction. The ellipse has semi-axes a_c and b_c coincident with the y and x axes so that the boundary of the hole is described by

$$\frac{x}{b_c^{\,2}} + \frac{y}{a_c^{\,2}} = 1 \tag{5. 25}$$

The eccentricity of the ellipse is defined as $\varepsilon = b_c / a_c$. The elastic solution (Bishop, 1972) involves four elastic material constants G_{xy} , ν_{xy} , E_{yy} and E_{xx} . Assuming the lamina is in a state of plane stress, we substitute the stress components expressed by the Airy stress function χ in the compatibility equation and get the following fourth-order homogeneous partial differential equation,

$$\frac{1}{E_y}\frac{\partial^4 \chi}{\partial x^4} + \left(\frac{1}{G_{xy}} - 2\frac{\nu_{xy}}{E_x}\right)\frac{\partial^4 \chi}{\partial x^2 \partial y^2} + \frac{1}{E_x}\frac{\partial^4 \chi}{\partial y^4} = 0 \tag{5. 26}$$

This can be rewritten as

$$\left(\beta_1^{\,2}\frac{\partial^2}{\partial x^2} + \frac{\partial^2}{\partial y^2}\right)\left(\beta_2^{\,2}\frac{\partial^2}{\partial x^2} + \frac{\partial^2}{\partial y^2}\right)\chi = 0 \tag{5. 27}$$

where

$$\beta_1^{\,2} = \alpha E_y \left[1 + \sqrt{1 - \frac{1}{\alpha^2 E_x E_y}}\right] \tag{5. 28}$$

$$\beta_2^{\,2} = \alpha E_y \left[1 - \sqrt{1 - \frac{1}{\alpha^2 E_x E_y}}\right] \tag{5. 29}$$

and

$$\alpha = \frac{1}{2G_{xy}} - \frac{\nu_{xy}}{E_x} \tag{5. 30}$$

Only two material constants, β_1 and β_2, which are functions of the elastic moduli and Poisson's ratio, are needed to define the stress field for the orthotropic lamina of material. For an isotropic material, $\beta_1 = \beta_2 = 1$ and the governing equation reduces to

$$\frac{\partial^4 \chi}{\partial x^4} + \frac{\partial^4 \chi}{\partial x^2 \partial y^2} + \frac{\partial^4 \chi}{\partial y^4} = 0 \tag{5. 31}$$

The Airy stress function can be determined by the boundary condition that the edge of the elliptical hole has zero normal and shear stresses. The stress components are found to be as follows:

$$\frac{\sigma_x}{\sigma_\infty} = 1 + \mathrm{Re}\left\{\frac{1}{(\beta_1 - \beta_2)}\left[\frac{\beta_2}{1-\varepsilon\beta_1}\left(1 - \frac{Z_1}{\varphi_1}\right) - \frac{\beta_1}{1-\varepsilon\beta_2}\left(1 - \frac{Z_2}{\varphi_2}\right)\right]\right\} \qquad (5.\ 32)$$

$$\frac{\sigma_y}{\sigma_\infty} = -\mathrm{Re}\left\{\frac{\beta_1\beta_2}{(\beta_1 - \beta_2)}\left[\frac{\beta_2}{1-\varepsilon\beta_1}\left(1 - \frac{Z_1}{\varphi_1}\right) - \frac{\beta_1}{1-\varepsilon\beta_2}\left(1 - \frac{Z_2}{\varphi_2}\right)\right]\right\} \qquad (5.\ 33)$$

and

$$\frac{\tau_{xy}}{\sigma_\infty} = \mathrm{Im}\left\{\frac{\beta_1\beta_2}{(\beta_1 - \beta_2)}\left[\frac{1}{1-\varepsilon\beta_1}\left(1 - \frac{Z_1}{\varphi_1}\right) - \frac{1}{1-\varepsilon\beta_2}\left(1 - \frac{Z_2}{\varphi_2}\right)\right]\right\} \qquad (5.\ 34)$$

In these equations, $Z_1 = \frac{x}{a_c} + i\beta_1\frac{y}{a_c}$, $Z_2 = \frac{x}{a_c} + i\beta_2\frac{y}{a_c}$, $\varphi_1 = \sqrt{Z_1^2 - 1 + \varepsilon^2\beta_1^2}$ and $\varphi_2 = \sqrt{Z_2^2 - 1 + \varepsilon^2\beta_2^2}$.

The main stress maxima occur on the edge of the elliptical hole near the transverse sides. The maximum tensile stress concentration occurs at the tip of the elliptical hole where $y = 0$ and $x = a$. Its magnitude is given by

$$\left(\varepsilon\frac{\sigma_y}{\sigma_\infty}\right)_{\max} = \frac{\beta_1 + \beta_2}{\beta_1\beta_2} + \varepsilon \qquad (5.\ 35)$$

So the maximum tensile stress concentration for a crack will be

$$\left(\varepsilon\frac{\sigma_y}{\sigma_\infty}\right)_{\max} = \frac{\beta_1 + \beta_2}{\beta_1\beta_2} \qquad (5.\ 36)$$

and for a circular hole will be

$$\left(\varepsilon\frac{\sigma_y}{\sigma_\infty}\right)_{\max} = \frac{\beta_1 + \beta_2}{\beta_1\beta_2} + 1 \qquad (5.\ 37)$$

Since $\left(\varepsilon\sigma_y/\sigma_\infty\right)_{\max}$ is a linear function of ε, once we know the maximum stress concentration for a crack and a circular hole, the maximum stress concentration factor can be interpolated for other shapes based on the value of the eccentricity. To make connection with the discrete shear-lag model, instead of calculating the stress concentration of the edge of the whole, we shall investigate the tensile stress concentration on the surviving fibers flanking the elliptical hole. The hole length $2a_c$ in the y direction can be defined as in equation (5.38) in terms of the number of broken fibers, effective spacing of width $w^* = (h+w)$ and two end portions, each the fraction $(1-\phi)$ of $w^* = (h+w)$ whereby

$$2a_c = [(N-1)+2(1-\phi)](h+w) \tag{5.38}$$

The distance away from the crack tip is defined as

$$r_q = [\phi+(q-1)](h+w) \tag{5.39}$$

where q is the index of the surviving fibers. As in the wedge case, ϕ here is a small adjustment, being the fraction of the width w^* between the center line of the first surviving fiber to the edge or tip of the hole. As before, ϕ is also determined empirically by matching both solutions.

The stress distribution along the q_{th} surviving fiber can be determined by equation (5.32), where

$$Z_1 = \frac{r_q}{a_c} + i\beta_1\frac{y}{a_c} \quad \text{and} \quad Z_2 = \frac{r_q}{a_c} + i\beta_2\frac{y}{a_c} \tag{5.40}$$

and the tensile stress on the crack plane can be calculated using

$$Z_1 = Z_2 = \frac{r_q}{a_c} \tag{5.41}$$

The final result is

$$\left(K_{N,s}\right)_{cont} = 1 + \mathrm{Re}\left\{ \frac{1}{\left(\beta_1 - \beta_2\right)} \left[\begin{array}{l} \dfrac{\beta_2}{1-\varepsilon\beta_1}\left(1 - \dfrac{r_q}{\sqrt{r_s{}^2 - a_c{}^2 + a_c{}^2\varepsilon^2\beta_1{}^2}}\right) \\ -\dfrac{\beta_1}{1-\varepsilon\beta_2}\left(1 - \dfrac{r_q}{\sqrt{r_q{}^2 - a_c{}^2 + a_c{}^2\varepsilon^2\beta_2{}^2}}\right) \end{array} \right] \right\} \quad (5.42)$$

Thus, instead of using equation (5.35) for the maximum tensile stress concentration to compare with the shear-lag results, we shall use the maximum stress concentration on the first surviving fiber where $q = 1$. When the number of broken fibers is large enough that the radius of the tip of the hole is much bigger than the fiber diameter, the composite sheet may be viewed more as homogeneous continuum, and the maximum stress concentration at the edge of the hole is anticipated to be equivalent to the maximum stress concentration on the first surviving fiber.

Another important indicator of the fracture behavior for composite lamina is the tensile stress gradient along the crack plane. Potter (1977) pointed out that the direct application of conventional fracture mechanics takes no account of the influence of the mircro-structure on the fracture process. Experiments show that failure of the composite is initiated by the stress concentration at the edge of the hole and the load-carrying axial fibers fail sequentially by a process in which the failure of one fiber inevitably leads to the failure of one or more of its neighbors. In Potter's model, failure of the second flanking fiber following the first flanking fiber failure will occur if

$$\sigma_{q=2} + \rho \geq \sigma'_f \quad (5.43)$$

where $\sigma_{q=2}$ is the stress in fiber $q = 2$ before failure of fiber $q = 1$, ρ is the increase in stress on fiber $q = 2$ due to the failure of fiber $q = 1$ and σ'_f is the fiber

strength which is therefore equal to the stress $\sigma_{q=1}$ on fiber $q=1$ at the instant of failure. Assuming the composite plane is homogeneous, we have

$$\sigma_{q=1} - \sigma_{q=2} = \frac{\partial \sigma_f}{\partial y} w^* = \frac{\partial \sigma_x}{\partial y} \frac{w^*}{D} \tag{5. 44}$$

where σ_x is the laminate mid-plane stress resultant and D relates the axial fiber stress σ_f to the laminate tensile stress resultant, that is

$$\sigma_f D = \sigma_x \tag{5. 45}$$

The condition for sequential fiber failures to occur is therefore

$$\left| \frac{\partial \sigma_x}{\partial y} \right| \leq \frac{\rho D}{w^*} \tag{5. 46}$$

The parameter $\rho D / w^*$ is determined by the properties of the fiber, matrix and interface and governs the fracture sensitivity of the composite to the existence of the hole. It is possible to derive $\rho D / w^*$ from the properties of the fiber, matrix and interface, the fiber lay-up and volume fraction. It can also be measured experimentally as in Potter (1972). Equation (5.46) basically states that the sequential failure will occur only when the stress gradient is low enough.

From equation (5.32), we know the stress gradient near an elliptical hole in an infinite orthotropic sheet is

$$\left(\frac{\partial \sigma_x}{\partial y} \right)_{x=0} = \sigma_\infty \operatorname{Re} \left\{ \frac{1}{(\beta_1 - \beta_2)} \right.$$
$$\left. \left[\frac{\beta_2}{1 - \varepsilon \beta_1} \left(\frac{-1}{\left(y^2 - a_c^{\,2} + b_c^{\,2} \beta_1^{\,2} \right)^{1/2}} + \frac{y^2}{\left(y^2 - a_c^{\,2} + b_c^{\,2} \beta_1^{\,2} \right)^{3/2}} \right) \right. \right.$$
$$\left. \left. - \frac{\beta_1}{1 - \varepsilon \beta_2} \left(\frac{-1}{\left(y^2 - a_c^{\,2} + b_c^{\,2} \beta_2^{\,2} \right)^{1/2}} + \frac{y^2}{\left(y^2 - a_c^{\,2} + b_c^{\,2} \beta_2^{\,2} \right)^{3/2}} \right) \right] \right\} \tag{5. 47}$$

which at $y = a_c$ reduces to

$$\left(\frac{\partial \sigma_x}{\partial y}\right) = \sigma_\infty \,\mathrm{Re}\left\{\frac{\left[\dfrac{{\beta_2}^4 - {\beta_1}^4}{\beta_1\beta_2} + \left({\beta_2}^4 - {\beta_1}^4\right)\varepsilon\right]}{\left(\beta_1 - \beta_2\right)\varepsilon^3 a_c {\beta_2}^2 {\beta_1}^2}\right\} \tag{5. 48}$$

From this equation, we can see that the stress gradient is determined not only by the elastic constants and the eccentricity of the hole, but also by the transverse dimension of the hole. As the transverse dimension increases, the stress gradient decreases and eventually a huge region of entire plane is almost equally overloaded, asymptotically.

When the stress at the tensile stress maximum reaches the composite tensile strength σ'_f we have

$$\left(\varepsilon \frac{\sigma'_f}{\sigma_\infty}\right)_{\max} = \frac{\beta_1 + \beta_2}{\beta_1\beta_2} + \varepsilon \tag{5. 49}$$

Substituting equation (5.49) into equation (5.48) gives

$$\frac{\partial \sigma_x}{\partial y} = -\sigma'_x \frac{E_x}{E_y}\left[\frac{K_2 + \varepsilon}{\varepsilon^{*2}\, a_c\left(\varepsilon + K_1\right)}\right]\left(2\alpha E_y + \sqrt{\frac{E_y}{E_x}}\right) \tag{5. 50}$$

where

$$K_1 = \left\{2\left(\alpha E_x + \sqrt{E_x/E_y}\right)\right\}^{1/2} \tag{5. 51}$$

$$K_2 = \frac{2\alpha E_y \left\{2\left(\alpha E_x + \sqrt{E_x/E_y}\right)\right\}^{1/2}}{2\alpha E_y + \sqrt{E_y/E_x}} \tag{5. 52}$$

and we will set

$$K_3 = \left(E_y/E_x\right)\left(\alpha E_x + \sqrt{E_x/E_y}\right) = 2\alpha E_x + \sqrt{E_x/E_y} \tag{5. 53}$$

The sequential fiber failure criterion for an elliptical hole in an infinite orthotropic sheet is then calculated from equation (5.46) , (5.50) and (5.53) as

$$\frac{\varepsilon^2 a_c\left(\varepsilon + K_1\right)}{\left(\varepsilon + K_2\right)} \geq \frac{K_3 w^* \sigma'_x}{\rho D} \tag{5. 54}$$

Figure 5.43 is a typical failure locus for elliptical holes obtained by Potter (1972). Each point defines a particular elliptical hole by the parameters ε and a_c. For any composite plane containing holes defined by points on or above the locus, the sequential failure will occur such that the fracture stress can be predicted by the elastic analysis solution. For a laminate whose holes are defined by points below the locus, the first axial fiber failure does not precipitate the sequential failure and only forms a damage zone which blunts the hole.

Again, due to our discrete model, the comparison of the stress gradient at the first flanking fiber between the elastic analysis and the shear-lag solution is in fact at $y = a_c + \varphi w^*$. When the size of the elliptical hole is much larger than the fiber diameter, the difference due to ϕw^* will be negligible.

In the following subsection, we will focus on the stress field for a lamina containing an elliptical hole, especially the stress gradient at the edge or tip of the hole, and will determine how the hole affects the local stress distribution at the tip.

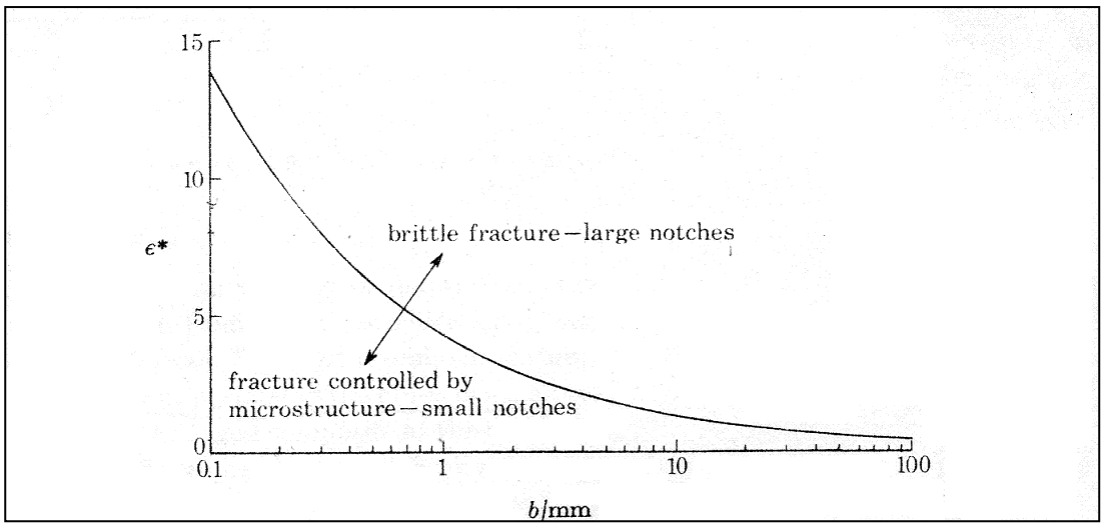

Figure 5. 43. A typical failure locus for elliptical holes (after Potter, 1972).

5.3.2 Stress distribution near an elliptical hole

The typical tensile stress distribution along the broken fiber in the hole is shown in Figure 5.44. As in the wedge case treated earlier, the tension on each broken fiber has a kink due to the end of its neighboring broken fiber. The shear stress distribution along the broken matrix bays is shown in Figure 5.45. Compared to a crack, the elliptical hole induces less maximum shear and tensile stress concentration. The figure also shows that the maximum tensile concentration drops down to about 2/5 by the second fiber, 1/4 by the second fiber and 9/48 by the third fiber, showing a slower load decay rate than for a crack. Removing or deactivating material in the crack in the fiber direction basically increases the overloaded area and puts more of the fibers in distress.

In Figure 5.46, the shear stress concentration drops down dramatically moving away from the hole edge. Therefore, matrix yielding and debonding are more likely to happen in the bay between intact and failed fibers. Figure 5.47 shows how the tensile stress profiles change in the surviving fibers, moving away from the hole.

Figure 5.48 presents a comparison of the tensile stress concentrations in fibers near the edge of a crack, a wedge and an elliptical hole with the same transverse length and where the wedge and the elliptical hole have the same eccentricity. Evidentially, the crack and the wedge have an almost identical stress distribution due to the small opening angle of the wedge except the crack has a slightly higher stress concentration at the tip. The elliptical hole reduces the stress concentration significantly for the first intact fiber and increases the stress in rest of the surviving fibers accordingly. The stress concentration factor decays more slower for elliptical holes than for the other two shapes, but the effect of the hole shape fades away after about two characteristic load transfer lengths.

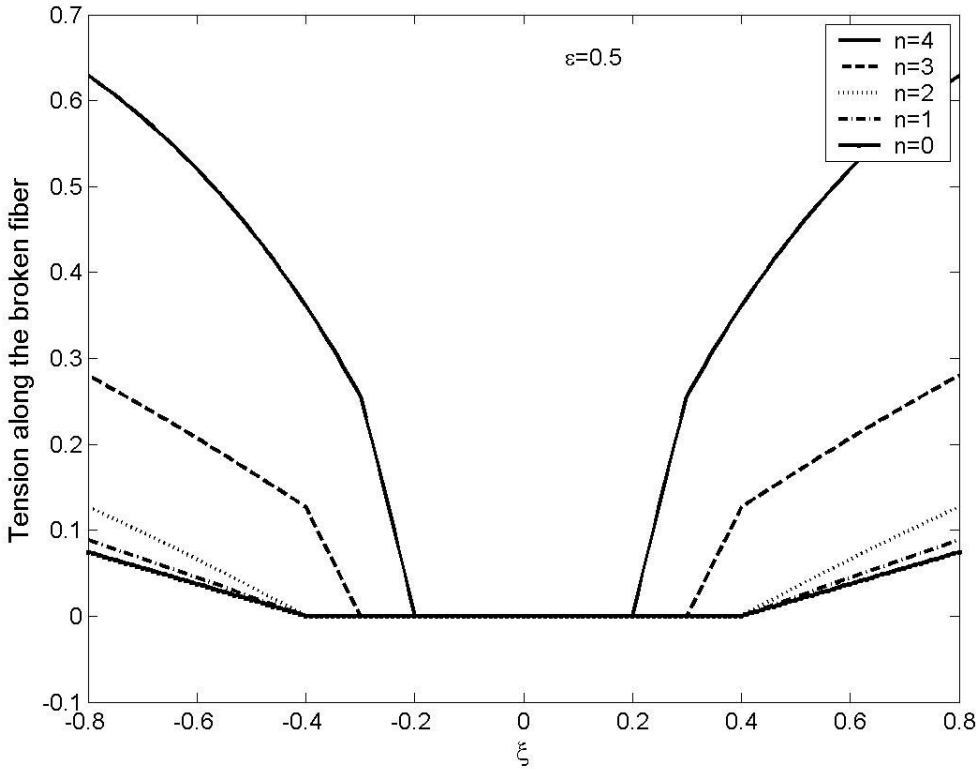

Figure 5. 44. Tension along the broken fiber near an elliptical hole, $N = 9$.

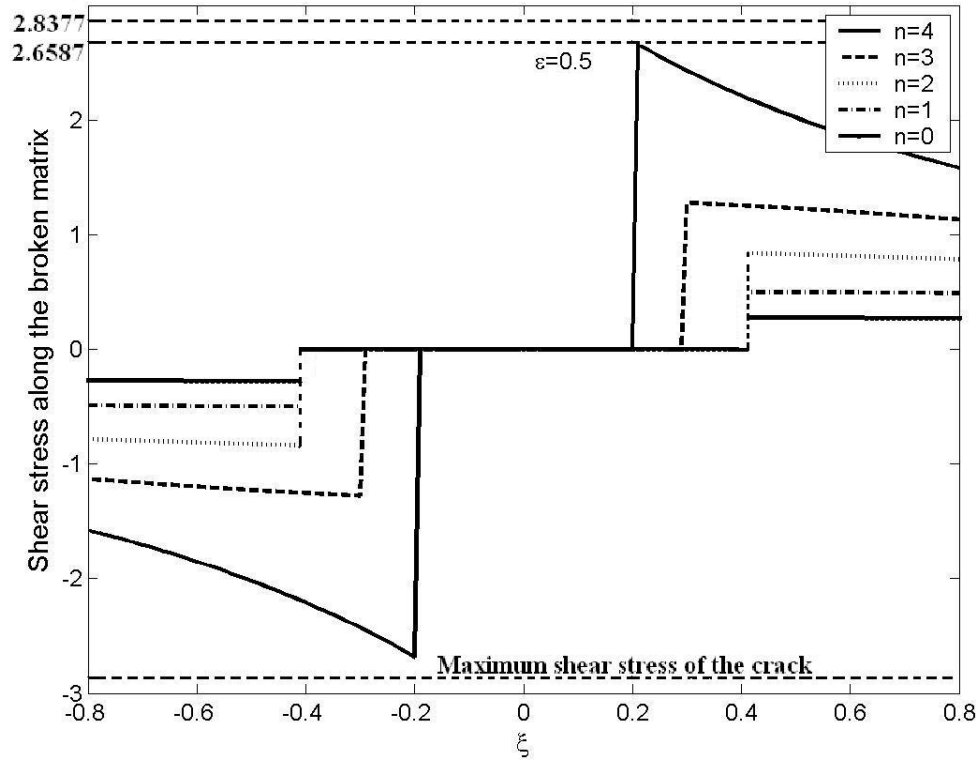

Figure 5. 45. Shear stress in the matrix bay next to the broken fiber for $N = 9$.

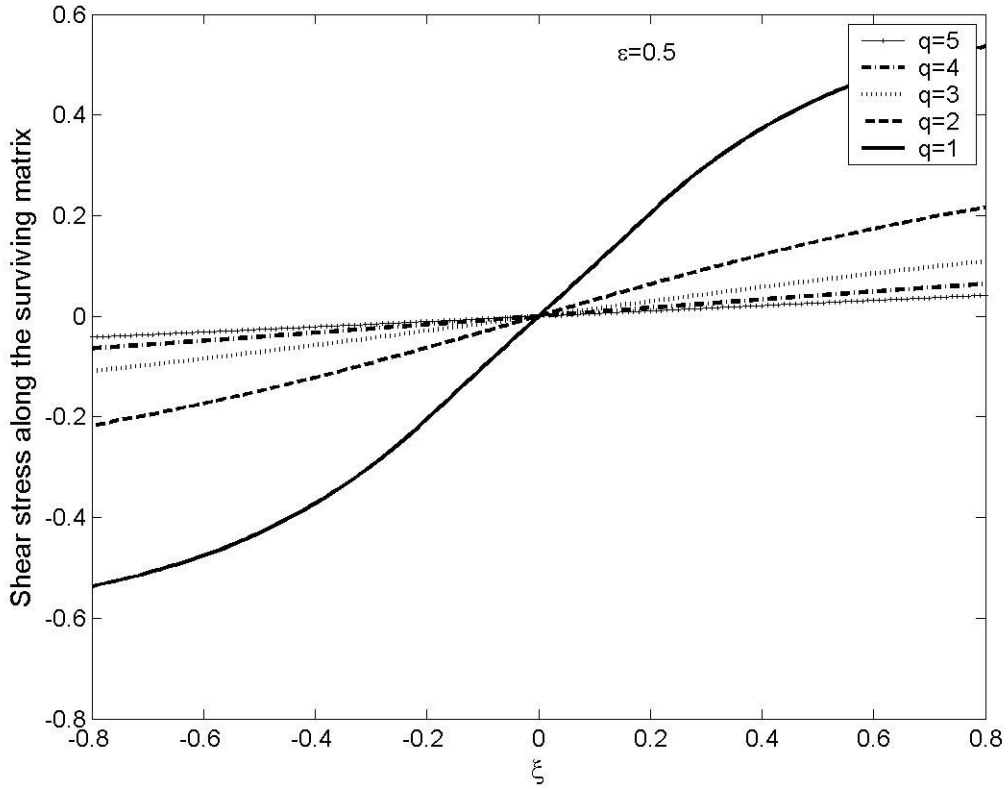

Figure 5. 46. Shear stress concentration along the surviving matrix bays, $N = 9$.

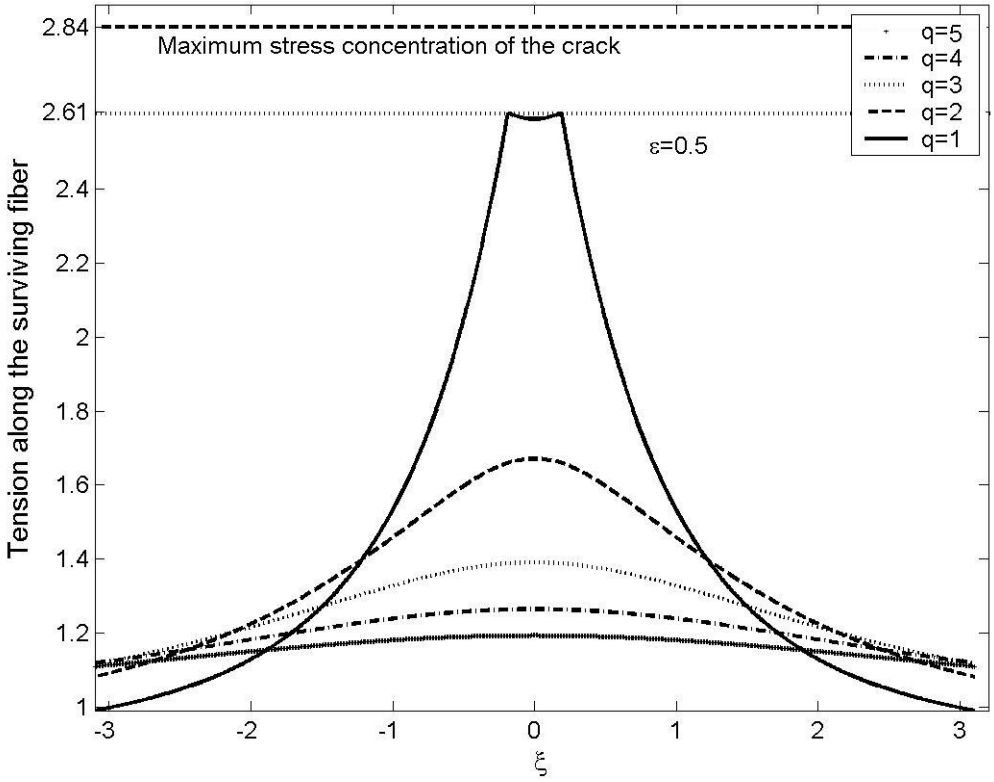

Figure5. 47. Tensile stress concentration along the surviving fiber, $N = 9$.

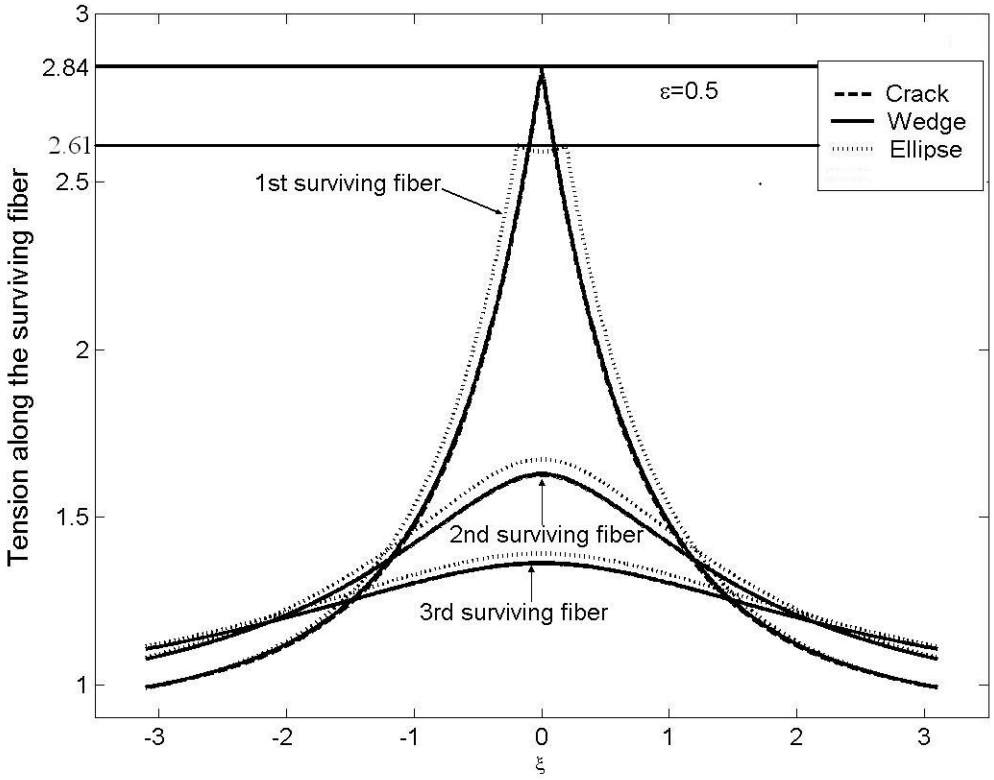

Figure 5. 48. Tension along surviving fibers for cavities of different shape, $N = 9$.

5.3.2 Comparison with the elastic analysis solution

Effect of elastic constants and the fraction factor ϕ for penetration.

In Subsection 5.3.1, we presented basics of the elastic solution of Bishop (1972). The maximum tensile stress intensity factor for an elliptical hole is only dependent on the elastic constants of the material and the eccentricity of the hole as shown by

$$\left(\varepsilon \frac{\sigma'_f}{\sigma_\infty} \right)_{\max} = \frac{\beta_1 + \beta_2}{\beta_1 \beta_2} + \varepsilon \tag{5. 55}$$

Four elastic constants G^*_{xy}, ν^*_{xy}, E^*_{yy}, and E^*_{xx} are involved in this solution. On the other hand, in shear-lag analysis, only two elastic constants, E^*_{xx} and G^*_{xy},

are used to derive the stress field. So before a comparison of results, we need to investigate the effect of ν^*_{xy} and E^*_{yy} on the maximum tensile stress.

Figure 5.38 shows the tensile stress concentration factor versus eccentricity for different transverse stiffness, E^*_{yy}. In the shear-lag solution, we assume that E^*_{yy} is infinitely large such that both the unbroken and broken fibers displace only in the fiber direction. Intuitively, one might expect the agreement between the elastic analysis and the shear-lag model will improve when E^*_{yy} is large. The figure shows the effect of E^*_{yy} on the maximum tensile stress in the continuum model. As the elastic constant E^*_{yy} increases, the maximum stress intensity factor decreases because of the constraining effect in the transverse direction that limits the shear at the tip of the hole and decreases the overload in the tensile direction.

The effect of Possion's ratio ν^*_{xy} on the maximum tensile stress is shown in figure 5.39. Most practical engineering materials have ν^*_{xy} between 0.0 and 0.5. The figure shows that Possion's ratio has less effect on the stress concentration factors than E^*_{yy}. The larger the Possion's ratio is, the smaller the maximum stress concentration there is.

Due to the discrete nature of the shear-lag model, it is not very practical to measure the stress concentration on the edge of the elliptical hole. The maximum tensile stress concentration is always at the first surviving fiber. The distance between the hole tip and the first surviving fiber is controlled by the penetration fraction ϕ in the model, as mentioned before. In the elastic analysis, the fiber away from the hole tip actually carries shear load thereby leading to a reduced tension compared to the shear-lag model. This suggests that we can use the fraction in elastic analysis to adjust the location to measure the stress and improve the agreement between the two solutions.

Figure 5.51 shows the maximum tensile stress concentration factors against eccentricity for different fraction ϕ in the elastic analysis calculated from equation (5.42). For $\phi = 0$, the curve has a shallow slope such that $\varepsilon\sigma_y/\sigma_\infty$ is of very similar magnitude in the range. For all the other ϕ values, as the distance away from the last broken fiber increases, the maximum tensile stress decreases in a significant manner and the slope of $\varepsilon\sigma_y/\sigma_\infty$ increases as well.

In summary, we have three parameters, E^*_{yy}, ν^*_{xy} and ϕ, the latter decided empirically such that two solutions achieve the best agreement.

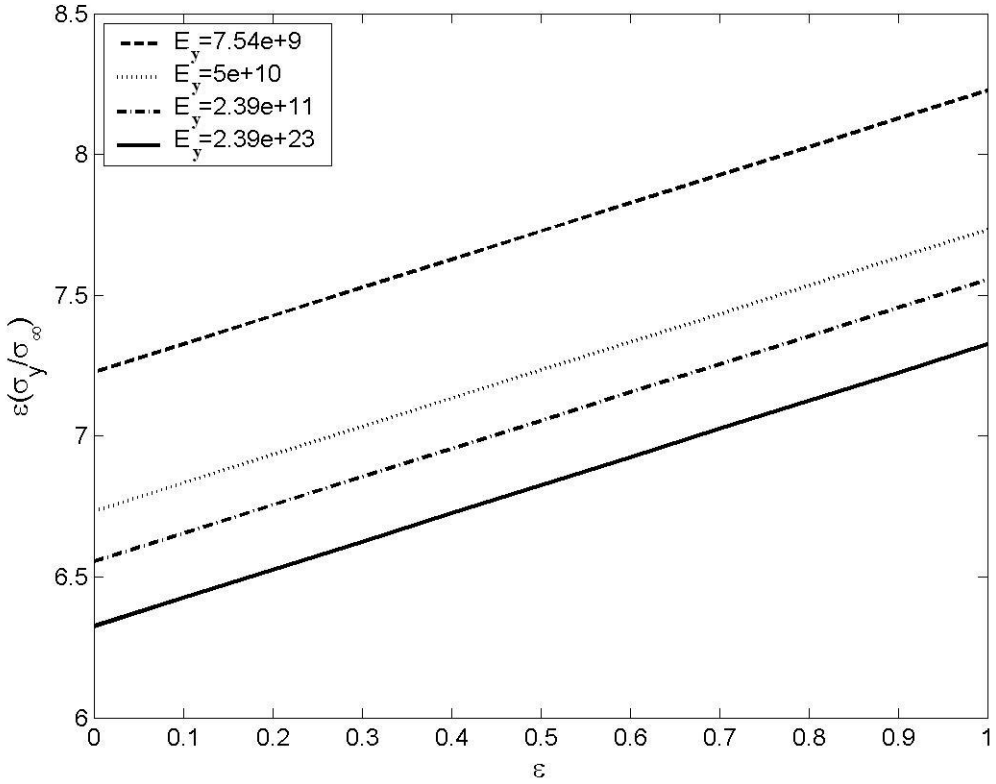

Figure 5. 49. Stress concentration factor vs different eccentricity for different E_y.

Maximum tensile stress concentration factor

Figure 5.52 plots the maximum stress concentration factor on the first surviving fiber for different transverse dimension in elastic analysis. The figure shows that for small sized holes, $\varepsilon\sigma_y/\sigma_\infty$ approximately increases linearly with eccentricity ε.

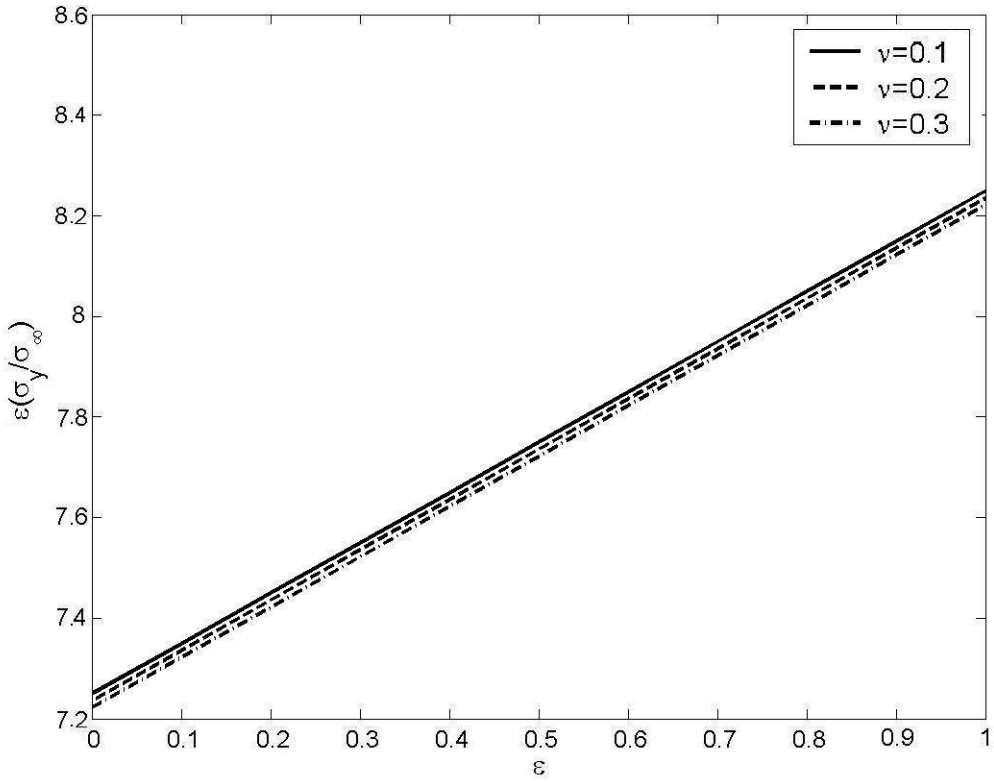

Figure 5. 50. Stress concentration factor vs different eccentricity for different ν.

As the size increases, the curve loses its linearity and most importantly, the effect of the eccentricity on $\varepsilon\sigma_y/\sigma_\infty$ for the first surviving fiber begins to decay. For extremely large holes, the fraction factor ϕ has little impact on the stress concentration factor because the first surviving fiber is 'close' enough to be approximately on the edge of the hole at this point and the material can be seen as homogeneous, thus leading to the conclusion in Bishop (1972) that the eccentricity and the material constants are the only factors to decide the maximum stress concentration factor.

Fraction factors $\phi = 0$ and $\phi = 1$ represent two extreme cases for the tip of the hole in the discrete model: $\phi = 0$ means the last broken fiber of the hole has a broken segment removed; on the other hand, $\phi = 1$ means that the tip is an isolated

fiber break. This value of ϕ doesn't make much difference in the homogeneous continuum, but in the discrete model, especially when the size of the hole is ony a few fiber diameters, it plays a key role in the stress distribution calculation. Figure 5.53 plots the effect of the fraction factor on the maximum tensile stress concentration factor for small hole sizes, where $N = 9$ and $N = 13$. The figure shows that larger ϕ values result in higher stress concentrations and larger slope due to the effect of the isolated fiber break at the tip. This effect fades away as the transverse dimension of the hole becomes large enough that the effective spacing is much less than the elliptical semi-axis, a_c.

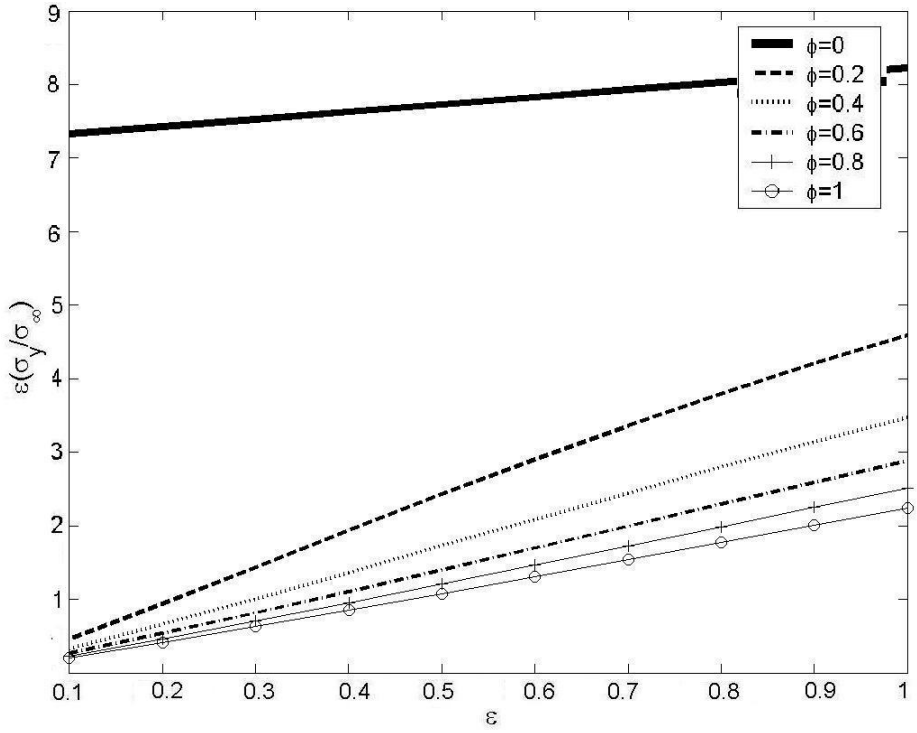

Figure 5. 51. Stress concentration factor vs different eccentricity for different ϕ.

Since we are focusing on a small sized hole in this study, ϕ is a very important adjustment factor to achieve the agreement between the elastic analysis and the shear-lag analysis. Or from another point of view, the local details of fiber

placement are not properly recognized by the continuum approximation. Due to the limitations of time and computational power, it's not very practical to compute the extremely large holes to get the asymptotic results. We will only focus on the comparison for small holes, and use ϕ as an adjustment factor to make a comparison for elastic analysis and shear-lag theory in the following section.

Figure 5.54 plots the tensile stress maxima multiplied by ε against ε in the range $0 \le \varepsilon \le 1$. Elastic analysis and shear-lag analysis achieve good agreement for different size of the elliptical holes. The figure also shows that the magnitude and slope of $\varepsilon\sigma_y/\sigma_\infty$ versus eccentricity increases with the size of the elliptical hole. As mentioned early, this size effect is expected to fade away when the hole size is much larger than the fiber diameter.

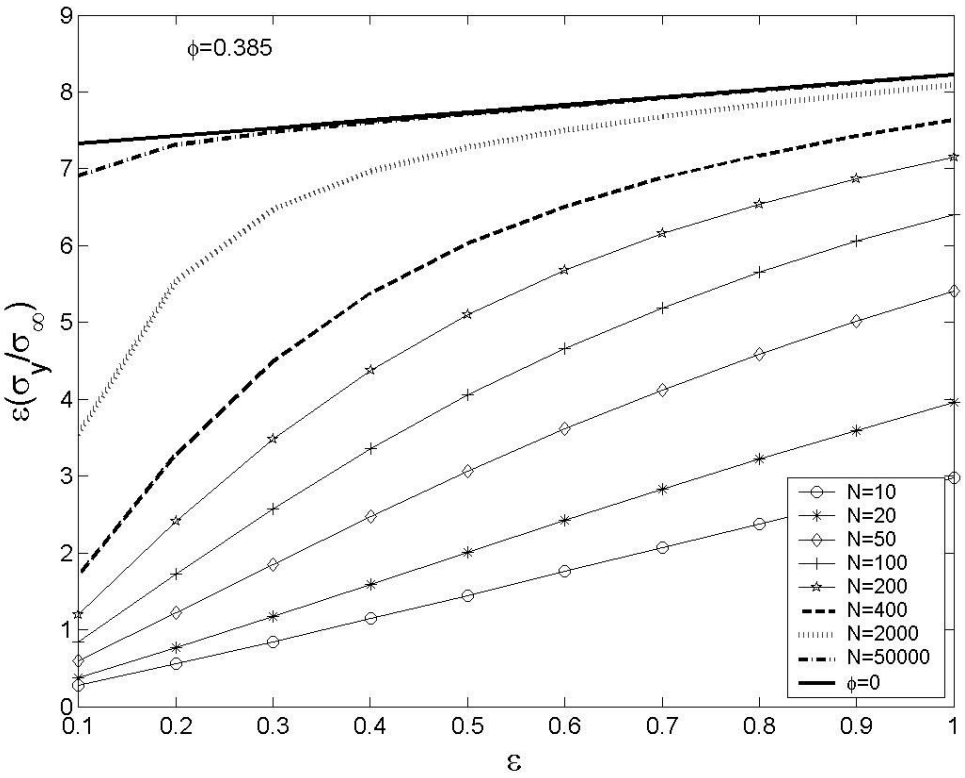

Figure 5. 52. Stress concentration factor vs different eccentricity for different N.

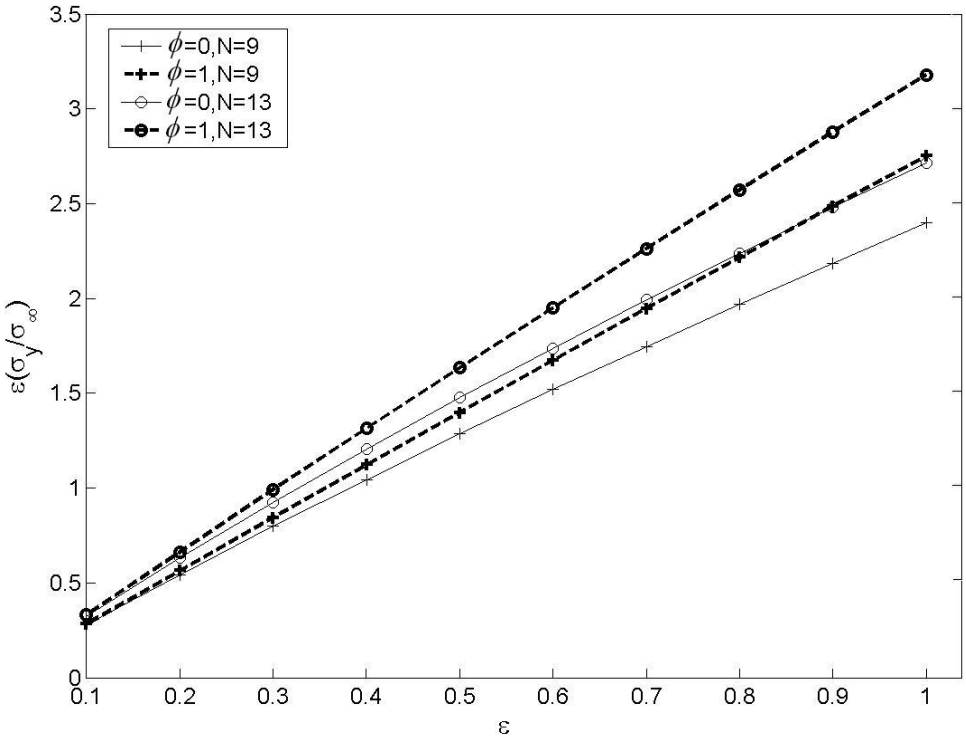

Figure 5. 53. Tensile stress concentration versus eccentricity for two extremes of ϕ.

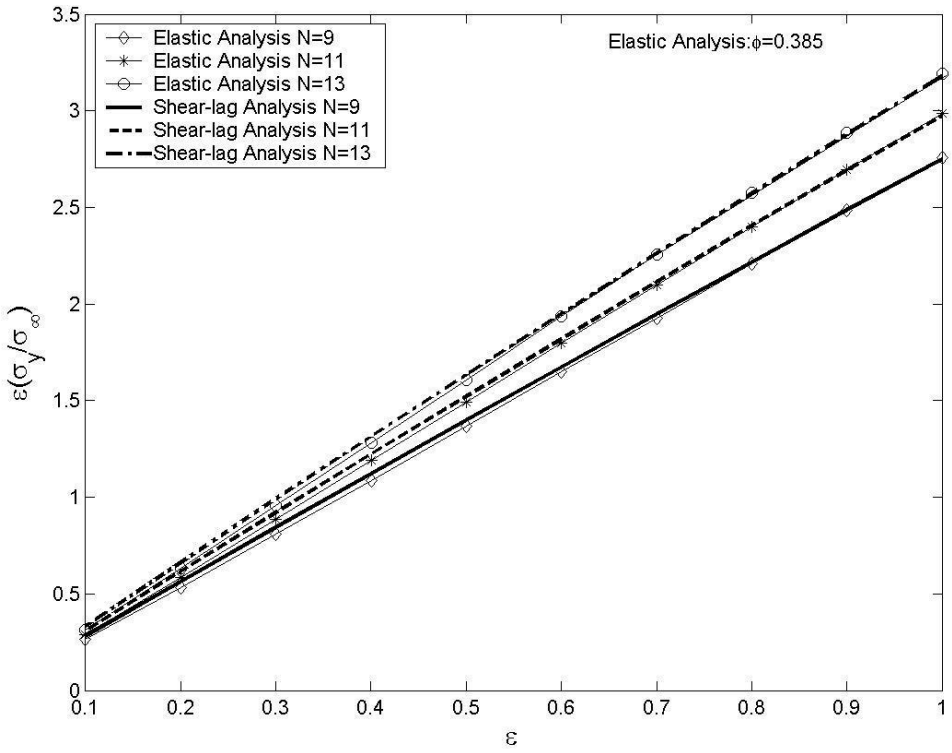

Figure 5. 54. Tensile stress concentration vs eccentricity predicted from both solutions.

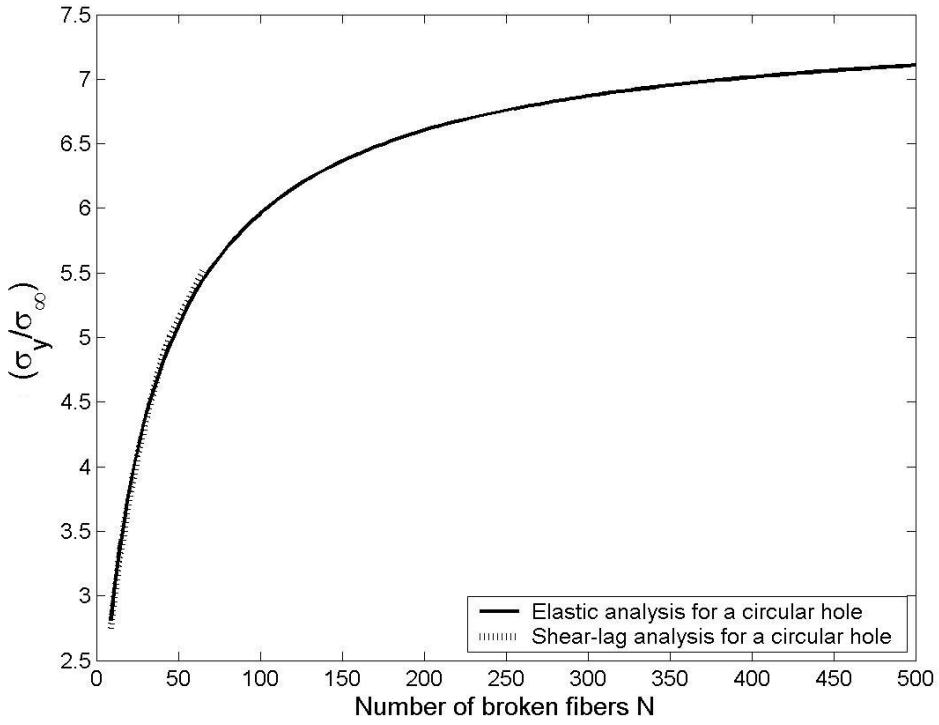

Figure 5. 55. Maximum tensile stress concentration factors for a circular hole.

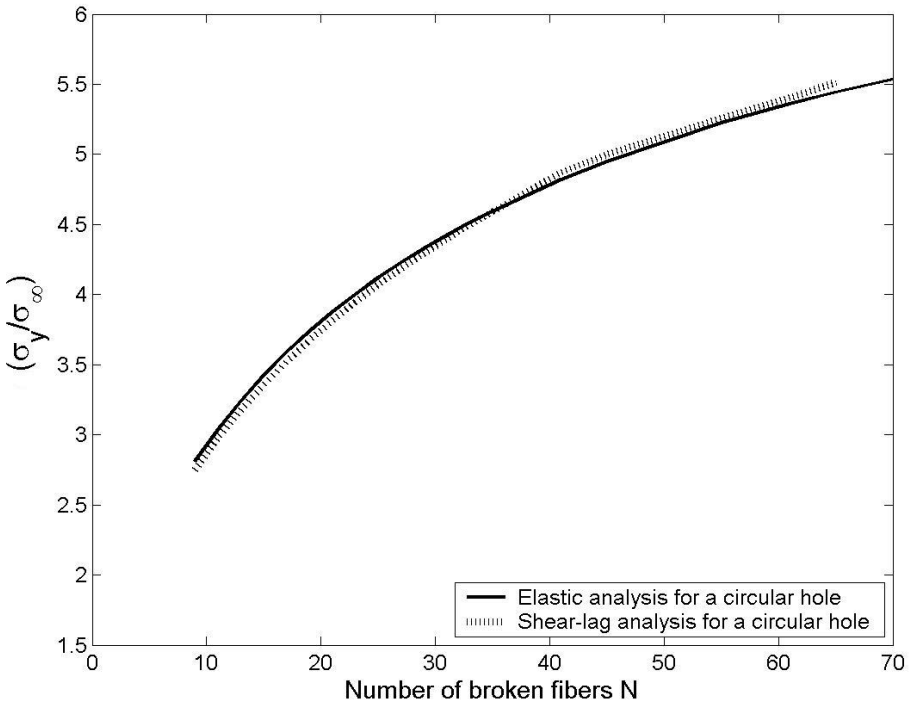

Figure 5. 56. Blowup of maximum tensile stress concentration factor in Figure 5.55.

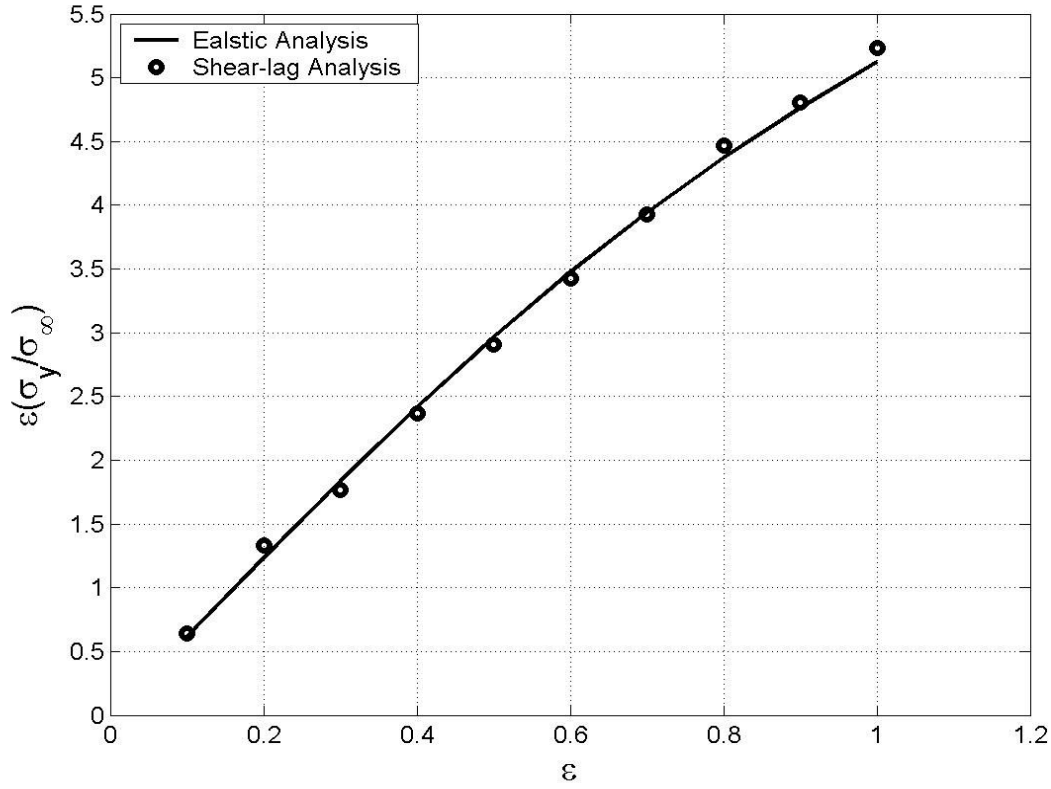

Figure 5. 57. Tensile stress maxima for the range of elliptical hole $0 \le \varepsilon \le 1$, $N = 51$

Figure 5.55 plots the maximum tensile stress concentration factor for a circular hole in the composite plane calculated from both analysis and Figure 5.56 is a magnified picture of Figure 5.55 for small holes. The figure shows excellent agreement between the two solutions and the elastic solution shows that the maximum stress concentration factor converges as the size of the hole ibecomes large enough that the transverse dimension of the hole is much larger than the fiber diameter. The asymptotical maximum stress concentration factor is determined solely by the elastic constants of the material as suggested by equation (5.35).

In figure 5.57, the tensile stress maxima multiplied by the eccentricity ε is plotted against ε in the range $0 \le \varepsilon \le 1$, for $N = 51$. Both solutions show good agreement and the slope is quite steep due to the small size of the hole. As shown in Figure 5.52, the transverse dimension of the hole has less impact on the stress concentration as the hole gets larger, and the maximum stress concentration factor

converges to the maximum stress on the edge of the hole as predicted asymptotically by the elastic analysis.

Tensile stress distribution near the elliptical hole

The tensile stress on the crack plane ahead of the edge or tip of the hole is shown in Figures 5.58 and 5.59 for both elastic analysis and shear-lag analysis. The two solutions show outstanding agreement even at the tip of the hole. The tension drops down along the crack plane very rapidly especially near the tip, and the effect of the hole size fades away around ten fibers away from the tip.

We have also investigated the tension distribution along the surviving fiber. Figures 5.60, 5.61 and 5.62 plot the tensile stress along the surviving fibers $q = 1, 2, 3$ respectively. In the discrete shear-lag model, the hole does not necessarily end with an isolated fiber break depending on the distance between the hole tip and the first surviving fiber ϕw^*, but in elastic analysis, due to the homogeneous continuum assumption, the hole tip is always an isolated fiber break. For fiber $q = 1$, the shear-lag model has its maximum at the end of last broken fiber, and elastic analysis always has its maximum stress at the crack plane. The effect of the penetration fraction ϕ decays along the crack plane. The tensile stress along the surviving fiber $q = 2, 3$ from both solutions matches well.

5.3.3 Stress gradient near the tip of the hole

In Potter (1978), the main focus was to study the tensile stress gradient and investigate how extra load ρ passed down to the second flanking fiber due to the failure of the first fiber near the hole can affect the fracture propagation behavior. He showed that holes can be divided into “large” and “small” categories as defined by the fracture behavior. For “large” holes, the stress gradient at the hole tip is so

small that combined with the extra load ρ due to the failure of the first flanking fiber, the second flanking fiber has reached the fiber strength, thus leading to a sequential failure which can be predicted by the elastic analysis. For a "small" hole, the stress gradient is large and the failure process is characterized by the formation of stable damage zones when the composite tensile strength is reached. He assumes that ρ only depends upon the properties of the fiber, matrix and interface and can be obtained experimentally by testing a number of specimens containing circular holes of various diameters in order to determine the minimum diameter at which failure may be predicted by the elastic stress concentration factor. The main goal in this section is to investigate the stress gradient of the tensile stress near the hole tip and study the impact on the fracture behavior of the composite material.

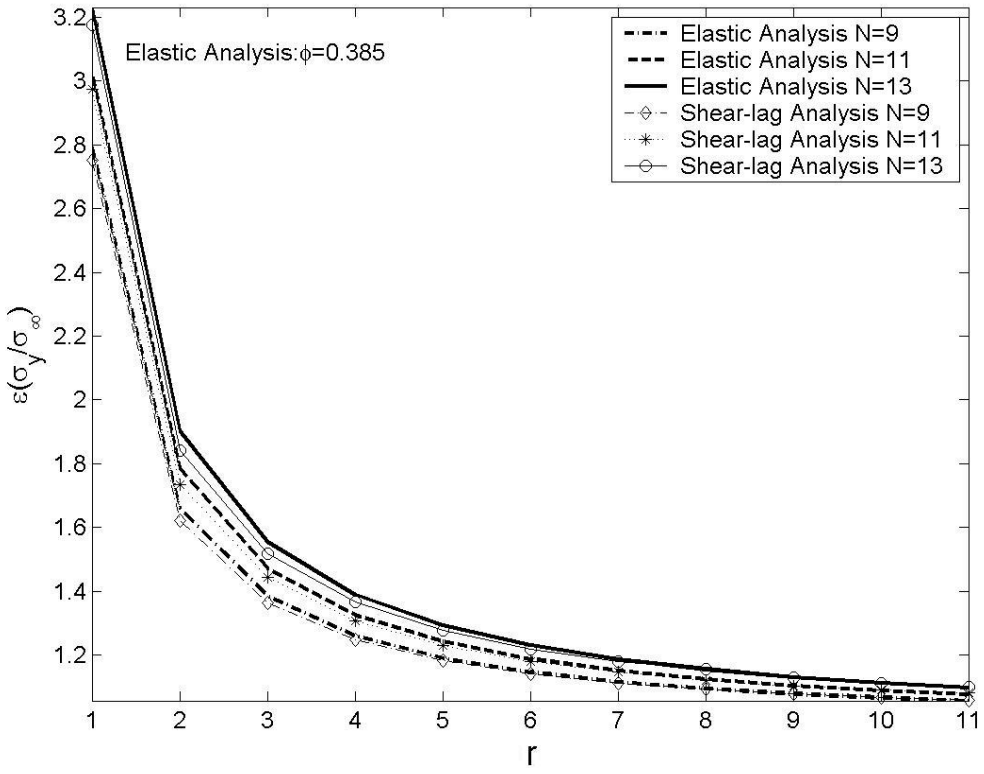

Figure 5. 58. Tension along the crack plane predicted both solutions, $\varepsilon = 1$.

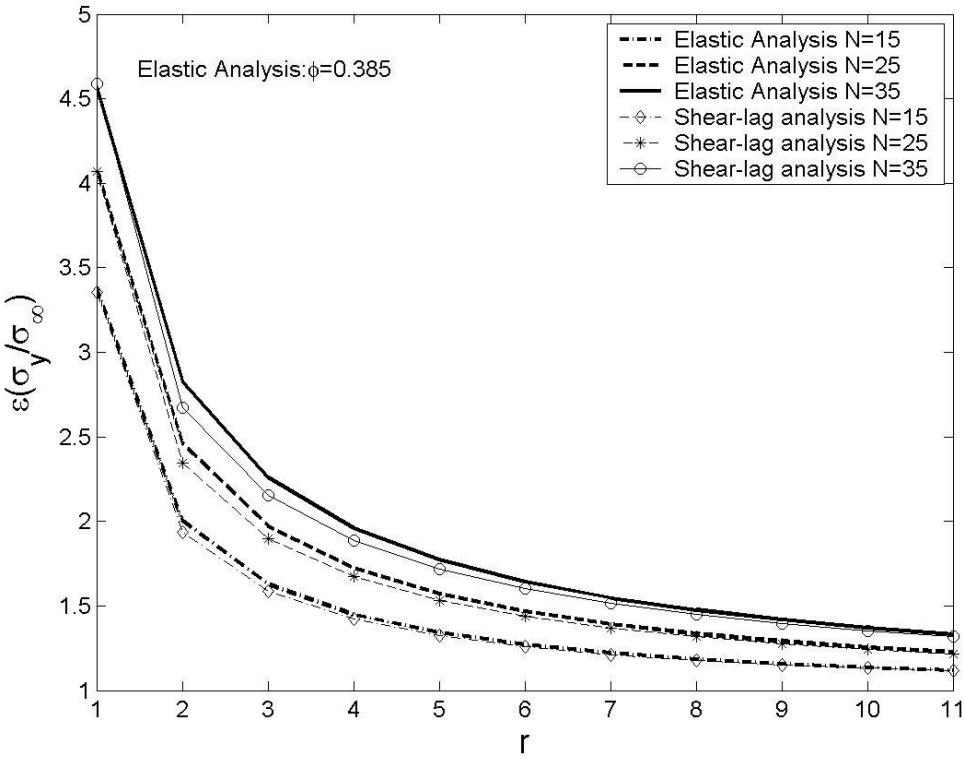

Figure 5. 59. Tension along the crack plane predicted from both solutions, $\varepsilon = 1$.

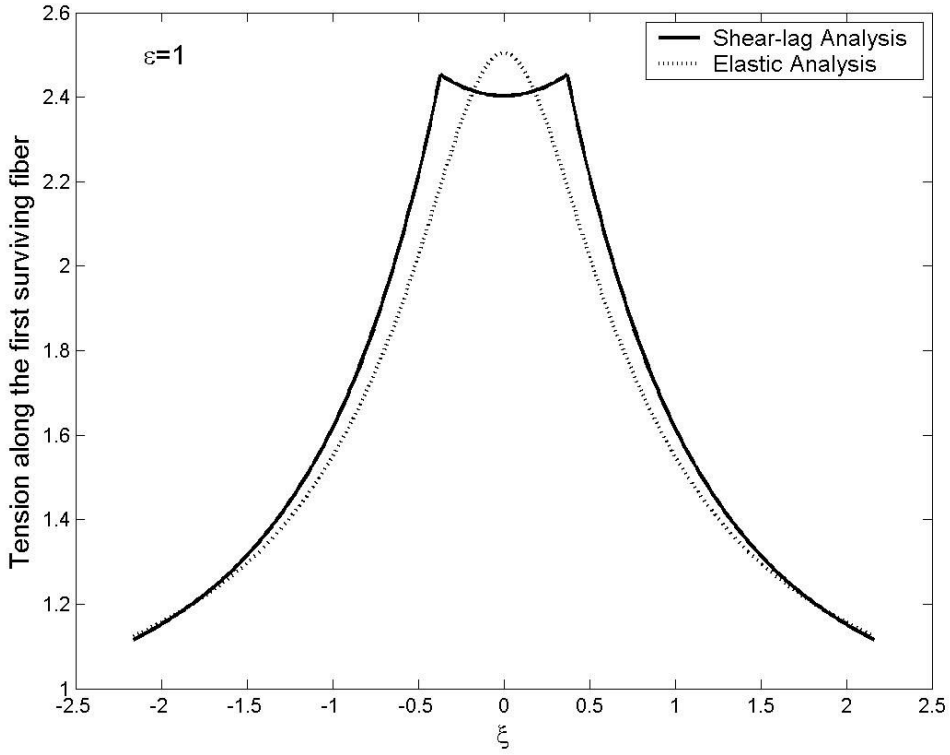

Figure 5. 60. Tension along the first surviving fiber when $N = 9, \phi = 0.333$.

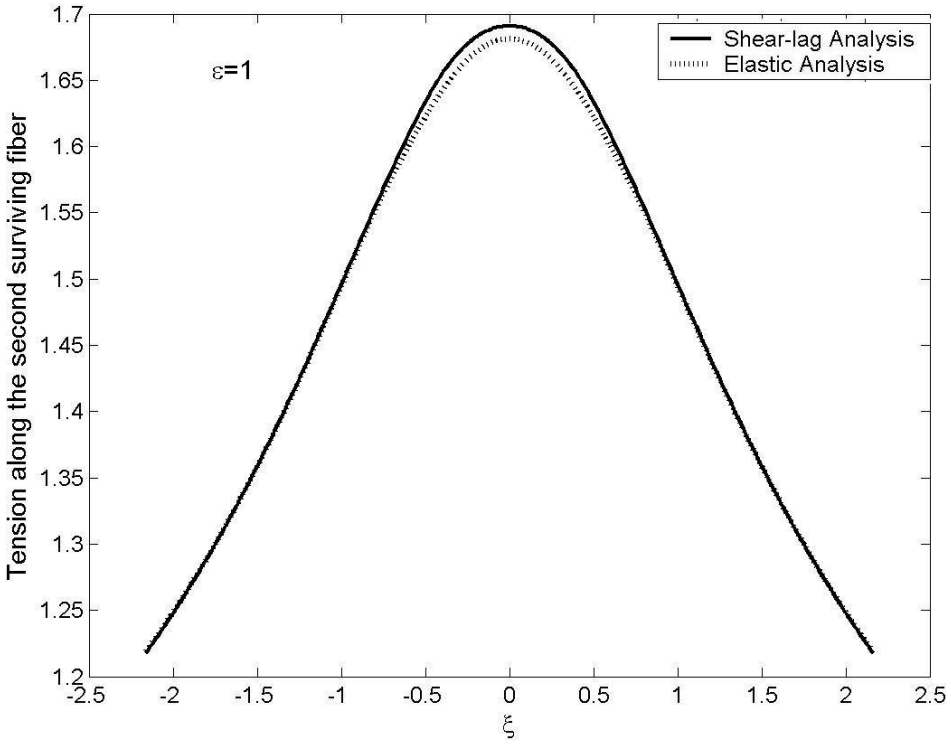

Figure 5. 61. Tension along the second surviving fiber when $N = 9, \phi = 0.333$.

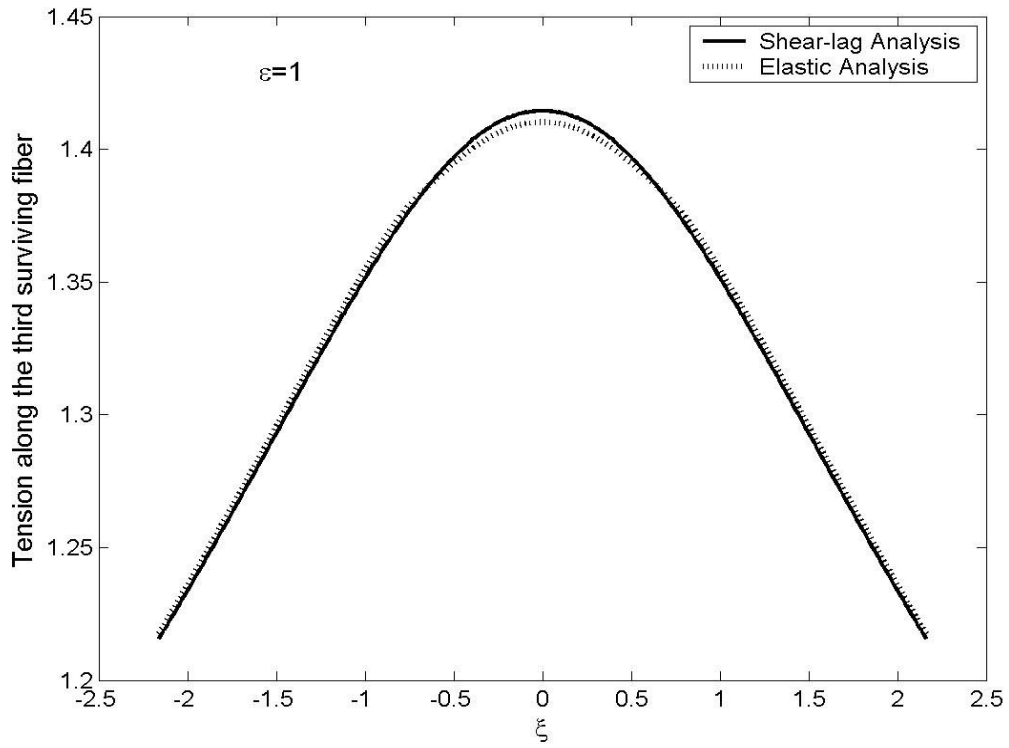

Figure 5. 62. Tension along the third surviving fiber when $N = 9, \phi = 0.333$.

Using the solution in Bishop (1972), we derive the stress gradient near an elliptical hole assuming the material is a homogeneous continuum.

$$\left(\frac{\partial \sigma_x}{\partial y}\right)_{x=0} = \sigma_\infty \,\mathrm{Re}\left\{\frac{1}{(\beta_1-\beta_2)} \cdot \left[\begin{array}{l} \dfrac{\beta_2}{1-\varepsilon\beta_1}\left(\dfrac{-1}{\left(y^2-a_c{}^2+b_c{}^2\beta_1{}^2\right)^{1/2}}+\dfrac{y^2}{\left(y^2-a_c{}^2+b_c{}^2\beta_1{}^2\right)^{3/2}}\right) \\ -\dfrac{\beta_1}{1-\varepsilon\beta_2}\left(\dfrac{-1}{\left(y^2-a_c{}^2+b_c{}^2\beta_2{}^2\right)^{1/2}}+\dfrac{y^2}{\left(y^2-a_c{}^2+b_c{}^2\beta_2{}^2\right)^{3/2}}\right) \end{array}\right]\right\} \quad (5.\ 56)$$

Here question of validity arises for this definition of the gradient. When the size of the hole is not much larger than the fiber diameter, the material can't be seen as continuum and the gradient needs to be taken discretely. Figure 5.63 plots the stress gradient ahead of the hole tip computed from equation (5.56) and the shear-lag model. The figure shows that the assumption of a homogeneous continuum predicts a much higher stress gradient than the shear-lag model. However, using the following discrete definition for the stress gradient, we get much better agreement between these two solutions as shown in Figure 5.64 and 5.65.

$$\left(\frac{\partial \sigma_x}{\partial y}\right)_{x=0,q} = \frac{\left|\sigma_{x=0,q+1}-\sigma_{x=0,q}\right|}{w^*} \quad (5.\ 57)$$

The discrepancy of the stress gradient also suggests that Potter's results only apply to the case where the material can be seen as homogeneous continuum. Therefore even his "small" holes are large holes for the discrete model. The elastic solution overall predicts somewhat higher stress concentration than the shear-lag model since the matrix bay in the elastic analysis also supports tension, leading to faster decay of tension along the crack plane.

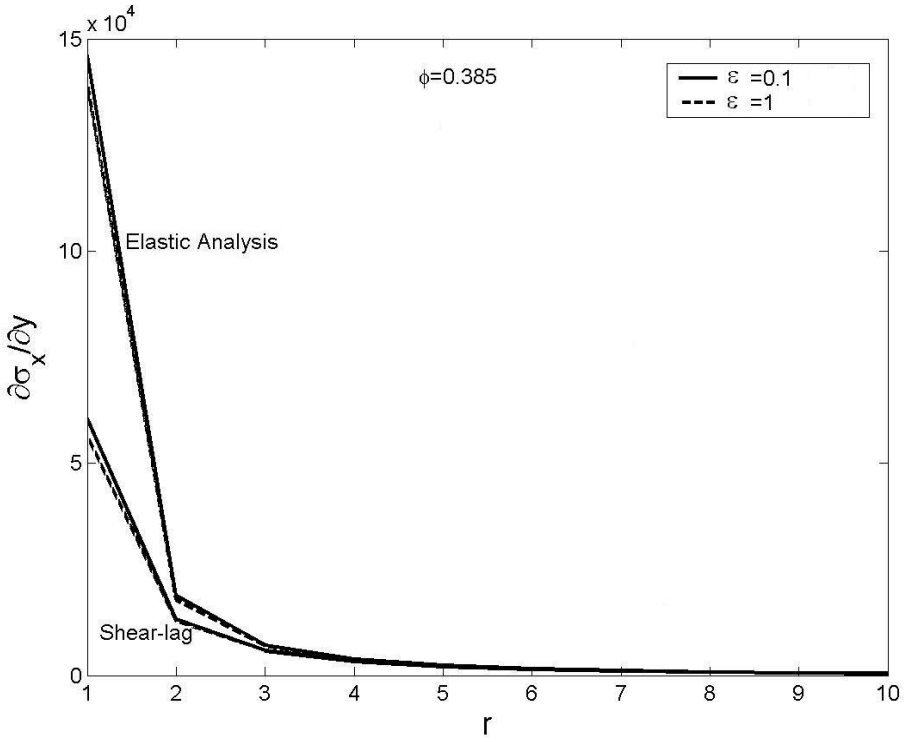

Figure 5. 63. Stress gradient ahead of the hole tip for an effective $N = 13$ hole, calculated using equation (5.56) and the shear-lag model.

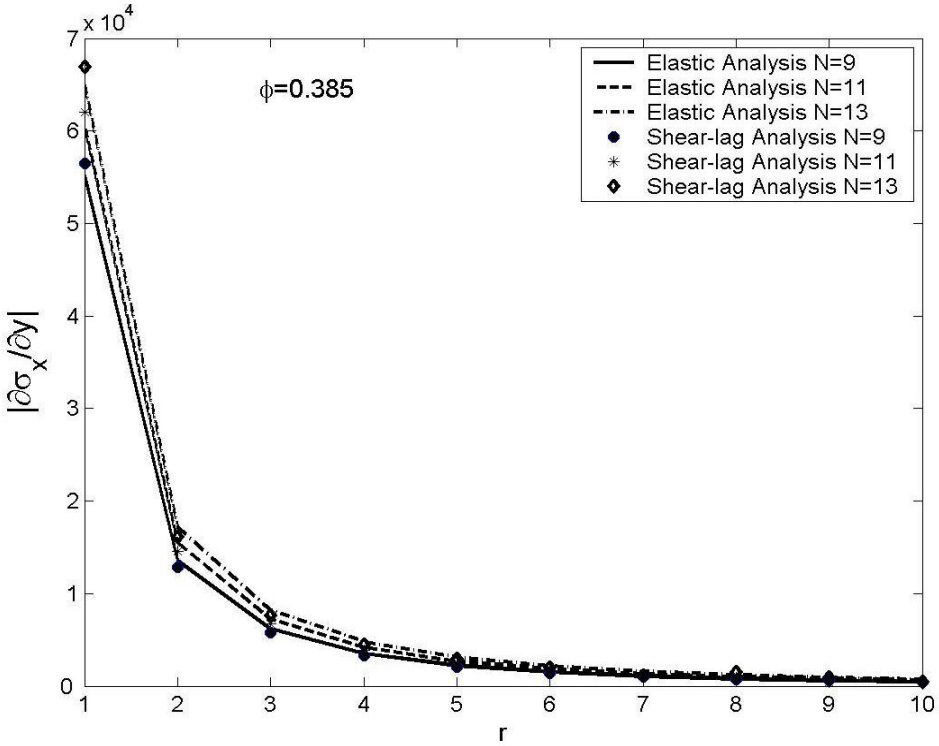

Figure 5. 64. Discrete tensile stress gradient ahead of the circular hole tip for $\varepsilon = 1$.

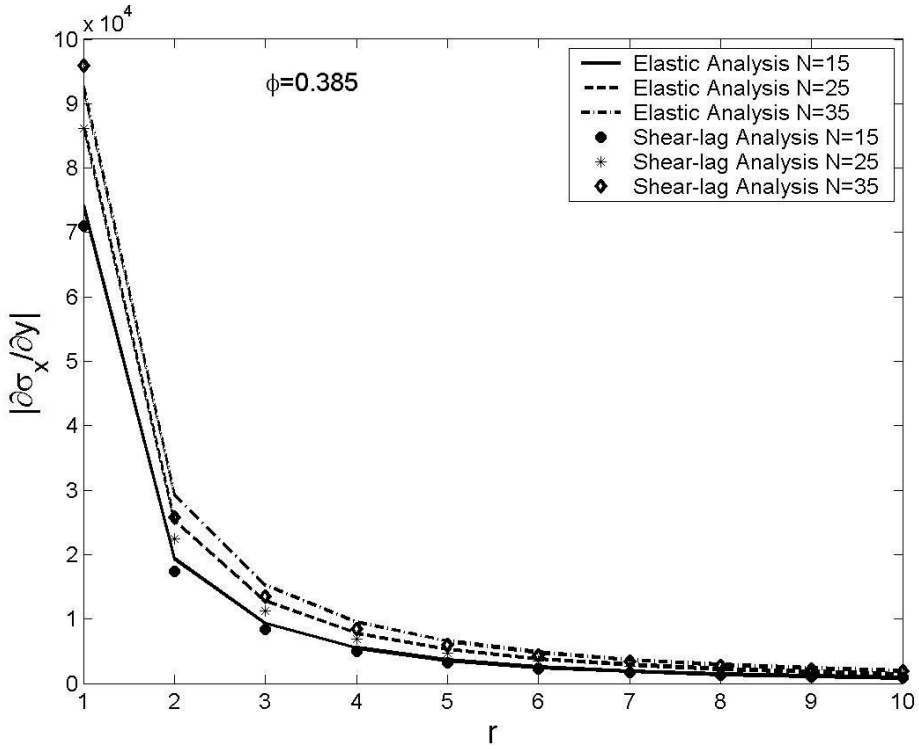

Figure 5. 65. Discrete tensile stress gradient ahead of the circular hole tip for $\varepsilon = 1$.

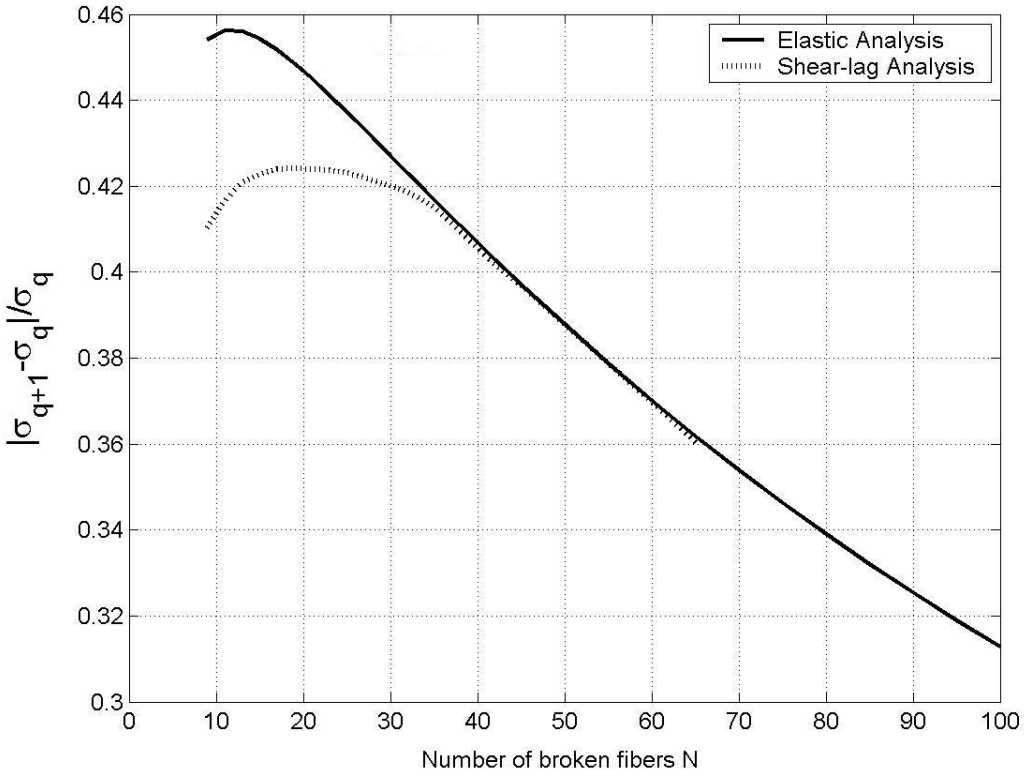

Figure 5. 66. Tensile stress gradient versus transverse size of a circular hole, $N = 51$.

Figure 5.66 shows the decrement in the normalized tensile stress on the first two surviving fibers, for different circular hole sizes. Both solutions achieve good agreement for the circular hole containing more than 40 broken fibers. For the hole that has less than 20 broken fibers, we can see that the decrement is actually an positive increment with the size of the hole, which suggests that larger holes in this range have less chance to initiate sequential failure than small holes. After this critical point, the decrement is a true decrease as the transverse dimension of the circular hole increases, suggesting that the stress gradient is decreasing and thus more fibers are overloaded significantly. Note that we concluded in last section that the maximum stress concentration factor increases with the transverse size of the hole until it converges to an asymptotic value, which is determined solely by the material elastic constants. Larger stress concentrations and smaller stress gradient suggest that bigger holes do more damage to the composite plane and more flanking fibers are overloaded significantly resulting in the likelihood of uncontrolled propagation.

5.3.2 Stress distribution for an elliptical hole with two extra fiber breaks

In this subsection, we investigate the maximum tensile stress concentration on the first surviving fibers when one fiber failure occurs next to the hole, and we check if the stress gradient at the tip of the hole is a good measure to predict the load on the second fiber when the first flanking fiber fails.

Experiments (Potter, 1972) show that the modification of the stress distribution due to the formation of damage zone eliminates any effect due to the initial shape of the hole. To verify this statement, we will also study the shear stress around the hole and investigate how the shear varies with the shape of the hole. In

this section, we will limit our case to ellipse and crack. The hole ends with a fiber break at the tip for in this example. Assuming the first flanking fiber has failed due to the overload caused by the elliptical hole, Figure 5.67 describes an elliptical hole in a two-dimensional composite plane with one additional fiber break at each side.

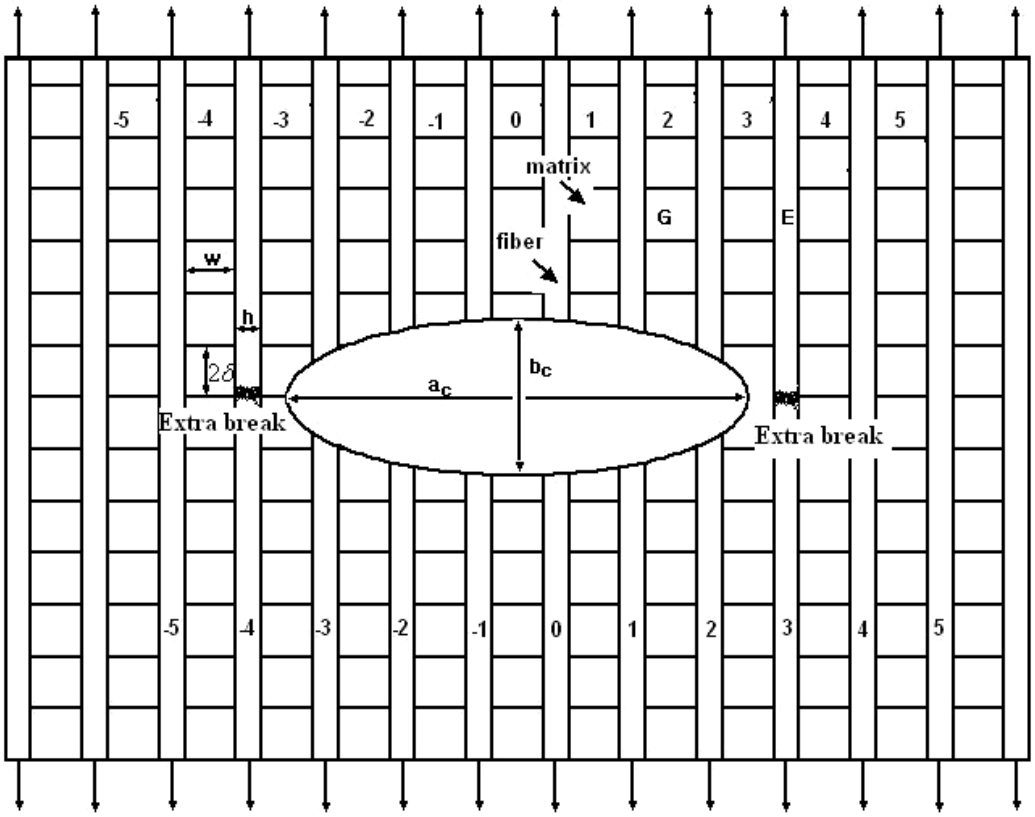

Figure 5. 67. An elliptical hole in a two-dimensional infinite lamina with one additional fiber break at each side

Figure 5.68 compares the tensile stress distribution along the first three flanking fibers near an elliptical hole, a wedge, and an elliptical hole with one additional fiber break at each tip. The tensile stress concentration grows significantly due to the new breaks overall, and the maximum tension is at the tip of the hole $\xi = 0$. The overload drops to about $1/3$ by the second fiber, $1/5$ by the third fiber. The extra fiber breaks make the load decay faster than for a comparable elliptical hole but still slower than for a crack.

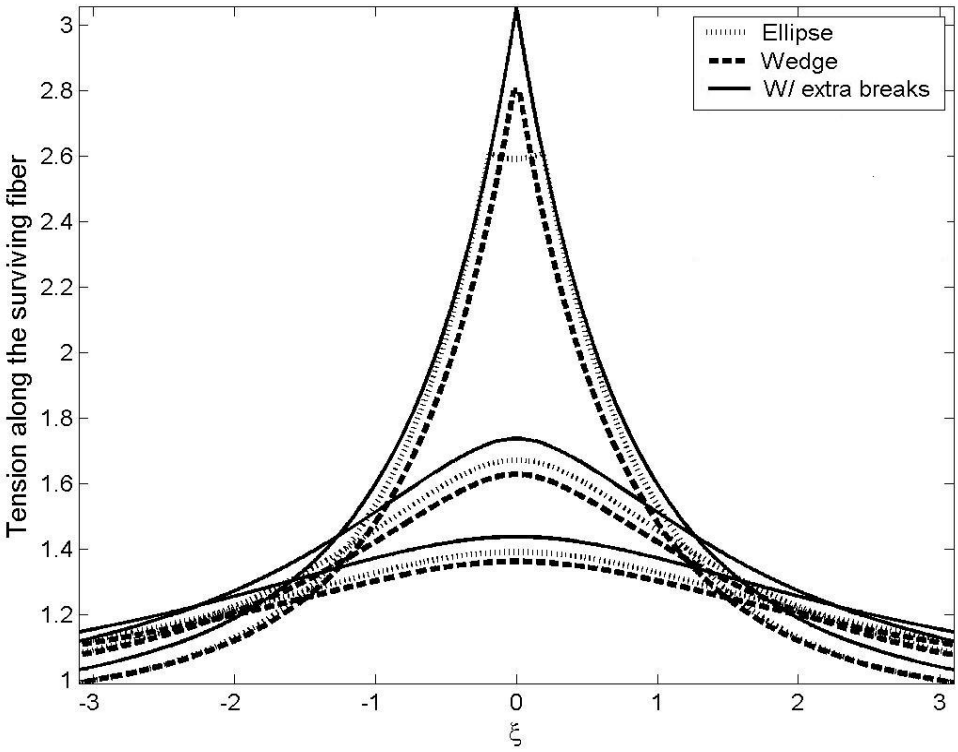

Figure 5. 68. Tension along the flanking fiber for cavities of different shape, $N = 9, \varepsilon = 0.5$.

Next, we compare the effect of the additional fiber failure on the stress field for different hole shapes. The initial shapes of the hole are a wedge, ellipse and crack with the same transverse dimension. As shown in Figure 5.48, their original stress distributions are quite different. With additional fiber breaks, the effect due to the shape of the initial hole is completely removed and all the shapes have very close stress distribution along the surviving fibers. Figure 5.70 shows the effect on the maximum tensile stress concentration factor along the crack plane for different eccentricity. The differences due to the eccentricity diminishes greatly when there is one additional fiber break at each tip for elliptical holes. Further away from the tip, all the stress intensity factors converge to the same value and the distinction due to the damage difference zone fades away. However, we expect this effect vanishes when the number of broken fibers is very large because the effect of one extra break will be much less significant compared to the damage caused by the original hole.

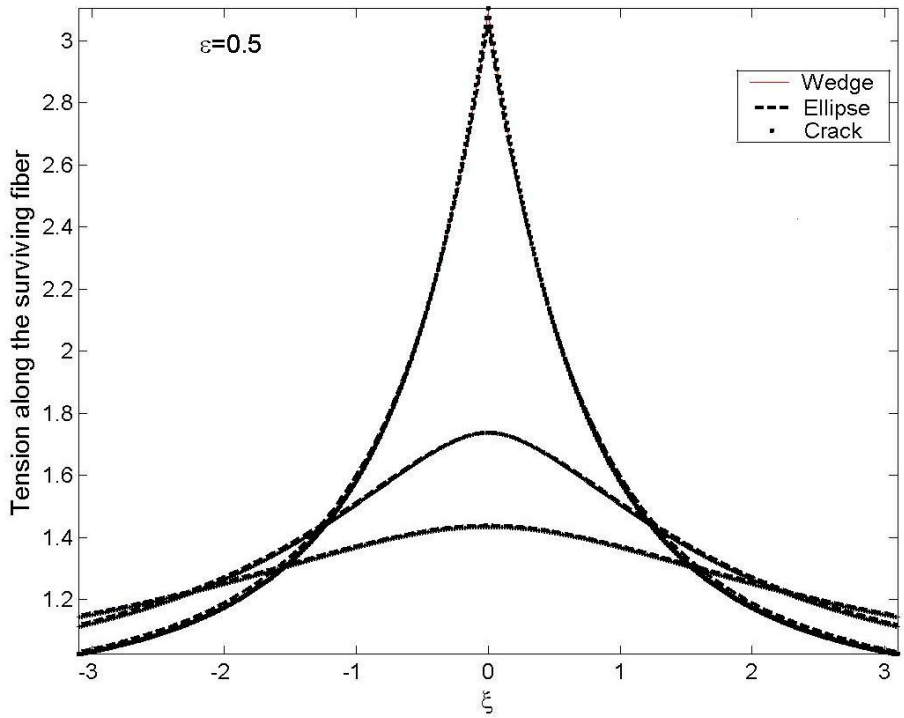

Figure 5. 69. Tension along the surviving fiber for holes of all shapes with one extra break on each end $N = 9,\ \varepsilon = 0.5$.

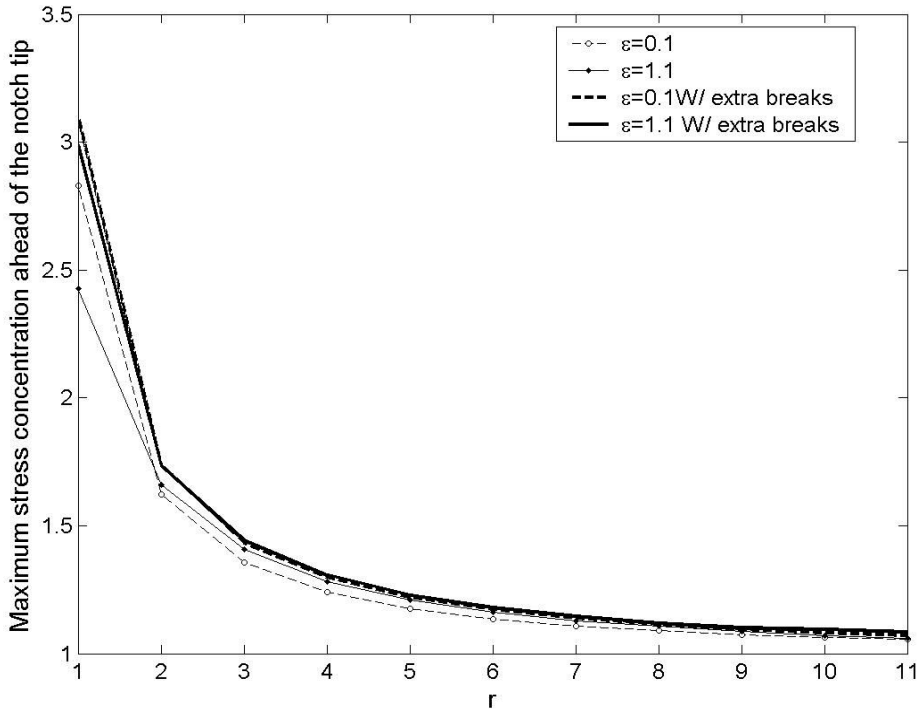

Figure 5. 70. Maximum tensile stress concentration factors along the crack plane, $N = 9$.

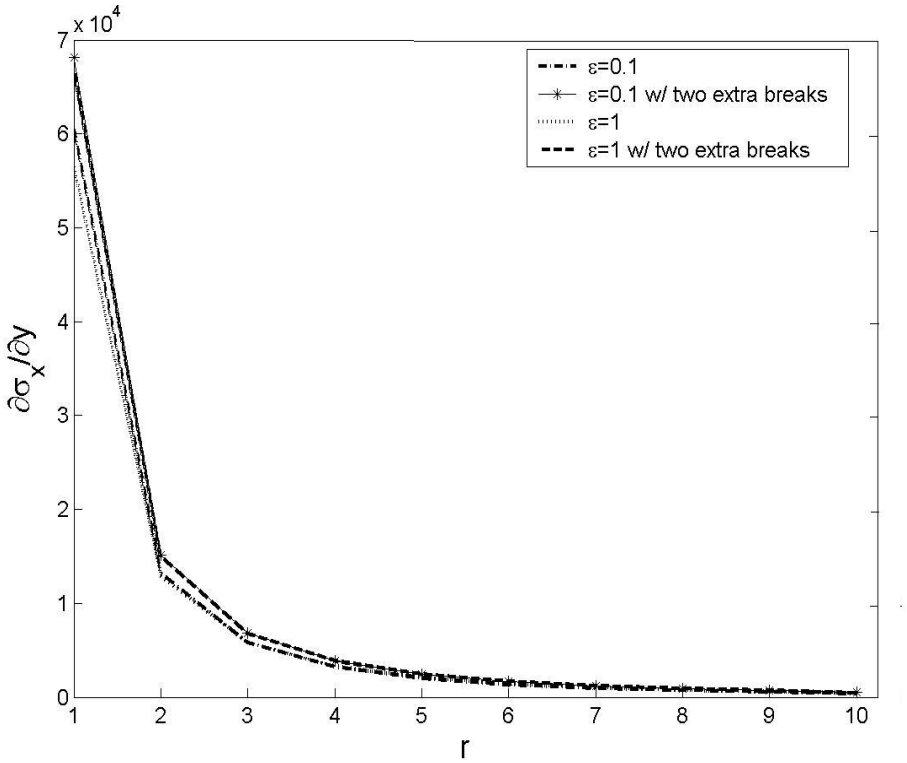

Figure 5. 71. Discrete tensile stress gradient ahead of the hole tip, $N = 13$

Figure 5.71 shows the tensile stress gradient along the crack plane for different eccentricity. The hole with less eccentricity has higher stress gradient than the circular hole, but with one additional fiber break at the tip, the two holes have about the same stress gradient. So when the size of the hole is small, the extra fiber breaks play a very important role. It takes away the difference of the stress field due to the original shape of the hole. Figure 5.72 compares the maximum tensile stress concentration due to an elliptical hole, an elliptical hole with one extra fiber breaks at each tip and an elliptical hole with equivalent transverse dimension as the one with extra fiber breaks. When the eccentricity is small, the shape of the hole makes little difference and the transverse dimension determines the maximum stress concentration factor. While for a circular hole, the one with extra fiber breaks has the highest stress concentration among all the cases. Again, this effect is also expected to vanish when the size of the hole is much larger than the fiber diameter.

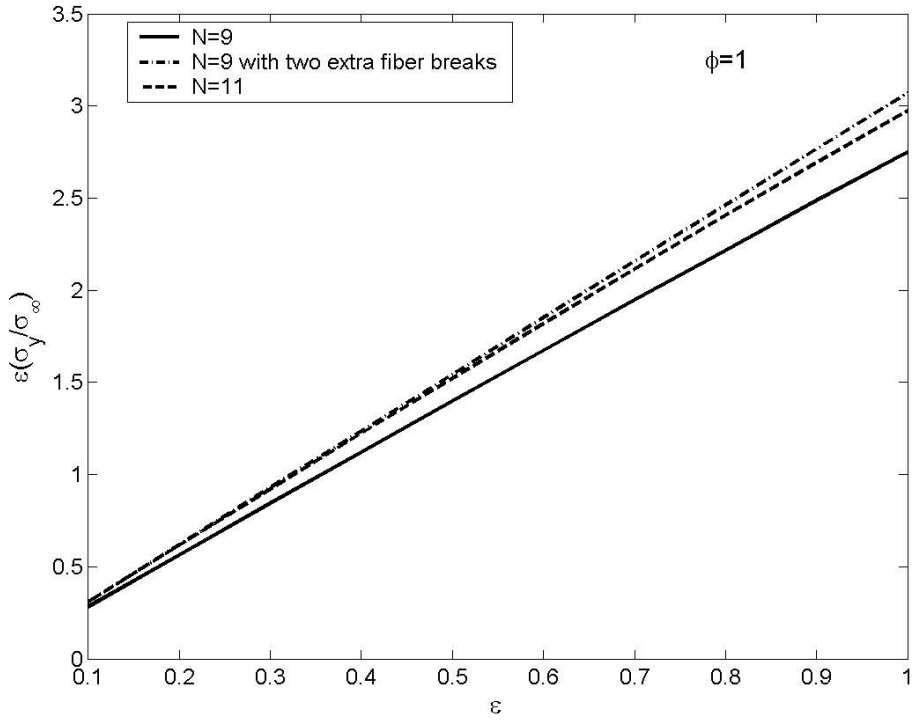

Figure 5. 72. Maximum tensile stress concentration factors versus eccentricity

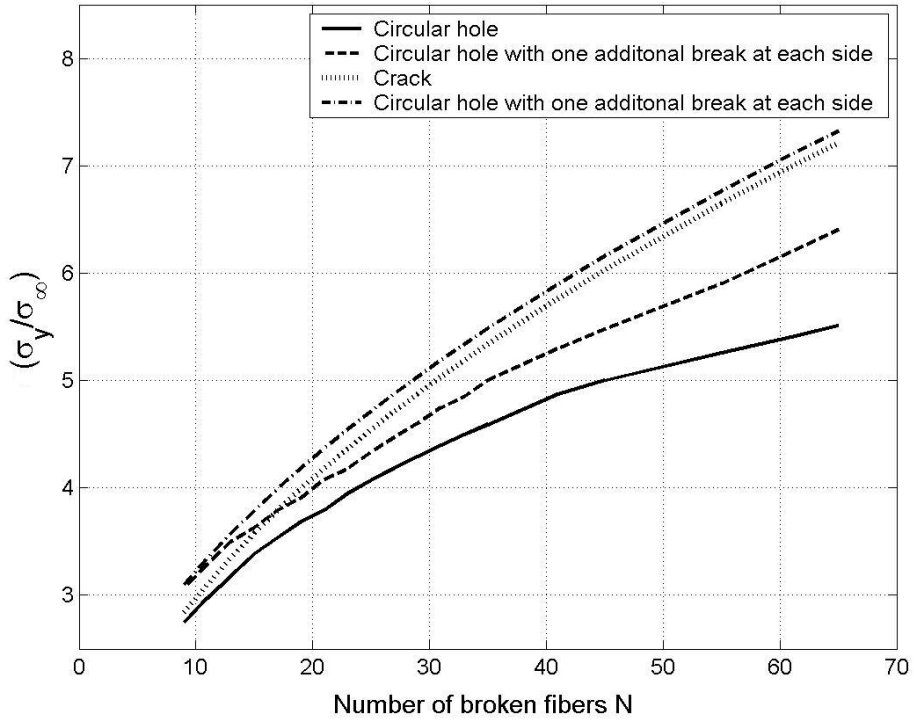

Figure 5. 73. Maximum stress concentration factors for a circular hole and a crack.

Figure 5.73 plots the tensile stress intensity factors versus the transverse dimension of the hole for four cases. The maximum tensile stress for a large crack is described in equation (5.3). Therefore with one additional fiber break at the tip, we have the stress intensity factor

$$K_{N+2} \approx \sqrt{1+\pi(N+2)/4} \tag{5. 58}$$

As N increases, we have

$$\frac{K_{N+2}}{K_N} \to 1 \tag{5. 59}$$

Equation (5.59) suggests that the effect of extra fiber breaks for a crack on the maximum tensile stress concentration factor vanishes as the transverse dimension increases. The same trend is also shown in Figure 5.73.

However, for a circular hole, a different story emerges for the size we tested. The extra breaks at the tip increase the maximum stress concentration factor significantly and as the size increases, the effect becomes more obvious. Intuitively, we expect that the extra fiber breaks don't shift the tensile stress concentration much when the size of the hole is much larger than the fiber diameter since all the large holes with the same transverse dimension have the same maximum stress concentration factor. Therefore, there must be a critical value for the number of broken fibers such that the difference of the stress concentration factors between the circular hole and the circular hole with extra fiber breaks starts narrowing down and eventually disappears.

Figure 5.74 shows that the extra fiber breaks slightly increase the stress gradient at the tip of the hole and overall the stress gradient decreases as the number of broken fibers increases over 30 for both cases. For a large hole, all the fibers are almost equally overloaded and a few fiber breaks near the tip of the hole don't affect the stress distribution much as suggested by Figure 5.74.

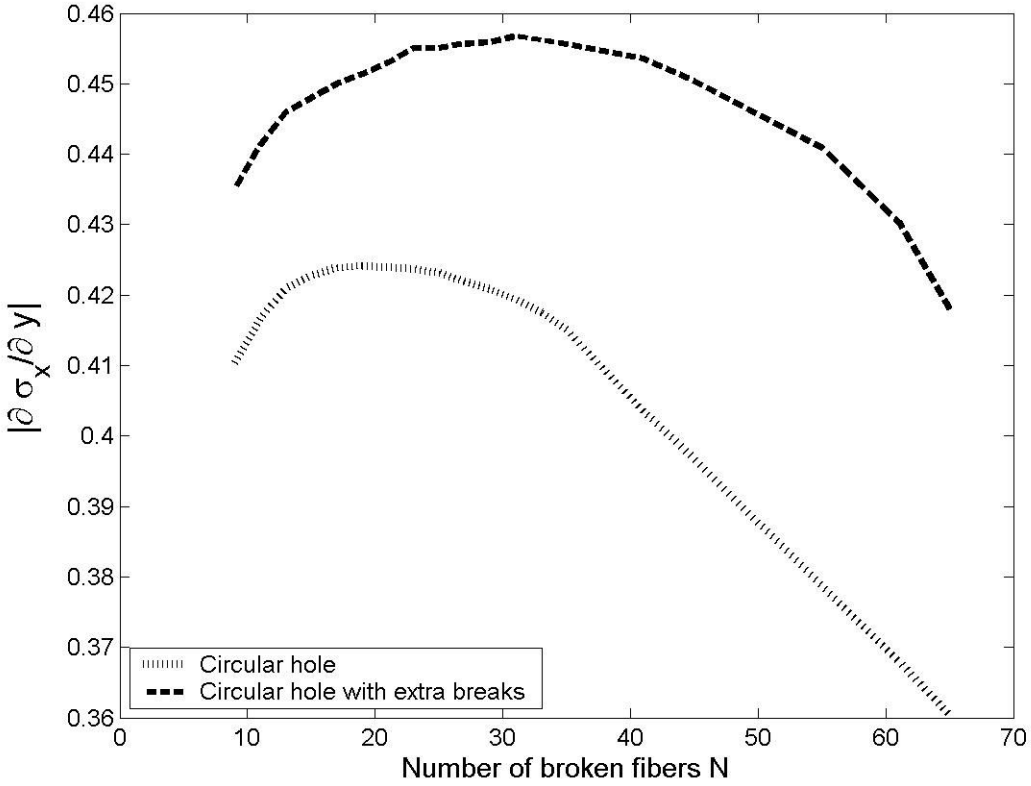

Figure 5. 74. Tensile stress gradient versus transverse dimension of the hole.

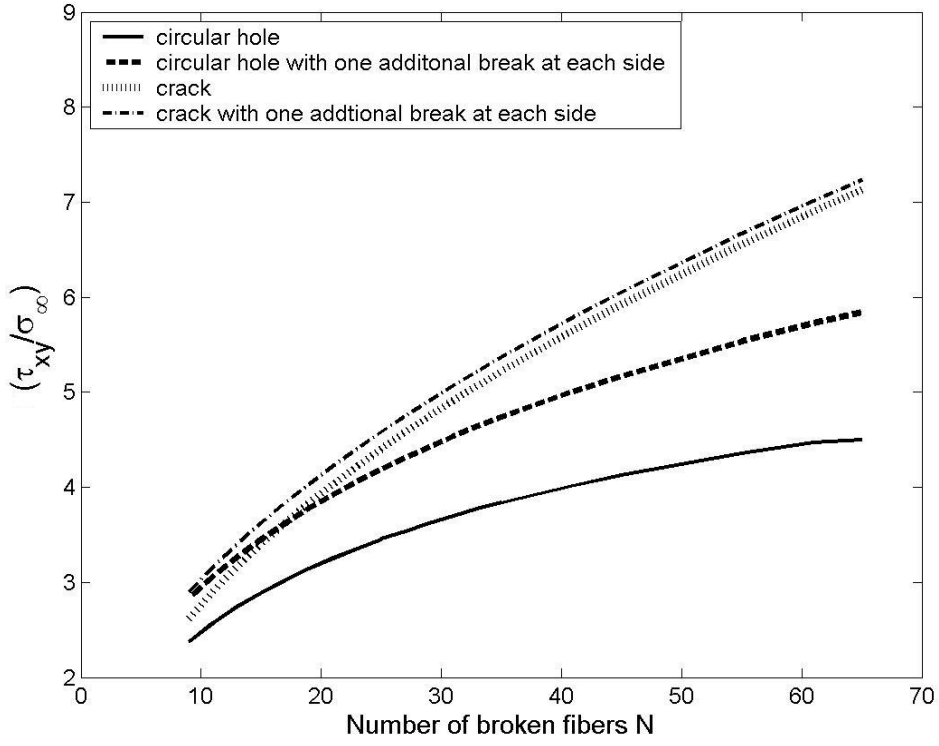

Figure 5. 75. Maximum shear stress in the matrix bay for a circular hole and crack.

Therefore considering the random distribution of the fiber strength, any fiber in the composite plane could fail and even overpower the original stress field. The failure process can be modeled by Monte-Carlo method in the future to predict the fracture stress.

The shear stress distribution shows similar properties as the tensile force on the fiber. Figure 5.75 plots the shear stress against the number of broken fibers for both a crack and a circular hole. We can see that one additional fiber break at each side has less impact for a crack than for a circular hole. The dramatic increase of the shear stress at the hole tip suggests a larger and more severe damaged area. Note that, the maximum shear stress for the crack in both cases is always much higher than for the circular hole, so the crack always has more severe matrix damage zone. This verifies Potter's experimental results (Potter, 1977) that the modification of the stress distribution due to the formation of damage zone eliminates any effect due to the initial shape of the notch. The crack not only has the highest tensile stress concentration, but also the highest shear stress, which causes more damaged matrix bays that reduces the efficiency of stress transfer near the tip of the crack, and thereby reduces the tensile stress on the fibers.

5.3.3 Conclusion

In this section, we studied the stress field near an elliptical hole containing up to seventy broken fibers and drew connection between the elastic analysis and the discrete shear-lag model.

Potter (1977) classified the holes into two categories: "large" and "small" based on the value of the stress gradient at the hole tip. Large holes initiate a sequential failure process and their effect is entirely predictable by orthotropic analysis on the assumption of material homogeneity. On the other hand, small holes are characterized by the fact that the fiber failure doesn't initiate the sequential fiber

failure process but forms stable damage zones that involve matrix yielding or debonding, or interface failure.

However, Potter (1977) still assumes that the material is homogeneous continuum. The fiber reinforced composite material is highly anisotropic and heterogeneous when the dimension of the hole is not much larger than the fiber diameter, which is the case our numerical experiment has been focused on. So in fact, our hole is even smaller than Potter's "small" category, which we call "tiny" hole. The results show that the tiny holes exhibits very different property than the "small" hole and the "big hole".

- The maximum tensile stress concentration for a tiny hole is determined by the elastic constants of the material, the eccentricity, the transverse dimension of the hole and the fraction of the width w^* between the centerline of the first surviving fiber to the hole tip. On the other hand, in elastic analysis, the maximum stress concentration factor is solely decided by the elastic constant and the eccentricity.
- The tensile stress gradient for a tiny hole increases with the transverse dimension of the hole first and then decreases as the size continues to increase. The turning point depends on the elastic constants and the eccentricity of the hole. This is not reflected in Potter's analysis since his small hole is still much larger than the tiny hole.
- The additional fiber breaks at the tiny hole tip add to the stress concentration, increase the stress gradient and eliminate the effect due to initial shape of the hole, but it's expected to have much less impact for a "large" hole.

- The fraction, ϕ, between the centerline of the first surviving fiber and the hole tip plays a fairly importantly role for a tiny hole, but this measure doesn't exist in the continuum elastic analysis.

Overall, elastic analysis and shear-lag analysis achieve good agreement on the stress field near an elliptical hole. For the stress gradient, the modified gradient definition for elastic analysis is needed to make comparison.

6. Stress Field near an Elliptical Hole in an Elastic Matrix with Local Yielding or Debonding

6.1 Introduction of the linear influence superposition

We now consider calculation of the local fiber and matrix stress concentrations due to holes where the material is removed and the matrix material may deform in an elastic-perfectly plastic manner, or debond from the fiber causing constant frictional forces at the interface.

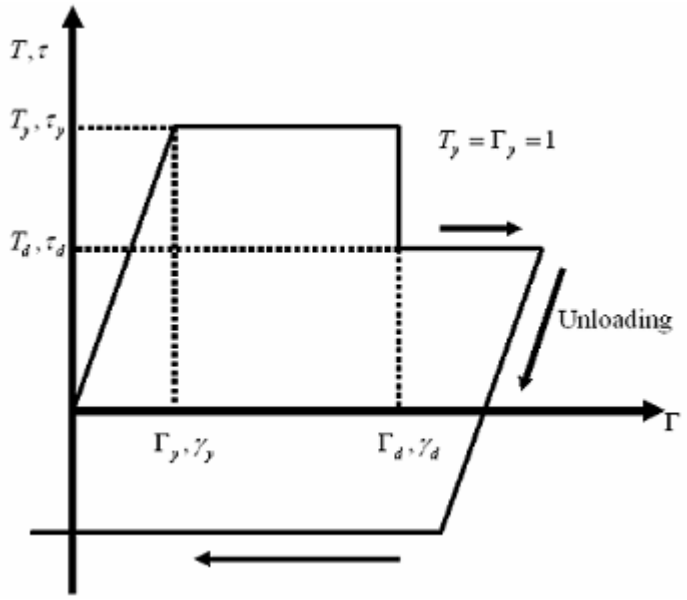

Figure 6. 1. Stress-strain curve of the matrix material in shear.

As shown in Figure 6.1, the shear reponse is elastic for $0<\gamma_n<\gamma_y$, and is perfectly plastic for $\gamma_y<\gamma_n\le\gamma_d$ and debonding occurs for for $\gamma_d\le\gamma_n$ after which a frictional shear traction applies. When the matrix deforms elastically, T_n and Γ_n are equivalent. By equation (2.8) and (2.11) the non- dimensional yield stress and debond criteria become

$$T_y=1,\ \ \Gamma_y=1 \tag{6. 1}$$

and

$$T_d=\tau_d/\tau_y,\quad \Gamma_d=\gamma_d/\gamma_y \tag{6. 2}$$

We let $\Gamma_d = \infty$ for pure yielding case and $T_y = \Gamma_y = \Gamma_d = 1$ for the pure debonding case. Combined with the fiber break problem and the isolated segment problem, the isolated shear couple problem as shown in Figure 6.2, which is the stress distribution due to a counter clockwise point shear force couple, is used to model the stress field near an elliptical hole in an elastic matrix with local yielding or debonding.

The linear influence superposition technique in terms of corrective body forces and couples, as initially developed by Beyerlein and Phoenix (1996), is applied to calculate the stress field. When the lamina is loaded at infinity by an edge force per fiber *P*, the matrix behaves elastically till P reaches P_y. Yielding or debonding of the matrix will spread as we increase *P* further and the normalized shear strain in the entire yielded or debonded matrix will become greater than the normalized critical yield strain or critical yield strain to cause interfacial failure. To compensate for the unwanted elastic behavior driven by the elastic solutions only, a linear shear load couple (a compensating body couple) is applied on the yielded or debonded matrix along its length 2δ, to approximate the effects of the plasticity or debonding.

As in the elastic case, we consider an auxiliary problem where the remote load is zero but the load at the boundary of the holes is $-P$. The normalized shear stress in all damaged matrix elements is T^*, where $T^* = T_y$ for a yielded matrix element and $T^* = T_d$ for a debonded matrix element. The total load on each of the matrix elements is equal to a weighted sum of the loads transmitted by the other damaged matrix, the fiber breaks, the isolated segments and the "self-applied" load.

6.1.2 Load transmission factors

As stated in Chapter 4, since the fiber break problem, the isolated segment problem and the isolated couple problem are all translation invariant, all the load transmission factors are only dependent on the distance between various pairs of fiber breaks, broken segments and damaged matrix elements $\left(n_i - n_j, \xi_i - \xi_j\right)$. We define X_{ki} as the effective force distribution transmitted onto fiber break k at $\left(n_k, \xi_k\right)$ due to a shear load couple $S_v(\zeta)$, $v = 0,\ 1$ imposed across matrix element i at position $\left(n_i, \xi_i + \zeta\right)$, where $-\eta \le \zeta \le \eta$, $i = 1,2,...,\lambda$ and λ is the number of the damaged matrix element. That is,

$$\begin{aligned} \mathrm{X}_{ki}^{(v)} &= \int_{\xi_i - \eta}^{\xi_i + \eta} S_v(\xi - \xi_k) L_{c,n_k - n_i}(\xi_k - \xi)\, d\xi \\ &= \int_{-\eta}^{\eta} S_v(\zeta) L_{c,n_k - n_i}(\xi_k - \xi_i - \zeta)\, d\zeta \end{aligned} \tag{6.3}$$

where

$$\begin{aligned} & L_{c,n_k - n_i}(\xi_k - \xi_i - \zeta) \\ &= -\operatorname{sgn}(\xi_k - \xi_i - \zeta)\frac{1}{2\pi}\int_0^{\pi} \left\{\cos\left[(n_k - n_i)\theta\right] - \cos\left[(n_k - n_i - 1)\theta\right]\right\} \\ &\qquad \times \exp -2\left|\xi_k - \xi_i - \zeta\right| \sin\left(\frac{\theta}{2}\right) d\theta \end{aligned}$$

and

$$\begin{aligned} S_0(\zeta) &= 1, \quad -\eta \le \zeta \le \eta \\ S_1(\zeta) &= \zeta, \quad -\eta \le \zeta \le \eta \end{aligned}$$

More specifically, $\mathrm{X}_{ki}^{(0)}$ is the load transmitted to the fiber at position $\left(n_k, \xi_k\right)$ due to a uniform shear couple $S_0(\xi - \xi_i) = S_0(\zeta)$ and $\mathrm{X}_{ki}^{(0)}$ is the load transmission factor at position $\left(n_k, \xi_k\right)$ due to a linear shear couple $S_1(\xi - \xi_i) = S_1(\zeta)$.

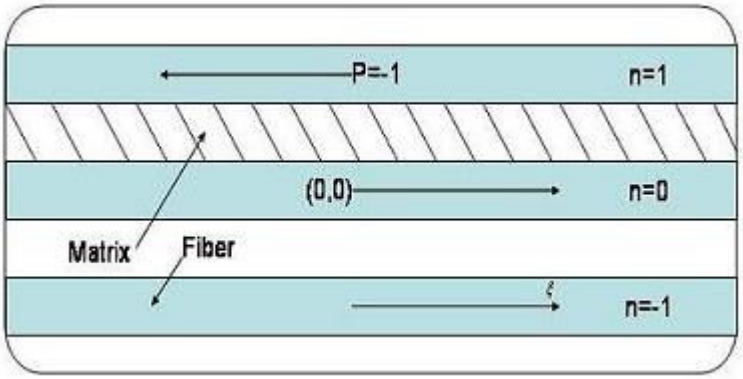

Figure 6. 2. Isolated shear couple problem.

Next, we define Π_{ki} as the effective force distribution transmitted onto isolated segment *k* centered at (n_k, ξ_k) due to a shear load couple $S_\nu(\xi)$, $\nu = 0,1$ imposed across matrix element *i* centered at (n_i, ξ_i). In our model, Π_{ki} is a first-order polynomial approximation fro the induced tension per unit length across the broken segment at $(n_k, \xi_k + \zeta)$, where ζ is the local axial coordinate about the center of a broken segment and $-\delta \le \zeta \le \delta$. Thus Π_{ki} has the following form:

$$\Pi^{(\nu)}{}_{ki}(\zeta) = \Pi^{(0,\nu)}{}_{ki} + \Pi^{(1,\nu)}{}_{ki}\zeta \tag{6. 4}$$

where

$$\Pi^{(0,\nu)}{}_{ki} = \int_{-\delta}^{\delta} S_\nu(\zeta) L_{c,n_k-n_i}(\xi_k - \xi_i - \zeta)\, d\zeta$$

and

$$\Pi^{(0,\nu)}{}_{ki} = \int_{-\delta}^{\delta} S_\nu(\zeta) \left.\frac{dL_{c,n_k-n_i}(\xi - \xi_i - \zeta)}{d\xi}\right|_{\xi=\xi_k} d\zeta$$

Lastly, we define $\mathrm{N}^{(v)}_{lk}$ as the effective shear load distribution across matrix element *l* at (n_l, ξ_l) due to shear distribution couple, $S_v(\zeta)$, $v = 0,1$ imposed across matrix element k centered at (n_k, ξ_k). Similar to $\Psi^{(v)}_{lk}$, we assume

$$\mathrm{N}^{(v)}_{lk}(\zeta) = \mathrm{N}^{(0,v)}_{lk} + \mathrm{N}^{(1,v)}_{lk}\zeta \tag{6. 5}$$

for $-\eta \le \zeta \le \eta$, $k = 1,2,...,\lambda$ and $v = 0,1$. Using a Taylor series, we get

$$\mathrm{N}_{lk}^{(0,v)} = \int_{-\eta}^{\eta} S_v(\zeta)\Gamma_{c,n_k-n_i}(\xi_k - \xi_i - \zeta)\,d\zeta + 1_{[l=k,v=0]}$$

and

$$\mathrm{N}_{lk}^{(1)} = \left.\frac{d\,\Gamma_{b,n_k-n_i}(\xi - \xi_i)}{d\,\xi}\right|_{\xi=\xi_k} + 1_{[l=k,v=0]}$$

where

$$1_{[l=k,v=m]} = \begin{cases} 1, & l = k,\ v = m \\ 0, & \text{otherwise} \end{cases}$$

The indicator function ensures that for a damaged matrix element, a given shear couple distribution is "self-transmitted" along its own length.

We can now solve for the weighting factors of all the fiber breaks and damaged matrix elements using the following matrix linear system:

$$\begin{bmatrix} \Lambda & \Phi^{(0)} & \Phi^{(1)} & \Phi^{(2)} & X^{(0)} & X^{(1)} \\ \Omega^{(0)} & \Psi^{(0,0)} & \Psi^{(0,1)} & \Psi^{(0,2)} & \Pi^{(0,0)} & \Pi^{(0,1)} \\ \Omega^{(1)} & \Psi^{(1,0)} & \Psi^{(1,1)} & \Psi^{(1,2)} & \Pi^{(1,0)} & \Pi^{(1,1)} \\ \Omega^{(2)} & \Psi^{(2,0)} & \Psi^{(2,1)} & \Psi^{(2,2)} & \Pi^{(2,0)} & \Pi^{(2,1)} \\ \Theta^{(0)} & \mathrm{H}^{(0,1)} & \mathrm{H}^{(0,1)} & \mathrm{H}^{(0,2)} & \mathrm{N}^{(0,0)} & \mathrm{N}^{(0,1)} \\ \Theta^{(1)} & \mathrm{H}^{(1,1)} & \mathrm{H}^{(1,1)} & \mathrm{H}^{(1,2)} & \mathrm{N}^{(1,0)} & \mathrm{N}^{(1,1)} \end{bmatrix} \begin{bmatrix} K_b \\ K_c^{(0)} \\ K_c^{(1)} \\ K_c^{(2)} \\ K_m^{(0)} \\ K_m^{(1)} \end{bmatrix} = \begin{bmatrix} -P_b \\ -P_I * \\ P_1 * \\ P_2 * \\ T_0 * \\ T_1 * \end{bmatrix}$$

In this matrix equation, $-P_b$ is N'-dimensional vectors, $-P_c$, P_1 and P_2 are both s-dimensional vectors and $T_0 *$ and $T_1 *$ are t-dimensional vectors. The $(N' + s)$-dimensional vector $[-P_b, -P_c]$ has components $-P_i = -P$ for $i = 1,2,...,N' + s$ and the s-dimensional vectors P_1 and P_2 have components $P_{k,1} = P_{k,2} = 0$ for $k = 1,2...,s$. For the matrix, the t-dimensional vector $T_0 *$ has components $T_{k,0} * = \pm T_y$ or $\pm T_d$ for $k = 1,2,...,\lambda$ depending on whether the corresponding matrix is yielded or debonded. Finally, $T_1 *$ has components $T_0 * = 0$ for $k = 1,2,...,t$.

We only calculate the stress concentrations in the local fibers and matrix regions near the hole tip and investigate the effect of matrix yielding and debonding. We assume that all the fibers have sufficiently high strength such that no fiber breaks occur. The stress applied to the composite is taken to be the stress applied to the fiber. We define $P_{y,N}$ be the applied load which initiates the damage in a composite lamina with an elliptical hole containing N broken fibers.

Two kinds of damage will be considered. In the first case, the matrix elements are elastic-perfectly plastic and perfectly bonded to the fiber. In the second case, once the shear strain reaches the debond threshold, the matrix will debond from the fiber and sliding occurs s under a constant interfacial traction, T_d.

We start with a simple example of one broken fiber and then move to the elliptical holes. In all the following examples, the applied load is non-decreasing. In another words, none of the damaged elements will unload, and once added, they will remain damaged. We will take advantage of the configuration's double symmetry for the following simulation: the stress field is only calculated in a quarter plane.

6.3 Case 1: One broken fiber

We use the computational scheme from Beyerlein, Phoenix and Sastry (1996). For the hole consisting of one broken fiber, $N=1$, in an infinite lamina with tensile force *P*, the composite will deform elastically till the load reaches $P_{y,1}$. When $P \geq P_{y,1}$, the matrix will begin to yield or debond around the fiber break ends in all four quadrants. Most likely, the "virtual elastic" strain will exceed the threshold strain Γ_y in many matrix elements, but in our simulation, we consider incrementally the most heavily overloaded group at a time and achieve the equilibrium for the composite plane accordingly. If the adjacent matrix elements are not overloaded, then the incremental process stops here and the stress field are

calculated accordingly. However, if the next set of four matrix elements' shear strain is greater then the threshold, the above process is repeated incrementally till the shear strain Γ_n in the adjacent matrix elements falls below the threshold. We Define v_i as the i^{th} set of four damaged matrix elements added when $P \geq P_i > P_{y,1}$ and P_i produces stability with v_i.

.

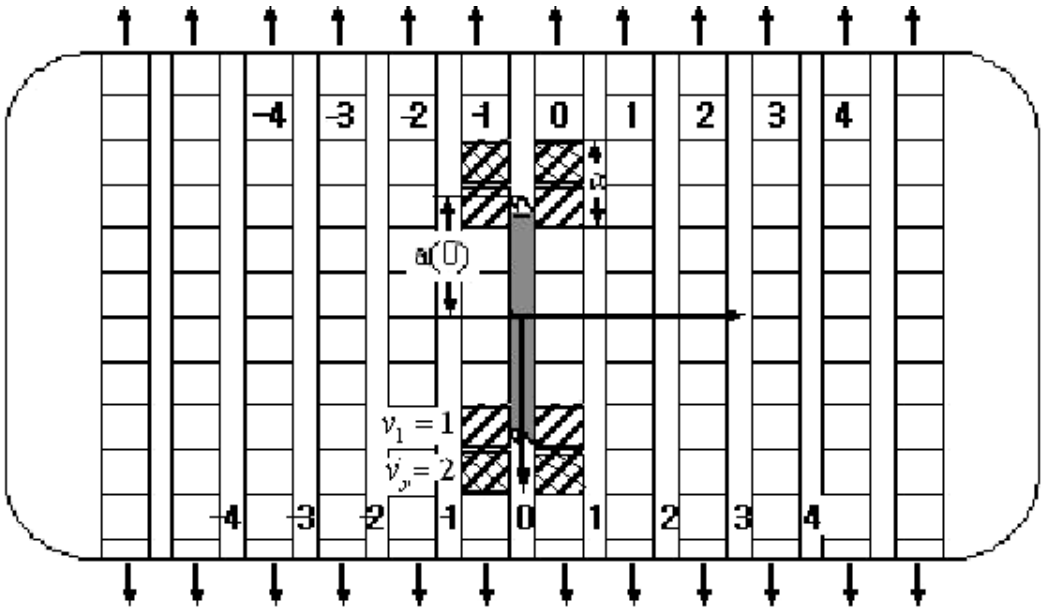

Figure 6. 3. Two dimensional infinite lamina with *N*=1 broken fiber and debond zone $0 \leq \xi \leq \alpha$.

We let v_y be the maximum value of v, in other words, v_y defines the boundary of the elastic/inelastic zone in a quarter plane of the composite for a given load P. Thus v_y satisfies the following condition

$$\Gamma_n\left(\left(2v_y+1\right)\delta\right) < \Gamma_y = 1 < \Gamma_n\left(\left(2v_y-1\right)\delta\right) \tag{6. 6}$$

where $\Gamma_n\left(\left(2v_y+1\right)\delta\right)$ is the normalized shear strain at the center of the elastic element adjacent to the damage zone, and $\Gamma_n\left(\left(2v_y-1\right)\delta\right)$ is the corresponding shear strain at the center of the last damaged matrix element inside the damage zone.

In another words, we determine the damage region by monitoring the normalized shear strain $\Gamma_n(\xi)$ at the center of the matrix elements in the vicinity of the hole. Thus from the definition of v_y, there are $\lambda = 4v_y$ damaged elements in total. Figure 6.3 shows the progression of the damage zone, which has two groups of damaged elements. As explained above, $v_y = 2$ in this case and there are eight damaged matrix elements.

The simplest case of "an isolated fiber break" with remote load $P = 1.5$, is studied first. Figure 6.4 plots the normalized shear distribution along the damaged matrix which is purely yielded or purely debonded with different sliding friction at the interface. The figure shows that the damage zone becomes larger and the shear stress drops faster as the sliding friction decreases. Outside the damage region, the normalized shear stress is below the normalized yield stress in shear and quickly decays to zero. Lower interface sliding friction leads to faster decay of the shear load.

Figure 6.5 plots the tensile stress concentration factor along the first surviving fiber accordingly. The figure shows that the debonding and yielding does reduce the stress concentration factors for the first surviving fiber. The maximum stress concentration is not necessarily at the crack plane $\xi = 0$. For very low friction, the maximum stress is at the boundary of the elastic and inelastic zone $\xi = (2v-1)\eta$. The ineffective, overloaded fiber lengths increase due to the increase in matrix damage.

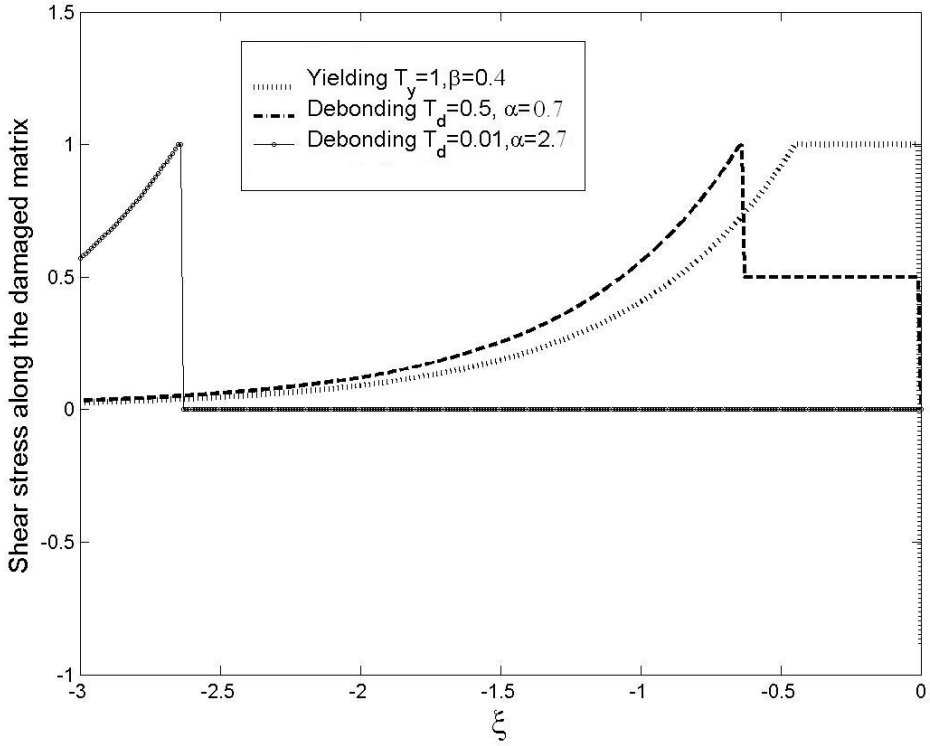

Figure 6. 4. Shear stress distribution along the damaged matrix near an isolated fiber break.

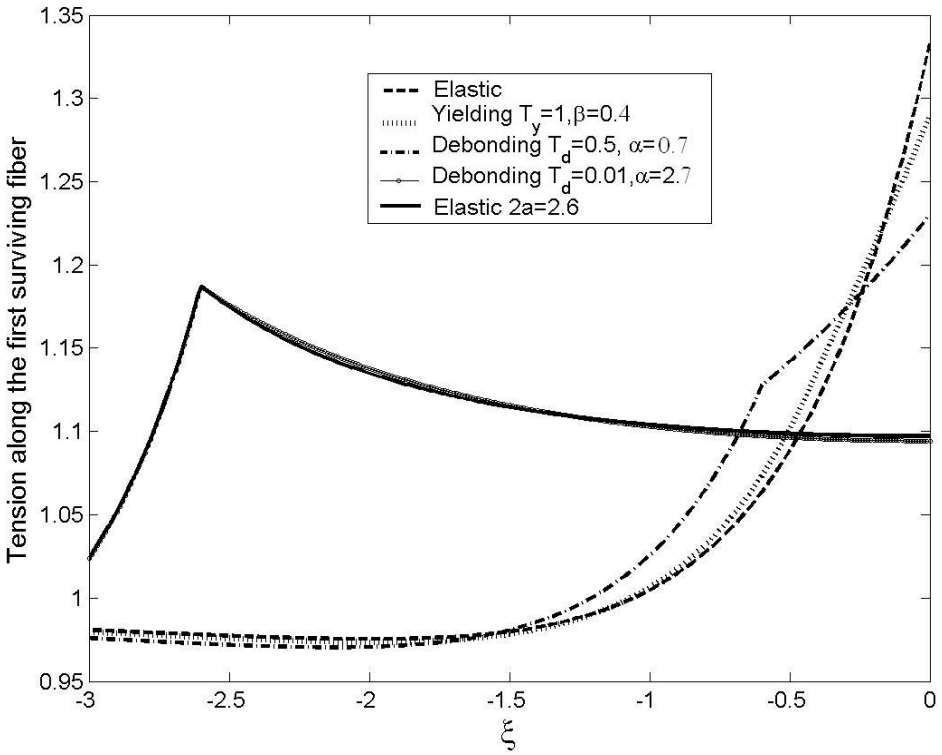

Figure 6. 5. Tension along the first surviving fiber near an isolated fiber break.

In the extreme case of pure debonding there is no sliding friction at the debonded interface of the fiber and matrix bay, suggesting that the damaged matrix in fact also disables the fiber element between the damaged matrix bays. In another words, the fiber element between the damaged matrix elements doesn't support any tension. Therefore, it is equivalent to the elastic case where the fiber element is removed. Figure 6.5 also compares the stress distribution between the elastic case where the fiber element at $-2.6 \le \xi \le 2.6$ is removed and the pure debonding case where matrix bay at $-2.6 \le \xi \le 2.6$ is damaged and $T_d = 0.01$. We can see that both cases have the same stress distribution and suggest the equivalence of both solutions.

Van Dyke and Hedgepeth (1969) obtained the analytical results for a single fiber break in an elastic matrix with local debonding and $\tau = 0.01$. For the maximum load ratio $P/P_y = 1.073$, their threshold debond length was approximately 2. Our numerical experiment shows excellent agreement with this solution.

We can also increase the damage region by increasing the applied load at infinity. Beyerlein and Phoenix (1996) did a very thorough study from this angle with the quadratic influence superposition (QIS) technique. They found that for all crack lengths N and rangees of P, the damage zone increases linearly with the applied load, which agrees with the simpler model of Beyerlein et. al. (1995) and the other shear lag models (Hedgepeth and Van Dyke, 1967; Zweben, 1974). They also found that larger cracks have larger damage regions due to a higher stress concentrations at the crack tip and the ratio of the plastic growth rate to debond growth rate is approximately the ratio of the debonding frictional stress to the yield stress.

Next, we investigate the matrix yielding and debonding near a single broken fiber with gap length $2a$. Figure 6.6 shows the normalized shear stress along the damaged matrix bay for a single broken fiber. Similar to the single fiber break case, pure debonding causes a larger damage region than pure yielding, due to less stress transfer at the interface. Figure 6.7 plots the normalized tensile stress along the first surviving fiber for yielding and debonding, both of which reduce the stress concentration necessarily. As expected, debonding has higher stress reduction for the same remote load.

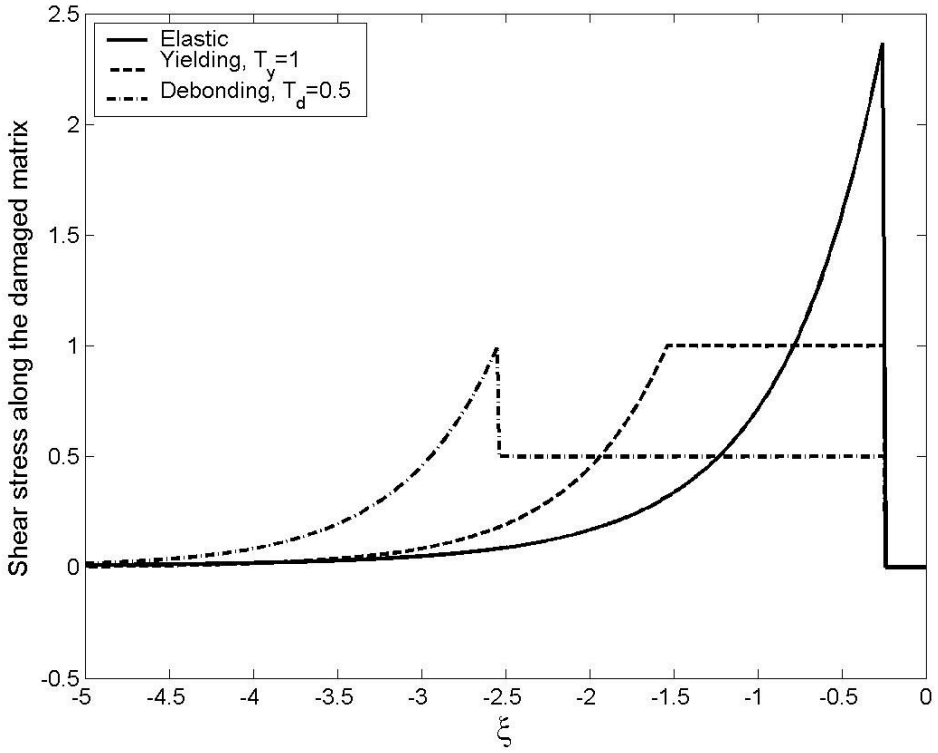

Figure 6. 6. Shear stress along the damaged matrix near a broken fiber
$P = 3.15, a = 0.5$

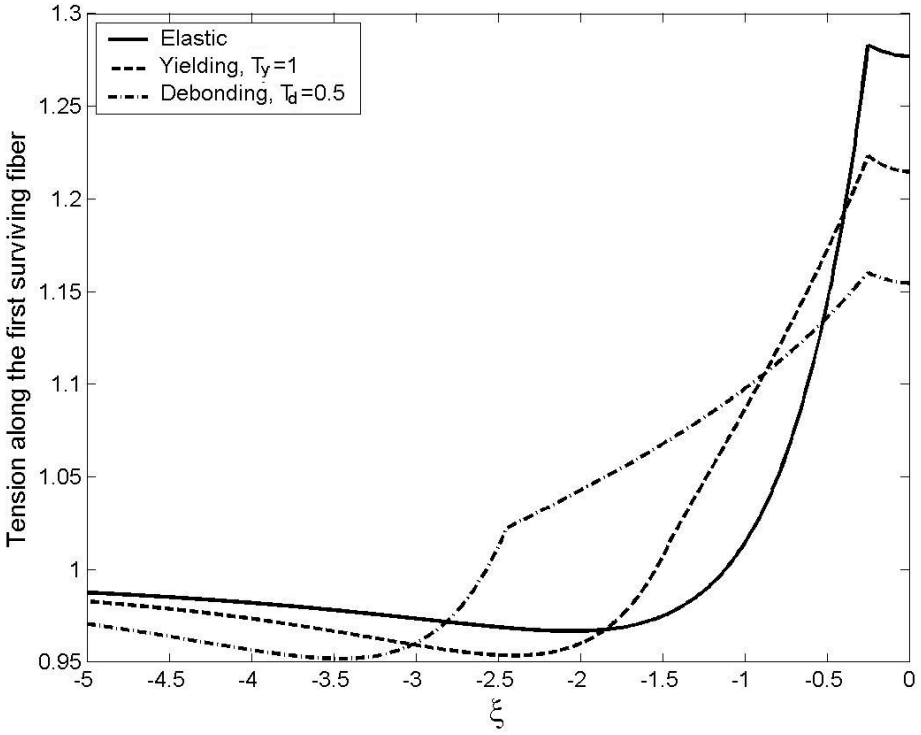

Figure 6. 7. Tension along the first surviving fiber near a broken fiber, $P = 3.15, 2a = 1$

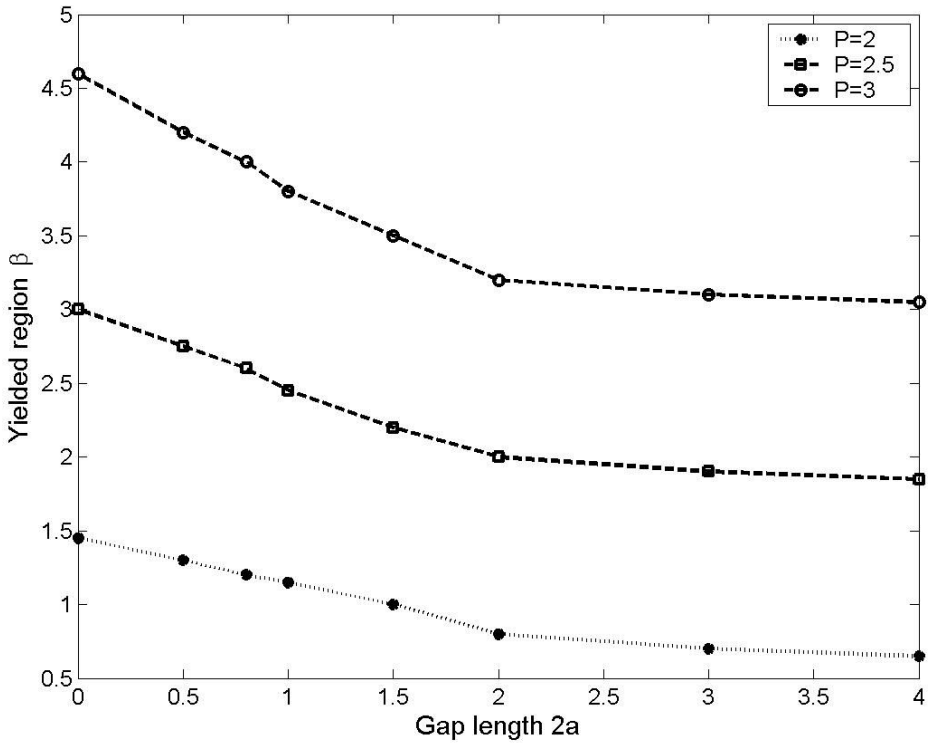

Figure 6. 8. Damage region versus different gap length

Figure 6.8 plots the extent of the yielded region for a broken fiber with gap length $2a$ and different load. We can see that the damage region decreases linearly with the gap length of the broken fiber and eventually converges to a stable amount. The remote load increases the damage region approximately linearly as seen from the graph, which is also observed for a crack in Beylerlein and Phoenix (1996).

6.4 Case 2: elliptical hole

Since the crack case was well studied in Beyerlein and Phoenix (1996), we will focus on holes where the material is removed and check how the shape of the hole influences the yielding or debonding of the matrix bays. Figure 6.9 shows an elliptical hole with the matrix bay at the hole tip either yielded or debonded in a two-dimensional composite lamina.

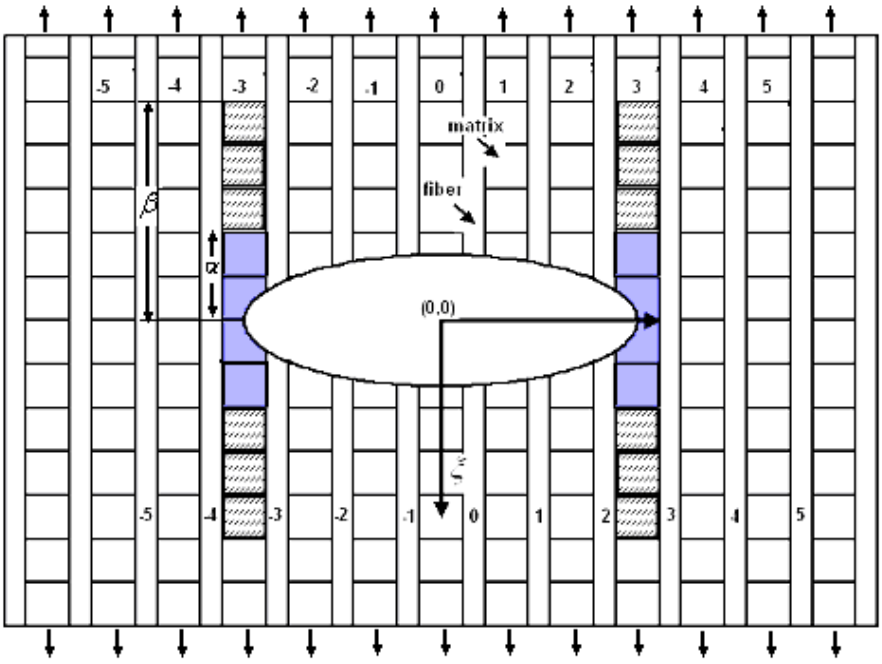

Figure 6. 9 Two dimensional infinite lamina with a central hole consisting of N broken fibers and debond zone $0 \le \xi \le \alpha$ and yield zone $\alpha \le \xi \le \beta$

As mentioned in Chapter 5, we only let the matrix bay between the last broken fiber and the first surviving fiber yield or debond. For convenience, we let the elliptical hole end with a fiber break, so the maximum stress concentration is always at the crack plane $\xi = 0$.

Similar to the case above when $N = 1$, the calculation is elastic in the first increment and if the shear strain $\Gamma_n(\xi)$ at the center of each of the four matrix elements surrounding the crack tip is above the threshold $\Gamma_n(\xi) = 1$, the entire group is considered damaged and yielding or debonding effects will be added to these matrix elements. After this, the virtual load on the matrix and fiber is calculated as the weighted sums of the influences of all the fiber breaks, segments and damaged matrix elements to that point. If equation (6.6) for the shear strain is satisfied, the simulation stops there. Otherwise, the damage zone is incremented and the whole procedure repeated till the equilibrium condition is satisfied.

Similarly, $v_{y,N}$ will be used to indicate the extent of the damage zone (i.e. there are $4 \times v_{y,N}$ damaged matrix elements in total) that depends on both the applied load P and shape of the hole.

6.4.1 Stress distribution near a crack

We first plot the stress field near a crack with size $N = 9$. Figures 6.10 and 6.11 show the tension along the first surviving fiber and the shear stress along the yielded ($T_y = 1$) matrix bays near a crack containing 9 broken fibers. Again, yielding significantly decreases the stress concentration on the surviving fiber ahead of the crack tip, and the overloaded fiber lengths increase due to an increase of the matrix damage. In order to compensate for the excess displacement of the overload, the fiber concentration factor drops slightly below the remote load before rising to recover its load. Furthermore, the matrix yielding also decreases the load recovery

rate in the fiber direction. Outside the damage region, the shear stress quickly decays to zero at a faster rate for an isolated fiber break than for a crack with $N = 9$.

Figure 6.12 shows the maximum stress concentration factor along the crack plane $\xi = 0$ immmediately ahead of the crack tip. As shown, the damage zone effectively reduces the stress concentration decay rate away from the tip. Thus, the load recovery rate is also reduced by the damage region in both direction. Beyerlein and Phoenix (1996) also observed the same effect of matrix damage on the stress decay. They pointed out that as a result, only the frist few surviving fibers experience a reduction in the stress concentration and the fibers further away would be more overloaded than the correponding elastic case.

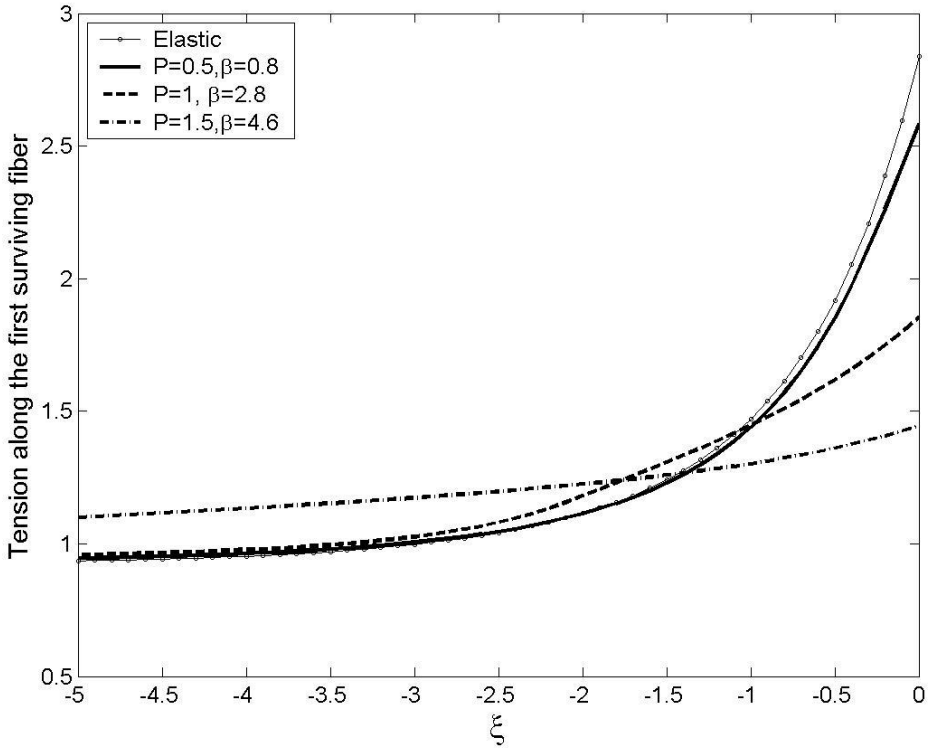

Figure 6. 10. Tension along the first surviving fiber near a crack, $N = 9$.

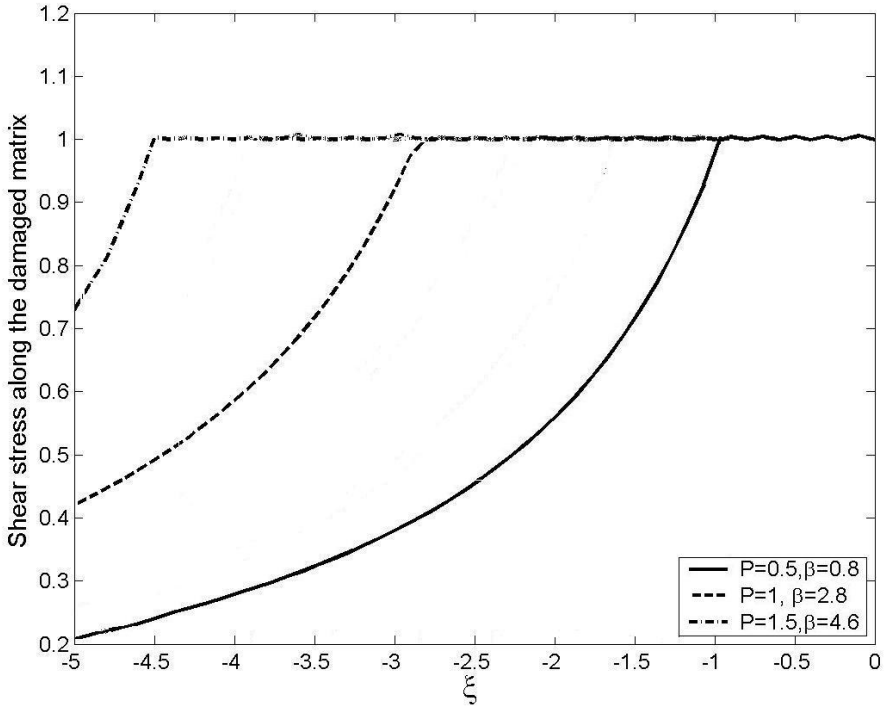

Figure 6. 11. Shear stress along the damaged matrix near a crack, $N = 9$.

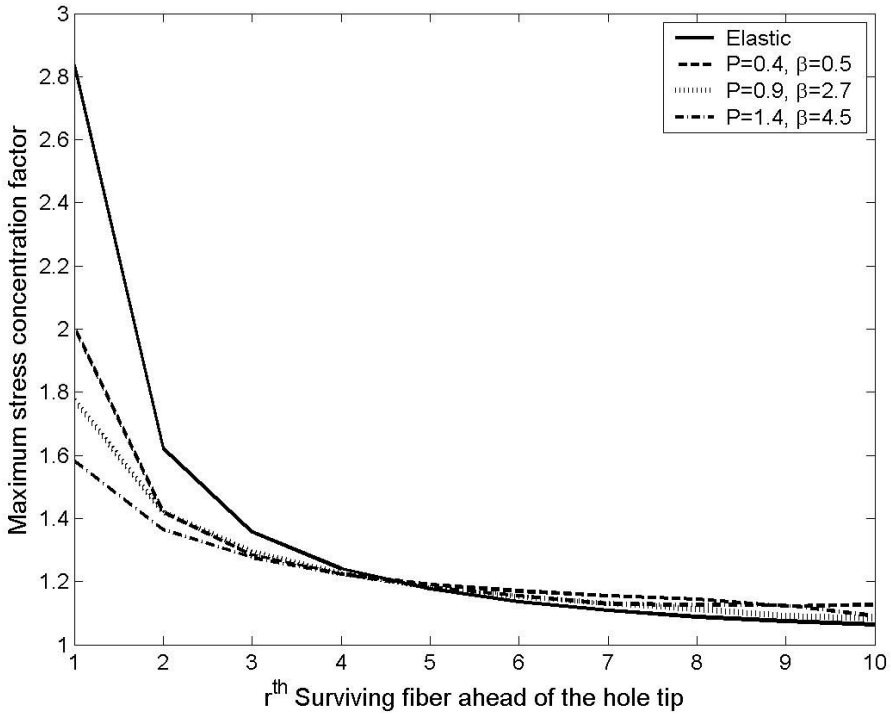

Figure 6. 12. Maximum stress concentration factor along the crack plane near a crack, $N = 9$.

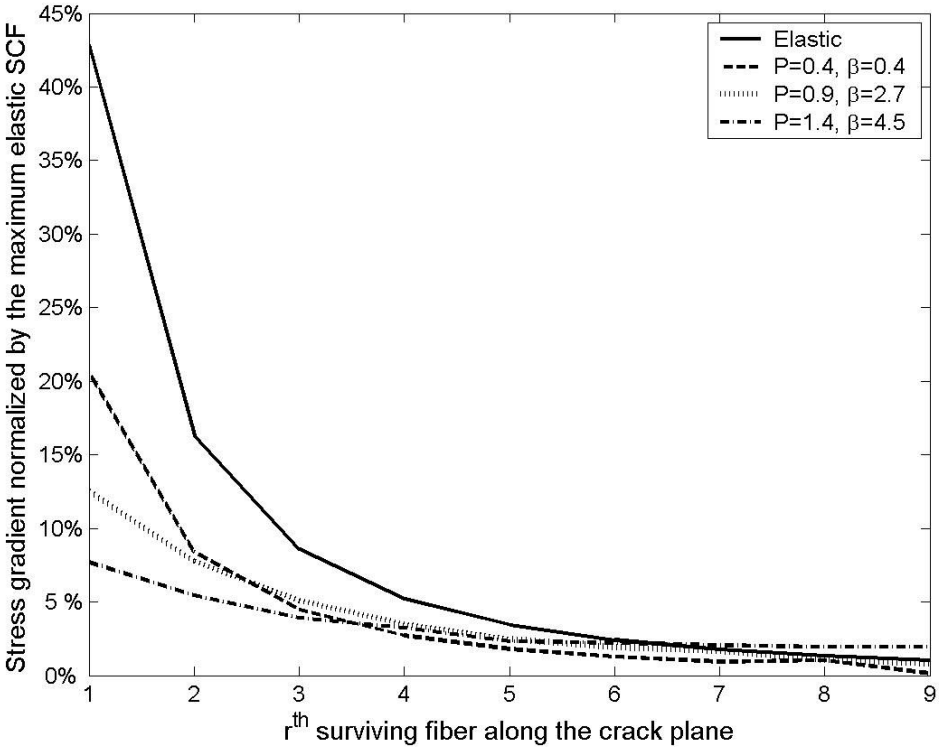

Figure 6. 13. Stress gradient normalized by the maximum elastic SCF near a crack.

Figure 6.13 plots the stress gradient normalized by the maximum stress concentration factor of a comparable elastic crack ahead of the crack tip for $N = 9$. The figure shows that larger matrix damage leads to a slower load decay rate near the crack tip but a slightly larger rate several fibers away from the tip. Overall, the stress gradient has been reduced greatly by the yielded matrix elements. This agrees with the conclusion in Beyerlein and Phoenix (1996) that only a few surviving fibers have their load reduced and the subadjacent fibers are more overloaded with yielding.

6.4.2 Stress distribution near an elliptical hole

Figure 6.14 compares the stress concentration factor near a circular hole consisting of 9 broken fibers along first surviving fiber between the elastic case and yielding cases for $\beta = 0.3, 2, 4.5$. In both cases, the maximum stress concentration

is at the crack plane, $\xi = 0$. The figure shows that matrix yielding significantly decrease the stress concentration factor immediately ahead of the hole tip and the overstressed fiber lengths increase due to an increase of matrix damage.

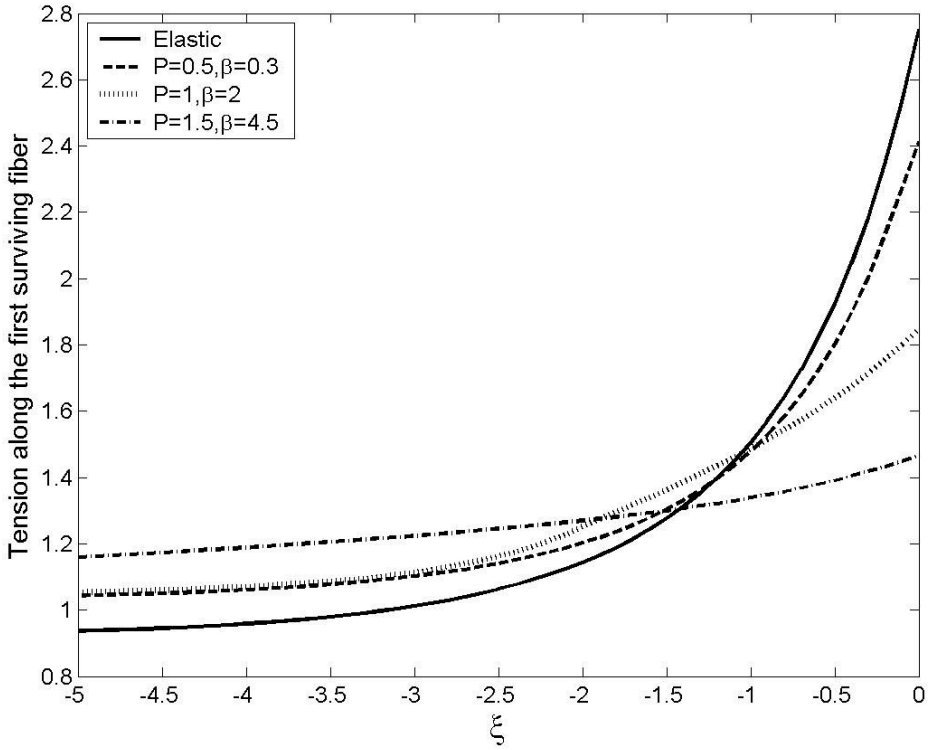

Figure 6. 14. Tension along the first surviving fiber near a circular hole, $N = 9$.

Figure 6.15 compares the shear stress distribution along the axis of the first surviving fiber between the elastic case and yielding cases for $\beta = 0.3,2,4.5$. The shear stress drops down at a faster rate for a circular hole than for a crack.

The effect of eccentricity of the elliptical hole on the maximum stress concentration factor with matrix yielding is shown in Figures 6.16 and 6.17. With the same remote load and transverse dimension, the damage region near the hole decreases due to an increase of the eccentricity. However, the impact of the eccentricity is less obvious as the load increases.

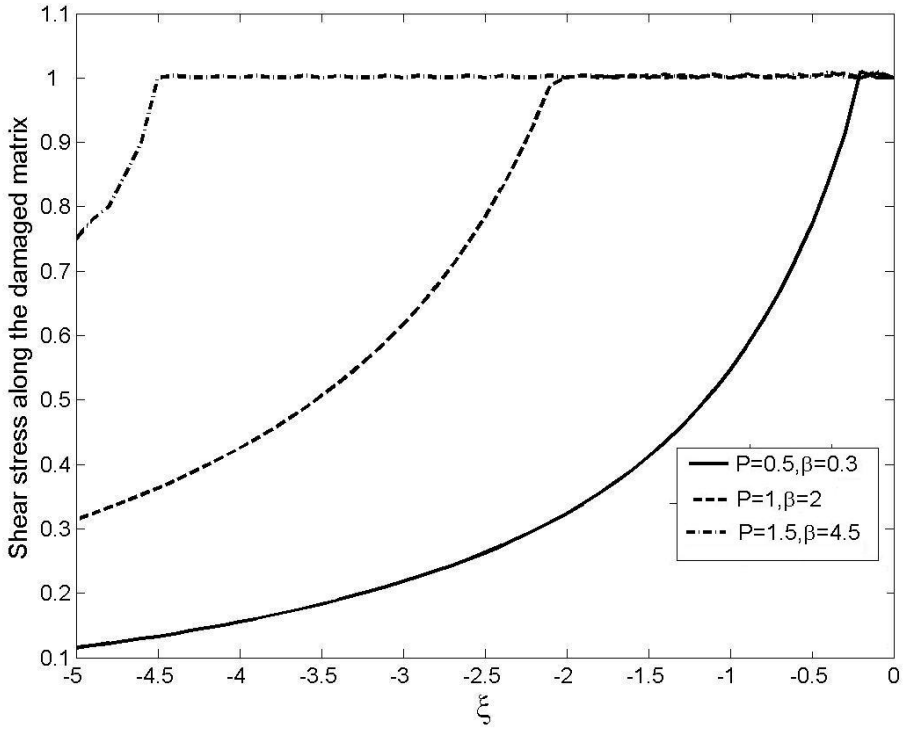

Figure 6. 15. Shear stress profile along yielded matrix near a circular hole, $N = 9$.

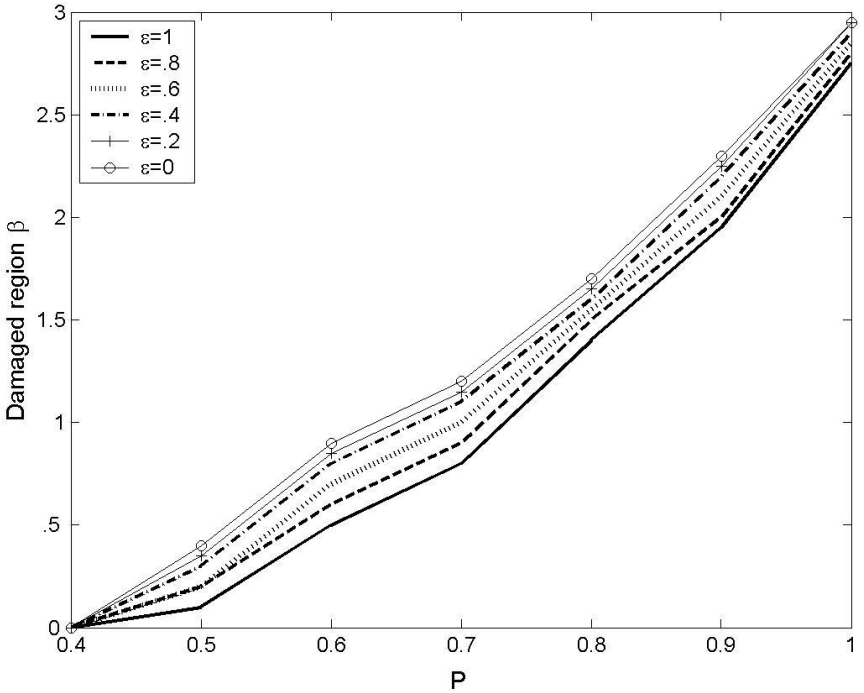

Figure 6. 16. Yielded region near an elliptical hole, $T_y = 1$, $N = 9$.

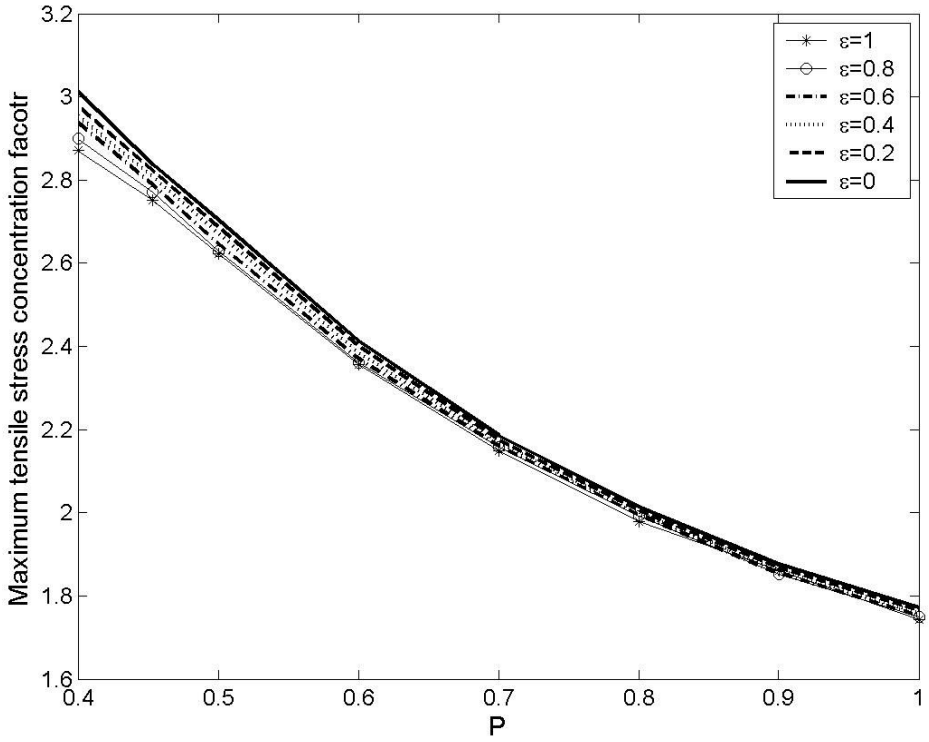

Figure 6. 17. Maximum stress concentration factor with local yielding $T_y = 1$, $N = 9$ near an elliptical hole

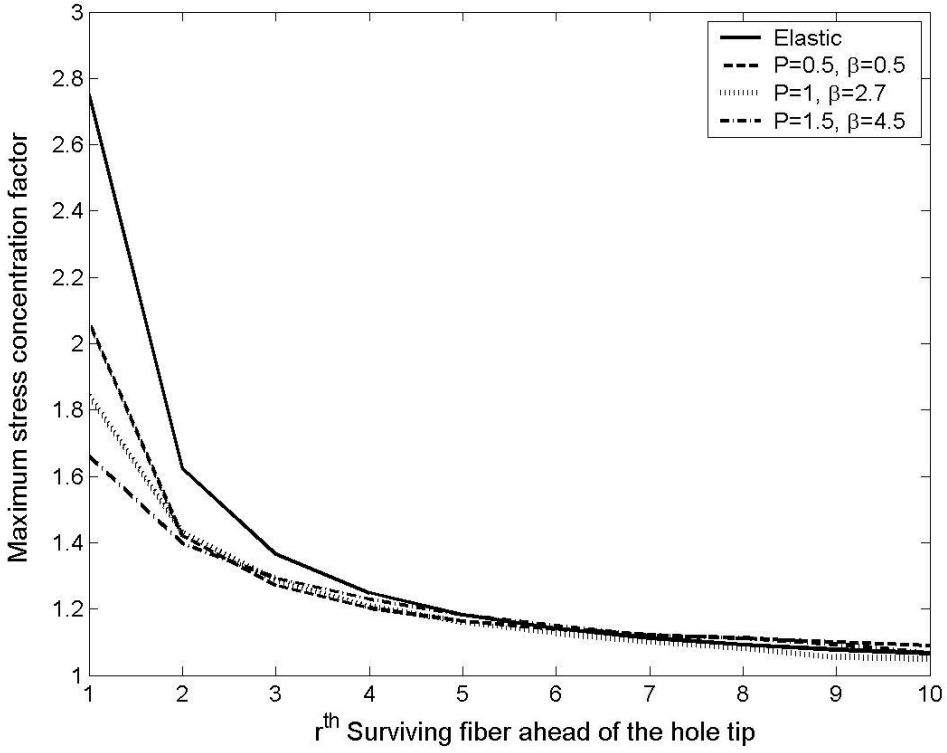

Figure 6. 18. Maximum stress concentration along the crack plane near a circular hole, $T_y = 1$, $N = 9$.

From the figure, we can see that the damage region approximately grows linearly with the remote load, which is also expected for pure debonding case. The slope of the yielded region versus the remote load is expected to increase with the transverse dimension of the hole since more broken fibers lead to a higher stress concentration factor.

Figure 6.17 shows that more matrix damage leads to a more significant reduction in the stress concentration ahead of the crack. At the onset of yielding, the maximum stress concentration factor decreases rapidly and the impact of the eccentricity is very obvious, but further increases in the remote load result in a slower decline and diminishes the influence of the eccentricity.

Figure 6.18 plots the maximum stress concentration factor along the crack plane near a circular hole. The stress concentration is reduced by the matrix damage significantly. Compared to the crack, the matrix damage decreases the tensile stress concentration slightly less for a circular hole.

Figure 6.19 shows the stress gradient along a crack plane of comparable dimensions. Although the circular hole has less stress gradient than a crack for the elastic case with no yielding, with comparable matrix damage the circular hole turns out to have the larger gradient. In other words, the matrix damage reduces the load decay rate and the stress concentration near the crack more than to the circular hole.

Considering the crack has a bigger stress concentration and higher stress gradient in elastic case, the difference of the stress field near a hole and a crack is smeared by matrix yielding. This agrees with the experimental results that the matrix damage blunts the hole and eliminate the effect of the original hole shape.

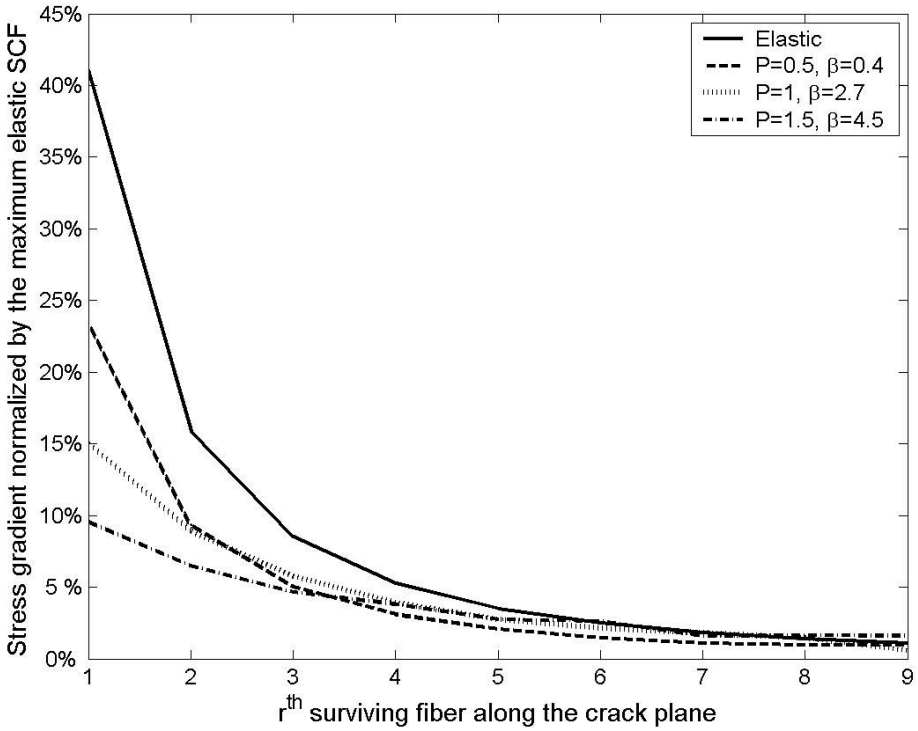

Figure 6. 19. Stress gradient along the crack plane at a circular hole $T_y = 1,\ N = 9$.

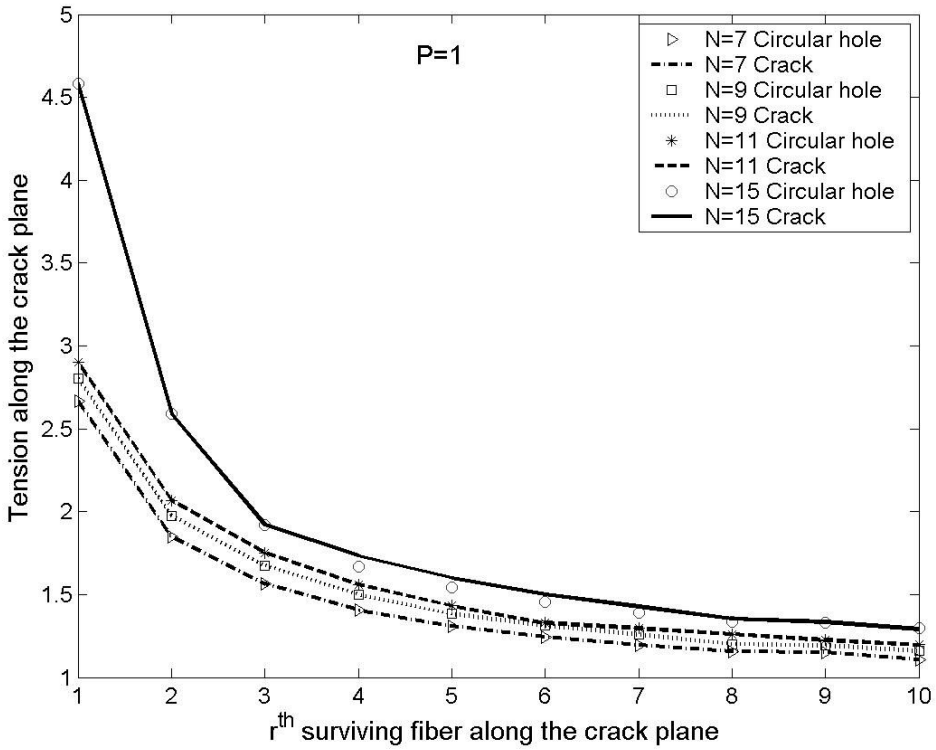

Figure 6. 20. Tensile stress concentration factor along the crack plane for holes with one additional fiber break at the tip.

6.4.3 Stress distribution with crack propagation

Figure 6.20 plots the stress distribution along the crack plane $\xi = 0$ when there is one additional fiber break at each side of a hole tip and crack tip, respectively. The figure shows that the stress concentration factors are almost identical for a circular hole and a crack with local matrix yielding and a large load at infinity. This is very strong evidence that yielding or debonding eliminates the effect of the initial size of the hole. So the size of the hole is much more important than the shape of the hole for the fracture behavior of the composite lamina.

6.5 Conclusion

In this chapter we studied the impact of matrix yielding or debonding on the stress field near a single broken fiber and an elliptical hole. The simulation shows that either yielding or debonding of the matrix reduces the stress concentration and the load recovery rate in both longitudinal and transverse directions. Larger damage region causes larger reductions accordingly. For the same remote load, the damage region decreases as the longitudinal dimension increases but eventually converges to a stable size.

Most importantly, the numerical experiments show that the modification of the stress field due to the formation of yielding or debonding zones modifies the stress field near a hole and eliminates the effect of the initial shape of the hole. When there is an additional fiber break at the tip of the hole, the circular hole and the crack lead to the same stress field with matrix yielded under sufficient remote load. On the other hand, the size has a strong influence on the fracture strength of the composite plane, which is clearly observed both in our numerical model and experimental results (Potter, 1977).

7. Discussion and Conclusions

We have developed a computationally efficient numerical technique to model the stress field near a hole where the material is removed or inactivated in a two-dimensional fibrous composite lamina based on shear-lag analysis. The model is an extension of the break influence superposition (BIS) technique and the quadratic influence superposition (QIS) technique, and also using elements based on distributed dislocation theory. This computational technique is capable of modeling the stress field near various holes of different shapes, such as an elliptical hole, wedge, and square hole, and accounting for various forms of damage, such as newly introduced fiber breaks, matrix yielding, and fiber-matrix debonding. Unlike the other computational approaches, we only need to discretize the damaged area, such as the hole or the damaged matrix, and thereby the computational load is only related to the extent of the damage area.

In the examples, we have illustrated its use on a single broken fiber, a diamond shaped wedge and an elliptical hole in an elastic composite lamina. The shear-lag solution shows excellent agreement with the results from the elastic solution (Williams et al. 1953; Bishop, 1972; Potter, 1977). The longitudinal dimension of the hole reduces the stress concentration ahead of the crack and the stress gradient both longitudinally and transversely.

For the wedge, we found that the maximum stress concentration increases with the size of the hole with approximately the same rate as a crack when scaled the opening angle is $\theta \le \pi/2$. Based on the observation of the shear stress distribution, we introduced an empirical power-law formula to compute the maximum tensile stress concentration factor ahead of the wedge tip.

For the elliptical hole, we have studied the size effect of the hole and related the stress gradient near the hole with the fracture behavior of the composite. We

found that the maximum stress concentration factor of a circular hole is determined only by the material elastic constants for large holes containing at least a few hundred broken fibers. For smaller holes, the stress maxima are increased by the size of the hole. The stress gradient near the hole tip increases for extremely small holes containing less than fifty broken fibers but starts decreasing once the hole gets larger. Both solutions achieve great agreement on these observations. Furthermore, we introduced new fiber breaks at the tip of the hole and investigated its effect on the stress distribution and stress gradient near the hole. The study shows that new fiber breaks at the tip of small holes increase the stress concentration and the stress gradient and eliminate the effect due to the initial shape of the hole, which is expected to be less obvious for large holes.

The next concentrated topic is the effect of matrix yielding or debonding on the fracture behavior of the composite. We focused on two examples: a single broken fiber and an elliptical hole. The results show that either plastic yielding or fiber-matrix debonding not only significantly reduces the stress concentration at the hole tip, it increases the load transfer length and decreases the stress gradient ahead of the crack tip. The hole tip is blunted by the matrix damage very effectively, and thereby the initial shape of the hole is less important than the transverse size of the hole for small holes.

Since fiber strengths and location of flaws are completely random and hard to predict, fibers don't necessarily fail sequentially although that's the location of the highest stress concentration. Experimental observations on metal-matrix composites show that subsequent fiber breaks don't exactly occur in line with the crack and the crack extends in a non-planar fashion. Our results show that both large holes and matrix damage cause smaller stress decay rate along the crack plane and decrease the maximum stress concentration at the hole tip, so it will be very

important to know which is more harmful to the composite strength, broader overloaded regions or higher stress concentrations. Studies using Monte-Carlo simulations assuming fibers following a Weibull distribution for strength (Goda and Phoenix, 1994) suggest that high, localized stress concentrations lower the notched strength but increase the composite strength. Some future study involving the statistics of fiber strength and this stress analysis will be needed to draw the conclusion on what's more important for composite strength.

In our fiber break propagation model, we conveniently assumed the fiber breaks are at the location of highest stress concentration and shear reversals and elastic unloading has not been considered. It's actually very straightforward to account for non-planar crack extension and treat shear reversals and elastic unloading using the current computational scheme. When the local stress on a fiber element reaches its assigned strength, the load on this newly introduce fiber break is unloaded to zero and the nearby matrix element is monitored and compared to its previous strain to determine whether it is elastic, yielded, debonded or unloaded elastically. The deformation history needs to be stored to determine which part of the constitutive stress-strain curve is applied. The newly calculated shear strain in the previously damaged matrix also needs to be checked to achieve consistency in all matrix elements. Once the status of the matrix element is taken care of, the method proceeds to the next increment until no new fiber element have their strength exceeded. This numerical method also allows non-linearity of the constitutive laws.

Compared to other computational techniques, our superposition technique is at least orders of magnitude more efficient and the computation load is only driven by the size of the damaged area, not the size of the composite plane. Agreement between the shear-lag theory and the elastic theory boosts confidence in the shear-

lag model and reinforces its validity. The capability of dealing with matrix damage and accounting for the shapes of holes including introducing new fiber breaks efficiently gives the shear-lag model the largest advantage over the elastic analysis and the other computational methods.

APPENDIX A

The following integration calculates the impact of an isolated segment of length 2δ with distributed fiber breaks. From the shear lag theory, we know the impact of an isolated break is

$$V_{b,n}(\xi) = \operatorname{sgn}\frac{1}{4}\int_0^{\pi}\cos(n\theta)\exp\left(-2|\xi|\sin(\theta/2)\right)d\theta$$

$$L_{b,n}(\xi) = -\frac{1}{2}\int_2^{\pi}\cos(n\theta)\sin(\theta/2)\exp\left(-2|\xi|\sin(\theta/2)\right)d\theta$$

$$\Gamma_{b,n} = \operatorname{sgn}(\xi)\frac{1}{4}\int_0^{\pi}\left\{\cos\left[(n+1)\theta\right]-\cos(n\theta)\right\}\exp\left(-2|\xi|\sin(\theta/2)\right)d\theta$$

Assuming the coefficient distribution is $T_{\kappa}(\zeta)$, the impact of the broken segment is :

$$V_{I,n}(\xi) = \int_{-\delta}^{\delta} T(\zeta)V_{b,n}(\xi-\zeta)d\xi$$

$$L_{I,n}(\xi) = \int_{-\delta}^{\delta} T(\zeta)L_{b,n}(\xi-\zeta)d\xi$$

$$T_{I,n}(\xi) = \int_{-\delta}^{\delta} T(\zeta)T_{b,n}(\xi-\zeta)d\zeta$$

where

$$T_1(\zeta) = 1$$
$$T_2(\zeta) = \zeta$$
$$T_3(\zeta) = \zeta^2 - \frac{\delta^2}{3}$$

For $T_1(\zeta) = 1$,

if $|\xi_i - \xi_k| \neq a$,

$$L_{I,n}(x) = \int_{-\delta}^{\delta}\int_0^{\pi} -\frac{1}{2}\cos((n_i-n_k)\theta)\sin(\frac{\theta}{2})\exp(-2|\xi_i-\xi_k-\xi|\sin(\frac{\theta}{2})d\theta d\xi$$

$$= \frac{1}{4}\int_0^{\pi}\cos((n_i-n_k)\theta)(\operatorname{sgn}(\delta-(\xi_i-\xi_k))\exp(-2(\delta-(\xi_i-\xi_k))\operatorname{sgn}(\delta-(\xi_i-\xi_k))\sin(\frac{\theta}{2}))$$

$$+\operatorname{sgn}(\delta+(\xi_i-\xi_k))\exp(-2(\delta+(\xi_i-\xi_k))\operatorname{sgn}(\delta+(\xi_i-\xi_k))\sin(\frac{\theta}{2})))d\theta$$

if $|\xi_i - \xi_k| = a$,

$$L_{I,n}(x) = \int_{-\delta}^{\delta}\int_{0}^{\pi} -\frac{1}{2}\cos((n_i - n_k)\theta)\sin(\frac{\theta}{2})\exp(-2|\xi_i - \xi_k - \xi|\sin(\frac{\theta}{2})d\theta d\xi$$

$$= \frac{1}{4}\int_{0}^{\pi}\cos((n_i - n_k)\theta)(-1 + \exp(-4\delta\sin(\frac{\theta}{2}))d\theta$$

For $T_2(\zeta) = \zeta$

if $|\xi_i - \xi_k| \neq a$,

$$L_{I,n}(x) = \int_{-\delta}^{\delta}\int_{0}^{\pi} -\frac{1}{2}\cos((n_i - n_k)\theta)\sin(\frac{\theta}{2})\zeta\exp(-2|\xi_i - \xi_k - \xi|\sin(\frac{\theta}{2})d\theta d\xi$$

$$= \frac{1}{8}\int_{0}^{\pi}\frac{\cos((n_i - n_k)\theta)}{\sin(\frac{\theta}{2})}((2\,\mathrm{sgn}(\delta - (\xi_i - \xi_k))\sin(\frac{\theta}{2})\delta + 1)\exp(-2(\delta - (\xi_i - \xi_k))$$

$$\cdot\,\mathrm{sgn}(\delta - (\xi_i - \xi_k))\sin(\frac{\theta}{2})) - (2\,\mathrm{sgn}(\delta + (\xi_i - \xi_k))\sin(\frac{\theta}{2})\delta + 1)\exp(-2(\delta + (\xi_i - \xi_k))$$

$$\mathrm{sgn}(\delta + (\xi_i - \xi_k))\sin(\frac{\theta}{2})))d\theta$$

if $|\xi_i - \xi_k| = a$,

$$L_{I,n}(x) = \int_{-\delta}^{\delta}\int_{0}^{\pi} -\frac{1}{2}\cos((n_i - n_k)\theta)\sin(\frac{\theta}{2})\zeta\exp(-2|\xi_i - \xi_k - \xi|\sin(\frac{\theta}{2})d\theta d\xi$$

$$= -\frac{1}{8}\int_{0}^{\pi}\mathrm{sgn}(\xi_i - \xi_k)\frac{\cos((n_i - n_k)\theta)}{\sin(\frac{\theta}{2})}(-1 + 2\delta\sin(\frac{\theta}{2}) + (2\delta\sin(\frac{\theta}{2}) + 1)\exp(-4\delta\sin(\frac{\theta}{2})))d\theta$$

For the displacement and shear stress distribution, when $T_1(\zeta) = 1$, $|\xi_i - \xi_k| \leq a$

$$V_{I,n}(x) = \frac{1}{4}\int_{-\delta}^{\delta}\int_{0}^{\pi}\cos((n_i - n_k)\theta)\exp(-2|\xi_i - \xi_k - \zeta|)\sin\left(\frac{\theta}{2}\right)d\theta d\zeta$$

$$= -\frac{1}{8}\int_{0}^{\pi}\frac{\cos((n_i - n_k)\theta)}{\sin\left(\frac{\theta}{2}\right)}\left(\exp\left(2(\xi_i - \xi_k - \delta)\sin\frac{\theta}{2}\right) - \exp\left(-2(\xi_i - \xi_k - \delta)\sin\frac{\theta}{2}\right)\right)d\theta$$

$$= -\frac{1}{4}\int_{0}^{\pi}\frac{\cos((n_i - n_k)\theta)}{\sin\left(\frac{\theta}{2}\right)}\exp\left(-2\delta\sin\frac{\theta}{2}\right)\sinh\left(2(\xi_i - \xi_k)\sin\frac{\theta}{2}\right)d\theta$$

$$T_{I,n}(x)=\frac{1}{4}\int_{-\delta}^{\delta}\int_{0}^{\pi}\{\cos(((n_i-n_k)+1)\theta)-\cos(((n_i-n_k))\theta)\}$$

$$\exp(-2|\xi_i-\xi_k-\zeta|)\sin\left(\frac{\theta}{2}\right)d\theta d\zeta$$

$$=-\frac{1}{8}\int_{0}^{\pi}\frac{\cos(((n_i-n_k)+1)\theta)-\cos(((n_i-n_k))\theta)}{\sin\left(\frac{\theta}{2}\right)}$$

$$\cdot\left(\exp\left(2(\xi_i-\xi_k-\delta)\sin\frac{\theta}{2}\right)-\exp\left(-2(\xi_i-\xi_k-\delta)\sin\frac{\theta}{2}\right)\right)d\theta$$

$$=-\frac{1}{4}\int_{0}^{\pi}\frac{\cos(((n_i-n_k)+1)\theta)-\cos(((n_i-n_k))\theta)}{\sin\left(\frac{\theta}{2}\right)}\exp\left(-2\delta\sin\frac{\theta}{2}\right)$$

$$\sinh\left(2(\xi_i-\xi_k)\sin\frac{\theta}{2}\right)d\theta$$

If $T_1(\zeta)=1$, $|\xi_i-\xi_k|\geq a$, we have the following

$$V_{I,n}(x)=\frac{1}{4}\int_{-\delta}^{\delta}\int_{0}^{\pi}\{\cos(((n_i-n_k)+1)\theta)-\cos(((n_i-n_k))\theta)\}\exp(-2|\xi_i-\xi_k-\zeta|)\sin\left(\frac{\theta}{2}\right)d\theta d\zeta$$

$$=\frac{1}{8}\int_{0}^{\pi}\operatorname{sgn}(\xi_i-\xi_k-\delta)\frac{\cos((n_i-n_k)\theta)}{\sin\left(\frac{\theta}{2}\right)}\exp\left(-2\operatorname{sgn}(\xi_i-\xi_k-\delta)(\xi_i-\xi_k)\sin\frac{\theta}{2}\right)$$

$$\cdot\left(\exp\left(2\delta\sin\frac{\theta}{2}\right)-\exp\left(-2\delta\sin\frac{\theta}{2}\right)\right)d\theta$$

$$=\frac{1}{4}\int_{0}^{\pi}\operatorname{sgn}(\xi_i-\xi_k-\delta)\frac{\cos((n_i-n_k)\theta)}{\sin\left(\frac{\theta}{2}\right)}\exp\left(-2\operatorname{sgn}(\xi_i-\xi_k-\delta)(\xi_i-\xi_k)\sin\frac{\theta}{2}\right)\sinh\left(2\delta\sin\frac{\theta}{2}\right)d\theta$$

$$T_{I,n}(x)=\frac{1}{4}\int_{-\delta}^{\delta}\int_{0}^{\pi}\{\cos(((n_i-n_k)+1)\theta)-\cos(((n_i-n_k))\theta)\}\exp(-2|\xi_i-\xi_k-\zeta|)\sin\left(\frac{\theta}{2}\right)d\theta d\zeta$$

$$=\frac{1}{8}\int_{0}^{\pi}\operatorname{sgn}(\xi_i-\xi_k-\delta)\frac{\cos(((n_i-n_k)+1)\theta)-\cos(((n_i-n_k))\theta)}{\sin\left(\frac{\theta}{2}\right)}\exp\left(-2\operatorname{sgn}(\xi_i-\xi_k-\delta)(\xi_i-\xi_k)\sin\frac{\theta}{2}\right)$$

$$\left(\exp\left(2\delta\sin\frac{\theta}{2}\right)-\exp\left(-2\delta\sin\frac{\theta}{2}\right)\right)d\theta$$

$$=\frac{1}{4}\int_{0}^{\pi}\operatorname{sgn}(\xi_i-\xi_k-\delta)\frac{\cos(((n_i-n_k)+1)\theta)-\cos(((n_i-n_k))\theta)}{\sin\left(\frac{\theta}{2}\right)}\exp\left(-2\operatorname{sgn}(\xi_i-\xi_k-\delta)(\xi_i-\xi_k)\sin\frac{\theta}{2}\right)$$

$$\cdot\sinh\left(2\delta\sin\frac{\theta}{2}\right)d\theta$$

APPENDIX B

The load transmission factors can be integrated semi-analytically.

$$\Psi_{lk}^{(1,\nu)}(\xi)=\int_{\delta}^{\delta}T_{\nu}(\zeta)\left.\frac{dL_{b,n_i-n_k}(\xi-\xi_k-\zeta)}{d\xi}\right|_{\xi=\xi_l}d\zeta$$

$$=\int_{\delta}^{\delta}\int_{0}^{\pi}T_{\nu}(\zeta)\operatorname{sgn}(\xi_l-\xi_k-\zeta)\cos[(n_l-n_k)\theta]\sin^2\left(\frac{\theta}{2}\right)\exp\left(-2|\xi_l-\xi_k-\zeta|\sin\left(\frac{\theta}{2}\right)\right)d\theta d\zeta$$

$$\Psi_{lk}^{(2,\nu)}(\xi)=\int_{\delta}^{\delta}T_{\nu}(\zeta)\left.\frac{d^2L_{b,n_i-n_k}(\xi-\xi_k-\zeta)}{d\xi^2}\right|_{\xi=\xi_l}d\zeta$$

$$=-2\int_{\delta}^{\delta}\int_{0}^{\pi}T_{\nu}(\zeta)\cos[(n_l-n_k)\theta]\sin^3\left(\frac{\theta}{2}\right)\exp\left(-2|\xi_l-\xi_k-\zeta|\sin\left(\frac{\theta}{2}\right)\right)d\theta d\zeta$$

If $|\xi_l-\xi_k|\neq\delta$

$$\Psi_{lk}^{(1,0)}(\xi)=-\int_{\delta}^{\delta}\int_{0}^{\pi}\operatorname{sgn}(\xi_l-\xi_k-\zeta)\cos[(n_l-n_k)\theta]\sin^2\left(\frac{\theta}{2}\right)$$

$$\cdot\exp\left(-2|\xi_l-\xi_k-\zeta|\sin\left(\frac{\theta}{2}\right)\right)d\theta d\zeta$$

$$=-\frac{1}{2}\int_{0}^{\pi}\cos[(n_l-n_k)\theta]\sin\left(\frac{\theta}{2}\right)$$

$$\cdot\left\{\exp\left(-2(-(\xi_l-\xi_k)+\delta)\operatorname{sgn}(-(\xi_l-\xi_k)+\delta)\sin\left(\frac{\theta}{2}\right)\right)+\right.$$

$$\left.\exp\left(-2((\xi_l-\xi_k)+\delta)\operatorname{sgn}((\xi_l-\xi_k)+\delta)\sin\left(\frac{\theta}{2}\right)\right)\right\}d\theta$$

$$\Psi_{lk}^{(1,1)}(\xi) = -\int_{\delta}^{\delta}\int_{0}^{\pi} \zeta\,\mathrm{sgn}(\xi_l - \xi_k - \zeta)\cos[(n_l - n_k)\theta]\sin^2\left(\frac{\theta}{2}\right)$$

$$\cdot \exp\left(-2|\xi_l - \xi_k - \zeta|\sin\left(\frac{\theta}{2}\right)\right)d\theta d\zeta$$

$$= -\frac{1}{4}\int_{0}^{\pi}\cos[(n_l - n_k)\theta]\times$$

$$\left\{\exp\left(-2(-(\xi_l - \xi_k) + \delta)\mathrm{sgn}(-(\xi_l - \xi_k) + \delta)\sin\left(\frac{\theta}{2}\right)\right)\right.$$

$$\cdot\left(2\delta\sin\left(\frac{\theta}{2}\right) + \mathrm{sgn}(-(\xi_l - \xi_k) + \delta)\right) + \exp\left(-2((\xi_l - \xi_k) + \delta)\mathrm{sgn}((\xi_l - \xi_k) + \delta)\sin\left(\frac{\theta}{2}\right)\right)$$

$$\left.\cdot\left(2\delta\sin\left(\frac{\theta}{2}\right) + \mathrm{sgn}((\xi_l - \xi_k) + \delta)\right)\right\}d\theta$$

If $|\xi_l - \xi_k| = \delta$

$$\Psi_{lk}^{(1,0)}(\xi) = -\int_{\delta}^{\delta}\int_{0}^{\pi}\mathrm{sgn}(\xi_l - \xi_k - \zeta)\cos[(n_l - n_k)\theta]\sin^2\left(\frac{\theta}{2}\right)$$

$$\cdot \exp\left(-2|\xi_l - \xi_k - \zeta|\sin\left(\frac{\theta}{2}\right)\right)d\theta d\zeta$$

$$= \frac{1}{2}\mathrm{sgn}(\xi_l - \xi_k)\left(\int_{0}^{\pi}\cos[(n_l - n_k)\theta]\sin\left(\frac{\theta}{2}\right)\left\{\exp\left(-4\delta\,\mathrm{sgn}(\xi_l - \xi_k)\sin\left(\frac{\theta}{2}\right)\right) - 1\right\}d\theta\right.$$

$$\Psi_{lk}^{(1,1)}(\xi) = -\int_{\delta}^{\delta}\int_{0}^{\pi}\zeta\,\mathrm{sgn}(\xi_l - \xi_k - \zeta)\cos[(n_l - n_k)\theta]\sin^2\left(\frac{\theta}{2}\right)$$

$$\cdot \exp\left(-2|\xi_l - \xi_k - \zeta|\sin\left(\frac{\theta}{2}\right)\right)d\theta d\zeta$$

$$= -\frac{1}{4}\int_{0}^{\pi}\mathrm{sgn}(\xi_l - \xi_k)\cos[(n_l - n_k)\theta]\left\{2\delta\sin\left(\frac{\theta}{2}\right) - 1\right.$$

$$\left.+ \exp\left(-4\delta\,\mathrm{sgn}(\xi_l - \xi_k)\sin\left(\frac{\theta}{2}\right)\right)\left(2\delta\sin\left(\frac{\theta}{2}\right) + \mathrm{sgn}(\xi_l - \xi_k)\right)\right\}d\theta$$

$$\mathrm{H}_{ji}^{(v)} == \int_{\delta}^{\delta} T_v(\zeta)\Gamma_{b,n_j - n_i}(\xi_j - \xi_i - \zeta)d\zeta$$

$$= \frac{1}{4}\int_{-\delta}^{\delta}\int_{0}^{\pi} T_v(\zeta)\mathrm{sgn}(\xi_j - \xi_i - \zeta)\{\cos[(n_j - n_i + 1)\theta] - \cos((n_j - n_i)\theta)\}$$

$$\cdot \exp\left(-2|\xi_j - \xi_i - \zeta|\sin(\theta/2)\right)d\theta d\zeta$$

If $|\xi_j - \xi_i| \neq \delta$

$$\mathrm{H}_{ji}^{(0)}(\xi)=\frac{1}{4}\int_{\delta}^{\delta}\int_{0}^{\pi}\operatorname{sgn}\left(\xi_j-\xi_i-\zeta\right)\left\{\cos\left[\left(n_j-n_i+1\right)\theta\right]-\cos\left(\left(n_j-n_i\right)\theta\right)\right\}$$

$$\cdot\exp\left(-2\left|\xi_j-\xi_i-\zeta\right|\sin\left(\frac{\theta}{2}\right)\right)d\theta d\zeta$$

$$=\frac{1}{8}\int_{0}^{\pi}\frac{\left\{\cos\left[\left(n_j-n_i+1\right)\theta\right]-\cos\left(\left(n_j-n_i\right)\theta\right)\right\}}{\sin\left(\frac{\theta}{2}\right)}\times$$

$$\left\{\exp\left(-2\left(-\left(\xi_j-\xi_i\right)+\delta\right)\operatorname{sgn}\left(-\left(\xi_j-\xi_i\right)+\delta\right)\sin\left(\frac{\theta}{2}\right)\right)+\right.$$

$$\left.\exp\left(-2\left(\left(\xi_j-\xi_i\right)+\delta\right)\operatorname{sgn}\left(\left(\xi_j-\xi_i\right)+\delta\right)\sin\left(\frac{\theta}{2}\right)\right)\right\}d\theta$$

$$\mathrm{H}_{ji}^{(1)}(\xi)=\frac{1}{4}\int_{\delta}^{\delta}\int_{0}^{\pi}\zeta\operatorname{sgn}\left(\xi_j-\xi_i-\zeta\right)\left\{\cos\left[\left(n_j-n_i+1\right)\theta\right]-\cos\left(\left(n_j-n_i\right)\theta\right)\right\}$$

$$\cdot\exp\left(-2\left|\xi_j-\xi_i-\zeta\right|\sin\left(\frac{\theta}{2}\right)\right)d\theta d\zeta$$

$$=\frac{1}{16}\int_{0}^{\pi}\frac{\left\{\cos\left[\left(n_j-n_i+1\right)\theta\right]-\cos\left(\left(n_j-n_i\right)\theta\right)\right\}}{\sin\left(\frac{\theta}{2}\right)^2}$$

$$\cdot\left\{\exp\left(-2\left(-\left(\xi_j-\xi_i\right)+\delta\right)\operatorname{sgn}\left(-\left(\xi_j-\xi_i\right)+\delta\right)\sin\left(\frac{\theta}{2}\right)\right)\right.$$

$$\left(2\delta\sin\left(\frac{\theta}{2}\right)+\operatorname{sgn}\left(-\left(\xi_j-\xi_i\right)+\delta\right)\right)+$$

$$\left.\exp\left(-2\left(\left(\xi_j-\xi_i\right)+\delta\right)\operatorname{sgn}\left(\left(\xi_j-\xi_i\right)+\delta\right)\sin\left(\frac{\theta}{2}\right)\right)\left(2\delta\sin\left(\frac{\theta}{2}\right)+\operatorname{sgn}\left(\left(\xi_j-\xi_i\right)+\delta\right)\right)\right\}d\theta$$

If $\left|\xi_l-\xi_k\right|=\delta$

$$\mathrm{H}_{ji}^{(0)}(\xi)=\frac{1}{4}\int_{\delta}^{\delta}\int_{0}^{\pi}\operatorname{sgn}(\xi_j-\xi_i-\zeta)\{\cos[(n_j-n_i+1)\theta]-\cos((n_j-n_i)\theta)\}$$

$$\cdot\exp\left(-2|\xi_j-\xi_i-\zeta|\sin\left(\frac{\theta}{2}\right)\right)d\theta d\zeta$$

$$=-\frac{1}{8}\operatorname{sgn}(\xi_j-\xi_i)\int_{0}^{\pi}\frac{\{\cos[(n_j-n_i+1)\theta]-\cos((n_j-n_i)\theta)\}}{\sin\left(\frac{\theta}{2}\right)}$$

$$\left\{\exp\left(-4\delta\operatorname{sgn}(\xi_j-\xi_i)\sin\left(\frac{\theta}{2}\right)\right)-1\right\}d\theta$$

$$\mathrm{H}_{ji}^{(1)}(\xi)=\frac{1}{4}\int_{\delta}^{\delta}\int_{0}^{\pi}\zeta\operatorname{sgn}(\xi_j-\xi_i-\zeta)\{\cos[(n_j-n_i+1)\theta]-\cos((n_j-n_i)\theta)\}$$

$$\cdot\exp\left(-2|\xi_j-\xi_i-\zeta|\sin\left(\frac{\theta}{2}\right)\right)d\theta d\zeta$$

$$=\frac{1}{16}\int_{0}^{\pi}\operatorname{sgn}(\xi_j-\xi_i)\frac{\{\cos[(n_j-n_i+1)\theta]-\cos((n_j-n_i)\theta)\}}{\sin\left(\frac{\theta}{2}\right)^2}$$

$$\left\{2\delta\sin\left(\frac{\theta}{2}\right)-1+\exp\left(-4\delta\operatorname{sgn}(\xi_j-\xi_i)\sin\left(\frac{\theta}{2}\right)\right)\left(2\delta\sin\left(\frac{\theta}{2}\right)+\operatorname{sgn}(\xi_j-\xi_i)\right)\right\}d\theta$$

REFERENCES

Awerbach, J. and Hahn, H. T. (1977). Fracture behavior of metal matrix composites. *Proc. Soc. Eng. Sci., Recent Advances in Engng Sci.* **4**, 342-350.

Beyerlein, I.J., Phoenix, S.L. and Sastry, A.M. (1995). Stress concentration around aligned fiber breaks in a unidirectional composite with an elastic-plastic matrix. *Simulation of Materials Processing: Theory, Methods and Applications,* 237-242. AA Balkema Publishers, The Netherlands.

Beyerlein, I. J. Phoenix, S. L. and Sastry, A. M. (1996). Comparison of shear-lag theory and continuum fracture mechanics for modeling fiber and matrix stresses in an elastic cracked composite lamina. *Int. J. Solids Struct.* **33**, 2543-2574.

Beyerlein, I. J. and Phoenix, S. L. (1996a) Statistics of fracture for an elastic notched composite lamina containing Weibull Fibers: Features from Monte-Carlo simulation. *Engineering Fracture Mechanics*, **57**, 241-265.

Beyerlein, I. J. and Phoenix, S. L. (1996b) Statistics of fracture for an elastic notched composite lamina containing Weibull fibers-Probability models of crack growth. *Engineering Fracture Mechanics*, **57**, 247-299.

Beyerlein, I. J. and Phoenix, S.L. (1996). Stress concentrations around multiple fiber breaks in an elastic matrix with local yielding or debonding using quadratic influence superposition***. J. Mech. Phys. Solids***, **44**, No12, 1997-2039.

Bishop, S. M. (1972). Royal Aircraft Establishment Technical Report no.72026.

Chang, C. I., Conway, H. D. and Weaver, T. C. (1972). The elastic constants and bond stresses for a three-dimensional composite reinforced by discontinuous fibers. *Fiber Sci. Tchnol.* **5**, 143-162

Connell, S. J., Zok, F. W., Du, Z. Z . and Suo, Z. (1994). On the tensile properties of a fiber reinforced titanium matrix composite- II. Influences of notches and holes. *Acta Metall. Mater*. **42**, 3451-3461

Case, S.W. and Reifsnider, L.L. (1995). Micromechanical analysis of fiber fracture in unidirectional composite materials. *Int. J. Solids Struc*. **33**, 3795-3812.

Chou, T.W. (1992). *Microstructural Design of Fiber Composites*. Cambridge University Press, New York.

Connell, S.J., Zok, F. W., Du, Z. Z. and Suo, Z. (1994) On the tensile properties of a fiber reinforced titanium matrix composite- II. Influences of notches and holes. *Acta Metall. Mater*, **42**, 3451-3461.

Cox, H. L. (1952) The elasticity and strength of paper. *Brit. J. Appl. Phys*. **3**, 73-79.

Dharani, L.R., Jones, W.F., and Goree, J.G. (1993). Mathematical modeling of damage in unidirectional composites, *Engng Fract. Mech.* **17**, 555-573

Dootson, M., Shaw, C. & Hinnels, G. (1976). British aircraft corporation technical report. No. 4503.

Fichter, W.B. (1969). Stress concentrations around broken filaments in a filament-stiffened sheet. NASA TN D-5453.

Fukuda, H. and Chou, T.W. (1981). An advanced shear-lag model applicable to discontinuous fiber composites. *J. Comp. Mater*. 15, 79-91.

Fukuda, H. and Chou, T. W. (1983) Stress concentrations in a hybrid composite sheet. *J. Appl. Mech.* **50**, 845-848

Goda, K. and Phoenix, S.L. (1994). Reliability approach to the tensile strength of unidirectional CFRP composites by Monte-Carlo simulation in a shear-lag model. *Comp. Sci. Tech.* **50**, 457-468.

Goree, J. G., Dharani, L. R. and Jones, W. F. (1989). Crack growth and fracture of continuous fiber metal matrix composites: analysis and experiments. Metal

Matrix Composites: Testing, Analysis, and Failure Modes, ASTM STP 1032 (ed. W. S. Johnson). 251-269.

Goree, J. G., and Gross, R. S. (1979). Analysis of a unidirectional composite containing broken fibers and matrix damage. *Engng Fract. Mech*. **13**, 563-578

Goree, J. G., and Gross, R. S. (1980). Stresses in a three-dimensional unidirectional composite containing broken fibers. *Engng Fract. Mech*. **13**, 395-405

Green A. E. (1945) Stress systems in isotropic and orthotropic plates. V. *Proc. Roy Soc. A,* **184**, 231-252

Griffith, A. A. (1920). *Phil. Trans. R. Soc. Lond.* **A 221**, 163-198

Hedgepeth, J.M. (1961). *Stress concentrations in filamentary structures*. NASA TN D-882

Hedgepeth, J.M. and Van Dyke,P. (1967). Local stress concentration in imperfect filamentary composite materials. *J. Comp. Mat.* **1**, 294-309.

Hikami, F. and Chou, T. W. (1990). Explicit crack problem solutions of unidirectional composites:elastic stress concentrations. *AIAA J*. **28**, 499-505

Irwin, G. R. (1948). In Fracturing of Metals. Cleveland, Ohio: American Society for Metals.

Jones, W.F. and Goree, J.G. (1983). Fracture behavior of unidirectional boron/ Al composite laminates. *Mech. Comp. Mat., ASME AMD***. 58**,171-178

Lekhnitskii, S.G. (1963). *Theory of Elasticity of an Anisotropic Body*. Holden-Day, San Francisco.

Mandell, J. F., Wang, S. S. & McGarry, F. J. (1975) *J. Comp. Mater*. **9**, 266-287

McClintock, F. A. (1969). Problems in the fracture of composites with plastic matrices. *Fourth Symposium on High Performance Composites, St Louis, MO. Monsanto Co. and Washington University*.

Nairn, J. A., Liu, S., Chen, H. and Wedgewood, A. R. (1991) Longitudinal splitting in epoxy and K-polymer composites: shear lag analysis including the effect of fiber bridging. *J. Comp. Mater*. **25**, 1087-1101.

Nairn, J. A. (1988). Fracture mechanics of unidirectional composites using the shear-lag model I: Theory. *J. Comp. Mater*. **22**, 561-588

Nairn, J. A. (1988). Fracture mechanics of unidirectional composites using the shear-lag model I: Experiment. *J. Comp. Mater*. **22**, 561-588

Nedele, M.R. and Wisnom, M.R. (1994). Three-dimensional finite element analysis of the stress concentration at a single fiber break. *Comp. Sci. Tech*. **51**,517-524

Ochiai, S., Schulte, K., and Peters, P. W. M. (1992). Strain concentration factors for fibers and matrix in unidirectional composites. *Comp. Sci. Tech*. **41**, 237-256

Potter R. T. (1978) On the mechanism of tensile fracture in notched fiber reinforced plastics. *Proc. R. Soc. Lond*. **A. 361**, 325-241 (1978).

Reedy, E. D. (1980) Analysis of center notched monolayers with application to Boron/Al composites. *J. Mech. Phys. Solids*. **28**, 265-286

Reedy, E. D. (1984). Fiber stresses in a crack monolayer: Comparison of shear-lag and 3-D finite element predictions. *J. Comp. Mat.* **18**, 595-607.

Rossettos, J.N. and Olia, M. (1993). Stress concentration and post matrix yield at fiber breaks in hybrid composites. In *Proc 13th Army Symp. Solid Mechanics*. Plymouth, MA, pp. 201-212

Rossettos, J. N. and Shishesaz, M. (1987). Stress concentration in fiber composite sheets including matrix extension. *J. Appl. Mech*. **54**, 723-724

Savin A. E. (1961*). Stress concentration around holes*. 152-174, London Pergamon Pergamon Press

Sastry, A.M. and Phoenix, S.L. (1993). Load redistribution near non-aligned fiber breaks in a two-dimensional unidirectional composite using break-influence superposition, *J. Mat. Sci. Lett.* **12**, 1596-1599

Sastry, A. M. (1994). *Calculation of stress concentrations in damaged composite solids for determining strength distributions*. PhD thesis, Mechanical Engineering, Cornell University.

Sih, G.C. (1981). *Cracks in Composite Materials*. Martinus Nijhoff Publishers, Boston.

Smith, C. B. (1944). Effect of elliptic or circular holes on the stress distribution in plates of wood or plywood considered as orthotropic materials. U.S. Dept. Agric., For. Prod. Lab. Mimeo 1510.

Van Dyke, P. and Hedgepeth, J. M. (1969). Stress concentrations from single-filament failures in composite materials. *Textile Res. J.* **39**, 618-626.

Waddoups, M. E., Eisenmann, J. R. & Kaminski, B. E. (1971). *J. Comp. Mater.* **5**, 446-454

Wolla, J. M. and Goree, J. G. (1987). Experimental evaluation of longitudinal splitting in unidirectional composites. *J. Comp. Mat.* **21**, 49-67.